Atomic Force Microscopy for Characterizing Dust Particles of the Martian Arctic Soils

Thèse présentée à la Faculté des Sciences
Institut de Microtechnique
Université de Neuchâtel

Pour l'obtention du grade de docteur ès sciences

par

Daniel Parrat

Acceptée sur proposition du jury :

Prof. Urs Staufer, directeur de thèse
Prof. Nico de Rooij, rapporteur
Prof. W. Thomas Pike, rapporteur
Prof. Herbert Shea, rapporteur

Soutenue le 26 novembre 2007

Neuchâtel
2008

Université de Neuchâtel

FACULTE DES SCIENCES
Secrétariat-Décanat de la faculté
- Rue Emile-Argand 11
- CP 158
- CH-2009 Neuchâtel

IMPRIMATUR POUR LA THESE

Atomic Force Microscopy for Characterizing Dust Particles of the Martian Arctic Soils

Daniel PARRAT

UNIVERSITE DE NEUCHATEL

FACULTE DES SCIENCES

La Faculté des sciences de l'Université de Neuchâtel,
sur le rapport des membres du jury

MM. U. Staufer (directeur de thèse), N. de Rooij,
H. Shea (EPF Lausanne) et
W.T. Pike (Imperial College, Londres)

autorise l'impression de la présente thèse.

Neuchâtel, le 15 janvier 2008

Le doyen :

F. Kessler

Felix Kessler

■ Téléphone : +41 32 718 21 00 ■ Fax : +41 32 718 21 03 ■ E-mail : secretariat.sciences@unine.ch ■ www.unine.ch/sciences

Till Lotta

Abstract

Keywords: Atomic force microscope, Mars, dust particles.

This thesis describes the development, the fabrication and the characterization of an atomic force microscope (AFM) for Mars exploration. Onboard the Phoenix mission, this instrument should shortly collect precious information about the size and the shape of fine dust particles of the martian soil and atmosphere.

Atomic force microscopy is a three dimensional imaging technique determining the topography of the measured sample with a very high resolution. It is based on the detection of atomic forces acting between the sample and a very sharp sensor tip scanned across it. With its amazing resolution, this technique is used in many fields, such as microelectronics or bioscience. Due to its large size, relative fragility and complexity of operation, this instrument is not intrinsically intended for space missions. Nevertheless, the technological improvements in the field of microsystems allowed creating a miniaturized instrument with very high functionality.

The AFM presented in this dissertation is based on a previous model showing a few disadvantages when scanning at low temperature. Using an innovative polyimide spring system, this problem was solved for the new instrument. Since non linear distortions of the scan plane were observed, software tools have been created for correcting them. Before its delivery to NASA, the instrument has successfully passed the environmental testing required by the mission. In addition

to the hardware, the flight software commands allowing controlling autonomously the AFM were created and tested in collaboration with our partners. The autonomous operation of the instrument has then been demonstrated on a testbed and on a flight-like prototype of the Phoenix Lander.

In parallel to the technical achievements, the AFM was characterized by measuring different samples. Images of particles artificially fixed to their substrate have demonstrated that the instrument could characterize particles having a diameter from 0.1 to 5 micrometers. As the shape and the size of the particles were influenced by the geometry of the sensor tip, algorithms correcting these artifacts have been created and applied to images. The size distribution of a sample was also determined successfully based on an AFM image.

Measurement on Mars analogues has indicated that atomic force microscopy could not be performed on any sample. The particle size, their arrangement and their adhesion to the substrate were key parameters. In particular, it was observed that piles of particles were not appropriated for AFM measurements, and could possibly harm the sensor chip. However, it was proven that an optical inspection of the samples allowed estimating the potential risk for the AFM.

Résumé

Mots clefs : Microscope à force atomique, Mars, particules de poussière.

Cette thèse traite du développement, de la fabrication et de la caractérisation d'un microscope à force atomique (AFM) pour l'exploration de la planète Mars. A bord de la mission Phoenix, cet instrument devrait recueillir prochainement de précieuses informations sur la taille et la forme de fines particules de poussière présentes à la surface de Mars et en suspension dans l'atmosphère.

La microscopie à force atomique est une technique d'imagerie tridimensionnelle permettant d'établir avec une très haute résolution la topographie de l'échantillon mesuré. Elle se base sur la détection des forces atomiques agissant entre l'échantillon et une pointe microscopique balayée sur celui-ci. Grâce à sa formidable résolution, cette technique est utilisée dans des nombreuses applications, allant de l'industrie des semi-conducteurs à la biologie. La taille d'un AFM, sa relative fragilité et sa complexité d'utilisation ne favorise pas intrinsèquement son utilisation dans l'espace. Grâces aux progrès technologiques dans le domaines des microsystèmes, un maximum de fonctionnalité a pourtant pu être incorporé dans un instrument de taille très modeste.

L'AFM présenté dans cette dissertation est basé sur un modèle antérieur présentant quelques problèmes de balayage à basse température. Grâce à un système de suspension en polyimide, un matériau

connu pour sa stabilité en température, ce problème a été résolu pour le nouvel instrument. Des déformations non linéaires du plan de balayage ayant été observées, un logiciel de correction a été mis au point. Avant d'être délivré à la NASA, l'instrument a également passé avec succès les essais en environnement propres à la mission Phoenix. En plus des composantes matérielles de l'AFM, les commandes permettant de manoeuvrer l'instrument de manière autonome ont été crées et testées en collaboration avec nos partenaires. Le fonctionnement autonome de l'appareil a ensuite été démontré sur un banc d'essai ainsi que sur une reproduction de l'atterrisseur de la mission.

En parallèle aux développements techniques, la caractérisation de l'AFM a été réalisée par la mesure de différent échantillons. Les mesures exécutées sur des particules fixées artificiellement à leur substrat ont démontrées que l'instrument pouvait mesurer des particules de diamètre compris entre 0.1 et 5 micromètres. Comme la forme et la taille des particules étaient affectées par la géométrie de la pointe, des algorithmes corrigeant ces artefacts ont été créés et appliqués à des images. La distribution de taille des particules d'une image a également été déterminée avec succès.

Des mesures d'échantillons analogues à ceux qui devraient être observés sur Mars ont indiqué que l'instrument ne pourrait pas prendre des images de n'importe quel échantillon, la taille des particules, leur arrangement sur le substrat ainsi que leur adhésion étant critiques. En particulier, il a été observé que des particules empilées les unes sur les autres étaient très difficiles à mesurer, et constituaient un risque pour l'instrument. Finalement, des solutions ont été proposées afin d'évaluer pendant les opérations quels échantillons sont adaptés pour les mesures.

Contents

Chapter 1

Introduction

This introduction gives an overview of the scientific questions about Mars. Then, it described the Phoenix mission, and in particular the MECA payload, since the instrument described in this thesis was part of it. A small introduction to atomic force microscopy is given, followed by a description of the result obtained by the previous version of the instrument. Finally, a few comments about the development of microsystems for space applications are given.

1.1 The planet Mars

1.1.1 Overview

Mars is the fourth planet from the Sun in the Solar System. Based on its color, caused by a soil rich in iron oxides, it is also called the "Red Planet". The cold and dry landscape of Mars, with its deserts, valleys, canyons and volcanoes, makes it look very similar to some terrestrial regions. Despite its radius being half the one of Earth, it presents almost the same amount of land areas. Compared to Earth, the relief of Mars is extreme, showing the highest volcano - and mountain - of the Solar System, the 26-km high Mons Olympus, and the largest canyon - the 7-km deep Valles Marineris, extended for

Table 1.1: Mars compared to Earth.

Parameter	Mars	Earth
Average dist. from Sun	228 mio km	150 mio km
Mean orbital velocity	24.1 km s^{-1}	29.8 km s^{-1}
Equatorial radius	3,396 km	6,378 km
Polar radius	3,376 km	6,356 km
Tilt of Axis	25.2 degrees	23.5 degrees
Length of year	687 Earth days	365.25 days
Length of day	24 h 40'	24 h 00'
Gravity	3.71 m s^{-2}	9.80 m s^{-2}
Average temperature	-62.7 deg C	13.9 deg C
Temperature range	-133 to +22 deg C	-73 to +72 deg C
Satellites	Phobos, Demos	The Moon

more than 4000 km. However, large plains also exist on the planet, making its exploration easier. Table 1.1 shows a comparison of the general characteristics of both planets [1]. Despite several similarities with our planet, humans could not survive the martian conditions without spacesuits. Surface temperatures can decrease below -120 deg C during the polar winters, and the very thin atmosphere of the planet is composed mostly of carbon dioxide.

1.1.2 Atmosphere

The thin atmosphere of Mars, whose pressure is less than 1% of the surface pressure on Earth, is not only due to the small size of the planet, but also to the loss of its magnetosphere four billions years ago, exposing the ionosphere to the solar wind. Ionized atmospheric particles trailing off into space behind Mars have been recently observed by Mars Global Surveyor (MGS) and Mars Express [2, 3]. The atmosphere consists of 95% carbon dioxide, 3% nitrogen, 1.6% argon, and contains traces of oxygen, carbon monoxide and water [1],

a few other gases having been detected in very small quantities. As no protective ozone layer exists on Mars, the surface of the planet is exposed to the dangerous ultraviolet radiation.

The color of the sky seen from Mars would appear orange-brown, as many fine dust particles are transported by the martian winds. In his PhD thesis, S. Gautsch summarized the different estimations performed on the size of these particles [4]. At that time, the last results were those of the thermal emission spectrometer of MGS, which estimated the dust particles radii to be between 1.5 and 1.8 micrometers [5]. New measurements from the two Mars Exploration Rovers (MER) confirmed that the size of these particles should be about 1.5 micrometers [6].

1.1.3 Climate

As Mars presents about the same tilt axis as the Earth, seasons exist on Mars, and cause for example the sublimation of water and dioxide ice from the polar caps. In order to understand the climate, the exchanges of water between the subsurface ice and the atmosphere must also be studied, as well as the movements of the large amounts of dust by the atmosphere, which can sometimes lead to global dust storms, such as the one observed in 2001.

Having a good mapping of the weather during few years should allow improve the modeling of the past climate. In particular, the information on the water vapor and particles content of the atmosphere at different period of the year is critical. Based on accurate climate models, one could determine if the climate of Mars was ever like that of Earth. This could also be very useful information for understanding the climate changes of our own planet.

1.1.4 Geology

The geological feature observed at the surface of the planet were created by six different geological processes that are either currently operating on Mars or have operated during martian history. These

include the aeolian, cratering, hydrological, landslides, tectonic, and volcanic processes. The manifestations of each process can take many different forms. For the hydrological process for example, tree-shaped drainage systems, floods and gullies can be observed.

Looking at a smaller scale to the rocks, the grains and the fine particles of the surface, information on the past of the observed site can be determined. For example, if fine sediments of mud and silt are found at the site, it may support the hypothesis of an ancient ocean. Alternatively, coarse sediments of sand might indicate past flowing water, especially if these grains are rounded and well sorted.

1.1.5 Search for Life on Mars

The search of past or present life is the "holy grail" of Mars exploration. Any discovery in that field would certainly be as revolutionary as the first man step onto the Moon.

It is very likely that if life has rose on Mars, it was in presence of liquid water. Thus, the best places to look at are areas of the planet where liquid water was once stable. According to some theories, the famous gullies visible at the surface of the planets are the products of shallow and deep aquifers, which are geological formations containing water [7]. If these pockets of water are really in the subsurface on Mars, they could be a good habitat for microbes.

As water ice is present at the martian poles, these locations could be very interesting. Hence, due to the precession of the planet (the change of its axial tilt), liquid water may exist for short periods every 100,000 years. Based on recent discoveries in Greenland [8], one could imagine that a dormant microbial colony may exist in the martian arctic.

In addition to the search of areas favorable to life, biosignatures could indicate the past presence of life. On Earth, locations were fossils are preserved can be identified. Based on this knowledge, search of such environments are on their way on Mars. If fossils are present on Mars, they should not be larger than a few micrometers, single-

cell structures resembling bacteria on Earth. There is no evidence or suggestion that any higher life form ever existed on Mars.

1.2 The Phoenix Mars Mission

Launched on the 4th of August 2007, the Phoenix Mars Mission is the first in NASA's Scout Program (see 1.2.3). It should land in May 2008 in the northern plains of Mars, where large amounts of water ice are expected below the surface. Using a robotic arm, it will dig through the top soil layer to the ice below and deliver samples to sophisticated instruments on its platform.

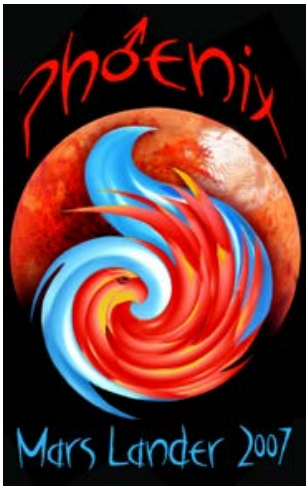

Figure 1.1: The logo of the Phoenix mission.

1.2.1 Objectives

The two objectives of the mission are to study the history of water and to search for habitable conditions in the martian arctic.

History of water in all its phases

At the poles, interactions between the water ice at or below the surface and the water vapor in the atmosphere certainly plays a great role for the weather and the climate of Mars. Thus, Phoenix will collect meteorological data which will help to model Mars' past and future climate.

While liquid water is not present at the surface of Mars, observations suggested that water has flown in the past on the surface of Mars. Phoenix will therefore try to find evidence of past liquid water at the landing site. The martian arctic is a good area for investigations, as liquid water may have existed there for short periods about every 100,000 years, due to the precession of the planet.

Habitable conditions in the martian arctic

Recently, it has be shown that life can exist in the most extreme conditions. Phoenix will determine the habitability of the martian arctic soil by performing chemical experiments. In addition to the pH, it will measure the amount of selected element such as carbon, nitrogen and phosphorus, and also the amount of materials which prevent biological growth, such as powerful oxidants. These elements are present at the surface of the planet, as it is exposed to the solar radiation. However, a few centimeters below the surface, the soil could protect the organisms from the radiation, and Phoenix could find there organic signatures and potential habitability.

1.2.2 Instrumentation

The Phoenix Lander, depicted in figure 1.2, was built by the Lockheed martin Space Systems (Denver, Colorado), and is very similar to the spacecraft originally planned for the canceled Mars Surveyor Program 2001 (MSP'01) mission. Aboard its deck, many advanced instruments developed by different teams are settled, and briefly described hereafter.

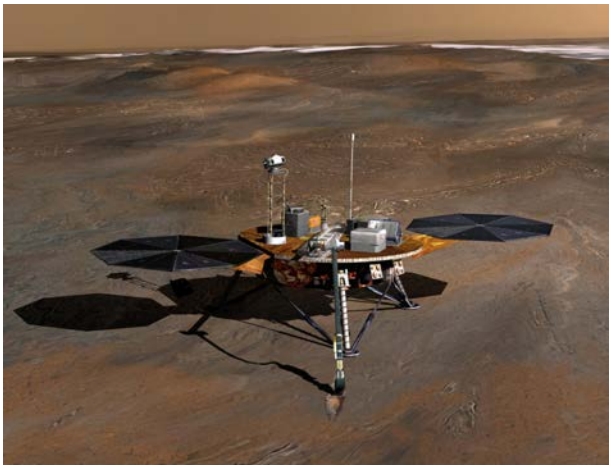

Figure 1.2: Artistic view of the Phoenix Lander on Mars.

The Robotic Arm[1]

The Robotic Arm (RA) is designed to dig trenches, scoop up soil and water-ice samples, and deliver them to the Thermal and Evolved Gas Analyzer (TEGA) and the Microscopy, Electrochemistry, and Conductivity Analyzer (MECA) instruments for detailed analysis.

The Robotic Arm Camera[2,3]

The Robotic Arm Camera (RAC), attached to the RA, will provide full-color images of the martian surface and of the collected samples in the RA scoop.

[1] Jet Propulsion Laboratory
[2] University of Arizona
[3] Max Planck Institute

The Surface Stereoscopic Imager[2]

The Surface Stereoscopic Imager (SSI) will provide high-resolution, stereoscopic, panoramic images of the martian arctic. It will survey the landing site for geological context, provide range maps for the digging operations, and measure atmospheric dust and clouds.

Thermal and Evolved Gas Analyzer[2,4]

TEGA will measure the temperature and evolved gas profiles that uniquely identify volatile-bearing minerals. It will give important information about the chemical character of the soil and ice.

Microscopy, Electrochemistry, and Conductivity Analyzer[1,2,5]

MECA is a combination of several scientific instruments, and will be used to characterize the martian soil. Since it includes the instrument built during this thesis project, it is described more in detail in 1.3.

Mars Descent Imager[6]

The Mars Descent Imager (MARDI) should have acquired a series of wide-angle, color images of the landing site during the descent. However, it was decided not to use this camera as a potential problem related to data handling was identified in pre-launch testing of the spacecraft.

Meteorological Station[7]

The Meteorological Station (MET) will record the daily weather of the landing site using temperature and pressure sensors, as well as a light detection and ranging (LIDAR) instrument. It will therefore

[4]University of Texas
[5]University of Neuchâtel
[6]Malin Space Science Systems
[7]Canadian Space Agency

provide information on the current state of the atmosphere and on the water cycle in the martian arctic.

1.2.3 History

The mission was dubbed from a mythological firebird. According to the legend, the Phoenix burns fiercely at the end of his life and is reduced to ashes, from which a new bird arises. For the spatial mission, the "ashes" were two previous attempts to explore the Red Planet, the Mars Polar Lander (MPL) and the MSP'01 Lander.

MPL was an ambitious mission to set a spacecraft down on the frigid terrain near the edge of Mars' south polar cap and dig for water ice with a robotic arm. It was lost at arrival on the 3rd of December 1999. The probable cause of the loss was a premature shutdown of the descent engines, resulting from a vulnerability of the software to transient signals. The crash of MPL came three months after the loss of Mars Climate Orbiter (MCO), during its insertion in the Mars orbit. These incidents caused the cancellation of the MSP'01 mission, scheduled to be launched in April 2001, also because the Lander of MSP'01 was similar to MPL. However, it should have carried new experiments, among which the MECA payload, described in 1.3.

As the "faster, better, cheaper" motto had showed its limits, NASA developed a new strategy for the Mars exploration. In parallel to large and expensive missions, it was decided to send a series of small, low-cost missions to Mars, as part of the Mars Scout Program. About every three years, it was decided to select such a mission from innovative proposals by the scientific community.

In June 2001, 10 projects were selected among the 43 proposed for the first NASA scout mission, whose budget was initially fixed to $300 millions. In December 2002, NASA announced the four finalists for this mission: ARES (Aerial Regional-scale Environmental Survey), MARVEL (Mars Volcanic Emission and Life Scout), SCIM (Sample Collection for Investigation of Mars) and of course Phoenix. To the delight of the author, the latter was selected on the 4th of August

2003. Exactly four years later, Phoenix was launched from Cape Canaveral, boosted into space on a Delta II rocket.

1.3 The MECA payload

1.3.1 Introduction

In its early youth, the MECA payload was part of the MSP'01 mission, and its acronym stood for Mars Environmental Compatibility Assessment, as its main objective was to determine the possible hazards which could be encountered during human exploration of the planet, mainly by studying the dust and soil properties [9]. After the cancellation of the MSP'01 mission in 2000, the MECA payload was waiting for a new flight opportunity. Its architecture required a stable platform equipped with a robotic arm, as well as a camera to perform data analysis with all experiments. A new flight opportunity came a few months later with the Phoenix mission, described above. MECA was renamed Microscopy, Electrochemistry, and Conductivity Analyzer, as the science requirements of the new mission were different.

However, the goal of MECA was still to characterize the martian soil, but this time in an environment where clues of water ice could be found. The instruments of the payload were therefore kept the same, except that two plates which should have measured natural dust accumulation on engineering materials were not reloaded. For the Phoenix mission, the MECA payload includes the following experiments:

- The Wet Chemistry Laboratory (WCL), composed of four single-use beakers [10]. Each beaker will be prepared by melting ice from a reservoir, and will then receive a sample from the martian soil delivered by the RA. An electrochemical analysis of the solution performed by means of ion selective electrodes and electrochemically-based sensors should determine the total

dissolved solids, redox potential, pH, and the concentration of many soluble ions and gases.

- The Thermal and Electrical Conductivity Probe (TECP), attached to the RA. It consists of four small spikes that can be inserted into the martian soil. In addition to measuring temperature, the probe measures thermal conductivity, which could reflect the presence of ice, and electrical conductivity, which could detect unfrozen water.

- The microscopy station, combining optical and atomic force microscopy in order to characterize soil particles from millimeters to nanometers in size. It is described in detail in 1.3.2.

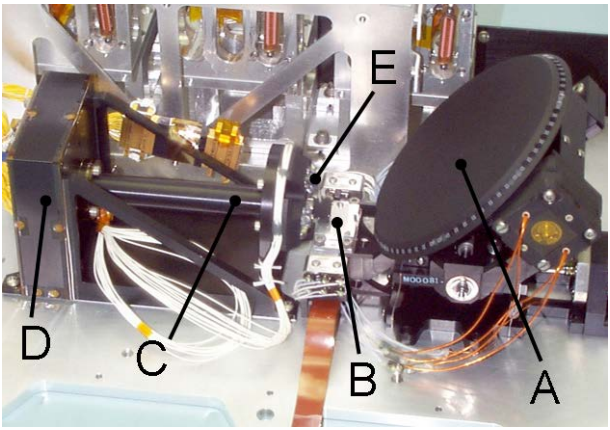

Figure 1.3: A testbed of the MECA microscopy station. A) Sample wheel, B) AFM, C) Optical microscope, D) CCD (Charge Coupled Device) camera, E) RGB and UV LEDs. Note that the electronics boards, which are attached on the lateral walls of the MECA enclosure, are not yet mounted.

1.3.2 The microscopy station

The MECA microscopy station, illustrated in figure 1.3, will characterize martian dust and soil particles at a scale never observed on Mars. It is composed of an optical microscope (OM), an atomic force microscope (AFM), and a delivery unit called the Sample Wheel and Translation Stage (SWTS), which brings the samples acquired from the outside of the MECA enclosure in front of the two microscopes. The optical microscope is accompanied by a CCD (Charge Coupled Device) camera, as well as an illumination system constituted of a set of different LEDs. Except the AFM, theses components are described hereafter.

The Optical Microscope

The Optical Microscope (OM), built at the University of Arizona, is a fixed-focus imaging system whose characteristics are given in table 1.2. Its CCD camera, provided by the Max Planck Institute and shown in figure 1.3, is the same as the one of the RAC, and both instruments share a common readout electronics that is located elsewhere on the Lander. The illumination can be changed by means of the RGB and the UV LEDs located near the objective. Taking images under different light conditions will provide color information about the samples and allow generating true-color images. The UV LEDs will be used to reveal eventual luminescence of the samples.

Table 1.2: Characteristics of the Optical Microscope.

Parameter	Value
Magnification	5.75
CCD size	256 x 512 pixels
Field of view	1 mm x 2 mm
Pixel resolution	4 μm/pixel

As the pixel resolution of the OM is 4 micrometers per pixel, it should be able to detect particles down to less than 10 micrometers, if one considers that a particle could be detected if it occupies 2x2 pixels.

The Sample Wheel and Translation Stage

The SWTS is the component which ensures the sample delivery from the outside of MECA to the two microscopes. Before describing the sample delivery, a brief description of the two components of the SWTS is given hereafter.

The Sample Wheel. As shown in figure 1.4, the sample wheel is populated with sixty-nine different substrates, having a diameter of three millimeters. The wheel axis is tilted with 45 deg, in order to position the substrates horizontally when collecting the samples and vertically when imaging them with the OM or the AFM. Among these substrates, ten sets of six substrates are dedicated to the sample collection. Each set of substrates is composed of:

- Two "micro-buckets"
- A weak magnet substrate
- A strong magnet substrate
- A microfabricated substrate
- A silicone substrate

All these substrates are intended for AFM measurements, except the micro-buckets which are not appropriate for this application. Note that one micro-bucket per set is used as a buffer preventing the deposited particles from contaminating the next set of substrates. In addition to these sixty substrates, four are dedicated to the OM calibration and five to the AFM operation. The AFM substrates are the

tip characterizer substrate, the linear calibration substrate, the tip finder substrate, the tip breaking tool substrate and the tip cleaning substrate. The first two substrates are used to calibrate the sensor tip and the scanner of the AFM, respectively. Imaging the tip finder substrate allows the determination of the position of the sensor tip relative to the sample wheel. The tip breaking tool substrate is used to remove a sensor in order to access the next one, as we will see that the AFM is composed of eight sensors. Finally, the tip cleaning substrate allows cleaning the sensor tip. Each substrate can be placed in front of the two microscopes by rotating the wheel. The rotational step size is fifteen micrometers.

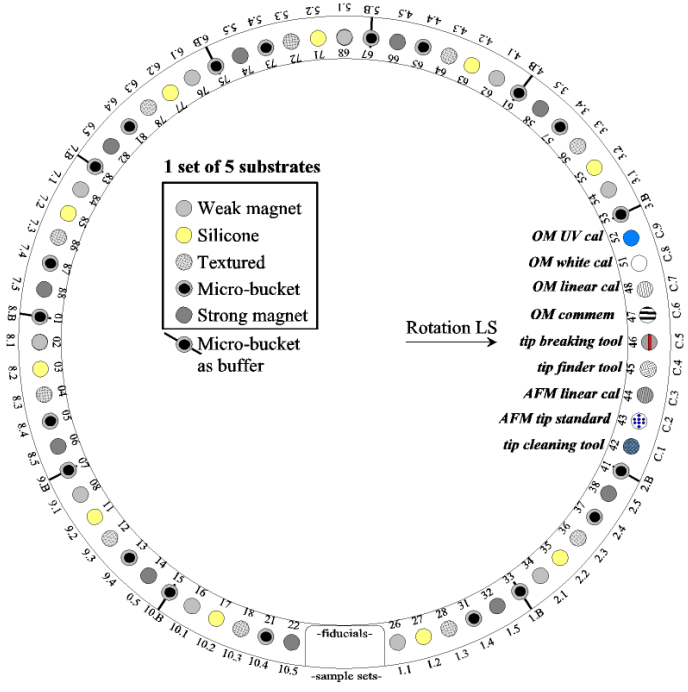

Figure 1.4: Schematic positions of the substrates on the SWTS.

The Translation Stage. The translation stage allows translating the sample wheel forward and backward. Specific positions of the stage are monitored by limit switches with redundant switches in case of failure. These positions are described hereafter, starting from the furthest position. The latter is the sample acquisition position, informally called the "tongue-out" position, which exposed a portion of the sample wheel to the outside. The second position is the "safe-to-rotate" position, where the sample wheel can be rotated without risking damaging the AFM or the OM. Then, if the stage is translated toward the microscopes, the "OM-focus" position is reached, which corresponds to the expected position for the focus point of the OM. The last position is when the wheel is in contact with the tips of the AFM. Note that this position does not correspond to a limit switch, but is defined by the AFM itself (see 3.2.5).

Sample delivery. The sample delivery starts with the SWTS in the sample acquisition position, with six substrates exposed to the open air. The particles can be delivered to the substrates either by the scoop of the RA or by air fall experiments, collecting dust particles from the atmosphere. Samples delivered by the scoop are acquired at different depths of the martian soil, which allows studying different layers in the arctic underground.

When the particles are deposited, the wheel is translated into the MECA enclosure. A scraper installed on the aperture of the housing should limit the height of the deposited material to about 200 micrometers. Once inside, the wheel is rotated by about 180 deg to position the desired substrate in front of the microscopes. The sample wheel is then translated to the "OM-focus" position, where OM images can be taken. If AFM measurements are planned, the stage moves slowly toward the AFM sensor, until the latter detects the contact and stops the motion of the stage by sending a signal to the electronics. After a measurement session, the wheel is left in the "safe-to-rotate" position, or possibly in the sample acquisition position if a new sample acquisition is planned.

1.4 Atomic Force Microscopy

The AFM is part of the family of the scanning probe microscope (SPM). The first SPM, the scanning tunneling microscope (STM), was developed by G. Binnig and H. Rohrer in the early 80's at the IBM research laboratory in Rüschlikon, Switzerland [11]. This technology made it possible to look into the fascinating world of atoms. For this revolutionary innovation Binnig and Rohrer were awarded the Nobel Prize in Physics in 1986.

The STM technique, however, is restricted for use on electrically conductive surfaces. G. Binnig, C. Quate and C. Gerber developed an enhancement to the STM, called the AFM, which extended the capabilities of the SPM to include insulated materials [12].

1.4.1 Principle

An AFM works without any optical focusing elements. Instead, a small sharp probing tip is brought very close to the sample's surface. The tip is positioned to the end of a "soft" micromachined cantilever, which is bent by the atomic-range forces acting between the sensor tip and the surface. A detector measured this deflection as the tip is scanned over the surface.

In static mode, a feedback loop usually maintains a constant force between the sample and the tip (i.e. a constant deflection) by moving the cantilever up and down as it scans, as shown in figure 1.5. In general, static mode AFM is performed in contact with the surface, i.e at a distance where the overall force is repulsive. Consequently, this technique is often called contact mode. The main drawback of remaining in contact with the sample is that large lateral forces exist on the sample as the tip is scanned over the surface.

In dynamic mode, the cantilever is vibrated near its resonance frequency using a piezoelectric element. When the sensor tip is brought close to the surface, this vibration is influenced by the gradient of force acting between the tip and the sample. This change

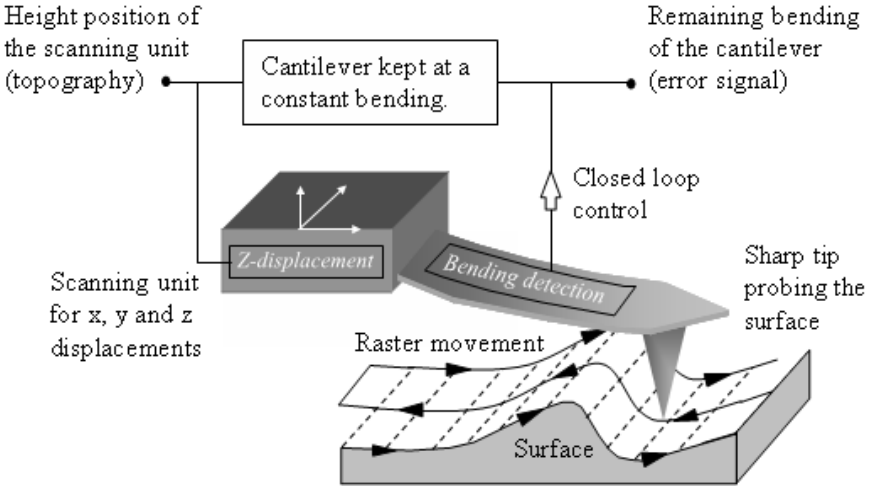

Figure 1.5: Schematics of an AFM operating in static mode. The deflection of the cantilever is kept constant by a feedback loop.

is then detected by measuring the amplitude, the frequency or the phase shift of the oscillation. The term "dynamic mode" includes therefore several modes of operations.

In amplitude modulation AFM (AM-AFM), the oscillation frequency is kept constant, and the amplitude is used as a feedback parameter to measure the topography of the sample. Additionally, the energy dissipation (i.e. the material properties) variations can be mapped by recording the phase shift between the driving force and the cantilever oscillation.

In frequency modulation AFM (FM-AFM), the phase shift is kept constant by a phase locked loop (PLL) circuit and the frequency is used as the feedback parameter. The amplitude of the excitation is adapted by an auto gain controller (AGC) to keep constant the amplitude of oscillation of the cantilever. Thus, the variations in the amplitude of the excitation give the variations of the material properties.

In addition, the terms "non contact mode" and "intermittent contact mode" (or tapping mode) are often used for the FM-AFM and the AM-AFM modes, respectively. However, it was shown that it is possible to use FM-AFM in intermittent contact mode and AM-AFM in non contact mode [13]. The difference between non contact mode and intermittent contact mode is not the feedback parameter that is used, but the working distance relative to the surface, which can be adjusted by the setpoint value. Figure 1.6 shows the working tip-sample distances for the contact, non contact and intermittent contact modes. In this thesis, the dynamic mode refers to intermittent contact FM-AFM mode.

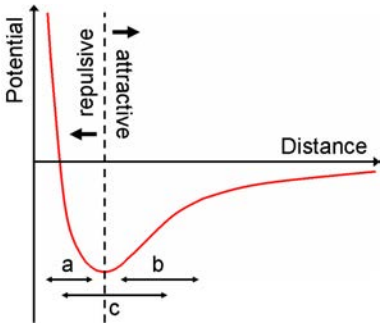

Figure 1.6: Schematics of the potential as function of the tip-sample distance. The working distance is indicated for contact mode (a), non contact mode (b) and intermittent contact mode (c).

Scanning technique

For standard AFMs, the scanning is performed by applying large voltages on a piezoelectric ceramic tube. The tip is generally scanned forward and backward over the same line before stepping to the next. Figure 1.5 shows an alternative way of scanning - not used for our instrument - where each line is either recorded in forward or backward motion.

Deflection detection

In most commercial AFMs, the deflection is measured by focusing a laser onto the back of the cantilever and measuring its reflected intensity using a photodiode. However, for certain applications, a piezoresistor integrated into the cantilever and connected to a Wheatstone bridge circuit can be used, as we will see in 2.2.

1.4.2 Why was an AFM chosen to characterize martian soil particles?

In order to characterize martian soil particles in detail, scientists need information from the millimeter scale to the nanometer scale - a scale never examined on Mars so far. The optical microscope of MECA, with its resolution of four microns per pixel, allows detection of particles ranging from about ten micrometers up to the size of its field of view, i.e. 1 or 2 mm. Large grains can be investigated by stitching several images together. Thus, a tool with a resolution of a few tens of nanometers was also needed to give detailed information on the shape, the size and the surface texture of the grains. AFM can easily reach this resolution, and it offers several advantages compared to other terrestrial tools having similar resolution, e.g. the scanning electron microscope (SEM). First, AFM does not require a special medium (e.g. vacuum, conductive surface), contrary to SEM. Secondly, the miniaturization of the AFM is possible using microfabrication. In regards with the Phoenix mission objectives, the information on the particles:

- will help understanding the history of water by looking for erosion signatures on particles,
- will improve the modeling of the martian climate, as particles sizes and shapes are key parameters for describing the exchange of heat or the water cycles through the soil surface,
- could prove that life existed on Mars by identifying fossilized micro-organisms.

1.5 Heritage of Famars 1

When the author started to work on this project, an instrument had already been designed, fabricated and characterized for the MSP'01 mission [4]. The status of its hardware and software after the cancellation of the mission is briefly described hereafter, as well as the results of measurements performed on particles.

1.5.1 Hardware

The hardware of the instrument had been delivered to the JPL for assembly on MECA a few months before the cancellation of the mission. Considering the very short time of development (about two years), this instrument showed very good characteristics. It had passed the space requirements (defined in 2.1), and taken hundreds of images in static and dynamic mode. The main drawback of the instrument was that a standard scan speed could not be used at low temperature (see 2.3). At those temperatures, vibration patterns were also observed in the images, even at low scan speeds.

1.5.2 Software

The software of the instrument had to allow autonomous operations on Mars. When the MSP'01 mission was canceled, the AFM commands of the software had not been coded yet. However, algorithms had been written in pseudo-language. They were neither complete nor tested, but all functions blocks needed to control the instrument had been described, as well as strategies for their use.

1.5.3 Particles measurements

It had been shown that the instrument was able to characterize the size, the shape and the distribution of particles. However, the measurements were performed on small particles (from 0.2 to 3 micrometers) fixed on a layer of photoresist baked after the deposition of

the particles. These first measurements allowed characterizing the instrument, but further imaging of more realistic samples was still pending, as explained hereafter.

First, while the size of the martian dust particles is effectively comprised between 0.2 and 3 micrometers, the soil particles can be much larger. In addition, piling of the particles can possibly happen. This is a very important point for atomic force microscopy, as this technique is not adapted to samples showing large dynamic in the vertical range.

Second, the fact that the particles had been fixed to their substrate had prevented the particles from being detached by lateral forces applied by the AFM tip. As it had been suggested that loose particles collected on Mars could probably not be imaged properly, design of substrates had been proposed to increase the adhesion of the particles, but had not yet been fabricated.

Finally, it had been observed that tip artifacts, mainly due to the opening angle of the AFM tips, limited the accuracy of the particles measurements. As a solution, it had been proposed to use carbon nanotubes (CNT) glued or grown onto the silicon tips.

1.6 MEMS for Space

Micro Electro Mechanical Systems (MEMS) are devices combining mechanical structures with electronics at the micrometer scale. They are often made from silicon (using micromachining by selective etching), though other materials can be used, such as polymers. Because MEMS fabrication is based on integrated circuit (IC) batch processing, high functionality can be placed on small chips at a relatively low cost. Thus, they can perform the same tasks as those performed by bulky devices, often with some enhancement. In addition to their small size and power consumption, MEMS generally present a great robustness and a long lifetime. Thus, they have been commercialized in large volumes in a vast range of applications, such as automotive industry (accelerometers), medical science (blood pressure sensors)

or telecommunications (optical switches). They are also common in daily life, in inkjet printers or in video projectors.

As space missions requires low mass, volume and power consumption, MEMS are good alternatives for those applications. In this field, they are used for example as accelerometers, pressure sensors, seismometers, mirror arrays or propulsion devices. At the moment, MEMS components are parts of larger standard systems, but in the long term, fully integrated systems could be composed mainly of MEMS assembled together. In the context of planetary exploration, where miniaturization is a key parameter, the use of MEMS could allow sending on different planets very small and highly sophisticated spacecrafts for both robotic and human missions.

While MEMS have demonstrated their reliability for Earth-bounded applications, the conditions encountered by devices during a space mission can lead to additional failures. While details depend on the design of each device, general causes of failures are typically vibration, shock, temperature changes, radiation, fatigue or corrosion [14, 15]. In order to check if a microsystem withstands the conditions of a mission, testing has to be performed using standard methods, as it was performed for the instrument described in this thesis (see chapter 2).

References

[1] D.R. Williams. Mars fact sheet, 2004. `http://nssdc.gsfc.nasa.gov/planetary/factsheet/marsfact.html`.

[2] R. Lundin et al. Solar Wind-Induced Atmospheric Erosion at Mars: First Results from ASPERA-3 on Mars Express. *Science*, 305:1933–1936, September 2004.

[3] D.A. Brain. Mars Global Surveyor Measurements of the Martian Solar Wind Interaction. *Space Science Reviews*, 126:77–112, 2006.

[4] S. Gautsch. *Development of An Atomic Force Microscope and Measurement Concepts for Characterizing Martian Dust and Soil Particles*. PhD thesis, University of Neuchâtel, Switzerland, 2002.

[5] K.M. Pitman et al. On the shape of martian dust and water ice aerosols. In *Bulletin of the American Astronomical Society*, volume 32, page 1095, October 2000.

[6] M.T. Lemmon et al. Atmospheric Imaging Results from the Mars Exploration Rovers: Spirit and Opportunity. *Science*, 306:1753–1756, 2004.

[7] K.J. Kolb, A.S. McEwen, V.C. Gulick, and the HiRISE Team. Gullies Potentially Formed By Water From The Subsurface. In *Lunar and Planetary Science XXXVIII*, page 1391, League City, Texas, March 2007.

[8] V.I. Miteva and J.E. Brenchley. Detection and isolation of ultrasmall microorganisms from a 120,000 year old Greenland glacier ice core. *Applied and Environmental Microbiology*, 71:7806–7818, 2005.

[9] M.H. Hecht et al. The MSP '01 Mars Environmental Compatibility Assessment (MECA). In *The Fifth International Conference on Mars*, page 6134, Pasadena, CA, USA, July 1999.

[10] S.P. Kounaves et al. Mars surveyor program '01 mars environmental compatibility assessment west chemistry lab: a sensor array for chemical analysis of the martian soil. *J. of Geophysical Research*, 108:13.1–13.12, 2003.

[11] G. Binnig, H. Rohrer, Ch. Gerber, and E. Weibel. Tunneling through a controllable vacuum gap. *Applied Physics Letters*, 40:178–180, January 1982.

[12] G. Binnig, C.F. Quate, and Ch. Gerber. Atomic force microscope. *Physical Review Letters*, 56:930–933, March 1986.

[13] R. Garcia and R. Perez. Dynamic atomic force microscopy methods. *Surface Science Reports*, 47:197–301, 2002.

[14] H. Shea. Reliability of MEMS for Space Applications. In *Proceedings of the 11th European Space Mechanisms and Tribology Symposium*, pages 17–24, Lucern, Switzerland, September 2005.

[15] B. Stark (editor). *MEMS Reliability Assurance Guidelines for Space Applications*. Jet Propulsion Laboratory Publication 99-1, Pasadena, CA, USA, January 1999.

Chapter 2

Hardware

The Famars instrument is composed of three different parts: a scanner head, a microfabricated sensor chip and an electronic board. As these components had been built in the past for the canceled MSP'01 mission [1], this chapter mainly describes the changes made during the present thesis project.

The sensor chip (see 2.2) had already been designed by Terunobu Akiyama from IMT. With his help, new chips were fabricated, using a fabrication process close to the one used in 1999 [1]. The main modification was the method for creating the deflection sensors (see 2.2.4). The characterization of the chips allowed identifying their main source of noise, as well as an unexpected behavior of the cantilevers when operated in dynamic mode (see 2.2.5).

A scanner head had been fabricated in the past by S. Gautsch in collaboration with Nanosurf AG. However, this scanner showed limitations when working at low temperatures [1]. Therefore, a new scanner was designed, fabricated and characterized during this thesis project (see 2.3). After assembly, the scanner and the sensor chip were qualified for space (see 2.5).

Design, fabrication and testing of the electronic board have been performed by our partners at the University of Basel. Thus, a brief description of the electronics is given for information in section 2.4.

2.1 Space qualification requirements

The hardware of MECA, including First AFM on Mars (Famars), had to fulfill space qualification requirements established primarily for the canceled MSP'01 mission. They were kept for the Phoenix mission, with the exception of a few changes in the intervening years.

2.1.1 Mass, volume and power

During the preparation of the MSP'01 mission, the envelope of the scanner of Famars was limited to 50 x 30 x 15 mm and its mass to 30 grams, whereas the controller card should not exceed a mass of 220 grams. At the time, a scanner measuring 35 x 18 x 15 mm was built, with a mass of only 16 grams. The fabricated electronic card had an overall size of 300 x 110 x 10 mm and a total mass of 190 grams. As the total mass of Famars was below the threshold, it allowed relaxing the constraints for other instruments of MECA, whose total mass had to be below 8.6 kg. Thus, when MECA was reloaded onboard the Phoenix mission, mass and dimensions of the new instrument had to be kept the same as those of the one built for MSP'01. The power consumption of Famars had to be smaller than 8.3W.

2.1.2 Shock and vibration

The Lander is submitted to random vibration mainly during the launch. The driving source for the shock is the backshell separation. Although the shock levels are significant, the energy quickly dissipates through each joint and with increasing distance from the shock source. Thus, the Lander is divided into different zones with their own shock level, given by a specific shock response spectrum. Famars had to withstand the shock level specified for the "Instrument Deck and Equipment Enclosure" zone.

Table 2.1: Lander temperatures during the Phoenix mission.

Mission Phase	Lander Temperatures
Launch	+ 13 deg C to + 45 deg C
Cruise	- 45 deg C to + 45 deg C
Entry, Descent and Landing	- 45 deg C to + 45 deg C
Diurnal cycle, cold day	- 87 deg C to - 29 deg C
Diurnal cycle, hot day	- 85 deg C to + 40 deg C

2.1.3 Temperature

The Lander will be exposed to a large range of temperatures during the mission, as shown in table 2.1. The temperature of Famars depends on the thermal inertia of the Lander and its instruments, but will be in the same order as the temperature of the Lander. The temperature of the Lander components during handling, transportation and storage on Earth does not exceed + 45 deg C by requirement.

2.1.4 Pressure

Due to the low atmospheric pressure of Mars (about 7 mbar), electrical discharges can take place through corona discharge over millimeter to centimeter distances at a few hundred volts and over centimeter to meter distances at a few thousand volts. Thus, the design of Famars required low voltages to prevent any electrical discharge.

2.1.5 Radiation

On Mars

Unlike Earth, Mars does not have a magnetic field to shield it from solar flares and cosmic rays. As its atmosphere is less than 1% of that of Earth, it provides shielding from the solar flare radiation, but not from the cosmic rays consisting mostly of heavy atomic nuclei. Thus,

the hardware, and in particular the electronics, had to be resistant to the heavy ions bombardment.

In cruise

In outer space, the total radiation dose behind 0.1 inch of aluminum shielding is 1.43 kRads per year. For the mission, a safety factor of 2 was added, for a final radiation tolerance of about 3 kRads (Si) behind 0.1 inch of aluminum.

2.1.6 Outgassing

Due to the vacuum that reign in space, some materials such as polymers outgas. The contamination due to this outgassing must be below the level that could produce a detectable contribution to MECA and other payload experiments. Thus, the components of Famars have to show low outgassing characteristics.

A standard test method called ASTM (American Society for Testing and Materials) E 595-77/84/90 allows determining the volatile content (e.g. trapped solvent, water, or un-reacted, low boiling point substances) of materials, when exposed to a vacuum environment at 125 deg C. The requirements for outgassing are a total mass loss (TML) lower than 1% and a total collected volatile condensable materials (CVCM) lower than 0.1 %. Materials showing a TML between 1% and 1.5% in which the material loss is water vapor are also allowed.

2.1.7 Finishing

All parts had to be suitably finished to provide protection from corrosion. For example, aluminum surfaces requiring electrical bonding had to be anodized in accordance with the American military standard MIL-C-5541, Class 3. For the Famars instrument, the main requirement was a black finishing, light reflection toward the optical microscope had to be avoided.

2.1.8 Planetary protection

NASA's planetary protection objective is safeguarding the planets, including our own, during space exploration. For the Phoenix mission, this means avoiding any contamination of the martian surface by terrestrial micro-organisms. Thus, all parts of Famars had to be assembled in a clean environment. A cleaning procedure had also to be carried out as part of the hardware delivery. There had to be a reasonable expectation that residual contamination or cleaning agent residue would not affect experimental results of any element of the Phoenix payload.

2.1.9 Autonomy

Real time operations of the instrument made impossible by the travel time of electromagnetic signals between Earth and Mars, being between 8 and 22 minutes. Thus, autonomous procedures had to be developed for the measurements on Mars. This implied the creation of software commands which could be grouped in control sequences (see chapter 3). As these control sequences are sent to Mars once a martian day, any support from the ground requires a waiting time of at least one day before the measurements can continue. In addition, the amount of data generated is limited, as the downlink of the data to Earth does not support large data volumes.

2.2 Famars chip

The chip is an essential component of the AFM, allowing a precise sensing of the sample topography. This requires a sharp tip located at the end of a cantilever fulfilling different criteria. First, the spring constant of the cantilever has to be small enough for detecting the weak forces (in the order of 10^{-9} N) acting between the tip and the sample. In addition, a cantilever with a high resonance frequency allows a faster scan speed and makes the AFM less sensitive to external

vibrations, which are often in the low frequency range. In order to achieve a low spring constant and a high resonance frequency, the dimensions of the cantilever should be small. Another important aspect is the deflection readout technique, since a method fulfilling the space requirements on volume, mass and power was required. Finally, an array of several cantilevers was needed, in case of contamination or wear of the sensor tip. The number of cantilevers was fixed to eight, with a required lifetime of at least five hours of operations each.

Among the different methods existing to fabricate AFM probes, silicon microfabrication was chosen. It utilizes well-known IC-process technologies together with additional etching techniques. First, the fabrication of sharp silicon tips by anisotropic etching in a potassium hydroxide (KOH) solution is a well-established technique [2]. Second, small mechanical structures can be created by bulk micromachining [3]. This technique was therefore employed for the fabrication of the cantilevers, as well as for their supporting beams which can be cleaved off to remove the cantilevers after use. Third, another important advantage of microfabrication is the possible implantation of a piezoresistive deflection readout directly into the cantilevers [4]. Finally, microfabrication allows the production of several chips in one run (50 Famars chips per wafer).

This section describes the main characteristics of the Famars chip, with a special emphasis on the silicon tips (see 2.2.2) and the piezoresistive deflection sensors (see 2.2.3). The fabrication of the chip and its characterization is also described. The verification of the space requirements described in 2.1 is introduced in a further section (see section 2.5).

2.2.1 Overview

The microfabricated sensor chip, shown in figure 2.1, consists of an array of eight cantilevers with integrated, piezoresistive deflection sensors. These cantilevers are aligned in a row and mounted on the scanner with two tilt angles of ten degrees relative to the sample,

as illustrated in figure 2.2. Thus, they can be engaged one after the other to provide redundancy in case of tip or cantilever failure. Sharp silicon tips at the end of the cantilevers are used for probing the sample. When the AFM operates in dynamic mode, excitation of the resonance frequencies of the active cantilever is achieved by vibrating the whole chip by means of a piezoelectric plate mounted behind it (see figures 2.2 and 2.41). The dimensions of the Famars chip are given in appendix A-1.

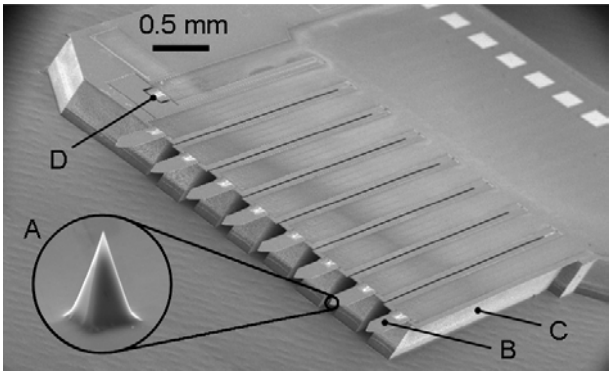

Figure 2.1: SEM image of the Famars chip. For redundancy, the chip carries eight sensors, composed each of a sharp tip (A) located at the end of a cantilever (B). The cantilever itself is supported by a thick beam (C). If a sensor is unusable (worn or contaminated tip, broken cantilever, etc.), the corresponding beam can be broken in order to access the measured sample with the next sensor. In addition to the eight sensors, a reference piezoresistor (D) allows to compensate thermal drifts.

2.2.2 Sensor tips

The sharp silicon tips were fabricated by wet etching in a 40% KOH solution at 60 deg C. At the future location of a tip, a small square mask in oxide was defined on the silicon. As (100)-oriented wafers

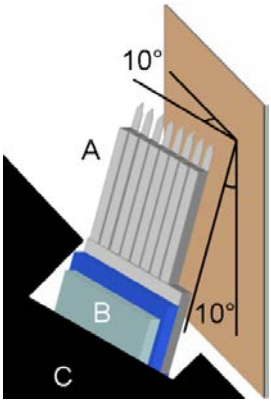

Figure 2.2: Orientation of the chip (A) relative to the sample. The piezoelectric plate (B) and the top of the scanner (C) are also represented.

were used, the silicon was anisotropically etched under this mask in the KOH solution, until the different slow etching planes intersected each other. At this point, the mask fell away, leaving a well-defined silicon tip. In this process, overetching led only to a reduction of the tip height, but does not influence its general shape [5]. Thus, all the fabricated tips should show the same opening angle and the same aspect ratio. This method also demonstrates an excellent uniformity over the whole surface of the wafer. After the KOH etching, the tips were sharpened using a thermal oxidation process. An SEM image of a Famars tip is shown in figure 2.3.

The use of carbon nanotubes (CNTs) as sensors was investigated. In order to do that, Famars chips were sent to a group at the NASA Ames Research Center [6], and multi-walled CNTs were attached successfully to a few of the silicon tips. The chips were then tested at the Institute of Microtechnology (IMT) to see if we could improve the resolution of the AFM images using them. Unfortunately, a detachment of the carbon nanotube from its silicon tip was observed repeatedly as soon as the sensor made contact with the sample. As

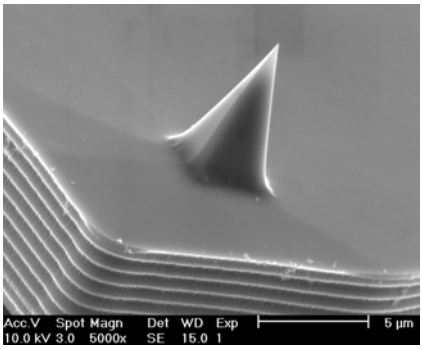

Figure 2.3: SEM image of a silicon tip at the end of a cantilever. The DRIE patterns are visible on the edge of the cantilever.

the nanotubes were several micrometers long, it was suggested that they were bent, creating a force sufficiently strong to break the joint between the CNT and the tip. More work could have been performed to investigate this, but after discussion between members of the project, the option of using CNT tips was not retained.

2.2.3 Piezoresistive deflection sensors

As it was mentioned in 2.2.1, the deflection of the active cantilever was measured using an integrated piezoresistor, reducing the size and the complexity of the AFM. The principle of piezoresistive detection and its implementation to the Famars chip are presented in this section.

The piezoresistive effect

In 1856, Lord Kelvin observed that metal wires exhibited a change in resistance if they were stretched, different materials showing different sensitivities. As the resistance of a wire is given by

$$R = \rho \, \frac{L}{A} \, , \tag{2.1}$$

where ρ is the resistivity of the material, L the length and A the cross-sectional area, the stress induced change of resistance can be expressed as

$$\frac{dR}{R} = \frac{d\rho}{\rho} + \frac{dL}{L} - \frac{dA}{A} \ . \tag{2.2}$$

The first term reflects a stress dependent change of resistivity, while the two last terms come from dimensional changes. Introducing the Poisson's ratio ν, one obtains

$$\frac{dR}{R} = \frac{d\rho}{\rho} + \epsilon_L(1 + 2\nu) \ , \tag{2.3}$$

where ϵ_L, defined as dL/L, is the longitudinal strain. The longitudinal strain sensitivity S_a, defined as $(dR/R)/\epsilon_L$, is therefore given by

$$S_a = \frac{1}{\epsilon_L} \frac{d\rho}{\rho} + 1 + 2\nu \ . \tag{2.4}$$

In 1938, a practical strain gauge based on Kelvin's principles was fabricated by E. Simmons. It consisted simply of a small diameter metal wire bonded to a piece of paper backing. It was simple and cheap, and quickly proved indispensable to the wartime aircraft industry. In 1952, the Saunders-Roe company (UK) developed metal foil gauges fabricated by a photo-etching process. As this method allowed faster and cheaper production, these gauges were more extensively used and are still the most common type today.

The performance of a strain gauge is given by the gauge factor K, which is defined the same way as the strain sensitivity, i.e.

$$K = \frac{dR/R}{\epsilon_L} \ . \tag{2.5}$$

The difference is that the strain sensitivity is a material property while the gauge factor is a property of an individual strain gauge, depending on the material used and on its geometry. The gauge factor K of common metal foil gauges is typically around 2.

Around 1970, the first semiconductor strain gauges, also called piezoresistors, were developed for the automotive industry. They showed a larger piezoresistance effect than the metal-based devices, with gauge factors between 50 and 200 [7]. This is explained by the fact that the strain sensitivity S_a in metals is mainly due to dimensional changes, whereas the change of resistivity is the dominant phenomenon in semiconductors. The resistivity of an extrinsic semiconductor is given by

$$\rho = \frac{1}{qn\mu} \ , \tag{2.6}$$

where q is the electronic charge, n the concentration of majority charge carriers and μ their average mobility. If stress is applied, the concentration of carriers as well as their average mobility can change, modifying the resistivity [8]. This change can be written as

$$\frac{d\rho}{\rho} = \Pi_L \ \sigma_L \ , \tag{2.7}$$

where Π_L is the longitudinal piezoresistive coefficient and σ_L the applied longitudinal stress. The magnitude and sign of Π_L depends on the material, dopant type and level, carrier concentration and crystallographic orientation. The values of Π_L have been determined experimentally for silicon by C.S. Smith [8] and are given in table 2.2. Using equation 2.7 and introducing the Young's modulus E, one can express equation 2.3 as a function of the applied stress:

$$\frac{\Delta R}{R} = (\Pi_L + \frac{1+2\nu}{E}) \ \sigma_L \ . \tag{2.8}$$

Table 2.2: Values of the longitudinal piezoresistive coefficient Π_L in units of 10^{-11} m^2/N for n-type and p-type silicon, along direction [100] and [110].

Type and resistivity	along [100]	along [110]
n-type, 11.7 ohm cm	-102.2	-31.2
n-type, 18.6 ohm cm	-102.2	-31.0
p-type, 7.8 ohm cm	+6.6	+71.8
p-type, 22.7 ohm cm	+6.5	+71.9

This change of resistance in piezoresistors is generally converted by a Wheatstone bridge into a voltage suitable for amplification and processing. This circuit is shown in figure 2.4, where R_1, R_2, R_3 and R_4 are resistors. Assuming that the condition $R_1/R_2 = R_3/R_4$ is satisfied, the bridge is balanced, and the output $V_{out} = V_1 - V_2$ remains zero.

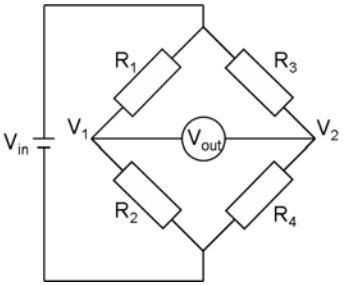

Figure 2.4: Schematics of a Wheatstone bridge. This circuit converts a change of resistance into an output voltage V_{out}.

Now assume that a change occurs in the resistance R_1. This will unbalance the bridge and produce a voltage across the output terminals. If a similar change occurs in an adjacent arm of the bridge (i.e. R_2 or R_3), the output voltage will remain at zero. However, if

this change in the adjacent arm has equal magnitude but opposite polarity, then the output voltage will be twice that due to resistance changes in one arm. For strain gauge purposes the output equation for the bridge is given by

$$V_{out} = V_1 - V_2 = \frac{N}{4}\ K\ \epsilon_L\ V_{in}\ , \tag{2.9}$$

where N is the number of active arms, K the gauge factor of each piezoresistor and ϵ_L the strain applied to them.

Implementation for Famars

A piezoresistor integrated in each cantilever was used to measure the deflection caused by the interaction between the probe and the sample (see figure 2.5). The type of dopant for the piezoresistor was chosen to have the best possible piezoresistive coefficient as a function of the orientation of the cantilevers. As the fabrication of the AFM tips required (100)-oriented wafers, the cantilevers were built along a <110> direction. Based on table 2.2, p-type silicon was chosen, as it shows better sensitivity than n-type silicon for this orientation. Thus, the piezoresistors were defined by p-type diffusion into a lightly n-doped bulk.

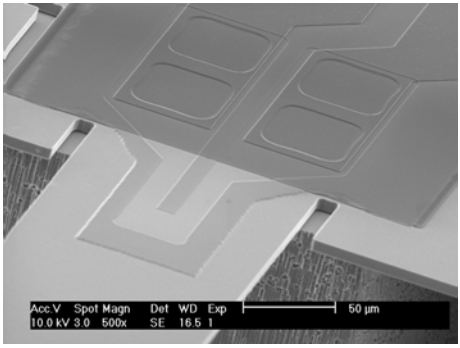

Figure 2.5: SEM image of a piezoresistor at the base of a cantilever.

The resistors were fabricated at the base of the cantilevers, where the stress is the highest. Their shape was defined by photolithography and diffusion of boron atoms in the silicon bulk. Aluminum lines were deposited to connect the two terminals of each piezoresistor to bonding pads on the silicon chip. Finally, the piezoresistors and the metal lines were protected with a silicon nitride layer.

A Wheatstone bridge was employed to detect the change of resistance in the active piezoresistor. Schematics of this circuit is shown in figure 2.6. The resistances R_1 were parts of the electronics, whereas one of the resistances R_2 was located on the active cantilever and the other on a reference cantilever. This reference piezoresistor, shown in figure 2.7, allows compensating thermal drift; a change of temperature of the chip modifies equally the two resistances R_2, leaving the bridge balanced. Similarly, a change of temperature in the electronic board induces the same change in the two resistances R_1. The equation for the output voltage of the bridge is given by

$$V_{out} = V_1 - V_2 = -\frac{\Delta R \; R_1}{(R_1 + R_2)(R_1 + R_2 + \Delta R)} \; V_{in} \; . \tag{2.10}$$

As $\Delta R << R_1 + R_2$, it follows that

$$V_{out} \cong -\frac{\Delta R \; R_1}{(R_1 + R_2)^2} \; V_{in} \; . \tag{2.11}$$

Note that if $R_1 = R_2$, one obtains

$$V_{out} \cong -\frac{1}{4} \; \frac{\Delta R}{R_2} \; V_{in} \; . \tag{2.12}$$

The factor 1/4 is in accordance with equation 2.9, as only one arm of the bridge is active. Due to fabrication variations, the resistances on the active cantilever and on the reference cantilever are sometimes slightly different. Thus, to compensate the resulting offset in V_{out}, an arm was added to the bridge. This is not shown here and will be discussed in section 2.4. That section will also hold a description of how the output of the bridge is amplified and processed.

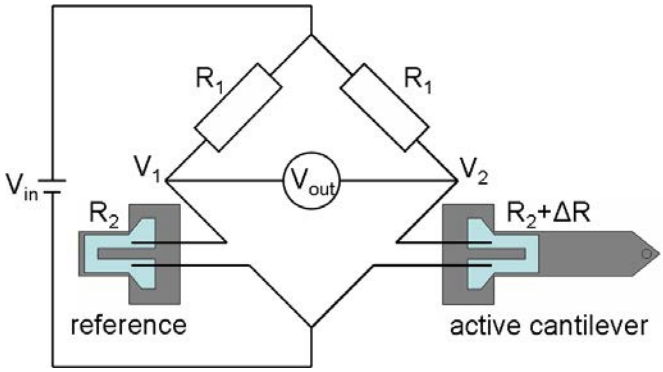

Figure 2.6: Schematics of the Wheatstone bridge used for the deflection measurement. This circuit allows converting the change in resistance ΔR due to the deflection into a DC-voltage V_{out}.

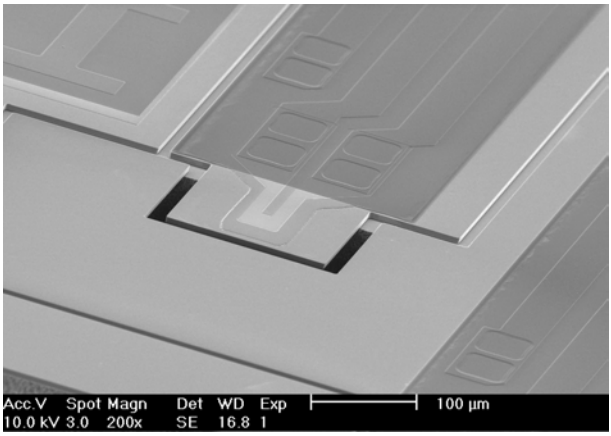

Figure 2.7: SEM image of the reference sensor.

2.2.4 Fabrication

Chips had already been designed and fabricated successfully in the past by T. Akyiama and S. Gautsch [1]. Since only a few chips were remaining, a new batch of wafers was processed. A similar work flow was followed, except for the creation of the piezoresistors. While Gautsch used ion-implantation, we doped the silicon bulk by diffusion from a borosilicate glass (BSG) layer, which allowed entirely realizing the chips in our clean room facilities. After the experimental determination of the diffusion parameters, new chips were fabricated using the process described hereafter.

Fabrication steps

For the fabrication of the Famars chip, silicon-on-insulator (SOI) wafers were used. The cantilevers were defined in the top layer (device layer) and the support beams in the bottom layer (handle). The wafers had a device layer of 20 μm and a handle thickness of 370 μm, insulated from each other by a thermal oxide layer of 1 μm. The wafers were (100)-oriented and lightly doped (n-type, phosphorus), having a resistivity of about 5 Ω cm. This corresponds to a dopant concentration of about 10^{15} atoms per cm^3 [9].

Figure 2.8 illustrates the fabrication process. First, thermal oxide was grown on both sides of the SOI wafers (step a). Then, the masks for the tips were defined in the top oxide layer by photolithography and dry etching. After that, the tips were formed in silicon by anisotropic etching in a KOH solution (step b). In order to improve the sharpness of the tips, a thermal oxidation was performed (step c). The oxide layer on the topside was removed afterwards in a buffered HF (BHF) solution, while the oxide on the backside (1 μm) was protected with photoresist. Then phosphosilicate glass (PSG) and oxide layers were grown by chemical vapor deposition (CVD) (step d). These layers were thermally densified to minimize the underetching during the next etch. Then, the piezoresistors shape was defined by photolithography and wet etching (step e). After that,

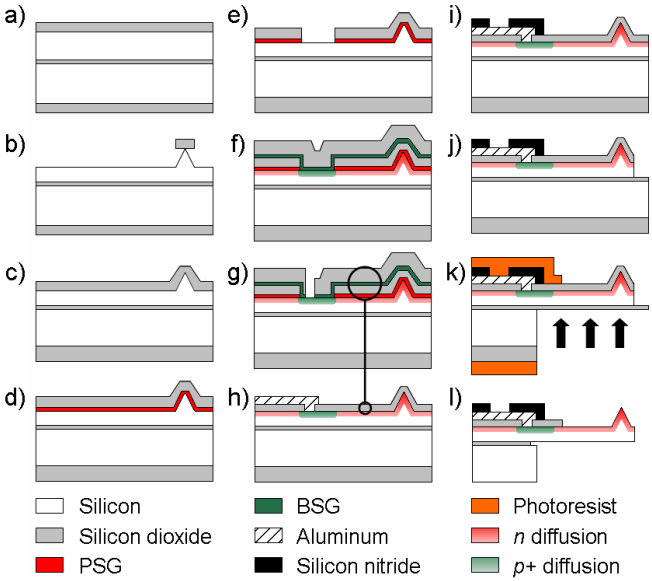

Figure 2.8: Flow chart of the Famars chip process (side views are not scaled). a) Thermal oxide growth (400 nm); b) Lithography (tips), oxide etching (RIE), silicon etching (40% KOH, 60 deg C); c) Thermal oxide growth for tip sharpening (600 nm), oxide stripping (BHF); d) PSG deposition (CVD, 100 nm), oxide deposition (CVD, 300 nm), oxide densification (600 deg C); e) Lithography (piezoresistors), oxide and PSG etching (BHF); f) BSG deposition (CVD, 100 nm), oxide deposition (CVD, 500 nm), diffusion (30 min at 950 deg C); g) Lithography (contacts), oxide and BSG etching (BHF); h) Al evaporation (500 nm), lithography (metal paths and pads), Al etching (for simplicity, the PSG, BSG and oxide layers are now represented as a single oxide layer); i) SiN deposition (PECVD, 500 nm), lithography (openings to the pads), SiN plasma etching; j) Lithography (cantilevers), oxide etching, silicon etching (topside DRIE); k) Lithography (protection topside), lithography (beams), oxide etching, silicon etching (backside DRIE); l) Oxide etching (BHF).

BSG and oxide layers were deposited by CVD. The dopants (phosphorus and boron atoms) were subsequently diffused in the device layer by a thermal treatment (step f). The contacts to the hence created piezoresistors were defined by photolithography and oxide etching (step g). An aluminum layer was then evaporated, and the the contact paths and pads were defined by photolithography and aluminum etching (step h). A protective silicon nitride layer was deposited by plasma-enhanced chemical vapor deposition (PECVD) and holes to the contact pads were opened by photolithography and plasma etching (step i). The topside oxide layer was structured by photolithography and wet etching and used as a mask to define the cantilevers by deep reactive-ion etching (DRIE)(step j). This step was followed by two photolithographies for the DRIE defining the support beams and the final chip shape. On the topside, the photoresist was used as a protection, while it was used as a mask for the oxide etching on the backside. During the backside DRIE, both photoresist and oxide were used as a mask. The oxide layer underneath the cantilevers was used as an etch stop (step k). As a final step, the oxide layers remaining underneath and above the cantilevers, as well as underneath the chips, were removed by wet etching (step l). At the end of the process, the chips were still connected to the silicon frame via three thin bridges, which could be broken for releasing the chip.

Discussion

The complexity of this process was quite high, with eight depositions or growths, eight photolithographies, seven wet etchings and six dry etchings. However, since we followed a well-established work flow, the processed wafers showed a satisfying yield. The main cause of unusable chips was the final backside DRIE, as the regions to be opened showed different aspect ratios. As it takes more time to open completely the regions with high aspect ratio, those with low aspect ratio were overetched. If this overetching overcame the one μm thick

oxide layer, the topside structures were damaged. In particular, the cantilevers' size was sometimes reduced, as shown in figure 2.9. While it was a benefit to have the tip very close to the end of the cantilever, this caused the sensor tip to disappear in rare cases. If new chips have to be fabricated in the future, one could probably reduce this effect by designing a new mask such as the backside DRIE opens regions having similar aspect ratios.

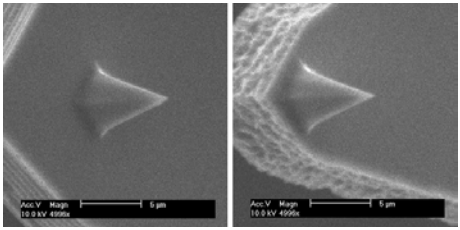

Figure 2.9: SEM images of the end of cantilevers without (left) and with (right) overetching from the backside DRIE. In this case, the overetching was a benefit, as it reduced the distance between the tip and the extremity of the cantilever, leaving the tip untouched.

There was another disadvantage in this process. Each time oxide had to be etched on the topside in a BHF solution, the oxide on the backside had to be protected by a layer of photoresist. This could be avoided by depositing a nitride layer on the backside at the beginning of the process. This layer could then protect the oxide during the BHF etchings, and could be structured by dry etching after the last photolithography.

2.2.5 Characterization

The characterization of the Famars chips consisted first of SEM observations. The presence of eventual defects or contaminations was investigated, and the sharpness of the silicon tips was checked. Then, the resistances of the piezoresistors were measured to check that the values were in the expected range. The two best chips were selected

for gluing to the flight model (FM) and the flight spare model (FS) scanners. Once the chips were mounted and bonded to a scanner, the operating frequency of each cantilever was determined. Then, the noise level was verified, leading to a study of the *p*-*n* junction formed within the chip.

Sensor tips

The SEM inspection showed tips with the expected characteristics. The height of the tips was about 7 μm, with an aspect ratio larger than 1.5. The opening angle was about 35 degrees, which is typical for fabrication by anisotropic etching in a KOH solution followed by sharpening by thermal oxidation. A few anomalies were observed, consisting mainly of blunt tips or tips still surrounded by a thin oxide belt, as shown in figure 2.10. However, most of the tips were clean and sharp. The tips belonging to the FM chip are shown in figure A-IV in the appendix.

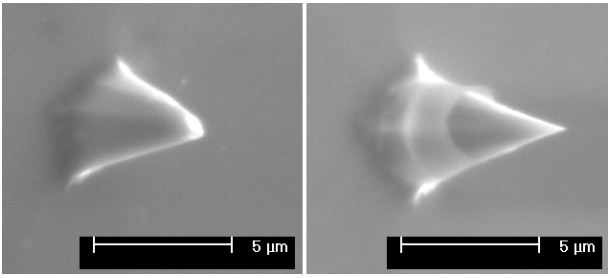

Figure 2.10: SEM images of a blunt tip (left) and a tip surrounded by an oxide belt (right).

Cantilevers

The dimensions of the obtained cantilevers are indicated in table 2.3. L, w and t are respectively the length, width and thickness of the cantilevers. The design of the chip had been optimized by Gautsch

Table 2.3: Dimensions and calculated mechanical characteristics of the fabricated cantilevers. f_0 is the resonance frequency, $f_1 = \frac{3}{2} f_0$ the first harmonic frequency and k the force constant. Note that the thickness t varied from chip to chip.

#	$L(\mu\text{m})$	$w(\mu\text{m})$	$t(\mu\text{m})$	f_0(kHz)	f_1(kHz)	k(N/m)
1	568	160	7	24.0	36.0	12.7
2	603	160	7	21.3	32.0	10.6
3	575	160	7	23.4	35.1	12.2
4	613	160	7	20.6	30.9	10.1
5	584	160	7	22.7	34.1	11.6
6	624	160	7	19.9	29.8	09.5
7	594	160	7	22.0	32.9	11.1
8	633	160	7	19.3	29.0	09.1

and Akiyama [1] in order to minimize cross-talking between the different sensors. Thus, the cantilevers of the Famars chip have different lengths L, and therefore different resonance frequencies. The thickness of the cantilevers depended on the KOH etching, and measurements performed on a few chips gave values close to 7 μm.

The resonance frequency f_0, the first harmonic frequency f_1 and the force constant were calculated for each cantilever using the formulas for a simple rectangular parallelepiped, i.e. 2.13, 2.14 and 2.15:

$$f_0 = \frac{t}{\sqrt{6}\pi L^2} \sqrt{\frac{E}{\rho}} \,, \tag{2.13}$$

$$f_1 = \frac{3}{2} \, f_0 \,, \tag{2.14}$$

$$k = \frac{E w t^3}{4 L^3} \,, \tag{2.15}$$

where E is the Young's modulus (1.69 kPa for silicon along [110]) and ρ the density (2330 kg/m^3 for silicon).

Once the chips were mounted on their respective scanner, the working frequency of each cantilever was determined. According to the theory, it was expected to be the fundamental frequency. By means of the easyScan software, the Wheatstone bridge was initialized and the excitation frequency inducing the largest deflection was found. The obtained values for the FM and the FS chips are presented in table 2.4. Since these values were very close to the first harmonic of the cantilevers, we supposed that the cantilever was not operating in its fundamental mode.

In order to verify this, a vibrometer[1] was used to measure the displacements at different positions along the cantilever. As it was guessed, the displacement was not maximal at the extremity of the cantilever, but somewhere near one third of L, as illustrated in figure 2.11. The amplitude of oscillation at the extremity varied from 50 nm to 300 nm depending on the cantilevers. The software did not choose the fundamental frequency probably because the stress at the base of the cantilever was too weak to generate a good signal. As a matter of fact, one can guess from figure 2.11 that the stress was higher in the upper mode, producing a better signal. As the feedback loop in dynamic mode is based on a frequency shift, using an upper mode did not prevent the AFM from sensing the topography, as the shift happens also for the first harmonic frequency.

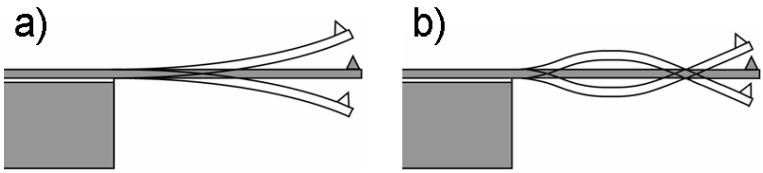

Figure 2.11: Illustration of the fundamental (a) and the first harmonic mode (b) of a cantilever. In the first harmonic mode, the measured amplitudes at the extremity varies between 50 and 300 nm, depending on the cantilever.

[1]PolyTec Vibrometer OFV-551

Table 2.4: First harmonic frequencies for the FM and FS chips (T = 20 deg C, p = 10 mbar).

#	f_1^{FM}(kHz)	f_1^{FS}(kHz)
1	38.3	37.8
2	33.4	32.5
3	37.1	35.8
4	32.3	31.3
5	36.2	34.6
6	31.3	30.3
7	34.7	33.4
8	30.6	29.5

The characterization of the FM and FS cantilevers consisted also in measuring their first harmonic frequency at temperatures between - 50 deg C and 20 deg C (p = 5 mbar). The changes were small, and the values at -50 deg C were only about 0.1 kHz larger than those at 20 deg C. Even if the amplitude of oscillation was in general reduced at low temperature, it was still in an acceptable range for AFM imaging in dynamic mode. The exact values can be found in the AFM User Guide written at JPL [10]. As we will see in 2.5.3, the cantilevers could withstand a temperature of -85 deg C.

Piezoresistors

Before mounting the chip on the scanner, the piezoresistor of each cantilever was tested. First, its resistance R_2 was compared to the resistance R_1, i.e. 2 kΩ (see figure 2.6). The measured values on several wafers were comprised between 2.5 kΩ and 4.5 kΩ, with a variation of about $\pm$ 0.1 kΩ between resistors located on the same chip. The fact that R_2 was slightly different from R_1 did not affect the behavior of the device. However, equation 2.12 for the output of

the bridge is modified as follows

$$V_{out} = -\alpha \, \frac{\Delta R}{R_2} \, V_{in} \, , \tag{2.16}$$

where $\alpha = 0.23 \pm 0.02$ for our values of R_1 and R_2. Note that this value is very close to 1/4.

Knowing that the values of the resistances were as expected, it was also important to ensure that the piezoresistors were sufficiently sensitive to the deflection resulting from the forces acting on the tip. An approximation of the sensitivity of the fabricated cantilevers was derived from the theory, and measurements were then performed to compare theoretical and experimental values.

As we will see later, the bridge output V_{out} is amplified by a factor A to produce the signal V_{SIG}, called the lever signal. When the cantilever is free, V_{SIG} is equal to zero, and when the cantilever is bent, V_{SIG} varies. Based on the theory, this change of voltage was quantified for a given displacement. By definition,

$$V_{sig} = AV_{out} = -\alpha \, A \, \frac{\Delta R}{R_2} \, V_{in} \, . \tag{2.17}$$

As we know, the change of resistance is induced by the stress on the piezoresistor. As the piezoresistor thickness (about 0.3 μm) is small relative to the cantilever thickness (about 7 μm), only the stress at the surface of the cantilever is considered. The average longitudinal stress on the piezoresistor is therefore given by

$$\sigma_L^{top} = \frac{6F(L - l/2)}{t^2 \, w} \, , \tag{2.18}$$

where L, t and w are the dimensions of the cantilever, l the length of the two legs of the piezoresistor and F the (repulsive) force acting on the tip. Figure 2.12 shows a Famars cantilever deflected by a force F schematically. Since $F = kx$, where k is the force constant of the cantilever and x the displacement at its end, the stress can be

expressed as a function of this displacement. Using the expression for k given in equation 2.15, it follows that

$$\sigma_L^{top} = \frac{3Et(L - l/2)}{2L^3}\ x\ . \tag{2.19}$$

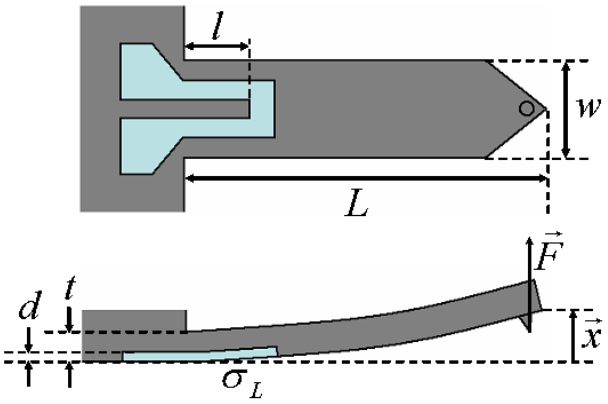

Figure 2.12: Top view and side view of a schematic bent cantilever, with length L, width w and thickness t. l is the length of the two piezoresistor's legs, while d is the thickness of the p-doped piezoresistive layer. When a force F acts on the tip, the cantilever is deflected with a magnitude x, inducing a longitudinal stress σ_L.

Substituting equation 2.19 in equation 2.8, one obtains

$$\frac{\Delta R}{R_2} = (\Pi_L + \frac{1+2\nu}{E})\ \frac{3Et(L - l/2)}{2L^3}\ x\ . \tag{2.20}$$

Finally, substituting 2.20 in equation 2.17, one obtains the change in voltage induced by a given displacement:

$$V_{sig} = -\frac{3\alpha A}{2}(\Pi_L + \frac{1+2\nu}{E})\ \frac{Et(L - l/2)}{L^3}\ V_{in}\ x\ , \tag{2.21}$$

Let's introduce the numerical values for all parameters. The value of Π_L for p-type silicon along the [110] direction is given in table 2.2 for dopant concentrations corresponding to 7.8 and 22.7 Ω cm. However, Tufte and Stelzer showed that Π_L decreases when the dopant concentration increases [11]. For our piezoresistors, the measured resistivity of 4 10^{-3} Ω cm indicates a dopant concentration of about 3 10^{19} atoms per cm^3 [9]. According to Tufte's measurements, the piezoresistive coefficient at this concentration is 55 % of the value given in table 2.2, i.e. about 40 10^{-11} m^2/N.

The two other parameters depending on the material are E and ν. For silicon along the direction [100], the literature gives $E = 169$ kPa and $\nu = 0.06$. The dimensions of the cantilevers are L = 600 $\pm$ 33 μm and t = 7 μm. Finally, the electronics circuit characteristics are $V_{in} = 3V$, $A = 97.7$, and $\alpha = 0.23 \pm 0.02$. Based on these values, one obtains

$$V_{sig} \cong -0.128\ 10^6\ x\ . \tag{2.22}$$

Experimental values were also obtained by using an engineering qualification model (EQM) of Famars. The AFM was initialized in static mode, and a flat substrate was brought into contact with the active cantilever. Then, the substrate was moved manually toward the AFM by means of a micrometer screw, bending slowly the cantilever. The resulting change of V_{SIG} was read on an oscilloscope. Figure 2.13 compares the obtained measurements with the theory. The slope of the linear fit of the measurements is $-0.119\ 10^6$ V/m, which is in accordance with the value found in equation 2.22. The difference could come from the approximations used in the theoretical part, as well as from the experimental setup.

As we saw, the piezoresistive coefficient Π_L could be increased if the piezoresistor was less doped, resulting in an higher sensitivity. However, the design of a piezoresistor is a trade-off between sensitivity and noise, and decreasing the doping would increase the noise. As Famars operated mostly in dynamic mode, the 1/f noise was not an issue and the main contribution was the Johnson noise [12]. The

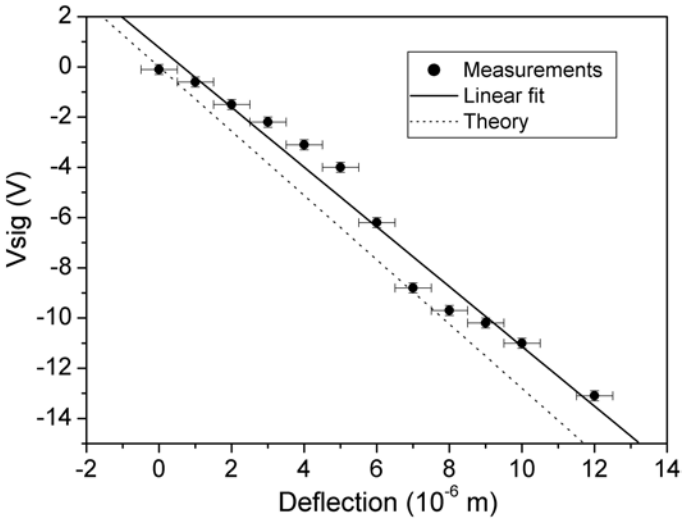

Figure 2.13: Lever signal V_{SIG} as a function of the deflection of the cantilever. The dashed line is the theoretical model and the points are experimental data. The straight line is a linear fit of the experimental data.

Johnson noise is set by the thermal energy of the carriers in the piezoresistor, and is proportional to the resistance and the temperature. Thus, reducing the concentration of dopants would increase the resistance and therefore the noise.

It is also interesting to know that operating the Famars instrument at martian temperatures should reduce the noise and improve the sensitivity. First, for our concentration of 3 10^{19} atoms per cm^3, Tufte showed that the piezoresistive coefficient increases when the temperature decreases: at -40 deg C, the value is about 20% higher than at room temperature [11]. At the same time, the Johnson noise will be reduced, as it is proportional to the temperature.

Despite these considerations, the signal V_{SIG} showed large amounts of noise for some chips. The source of this noise was current leakages in p-n junctions within the chip. This phenomenon is explained in detail hereafter.

The p-n junction

As we can see in figure 2.14, the p-type and n-type regions of each cantilever form a p-n junction. Current flows through this junction had to be avoided, since they would result in noise in the detection signal. The theoretical current-voltage characteristics of this junction are described in order to adjust the applied voltages.

The p-n junction, invented in 1949 by Shockley [13], plays an important role in modern electronic applications [9]. In addition to being a device used in many applications, it is the basic building block for other semiconductor devices. When a p-n junction is formed, there are uncompensated negative ions on the p-side and uncompensated positive ions on the n-side. Therefore, a depletion of mobile carriers is formed at the junction, in the so-called depletion region. This region, in turn, creates an electric field. At thermal equilibrium, the drift current due to the electric field is exactly balanced by the diffusion current due to the concentration gradients of the mobile carriers on the two sides of the junction. When a positive voltage

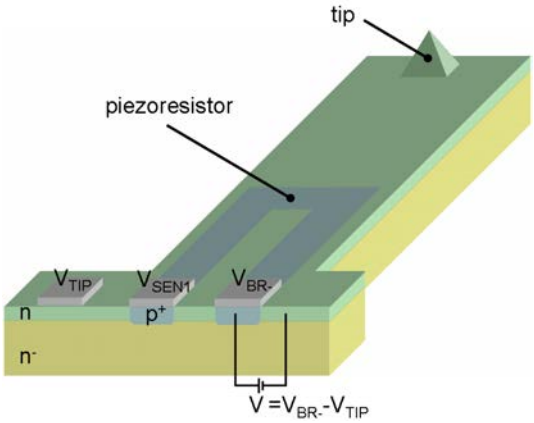

Figure 2.14: Schematics of the different doped regions for the AFM chip (first cantilever). V_{TIP} is the voltage applied on the sensor tip, V_{SEN1} and V_{BR-} are the voltages applied to each terminal of the p-channel.

is applied to the p-side with respect to the n-side (forward-bias), a large current will flow through the junction. When a negative voltage is applied (reverse-bias), virtually no current flows. However, when a sufficiently large reverse voltage is applied to a p-n junction, the junction breaks down and conducts a very large current [9]. Figure 2.15 shows the current-voltage characteristics of a typical silicon p-n junction.

Since current flows had to be avoided through the p-n junctions of the FAMARS chip, these junctions had to be reverse-biased, without overshooting the breakdown voltage. As shown in figure 2.14, three voltages are applied to each p-n junction: V_{BR-} and V_{SENn} (n = 1 to 8) for each terminal of the p-channel and V_{TIP} for the n-side. Based on the detection circuit shown in figure 2.61, p-n junctions are always reverse-biased, as V_{TIP} can not be smaller than V_{BR-} or V_{SENn}. Thus, the only necessary rule was to work above the breakdown voltage. This implies that the critical voltage on the p-

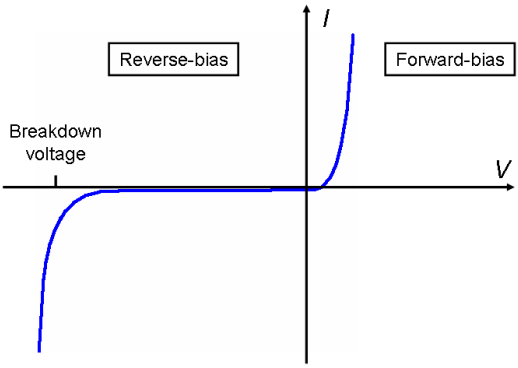

Figure 2.15: Current-voltage characteristics of a typical silicon p-n junction.

side is V_{BR-}, as it is more negative than V_{SENn}. The condition that the reverse-bias is less negative than the breakdown voltage is given by

$$V_{BR-} - V_{TIP} > V_{breakdown}. \tag{2.23}$$

In order to have the best sensitivity for V_{SIG}, V_{BR-} was set by default to its minimal value (-8V). Thus, the condition 2.24 becomes

$$V_{TIP} < -8V - V_{breakdown}. \tag{2.24}$$

In order to have a quantitative limit for V_{TIP}, the breakdown voltage was determined experimentally. On a Famars chip, a voltage V was applied to V_{BR-} with respect to V_{TIP}, as illustrated in figure 2.14. Since V_{BR-} and V_{TIP} are common to all piezoresistors, the measured current is the sum of the currents flowing through all the p-n junctions. The obtained current-voltage curve is shown in figure 2.16.

As expected, there is a current through the junctions if the bias voltage is too negative. However, it is difficult to give a precise value to the breakdown voltage. Thus, the limit was defined as the voltage

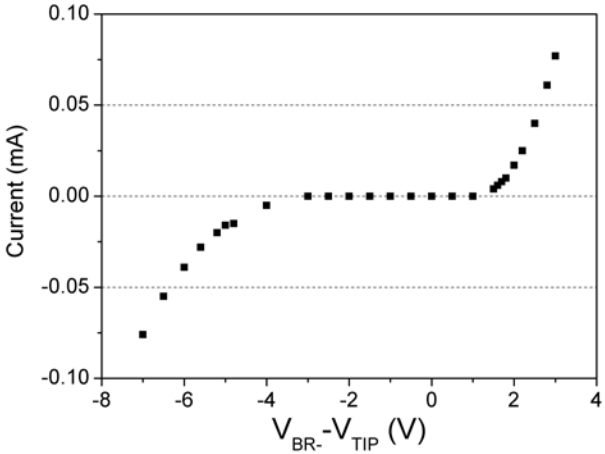

Figure 2.16: Measurements of the total current through the p-n junctions of the FAMARS chip as a function of the applied voltage.

for which the current leakage through the p-n junctions was "weak" compared to the current flowing through the active piezoresistor. If the maximal allowed leakage current is fixed to 5 % of the current flowing through the active piezoresistor, the limit voltage for this chip is about -5.5V. Thus, the condition for V_{TIP} becomes

$$V_{TIP} < -8V - (-5.5V) = -2.5V. \tag{2.25}$$

This value depended on the breakdown voltage of the measured chip, so each chip had its own limit for V_{TIP}. The FM showed good properties even with V_{TIP} equal to 0V, while the FS showed a large increase of the noise when V_{TIP} was superior to -3V. Thus, we assigned to V_{TIP} a default value of -4V, which ensured that the junction was correctly biased for any chip. This is particularly important as many different chips were used for the characterization of the Famars instrument.

2.3 Famars scanner

2.3.1 Technical requirements

The main characteristics describing a scanner are the maximum scan size, also called XY scan range, and the vertical stroke, also called Z scan range. In order to determine the size distribution of martian soil particles, which are in the micrometer range, several particles had to fit on the same image. Thus, several tens of micrometers were needed for the XY scan range. For Famars, the requirement was set to a minimum of 40 μm.

In terrestrial applications, AFM is mainly used for the characterization of relatively smooth samples, the height being small compared to the lateral dimensions of the observed structures. On the contrary, Famars has to measure three dimensional objects, which implies a large stroke perpendicular to the sample plane. A minimum stroke of 10 μm has been specified as an initial requirement. This value could be insufficient if particles pile up on each other due to e.g. electrostatic charging. Experiments under Mars-equivalent conditions are currently conducted by our partners to evaluate the risk of encountering this sort of piles. If this phenomenon is likely to happen, each sample will require an investigation with the OM before AFM imaging.

2.3.2 Scanning principle

In commercial AFM, piezo-ceramic actuators are used for scanning areas of several tens of micrometers. These actuators require driving voltages up to 100 V for such large strokes. This type of actuation would therefore have required a special design, since such voltages would ionize the martian carbon dioxide atmosphere of 0.7 mbar and create electrical discharges on the electronic circuits. An electrical discharge was probably the cause of the temporary downlink failure of the Viking 2 Lander (1976), its high voltage power converter having probably developed a corona discharge while on the surface

of Mars [14]. In addition to the discharge issue, the piezo-ceramic actuators are rather bulky and brittle. A different technique based on electromagnetic actuation was preferred, reducing the potentials of the driving signals to 12 V. This scanning principle is illustrated in figure 2.17. Three permanent magnets are attached to a spring-suspended platform. Underneath each magnet, a coil is rigidly attached to the body of the scanner. This allows exerting a force on the magnet above it by driving a current through it. This electromagnetic force is balanced by the restoring force of the springs sustaining the platform. The suspension system has to be critically damped in order to allow fast movements without ringing.

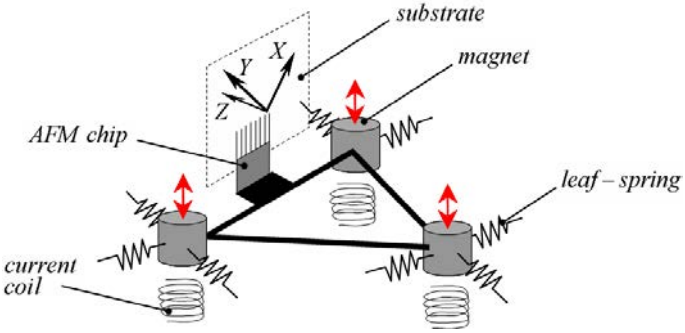

Figure 2.17: Famars scanning principle.

2.3.3 The first generation of Famars

Description

The scanning technique described in figure 2.17 was implemented for the first generation of Famars. Figure 2.18 shows a front view of the AFM scanner with a mounted chip on it. This first generation of scanner was not fabricated as part of this thesis and this section (2.3.3) only summarizes the work previously performed by S. Gautsch et al. [1, 15–21].

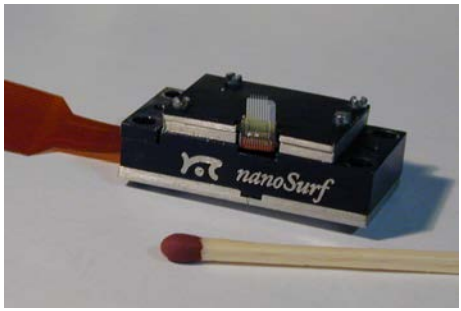

Figure 2.18: Front view of the AFM scanner (first generation) with a mounted AFM chip. The scanner had an overall size of 24mm x 18mm x 12mm and weights only 15g.

The body parts of the scanner had been made of a space compatible aluminum alloy with excellent corrosion resistance. The main part and the cover had been black anodized, in order to avoid any light reflection on the OM. The chip-bearing platform, suspended inside the scanner body, had been made of the same aluminum alloy.

Three neodymium-iron-boron (NdFeB) magnets[2] had been inserted at the extremities of the platform. NdFeB shows a remanence of 1.4 T and a magnetic field intensity of 11,000 Oe. By volume, it required about eighteen times as much ceramic magnet material to obtain the equivalent magnetic strength. For the electromagnetic actuation, three coils (copper wires insulated with polyamide) had been glued to the body part, beneath each magnet.

The platform had been suspended on three leaf-springs made of stainless steel (EN 1.4310). As they had a high quality factor, a film of viscous grease[3] had been applied to them to increase the loss of energy, i.e. for damping. The left part of figure 2.19 shows the three leaf-springs sustaining the platform at the magnets positions. The right part shows an enlarged view of a leaf-spring.

[2]NdFeB/N48, ref. M661032, Maurer Magnetic AG, Grüningen, CH
[3]Apiezon® N, Apiezon Products M&I Materials Ltd, Manchester, UK

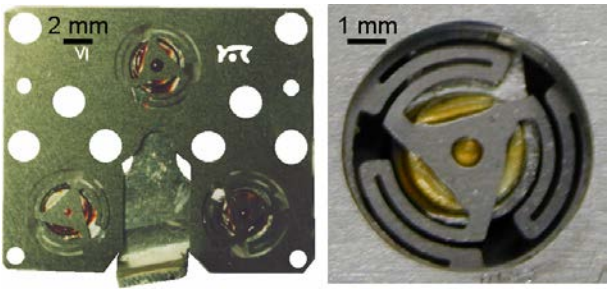

Figure 2.19: Left) Top view of the stainless steel sheet with the three springs sustaining the platform. Right) Top view of a leaf-spring. It was composed of three branches, on which special grease had been applied to increase the damping.

The AFM sensor-chip had been mounted vertically on the platform with two tilt angles relative to the substrate so that only the far right tip had been in contact with the surface. In order to vibrate the cantilevers in dynamic mode operation, a small piezo-electric plate was mounted on the backside of the chip holder.

The electrical contacts had been fed to the AFM chip, to the piezo-electric plate and to the current coils by a Kapton®,[4] flexprint printed circuit board (PCB), "flexprint" for short. The wiring between the flexprint and the chip was performed by wedge bonding using 45-μm aluminum wires. Figure 2.20 shows these wire bonds after their encapsulation in epoxy glue[5].

To reach the chip, the flexprint had been glued to the backside of the suspended platform. To reduce the mechanical constraints of the platform, the flexprint had been cut at the interface between the platform and the fixed part of the scanner. Then, soft 45-μm aluminum bond wires had been added to reconnect the copper lines (see figure 2.21). Two different epoxy glues had been used for the

[4]Kapton® HN, DuPont High Performance Materials, Circleville, OH, USA
[5]Araldit® Rapid, Novartis, Basel, Switzerland

assembly, one being non-conductive[6] while the other was silver-filled[7].

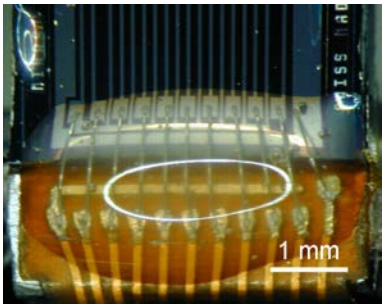

Figure 2.20: Zoom on the front of the scanner. The wire bonds between the extremity of the flexprint and the chip had been encapsulated in epoxy glue. The white oval in this image is light reflection on the epoxy glue.

Figure 2.21: Backside view of the platform. The flexprint had been cut at the interface and wire bonding had then been employed for reconnecting the copper lines.

[6]EPO-TEK® 353ND-T, Epoxy Technology, Billerica, MA, USA
[7]EPO-TEK® H20S, Epoxy Technology, Billerica, MA, USA

Performances

The AFM scanner had been characterized by recording AFM images of an orthogonal grid with known height and period. The calibration sample used to characterize the scanner had a step height of 200 nm and a pitch of 10 μm. At room temperature, a XY scan range of 53 μm with a corresponding Z range of 5.4 μm had been obtained. Due to the scanning method, the Z stroke depended on the scan range, and a Z range of thirteen μm had been obtained by reducing the XY scan range to five μm. The displacements produced by the electromagnetic actuation were therefore judged to be sufficient for fulfilling the requirements.

However, at temperatures below 0 deg C, the viscosity of the grease applied to the leaf-springs increased, causing distortions in the scan field, especially at the beginning of each scan line (see figure 2.22) [1]. This effect was even stronger at lower temperatures; the grease became so stiff that no movement was possible anymore.

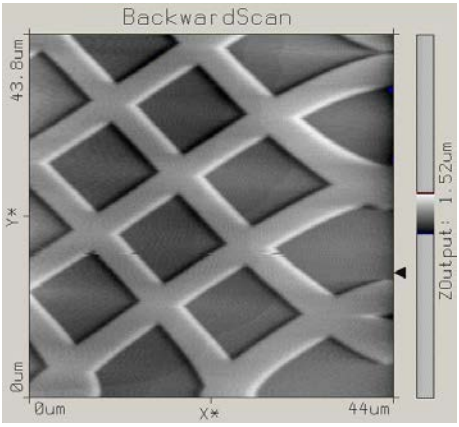

Figure 2.22: Image of a calibration grid taken by the first scanner generation at 0 deg C. The distortion due to the damping grease was visible at the beginning of each scan line.

The only short term solution to this problem had been to run the scanner without grease. The vibrations of the platform due to the reduced damping were then transmitted to the cantilevers. This was particularly true under Mars equivalent pressure (7 mbar), where also the surrounding gas could not provide useful damping. Interferences with these vibrations could have been reduced by adjusting the feedback loop settings and by significantly reducing the scan speed.

From an engineering point of view, the wire bonding at the interface of the platform, shown in figure 2.21, was not optimal, because it created an asymmetry in the design, constraining the platform at this location. In addition, two of the wire bonds on the heritage FS were diagnosed broken at Jet Propulsion Laboratory (JPL) in 2005. The cause of the failure was not investigated, as a decision had already been made to suppress the wire bonding at the interface of the platform.

2.3.4 The second generation of Famars

When MECA was selected for the Phoenix mission, a new design of Famars was needed to overcome the damping issue and the problem with the feeding of the electrical contacts to the chip. First, new materials for the leaf-springs were investigated. After the selection of a good candidate, a new scanner was built and characterized to quantify the improvement in term of damping.

Theoretical consideration

As described in chapter (1.4.1), the AFM scanner performs a raster movement during imaging. Ideally, the motion of the tip along each scan line is characterized by a step-like function (see figure 2.23), each step corresponding to a pixel in the AFM image. In reality, the scanner needs a certain time to move the tip to the desired position and can overshoot it and swing back and forth around it. As shown in figure 2.23, the behavior of the scanner depends on its damping. An overdamped scanner needs a “long time” to reach the desired

position. An underdamped scanner reaches it faster, but suffers from ringing. The best case is a critically damped scanner, the steady state being reached in the shortest time. In order to understand in detail the effect of the damping on the motion of the scanner, the theory of the linear harmonic oscillator is introduced hereafter.

A linear harmonic oscillator is a system with one degree of freedom, whose behavior versus time is described by a linear second-order differential equation with constant coefficients [22]. In classical mechanics, it is composed of a mass m which experiences a restoring force F_S from a spring proportional and opposite to the displacement x. According to Hooke's law

$$F_S = -kx \ , \tag{2.26}$$

where k is the force constant of the spring. In addition to F_S, a

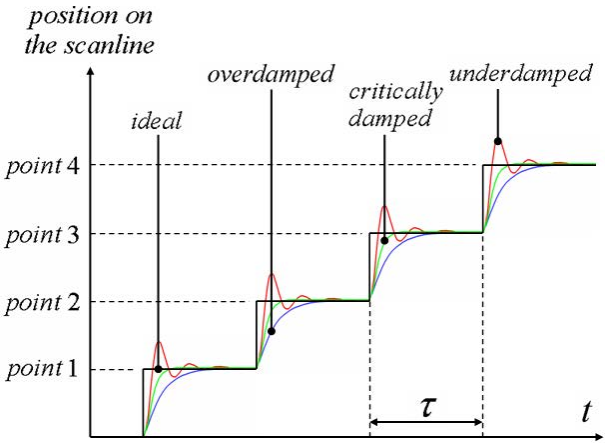

Figure 2.23: Schematics of the motion along a scan line of four points. Ideally, the displacement is described by a step-like function. In reality, the motion depends on the mechanical properties of the scanner. The three curves illustrate different behaviors as a function of the damping. In order to make a scanner work properly, the dwell time τ has to be equal to or larger than the ringing-down time.

frictional force proportional and opposite to the speed $\dot{x}$ can act on m. The damping constant c gives the relation between this force and the speed. In some cases, an external sinusoidal force $f(t) = Fcos(\omega t)$ drives the mass m. Figure 2.24 illustrates the elements of a linear harmonic oscillator. The motion $x(t)$ of the mass m is given by

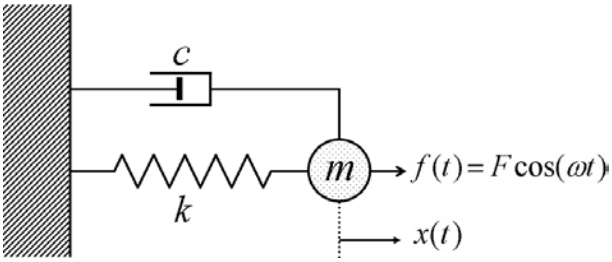

Figure 2.24: Schematics of a linear harmonic oscillator. m is the mass, k the spring constant, c the damping constant and $f(t)$ an external sinusoidal force acting on m.

Newton's second law

$$m\ddot{x} = -kx - c\dot{x} + f(t) \ ,$$

or

$$m\ddot{x} + c\dot{x} + kx = f(t) \ . \tag{2.27}$$

Dividing 2.27 by the mass m, there results

$$\ddot{x} + \frac{c}{m}\dot{x} + \frac{k}{m}x = \frac{1}{m}f(t) \ . \tag{2.28}$$

Defining

$$\omega_0 = \sqrt{\frac{k}{m}} \ , \tag{2.29}$$

$$\lambda = \frac{c}{2m} \ , \tag{2.30}$$

$$\eta = \frac{\lambda}{\omega_0} \ , \tag{2.31}$$

where ω_0 is the resonance angular frequency, λ the damping coefficient and η the loss factor, 2.28 can be rewritten as

$$\ddot{x} + 2\lambda\dot{x} + \omega_0^2 x = \frac{1}{m} f(t) \ . \tag{2.32}$$

This differential equation describes the general case of the harmonic oscillator. However, harmonic oscillators can have a simpler form if the friction is negligible and/or if no driving force is applied. We define hereunder three particular cases:

The free, undamped harmonic oscillator or simple harmonic oscillator, describes an oscillator without driving force ($f(t) = 0$) and without friction ($c = 0$). Thus, equation 2.32 becomes

$$\ddot{x} + \omega_0^2 x = 0 \ . \tag{2.33}$$

The solution of this equation can be written as

$$x(t) = Acos(\omega_0 t - \varphi) \ , \tag{2.34}$$

where the amplitude A and the phase φ are determined by the initial conditions. Figure 2.25 illustrates the displacement $x(t)$ of a simple harmonic oscillator.

The damped harmonic oscillator describes an oscillator without driving force ($f(t) = 0$), but with friction ($c \neq 0$). Its differential equation is then given by

$$\ddot{x} + 2\lambda\dot{x} + \omega_0^2 x = 0 \ . \tag{2.35}$$

The solution of this equation has the form

$$x(t) = A_1 e^{r_1 t} + A_2 e^{r_2 t} \ , \tag{2.36}$$

with

$$r_1 = -\lambda + \sqrt{\lambda^2 - \omega_0^2} \quad \text{and} \quad r_2 = -\lambda - \sqrt{\lambda^2 - \omega_0^2} \ .$$

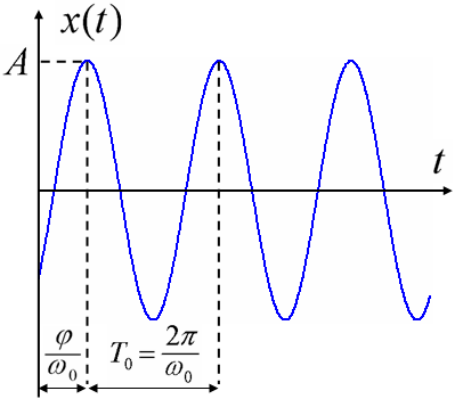

Figure 2.25: Displacement $x(t)$ of a simple harmonic oscillator.

The sign of the term in the square root of r_1 and r_2 depends on the value of the loss factor η ($= \lambda/\omega_0$). The solution of the equation will therefore be very different for $\eta = 1$ (critical damping), $\eta > 1$ (overdamping) and $\eta < 1$ (underdamping). Figure 2.26 shows the behavior of a damped harmonic oscillator depending on the loss factor. Note that the step responses corresponding to these three cases are illustrated in figure 2.23. If the system is underdamped ($\eta < 1$), 2.36 has the form:

$$x(t) = Ae^{-\lambda t}cos(\omega_1 t - \varphi) \; . \tag{2.37}$$

where ω_1, called the resonance angular frequency of the damped harmonic oscillator, is given by:

$$\omega_1 = \omega_0\sqrt{1-\eta^2} \; . \tag{2.38}$$

Figure 2.27 illustrates the displacement $x(t)$ of an underdamped harmonic oscillator. An important characteristic of these oscillations is the decay time t_0, defined as the time during which the amplitude of the oscillations decreases from A to A/e. Looking at the exponent in 2.37, it follows that

$$t_0 = \frac{1}{\lambda} \; . \tag{2.39}$$

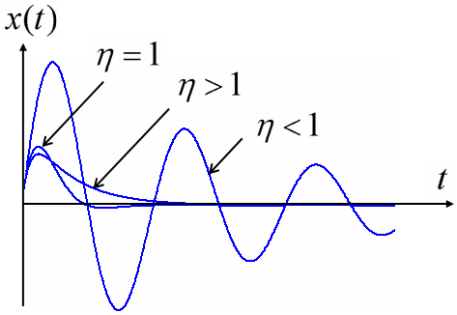

Figure 2.26: Behavior of a damped harmonic oscillator depending on the loss factor η. The steady state is reached in the shortest time if the scanner is critically damped. Note that these curves depend on the initial conditions.

Using 2.31 in 2.39,

$$t_0 = \frac{1}{\eta\omega_0} \; . \tag{2.40}$$

The damped, driven harmonic oscillator describes an oscillator with friction ($c \neq 0$) and with a sinusoidal driving force $f(t) = Fcos(\omega t)$. Writing explicitly this driving force in 2.32, it becomes

$$\ddot{x} + 2\lambda\dot{x} + \omega_0^2 x = Fcos(\omega t) \; . \tag{2.41}$$

Using the superposition principle, the general solution to 2.41 is the sum of a transient solution which depends on the initial conditions, and a steady state solution which is independent of the initial conditions. After a certain time, the transient solution tends toward zero and only the steady state solution survives. The displacement is then described by:

$$x(t) = Acos(\omega t - \varphi) \; . \tag{2.42}$$

Figure 2.28 illustrates the steady state solution for a damped, driven harmonic oscillator.

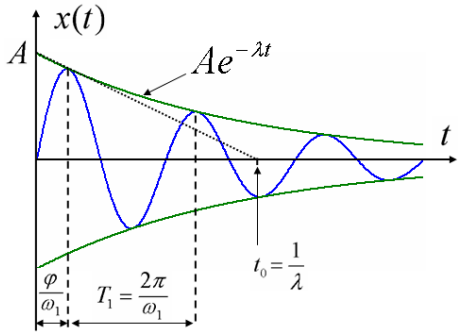

Figure 2.27: Displacement $x(t)$ of an underdamped ($\eta < 1$) harmonic oscillator. The decay time t_0 is inversely proportional to the damping coefficient.

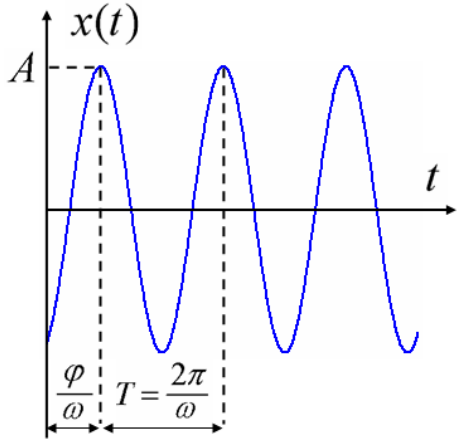

Figure 2.28: Steady state solution for the displacement $x(t)$ of a damped, driven harmonic oscillator.

The amplitude of oscillation A as a function of the excitation angular frequency ω could be recorded experimentally. The obtained curve $A(\omega)$ is called the frequency response or resonance curve of the system. An illustration of a resonance curve is given in figure 2.29. For a certain driving frequency, the amplitude A reaches its maximum A_{max} (except if $\eta \geq \sqrt{2}/2$). This occurs for the frequency

$$\omega_r = \omega_0 \sqrt{1 - 2\eta^2} \,, \tag{2.43}$$

called resonance angular frequency of displacement. Another important characteristic of the resonance curve is its bandwidth $\Delta\omega$, defined as the width of the peak at $A(\omega) = A_{max}/\sqrt{2}$.

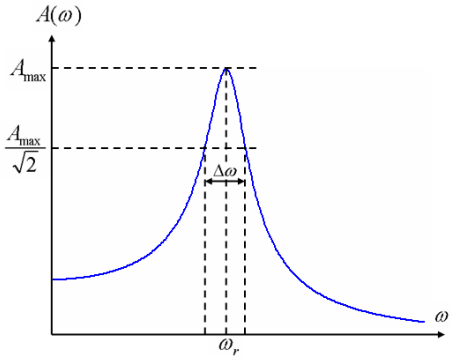

Figure 2.29: Amplitude of oscillation as a function of the angular frequency of the excitation. The amplitude is maximal for the angular frequency of displacement ω_r.

If the damping is weak ($\eta << 1$), the loss factor is given by

$$\eta = \frac{\Delta\omega}{2\omega_r} \cong \frac{\Delta\omega}{2\omega_0} \,. \tag{2.44}$$

Instead of the loss factor, engineers frequently use the quality factor Q, given by

$$Q = \frac{1}{2\eta} \,. \tag{2.45}$$

By substituting equation 2.44 into equation 2.45, one obtains

$$Q = \frac{\omega_r}{\Delta\omega} \cong \frac{\omega_0}{\Delta\omega} \ . \tag{2.46}$$

The relationship between the quality factor and the decay time t_0 can be found using 2.45 in 2.40:

$$t_0 = \frac{2Q}{\omega_0} \ . \tag{2.47}$$

The theory of the harmonic oscillator can be applied to the AFM scanner, $x(t)$ being the vertical motion of the platform, m the total mass of the suspended platform (including the three magnets and the chip), k the force constant of the leaf-springs, c the damping constant of the leaf-springs (the contribution of the atmosphere is negligible on Mars) and $f(t)$ the Lorentz force applied to the magnets by the current coils. Since this force is not sinusoidal during imaging, the damped, driven harmonic oscillator model was not valid for the scanner. However, this model was applied to the simple beams employed for the material selection described hereafter.

Material selection for the new leaf-springs

As understood from 2.23, the decay time t_0 of the AFM scanner has to be short enough for imaging at a reasonable scan speed. Based on equation 2.40, t_0 could be reduced in the new design by increasing either the loss factor η or the angular resonance frequency ω_0. This latter parameter depends only on the mass m of the suspended platform and on the force constant k of the leaf-springs (see equation 2.29). On the one hand, the mass of the platform could not be significantly reduced, because the size of the magnets prevented further miniaturization. On the other hand, an increase of the force constant of the leaf-springs - by increasing the thickness - was not considered, as a too large stiffness could prevent any motion of the scanner. Thus, the best way to decrease the decay time was to increase the loss factor of the leaf-springs.

As an alternative to viscous damping, internal friction inside the springs themselves was considered. An attractive material for that purpose is polyimide, since it has a higher loss factor than stainless steel, it is space compatible and it can be used as flexible PCB, thereby allowing integrating the electrical leads to the scanner into the suspension springs.

Thus, the damping properties of various types of polyimide (or polyimide laminates) were compared to those of stainless steel. In particular, their respective quality factor Q was measured, as it is inversely proportional to the loss factor η (see equation 2.45). This was performed by means of simple beams cut out of the materials illustrated in figure 2.30, namely stainless steel, Kapton®, the flexprint used in the former design (see figure 2.21) composed of Kapton® with copper lines in-between, and Upisel®-N (another flexible, copper clad laminate, based on the polyimide Upilex®-VT)[8].

The quality factors of the beams were determined by recording their respective frequency response $A(\omega)$. By extracting the resonance frequency of displacement and the bandwidth from this curve, the quality factor was calculated using equation 2.46. The beams, measuring 0.5 to 3.5 centimeters, were vibrated by means of a piezoelectric plate. The frequency sweep was performed using the internal sinusoidal reference of a digital instrument[9]. The deflection was measured by means of a laser interferometer[10] focused on the aluminum-coated end of the beam (see figure 2.31). The digital instrument monitored the resonance curve of the beam by plotting the output of the interferometer as a function of the excitation frequency. The experiments were performed at low pressure (about 10^{-3} mbar), and a liquid nitrogen circuit allowed decreasing the temperature to characterize the beams under Mars-equivalent conditions.

[8] Upisel®-N SE 1320, Ube Industries, Tokyo, Japan
[9] Stanford Research Systems, SR850 DSP
[10] Polytec OFV-3000 and OFV-502

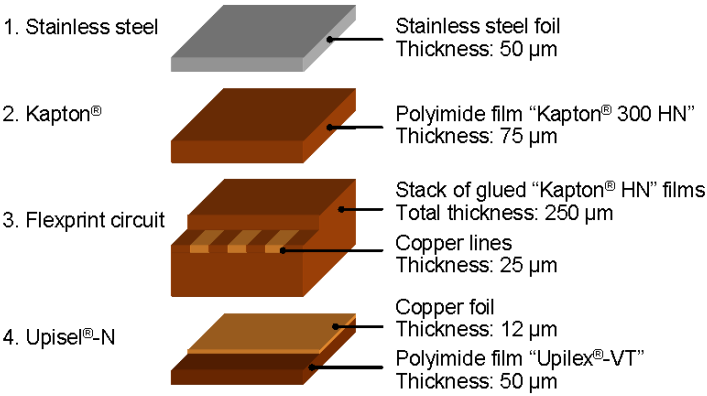

Figure 2.30: Schematics of the different materials used for the damping characterization: 1) Stainless steel, which was used for the first generation of leaf-springs, 2) Kapton®: polyimide extensively used for aerospace, 3) Flexprint, composed of Kapton layers, with copper lines in-between, 4) Upisel®-N, a flexible copper clad laminate based on the polyimide "Upilex®-VT".

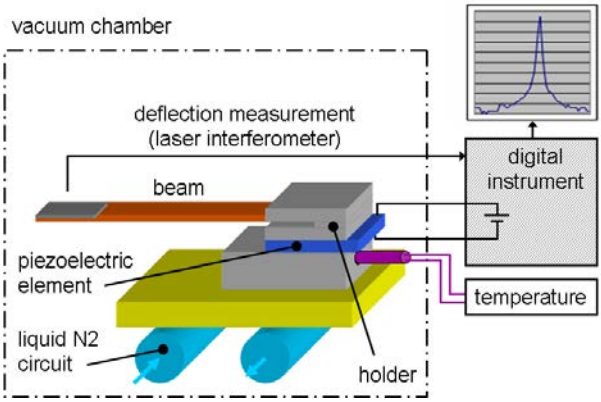

Figure 2.31: Schematics of the setup used to determine the resonance curve of the different beams under Mars-equivalent conditions.

According to equation 2.43, the resonance frequency of displacement $f_r(=\omega_r/2\pi)$ of a damped, driven oscillator is very close to the resonance frequency $f_0(=\omega_0/2\pi)$ of the free oscillator if the damping is weak ($\eta << 1$). In order to adjust the frequency sweep, we calculated f_0 for Kapton and stainless steel beams using

$$f_0 = \frac{h}{\sqrt{6}\pi l^2}\sqrt{\frac{E}{\rho}}\,, \tag{2.48}$$

where l is the length of the beam, h the thickness, E the Young's modulus and ρ the density of the material. Figure 2.32 compares the resonance frequency of displacement f_r of beams having different lengths with their calculated resonance frequency f_0. These two frequencies were very close for both materials, which indicates underdamping (see again equation 2.43).

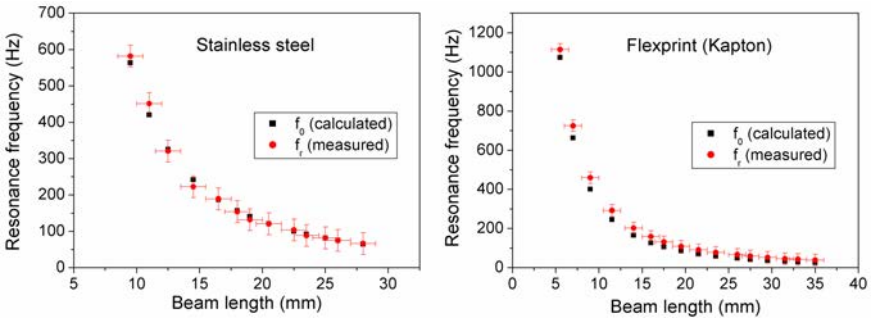

Figure 2.32: Resonance frequency f_0 (calculated with 2.48) and measured resonance frequency of displacement f_r as a function of the length of stainless steel (left) and flexprint beams (rigth) at room temperature.

The resonance curves for the different beams at temperatures between -50 deg C and +20 deg C, as the example illustrated in figure 2.33, provided quantitative values for the quality factor of each material within this range of temperature, as summarized in table 2.5.

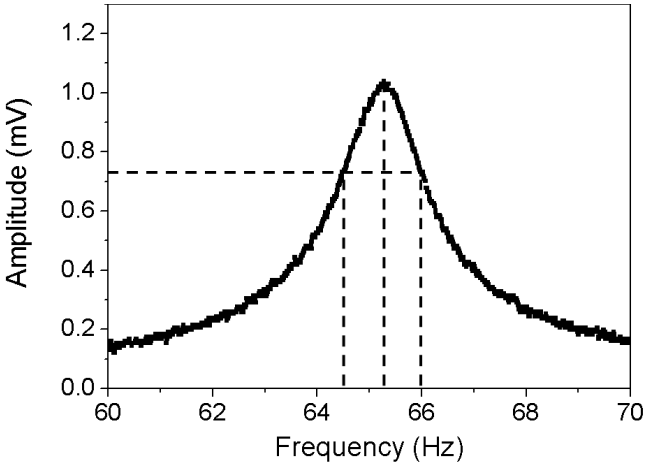

Figure 2.33: Frequency response of a flexprint beam (length = 28.5 mm) at room temperature. The resonance frequency of displacement f_r equals 65.3 Hz, and Δf = 66.0 - 64.5 = 1.5 Hz. Based on equation 2.46, Q equals 43.5 in this case.

Table 2.5: Quality factors of the tested materials for temperatures between - 50 deg C and + 20 deg C. The wide range of values obtained for stainless steel is probably due to stress induced when cutting the beams out the stainless steel sheet, since the creation of pleats could increase the energy dissipation.

Material	Quality factor
Stainless steel 1.4310	100-280
Kapton® 300 HN	51-65
Flexprint PCB	20-55
Upisel®-N SE 1320	82-89

As $Q > 0.5$ means $\eta < 1$ (see equation 2.45), the conclusion was that all beams were underdamped. However, polyimides showed a lower quality factor than stainless steel, i.e. a higher loss factor. While damping for Upisel-N was about two times higher than that of stainless steel, it was about three times higher for Kapton, which was expected because of the higher flexibility of Kapton compared to Upisel. For flexprint, essentially composed of Kapton, the damping was even higher. This was certainly due to the additional friction between the copper lines and the Kapton layers.

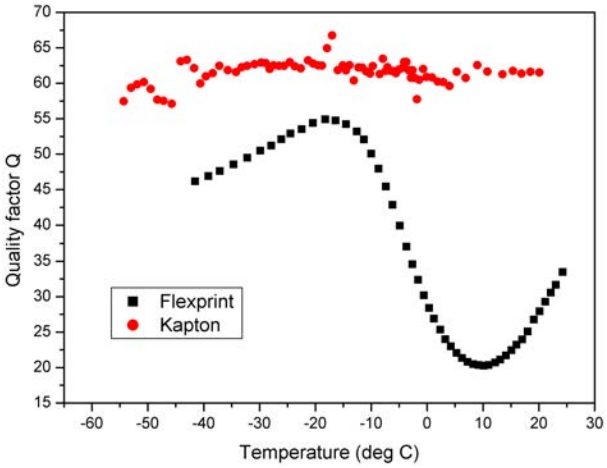

Figure 2.34: Quality factor measurements for Kapton and flexprint.

The results for Kapton and flexprint are represented more in detail in figure 2.34. Contrary to Kapton, which is known for its stable properties within a wide range of temperatures, flexprint showed a variation in damping, due to the copper lines. Moreover, the bimorph effect caused considerable bending of the beam at low temperature.

These first data indicated that using Kapton as material for the springs could improve the damping of the system [23]. However, as copper lines had to be integrated in the springs, the bimorph effect had to be avoided in the new springs design.

New design and fabrication

A new spring system was conceived in a flexprint compound. In order to avoid the bimorph effect, the flexprint sheet was designed with a symmetrical cross section, copper lines having been deposited on each side of a 50 μm layer of Kapton. Two 25 μm cover layers protected these lines (see figure 2.35). The flexprint PCB was structured by laser cutting; the minimal dimension was the width of the springs branches, which was 360 μm. The dimensions of the branches were designed to have the same stiffness as the stainless steel spring system of the first generation.

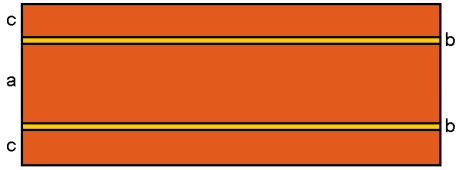

Figure 2.35: Schematic cross section of the flexprint PCB. a) Kapton layer, thickness 50 μm. b) Copper lines, thickness 15 μm. c) Kapton layers, thickness 25 μm. This symmetrical design avoids the bimorph effect.

Thirteen electrical connections were needed through the springs (eleven for the chip and two for the piezo-electric plate), and three springs with four branches each were built. Hence, two connections for each branch were designed. This implied that the copper lines needed to be only 50 μm wide, which was a challenge for the flexprint PCB manufacturer. The copper lines in the top layer of the flexprint were used for the electrical connections, whereas the lines in the bottom layer were present to compensate for the bimorph effect. Figure 2.36 and figure 2.37 show the flexprint designed under the framework of the present thesis project and fabricated by a commercial vendor[11].

[11] Cicorel SA, CH-2017 Boudry, Switzerland

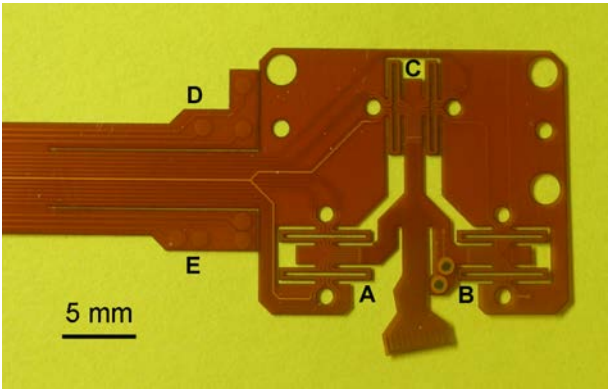

Figure 2.36: View of the flexprint sheet prior to mounting to the scanner-head. The two springs at the bottom (A, B) are the A-spring and B-spring and the upper one (C) the C-spring respectively. Two foldable strips (D, E) bring the electrical connections to the three coils.

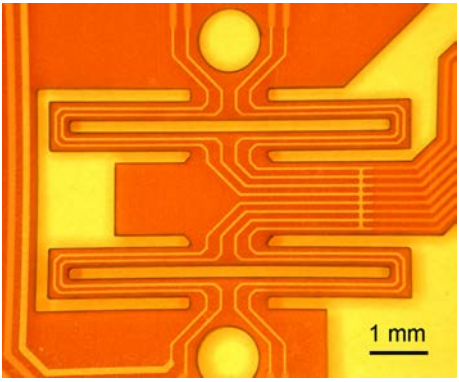

Figure 2.37: View of the A-spring. The copper lines on the visible side were designed to compensate the bimorph effect. The electrical connections were established by means of the copper lines on the hidden side.

Changing the flexprint design induced small modifications in the others parts as well. The main modifications affected the suspended platform. Contrary to the first design, the flexprint was glued to the top of the platform, since the magnets prevented from gluing it to the back. This necessitated milling a hole in the platform to access the AFM chip with the flexprint. Figure 2.38 shows the new platform and the old one. The arms of the new platform were also modified to allow gluing the fixed parts of the leaf-springs. Furthermore, spatial constraints due to the new shape of the leaf-springs led to a new way of inserting the magnets.

Because of the geometrical complexity of the platform, it was made of an aluminum alloy showing good machinability and good dimensional stability[12]. The same magnets were used for the second generation of scanner as for the first one. The mass of the new suspended platform (with magnets) was 0.65 g, compared to 0.60 g for the old one.

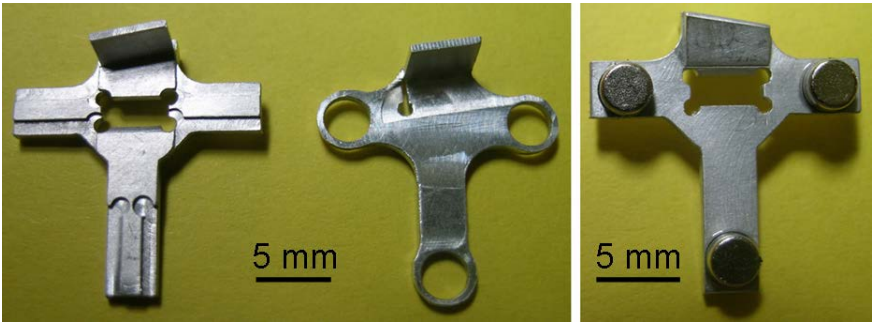

Figure 2.38: Left) Top view of the new platform (left) and the old platform (right). Right) Back view of the new platform with the magnets inserted in the holes.

Figure 2.39 illustrates the assembly of the flexprint on the suspended platform. The bonding was achieved by means of epoxy

[12]Alplan® (EN AW-5083), Alusuisse Nederland B.V., Breda, NL

glue[13]. A special mounting tool composed of two Teflon®,[14] sheets screwable on an aluminum block was used to allow a precise and safe gluing of the flexprint to the platform (see figure 2.40). The flexprint was squeezed between the block and the Teflon sheets, and then the platform was brought into contact with the flexprint. Each sheet had a slot, the size of the glued area, to protect the branches of the leaf-springs from a possible excess of glue. These slots were also very convenient for the alignment of the platform.

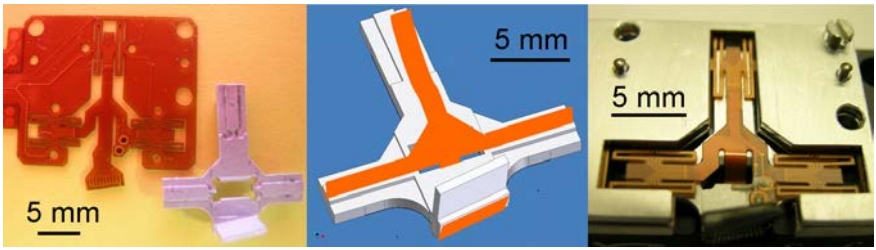

Figure 2.39: Left) Top view of the new flexprint sheet and platform prior to mounting. Center) Schematic illustration of the areas of the flexprint which were glued to the platform. Right) An open scanner showing the platform and the flexprint.

Figure 2.41 shows the new AFM scanner without cover, leaving visible the flexprint sheet sandwiched between two aluminum plates. The piezoelectric actuator contacted to the flexprint pads can be distinguished, as well as the AFM chip on the other side of the platform. The plates and the main part of the scanner were made of an aluminum alloy with excellent corrosion resistance[15]. The shape of each part was adapted to the new suspension system. As for the first generation, the main part and the cover were black anodized, in order to reduce light reflection into the OM. Appendix A-1 shows how these parts are positioned within the scanner (see figure A-II).

[13]EPO-TEK® 353 ND-T, Epoxy Technology, Billerica, MA, USA
[14]Teflon®, DuPont High Performance Materials, Circleville, OH, USA
[15]Anticorodal®(EN AW-6082), Alusuisse Nederland B.V., Breda, NL

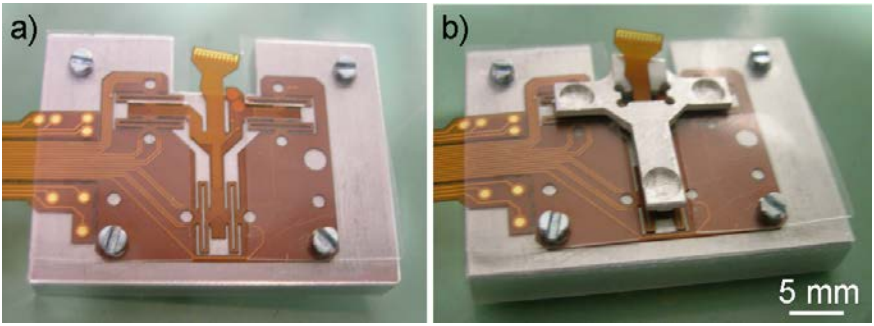

Figure 2.40: The tool used for gluing the flexprint to the platform; a) with the flexprint only, b) with the platform glued to the flexprint. The next step is gluing the flexprint extremity to the front of the platform.

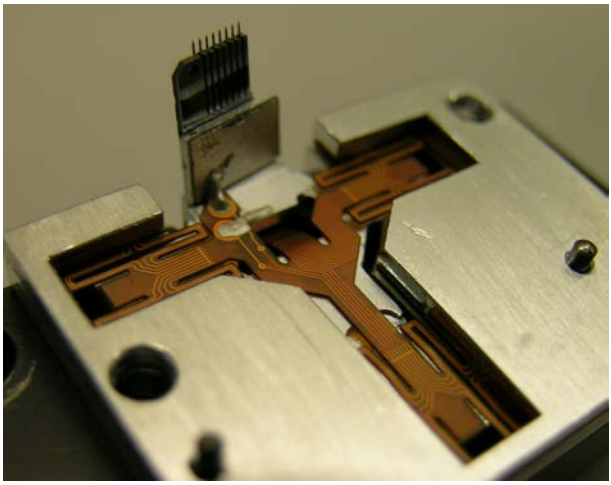

Figure 2.41: New AFM scanner without cover. The platform was suspended by the three Kapton springs. The sides of the piezoelectric plate were connected to the flexprint pads with conductive glue.

The left part of figure 2.42 shows the insertion of the coils in the bottom of the main part. The three inputs and the three outputs of the coils were connected to the electronics through two flexprint strips, indicated with (D, E) in figure 2.36. These two strips were separated from the flexprint part which was attached to the suspended platform, and after having been bent they were glued to the bottom of the main part. The right part of figure 2.42 shows the extremity of one strip with the coil input and output connected to the pads on the flexprint.

Figure 2.42: Left) Bottom view of the scanner main part with the A-, B- and C-coils inserted in their respective hole. Right) Larger view of the A-coil with its two connections to the flexprint pads. The two pads on the upper left of the image stood for the B-coil.

All these parts were assembled in a clean environment to meet the planetary protection requirements specified in [24]. All external dimensions, given in appendix A-1 (figure A-I), and the total weight of the assembled device were kept constant compared to the first generation of Famars. Figure 2.43 shows the new scanner with a chip; from the outside, there is no difference compared to the scanner depicted in figure 2.18.

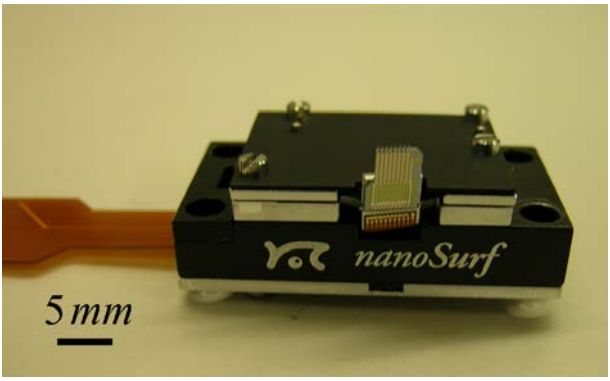

Figure 2.43: The AFM scanner of the second generation with an AFM chip mounted on it. The external dimensions of this scanner and its weight were kept constant compared to the model of the first generation.

2.3.5 Damping measurements

In order to compare the springs' properties of the first generation of Famars (Famars 1) to those of the second generation of Famars (Famars 2), their respective decay time t_0 was measured. Figure 2.44 shows the experimental setup schematically. For both scanners, a DC current was applied to the three coils, to deflect the platform to its highest position. Then, all currents were simultaneously switched off, forcing a step-like displacement of the platform. Due to the motion of the magnets, secondary currents were induced in the coils. Immediately after switching the currents off, the resulting variations in voltage on the C-coil (see figure 2.42) were recorded on an digitizing oscilloscope[16]. These oscillations decreased with time according to the underdamped harmonic oscillator solution. Thus, finding the best fit in the form of expression 2.37 gave the decay time t_0 and the angular frequency ω_1 of the scanner.

[16]Tektronix TDS 744A

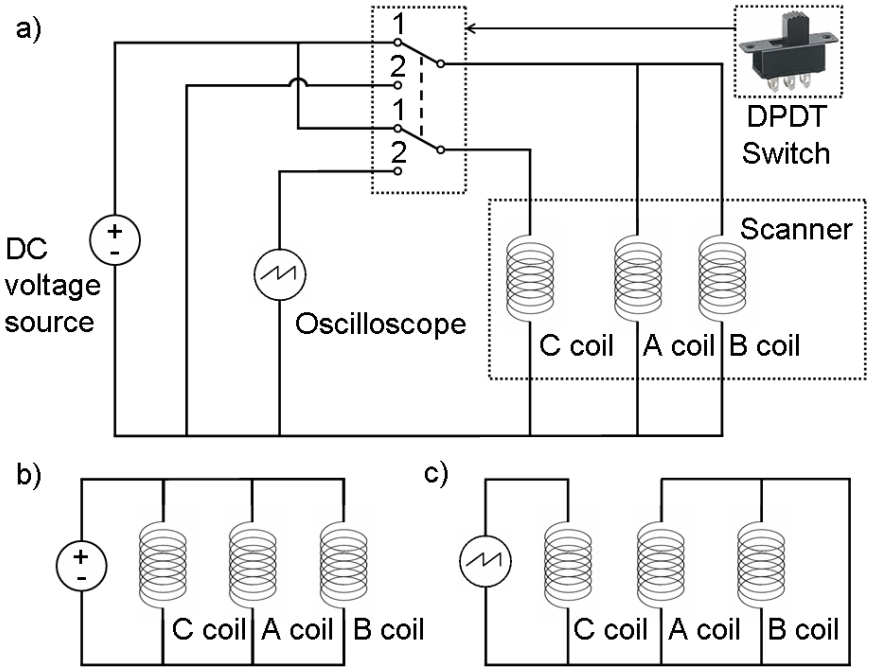

Figure 2.44: a) Schematic view of the circuit used to measure the damped oscillations of the platform. A DPDT switch (Double Pole, Double Throw switch) was used either to apply a DC voltage to the three scanner coils (position 1) or to monitor the voltage on the C-coil (position 2); b) Equivalent circuit for the switch in position 1; c) Equivalent circuit for the switch in position 2.

These experiments were performed at a pressure of 30 mbar, at temperatures varying from -128 to +20 deg C. For Famars 1, the tests were realized with or without viscous grease on the springs. Figure 2.45 illustrates examples of results for the scanners at different temperatures.

Using a dedicated software[17], each set of data was fitted for determining the corresponding decay time. Figure 2.46 illustrates the results for Famars 1 and Famars 2. At room temperature, Famars 1 with grease on the springs showed the shortest decay time, that of Famars 2 being about 1.5 times larger, as shown in charts b) and e) in figure 2.45. However, as observed by Gautsch et al. [15], grease prevented any motion below 10 deg C.

Thus, the comparison between the decay time of Famars 1 and that of Famars 2 without grease on the springs was more significant, especially at the operation temperatures, i.e. -40 deg C to +20 deg C. As shown in figure 2.46, the decay time of Famars 1 without grease on the springs was more temperature dependent than expected. Since the experiments started with grease on Famars 1, which was then removed by means of acetone and isopropyl alcohol, residue of grease probably remained on the springs after cleaning due to their complicated shape (see figure 2.19). The stiffening of this small amount of grease could explain why the decay time was lower at low temperature. In any case, the decay time was at least two to five times shorter for Famars 2 within the operation temperatures range, indicating an important improvement in terms of damping. The different decay times for the two scanners are also visible in figure 2.45 for -40 deg C (charts c and d) and +20 deg C (charts e and f).

[17] Origin® 6.1, OriginLab Corporation

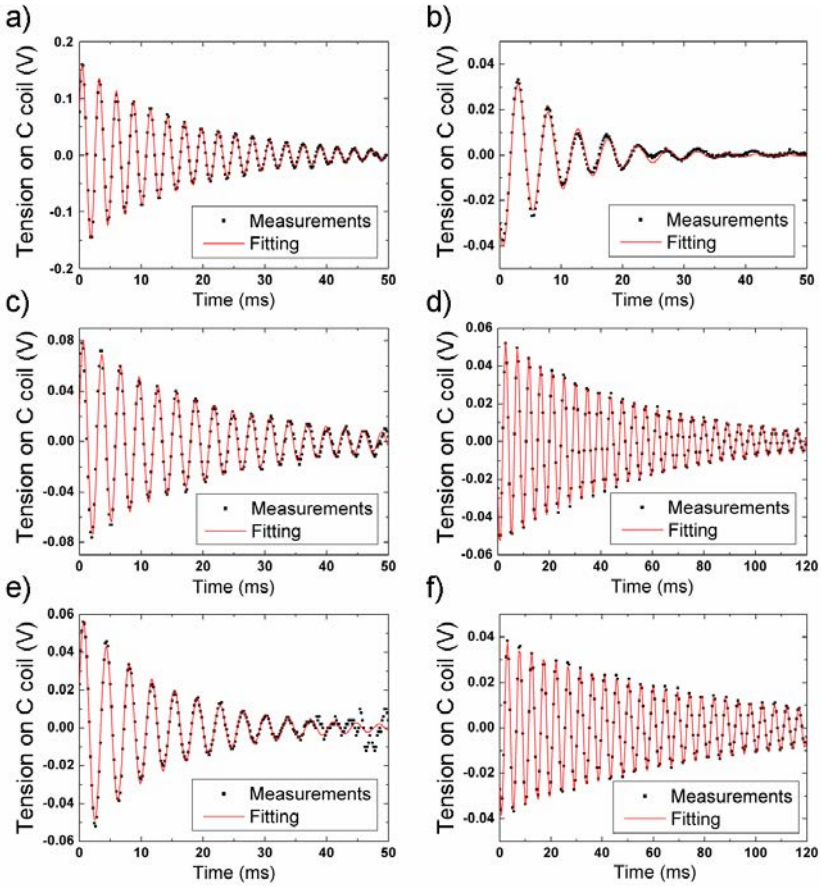

Figure 2.45: Damped oscillations on the C-coil after that the actuators had been switched off. The dots represent the data from the oscilloscope and the curve the best fitting based on the solution of the damped harmonic oscillator (see expression 2.37). The left column shows the damped oscillations for Famars 2 at a) -128 deg C, c) -40 deg C and e) +20 deg C. The right column shows results for Famars 1 with grease at b) +20 deg C and without grease at d) -40 deg C and f) +20 deg C. Note that the time scale is not the same for d) and f) as for the others.

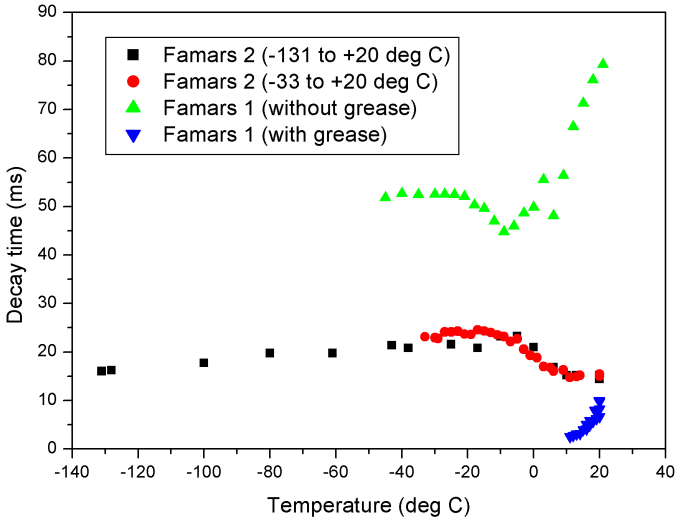

Figure 2.46: Decay times for Famars 1 and Famars 2 leaf-springs versus temperature. There are no data for Famars 1 with grease at low temperature, as the grease became too stiff below 10 deg C. Famars 2 was tested below the operation temperatures to evaluate the stability of the flexprint springs.

The higher damping of the flexprint springs was in accordance with the quality factors determined a priori (see table 2.5). The loss factor of the flexprint springs was even larger than expected, probably because the copper lines were deposited on each sides of the flexprint, increasing the internal friction. Figure 2.47 shows the quality factor of the flexprint springs compared to that of a flexprint beam. The quality factor of the springs was calculated by introducing the measured decay time and resonance frequency in equation 2.47. In addition to a lower quality factor, the new flexprint showed less variations as function of the temperature, as a result of the symmetrical design (see figure 2.35). In regard to these encouraging results, Famars 2 promised better scanning properties than Famars 1. However, the reliability of the new scanner had to be determined before starting imaging.

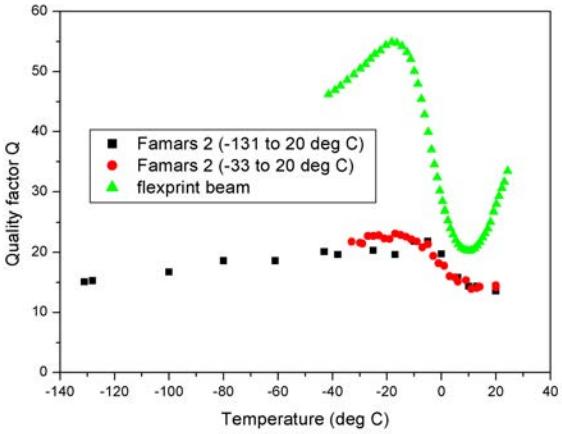

Figure 2.47: Comparison between the quality factor of flexprint determined a priori (see figure 2.34) and the quality factor of the new springs, determined a posteriori from the decay time and the frequency of the damped oscillations (see figure 2.46).

2.3.6 Fatigue test

Fatigue is the progressive deterioration of a structural component subject to cyclic stresses inferior to the ultimate tensile stress of the material. The deterioration consists first in the initiation of microscopic cracks at some locations of high stress concentration. Then these cracks propagate with each stress cycle, and finally lead to failure. In a phenomenological approach, the fatigue life of a component can be expressed as the number of loading cycles that a specimen can withstand before failure occurs. The fatigue life depends on the magnitude of the fluctuating loads, on the specimen structural characteristics and on the testing conditions.

The fatigue life of Famars 2 was scrutinized to see whether it could withstand several days of operations on Mars. The scanner was subject to different tests with distinct loading cycles and temperature. These tests and their results are described hereafter.

First test: loading 1

The goal of this test was to determine the fatigue lifetime of the scanner when submitted to large loads. The cycles were performed by applying an AC voltage to the three coils of the scanner, creating a periodic motion of the suspended platform. In order to create large displacements, the frequency of the applied signal was chosen to be the resonance frequency of the C leaf-spring (260 Hz), with an amplitude of 6 V_{pp}. This signal produced a vertical displacement of the platform of about $\pm$ 120 μm. The test was performed at room pressure and temperature.

During the test, the status of the scanner was tested by measuring its damping properties, following the procedure described in 2.3.5. The leaf-springs were also observed, as a possible delamination of the Kapton layers was of concern.

A prototype of the Famars 2 scanner went through 335 millions of cycles, and was stopped five times for performing the functionality testing. As shown in figure 2.48, the decay time for each spring did

not change significantly. This indicated that the mechanical properties of the scanner had not deteriorated.

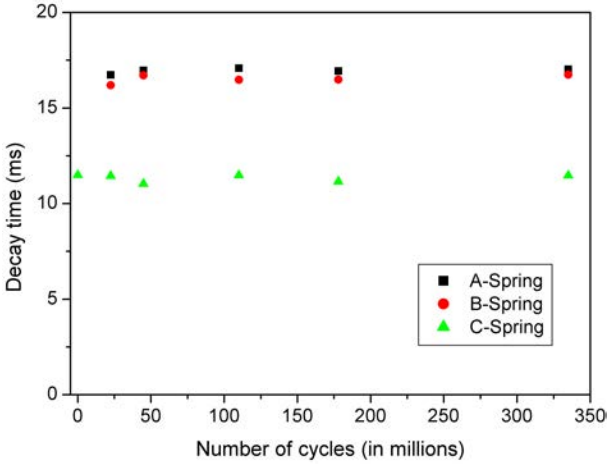

Figure 2.48: Decay time of the leaf-springs during the first fatigue test.

No delamination of the leaf-springs was observed. However, at the end of the test, a control of the electrical connections showed that some of them were not working. After an inspection of the copper lines, the locations of the cracks were found. They were all located on the C-spring, as illustrated in figure 2.49.

A simulation of the stress exerted on the leaf-springs, shown in figure 2.50, showed that the locations corresponded to areas with high concentrations of stress. Unfortunately, it was impossible to know when the cracks appeared during the experiments, as the electrical connections were only checked at the end of the testing.

We realized that the scanner was overtested, as the displacements of the leaf-springs were much larger than those expected during operations. It is also possible that the springs touched the neighboring aluminum plates, as vibrations of the whole scanner was observed. A new test was therefore needed, dealing with adapted stress loading.

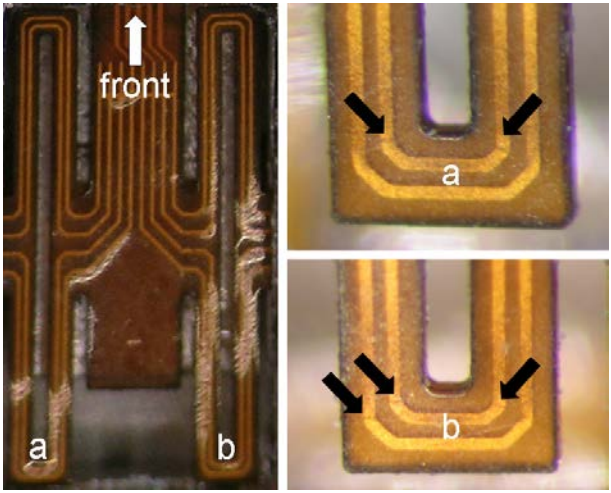

Figure 2.49: Cracks in the electrical connections after the first fatigue test. The cracks were located in the C-spring, in branches a and b.

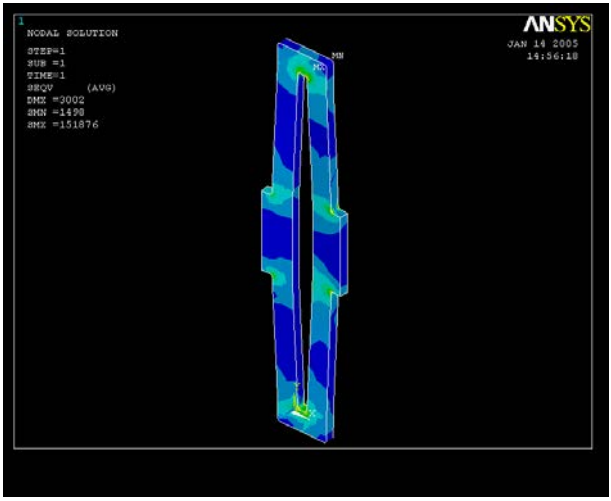

Figure 2.50: Simulation of the stress exerted on a leaf-spring. The bright area are subjected to high concentration stress.

Second test: loading 2

A new test was conducted, with a few changes compared to the first one. This test was meant to simulate the conditions of operations of the scanner when taking images. Typical AFM images are composed of 256 lines of 256 points. Since Famars takes in general 2.5 seconds to scan a line, the frequency of the excitation signal was set to 100 Hz. An amplitude of $\pm$ 12 V was used, which corresponds to the maximal voltage range applicable to the coils. This signal produced a vertical displacement of the platform of about $\pm$ 60 μm, versus $\pm$ 120 μm for the first test. During AFM measurements, the displacement of the tip between two points of the scan area does not require a displacement equivalent to a test cycle. However, if pessimistically considering that this would be the case, 5 millions of test cycles correspond to about 80 AFM images, which is twice the amount of images that the instrument should take during its required lifetime on Mars.

The set up for the test was also improved. In particular, a LabVIEW[18] program was used, which allowed stopping immediately the experiment if one of the wires was broken. For that purpose, all copper lines passing through the leaf-springs were connected in series, and a voltage was applied to them by a source controlled via LabVIEW. An ammeter connected to LabVIEW measured the current passing through this circuit, and if it decreased suddenly (indicating a broken wire), the experiment was stopped by the program, which stored the total number of oscillations before failure.

A new prototype of the scanner went through 108 millions of cycles at room temperature and pressure. As illustrated in figure 2.51, the mechanical properties of the scanner were not significantly modified by this test. In addition, the copper lines were still good at the end of this test, and no cracks were observed. As during the first test, no delamination of the spring was observed.

[18]LabVIEW, National Instruments Corporation

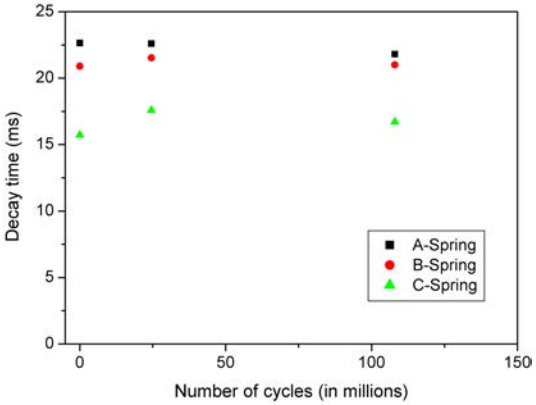

Figure 2.51: Decay time of the leaf-springs during the second test.

Third test: loading 2 at low temperature

As fatigue also depends on temperature, another test was performed at the lowest operational temperature in a vacuum chamber. The pressure was set to about 1 mbar and the scanner was cooled down to - 50 deg C by means of a liquid nitrogen circuit. As fatigue is cumulative, it is important to note that the scanner used for this test was the same one which passed successfully the test at room temperature. The testing procedure was exactly the same as for the second test, except that one had to keep the scanner at low temperature. This was done by adapting manually the flow of liquid nitrogen. The temperature during this test was always comprised between -55 deg C and -45 deg C.

The scanner went through 4.5 millions of cycles. The decay time was measured for the C-spring, and the value was found to be 17.5 ms at the beginning of the test and 17.7 ms at the end, showing no significant change. No damage to the leaf-springs or to the electrical connections were observed. The number of cycles corresponds to about two times the number of motions performed by the instrument on Mars.

Summary

During the first fatigue test, the scanner was subject to extreme amounts of stress. As a consequence, electrical connections cracks were observed in the leaf-springs, where the stress concentration was the highest. After this failure, tests subjecting the scanner to stress loads comparable to those encountered during operations showed good results both at room and low temperatures. This proved that the scanner lifetime was sufficient for the operations on Mars, and lead to the fabrication of ten scanners.

2.3.7 Wire bonds testing

The strength and the lifetime of the wire bonds between the Famars chip and the flexprint were tested for two possible causes of failure. First, an accelerated test was performed, which simulated the eventual growth of an intermetallic layer on the bond pads of the flexprint. Then, a second test was carried out with a current flowing through the wires, since electromigration can accelerate the formation of voids at the interfaces of the bonds. Galvanic corrosion was not taken into consideration, as the encapsulation of the wires bonds by glue should protect them against free mobile ionic contamination (chlorine, potassium, bromine or sodium) and moisture, preventing the formation of an electrolyte.

Test for failure induced by Kirkendall voiding

Introduction. The wiring between the chip and the flexprint were performed by wedge bonding using 45-μm aluminum wires. The bond pads of the chip were also in aluminum, while the bond pads of the flexprint circuit were in nickel, covered by a gold layer of 50 nm. While the *Al-Al* wire bond system is extremely reliable, the *Au-Al* interface could lead to failure, as explained hereafter.

Intermetallic compounds are created when two metals diffuse into one another creating species materials which are combinations of the two materials. This diffusion occurs via crystal vacancies made available by defects, contamination, impurities, grain boundaries and mechanical stress. For the *Au-Al* bonding case, there are five different intermetallic compounds that can form, the most famous being $AuAl_2$, often referred to as "purple plague" due to its purple color. These intermetallic compounds are always present in *Au-Al* bonds and should not thought to cause weak bonds. However, the different diffusion rates of *Al* and *Au* could form voids in these intermetallic layers, which can result in weakened wire bonds. These voids are called Kirkendall voids, named after the effect described by Kirkendall in 1947 [25, 26].

In 1972, C.W. Horsting published a paper which demonstrated the importance of the Kirkendall effect in *Au-Al* bond interfaces, showing that it was causing weakened areas in the bonds when they were subjected to high temperatures [27]. He noticed that this phenomenon was often accompanied by the presence of "purple plague", but he also observed that this purple intermetallic compound could be present in bonds remaining strong after exposure to high temperatures.

The intermetallic compound growth and the ratio of *Au-Al* in each phase depend on the diffusion rate and amount of material available. Intermetallic layer thickness can be estimated by the equation

$$x = K\ t^{1/2}\ , \tag{2.49}$$

where x is the intermetallic layer thickness, t the time and K the rate constant given by

$$K = C\ e^{-E_a/kT}\ , \tag{2.50}$$

where C is the rate constant, E_a the activation energy, k the Boltzmann constant and T the temperature in absolute scale.

Experiment. A Famars chip was mounted and wire bonded to a Famars scanner. To avoid the formation of *Au-Al* compounds, the gold layer at the surface of the bond pads was scratched, and the *Al* wires were bonded directly to the nickel. However, some remaining gold could have contaminated the *Al-Ni* interface, and a test was therefore performed to check the resistance of the wire bonds.

According to equations 2.49 and 2.50, the intermetallic layer forms faster at high temperature. Thus, the lifetime of the Famars wire bonds was estimated by performing an accelerated test, i.e. a test during which the temperature was increased to reduce the time required to obtain a deterioration similar to the one resulting from the mission conditions.

To obtain the time t_1 needed for an accelerated test at temperature T_1, it was necessary to estimate the contribution of each mission's phase to the total growth. As the growth is dominant at higher temperatures, the contributions from the cruise and the operations on Mars were considered to be small compared to those of the storage and the thermal tests performed on Earth. Prior to the mission, the scanner was stored during about t_2=2 years at T_2=300 K. During the thermo-vacuum tests at JPL, it was subjected to a temperature of T_3=313 K during t_3=1 day and a temperature of T_4=333 K during t_4=5 days.

By matching the total growth during the lifetime test with the growth happening during the storage and the thermo-vacuum tests, one obtains

$$Ce^{\frac{-E_a}{kT_1}}\ t_1^{1/2} = Ce^{\frac{-E_a}{kT_2}}\ t_2^{1/2} + Ce^{\frac{-E_a}{kT_3}}\ t_3^{1/2} + Ce^{\frac{-E_a}{kT_4}}\ t_4^{1/2}\ , \qquad (2.51)$$

By dividing equation 2.51 by $Ce^{\frac{-E_a}{kT_1}}$ and squaring the result, one obtains the time t_1 needed for the accelerated test:

$$t_1 = e^{\frac{-2E_a}{k}(\frac{1}{T_2}-\frac{1}{T_1})}\ t_2 + e^{\frac{-2E_a}{k}(\frac{1}{T_3}-\frac{1}{T_1})}\ t_3 + e^{\frac{-2E_a}{k}(\frac{1}{T_4}-\frac{1}{T_1})}\ t_4\ . \qquad (2.52)$$

A temperature of T_1= 360 K was chosen for the lifetime test. Thus, using a typical value of 1 eV for E_a, the required duration t_1 equals to 10.8 minutes.

Figure 2.53 shows the wire bonds between the chip and the flex-print prior to the accelerated test. The wire bonds were tested in a vacuum oven at 90 deg C during a time equal to 150% of the required test duration, i.e. 17 minutes. Finally, a destructive bond pull test was performed on the eleven wires, in accordance with the standard MIL-STD-883 2011.7 method (condition D). The pull was applied by inserting a home-made tiny hook under the lead wire with the pulling force applied approximately in the center of the wire in a direction normal to the substrate. The hook was attached to a dynamometer with a maximal measurable force of 10 gf (grams-force). Figure 2.52 gives the requirements of this standard method as a function of the diameter of the wire. As the diameter of our *Al* wires was 45 μm ($\cong$1.75 mil), the destructive pull force had to be larger than 5 gf.

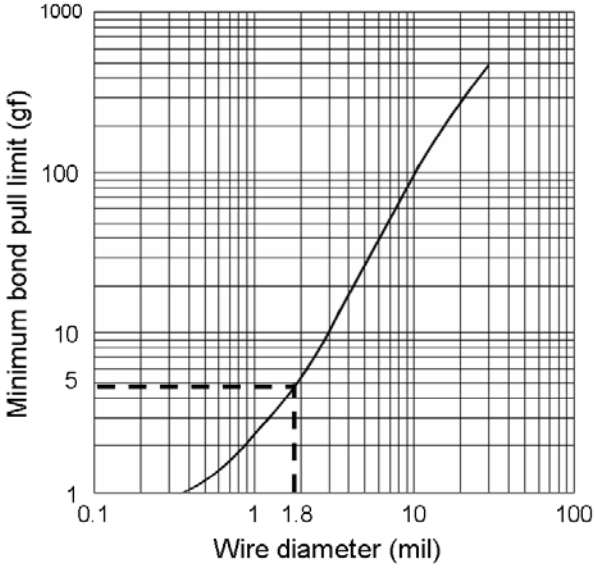

Figure 2.52: Minimum bond pull limit versus wire diameter.

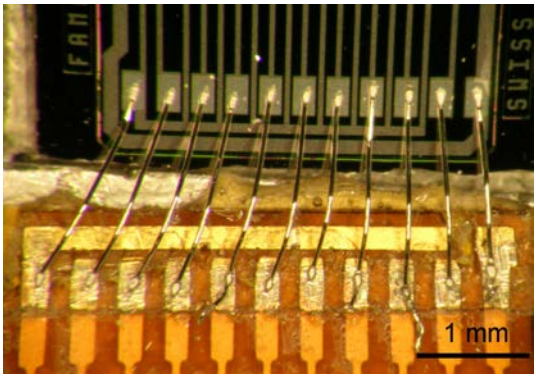

Figure 2.53: Wire bonds between the chip and the flexprint circuit prior to the accelerated test.

Results. The failure during the destructive pull test could occur at five positions in the wire bond:

1. Wire bond lift off (chip side)
2. Wire break (chip side)
3. Wire break (mid span)
4. Wire break (flexprint side)
5. Wire bond lift off (flexprint side)

When properly pulled, a "good" wire bond should fail at position 2 or 4. Figure 2.54 shows the flexprint bond pads after the destructive pull test, and table 2.6 gives the forces needed to break the wire bonds and the position of the failure. In the experiments, the failures always occurred at positions 2 or 4, except for the third wire bond, which was lifted off from the bond pad. In this case, the wire bonding is generally diagnosed as "bad". However, it should be considered that the pull test was performed manually, which could induce some imprecision in the procedure (pull angle, hook position along the wire, etc). In any case, the force necessary to remove this third wire was 9 grams-force, which was far above the requirement of 5 gf.

Table 2.6: Results of the destructive pull test performed after the the accelerated test. The force is given in grams-force (gf).

Wire	Force(gf)	Failure position
1	>10	4
2	8.5	4
3	9	5
4	>10	4
5	9	4
6	>10	2
7	>10	4
8	8.5	4
9	9.5	2
10	9.5	2
11	>10	4

In summary, the destructive pull force was far above the minimum bond pull force for all tested wire. The location of the failure was as expected for ten out of eleven tested wires. The fact that one of the wires lifted off was not considered to be a major failure as the test settings were not optimal. If an intermetallic layer was formed during the accelerated test, the associated voids were not sufficient to weaken significantly the wire bonds.

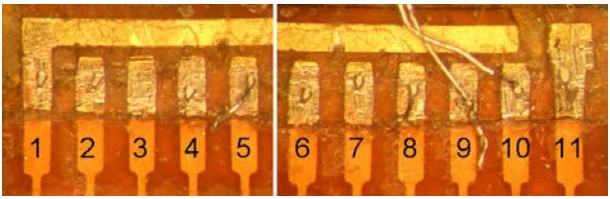

Figure 2.54: Flexprint bond pads after the destructive pull test.

Electromigration

Introduction. Electromigration is the gradual motion of ions in a conductor under the influence of an electric field. The total force F on each ion results from two contributions, the direct force and the wind force:

$$F_{total} = F_{direct} + F_{wind} = (Z_{direct} + Z_{wind})eE = Z^* eE \ . \qquad (2.53)$$

where Z_{direct}, Z_{wind} and Z^* respectively refer to the effective valences for the direct force, the wind force and the net force, and e is the elementary charge (positive). The direct force is due to the action of the applied field E on the charge of the ion. The wind force comes from the scattering of the conduction electrons off the ion, which results in a momentum transfer. In good conductors, such as the ones used for wire bonding, the electron wind force is the dominant force felt by the ion cores [28].

In an ideal conductor, where metal ions are arranged in a perfect lattice structure, there is no wind force, as the electrons move through it without experiencing collisions. In a real conductor, scattering between the conducting electrons and the ions of the conductor happens at defect locations (vacancies, impurities, grain boundaries, dislocations) or with ions moved about their ideal position by random thermal vibrations. This is the source of the electrical resistance, and also results in a wind force. In general, this wind force is too weak to move the ions of the conductor, except if a high current density is applied, typically 10^6 A/m^2.

At material interfaces, however, the ions are not well arranged, and much more scattering occurs. Thus, metal ions can be gradually moved by the wind force at lower current densities, e.g. 10^4 A/m^2. The diffusion mechanism in intermetallic compounds is complex, but in general the moving atoms are assumed to derive their mobility from repeated position exchanges with neighboring vacancies, in a mechanism called substitutional migration. A large vacancy fraction in the metal therefore ensures a high diffusion coefficient.

Consider the case of an *Au-Al* interface. We saw in subsection 2.3.7 that the different diffusion rates of *Au* and *Al* can result in Kirkendall voids. If a sufficiently large current is applied to this interface, electromigration occurs and results, for both species, in a higher diffusion rate in the direction of the electron flow and a lower diffusion rate in the opposite direction. Thus, the net diffusion rates of *Al* and *Au* are modified, changing the growth rates of the different intermetallic compounds, as well as the formation process of Kirkendall voids. Bertolino et al. showed that the incubation time and growth rate of the intermetallic compounds at an *Au-Al* interface were strongly influenced by an applied high current density, at a temperature between 400 and 500 deg C [29].

The contribution of electromigration to a possible failure process was not investigated by the test described in subsection 2.3.7. Thus, a new test was performed to see if the lifetime of the wire bonds was reduced by electromigration.

Experiment. As the scattering between the conducting electrons and the ions of the conductor increases as a function of the temperature, the electromigration is larger at high temperatures. Thus, the wire bonds had to be tested at the highest temperature during which the instrument was operated. This maximal temperature of operation was 60 deg C and happened during the thermo-vacuum test at the JPL.

The current flowing through the active piezoresistor, and therefore through the two wire bonds at its terminals, was calculated according to the schematic circuit shown in figure 2.61. Knowing that for the tested chip R_{SEN1} and R_{COMP} had a value of about 2.5 kΩ, a simple calculation based on Ohm's law gave the current through the two wire bonds. The latter was found to be 0.67 mA, with an opposite direction for the two wire bonds. As the wires had a diameter of 45 μm, the current density inside them was about 40 A/m^2. Even at a temperature of 60 deg C, this is probably not sufficient to lead to significant electromigration. However, as the *Ni-Al* interface on the

flexprint bond pad would perhaps weaken by gold contamination, an experimental validation was performed.

A flexprint circuit with a chip connected to its extremity was used for this test (see figure 2.55), instead of an entire AFM head. The main reason was that a flexprint circuit without a connector at its end simplified the application of a current to the chip. The first cantilever was taken as the active lever. Thus, two wire bonds were needed, one for the input of the piezoresistor and the other for the output (see figure 2.55). A voltage of 1.7 V was applied between the two wires, creating a current of 0.67 mA through both wires, as desired. In order to see if the current changed during the test, an ammeter was connected to a LabVIEW[19] program which allowed stopping the experiment immediately if the current decreased below a threshold fixed to 0.5 mA. The experiment took place in a vacuum oven heated to 60 deg C. Figure 2.56 shows the installation with the oven, the voltage source, and the ammeter connected to LabVIEW.

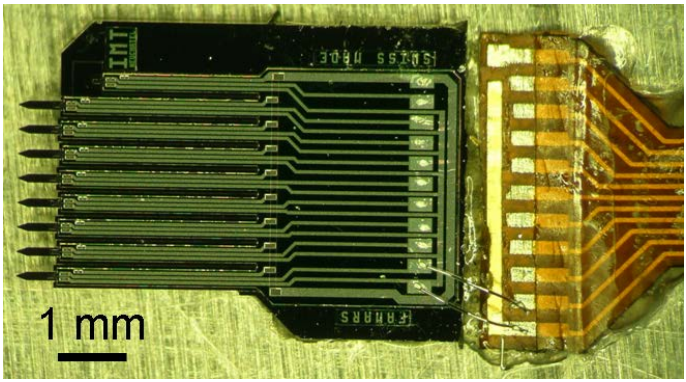

Figure 2.55: Assembly for the electromigration testing. The AFM chip and the flexprint circuit are simply glued on an aluminum surface, and two wire bonds connect the first piezoresistor.

[19]LabVIEW, National Instruments Corporation

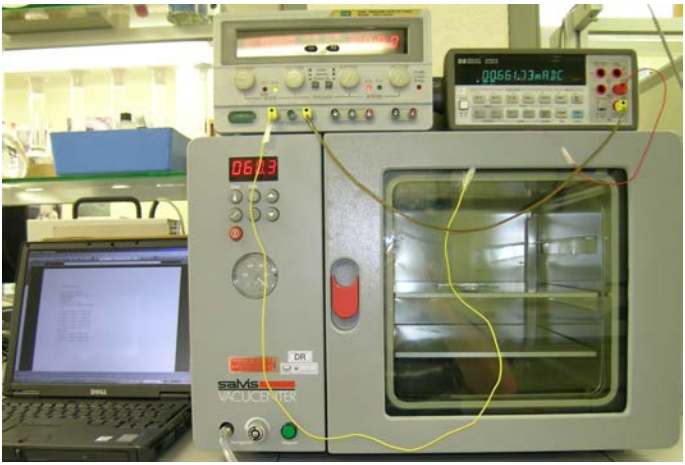

Figure 2.56: Setup for the electromigration testing.

Results. After 24 hours of testing, the value of the current flowing through the wire bonds was still 0.67 mA. However, the wire bonds could have been weakened by this test, and the same bond pull test as the one described in subsection 2.3.7 was performed.

The force needed to break the wire leading to the piezoresistor was larger than 10 gf, and the one needed to break the wire from the piezoresistor was 9 gf. These values were similar to those found during the first wire bond test (without electromigration), and mean that the wire bonds were sufficiently strong.

Summary

The two tests performed on the wire bonds, with or without current flowing through them, showed no failure of the bonds. A possible contamination of the *Ni-Al* interface with remaining gold atoms was thought to be a possible cause of failure, but fortunately the lifetime of the wire bonds was proven to be larger than needed.

2.3.8 Sterilization

In order to follow the prescriptions of planetary protection (see 2.1.8), the scanners were mounted in a clean environment, and all parts were cleaned using acetone and isopropyl alcohol. The flexprint circuit was cleaned only with isopropyl alcohol, as acetone was too strong for the glue between the Kapton sheets.

Even if the fabrication process has minimized the contamination of the scanner by micro-organisms, the aptitude of Famars to withstand a sterilization process was checked. This was performed at the Institute of Biology of the University of Neuchâtel, where a standard autoclave allowed performing the process. The latter lasted 1 hour 50 minutes, and reached a maximal temperature of 120 deg C. An EQM of Famars was sterilized, and AFM images were taken before and after its stay in the autoclave, as shown in 2.57.

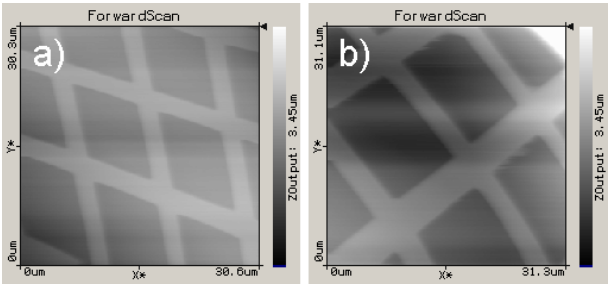

Figure 2.57: AFM images of a calibration grid (period=10μm) taken with the EQM a) before and b) after the sterilization. Both images were taken with a scanrange of 30 μm, but the respective scan area are different.

The scanner was still working after the sterilization test, but the scan properties were modified. Even if the alignment of the sample relative to the AFM was slightly different when taking these two images, it could not explain why the squares appeared larger on the right image, the scanrange being the same. A possible displacement

of the aluminum plates due to thermal expansion could be the answer. However, as it was decided later that Famars could be sent to Mars without going through sterilization, no further experiments were performed. The reasons why Famars could avoid the sterilization process were its small size and the fact that it will not be in direct contact with the martian soil. This sterilization test was followed by environmental testing of the Famars scanner and chip, described in section 2.5.

2.4 Famars electronics

This section describes the basics of the Famars electronics. It also gives also an overview of the main working configurations, depending on whether Famars is used alone or integrated into MECA. The design and the fabrication of the electronics were performed by our partners at the University of Basel and were not part of this thesis. However, good knowledge of the working principles of the electronics is needed in order to understand the software commands described in chapter 3.

2.4.1 MECA electronics architecture

MECA electronics encompasses several electronic boards, as shown in figure 2.58. The main board is the Control and Measurement Electronics (CME) board, which contains electronics for state logic and the data interface to the Lander computer. At the input of the CME board, a switch (controlled by a discrete line) allows communicating either with the AFM electronics board or with the field programmable gate array (FPGA) of the CME board. This FPGA is connected with the electronics of the WCL and of the TECP, as well as with the LED's and the SWTS of the microscopy station.

The Power board conditions the raw spacecraft power and converts it to +5V and ±15V sources. These output voltages are routed

into the CME board, which then switches and distributes them to the instrument components, including the AFM board.

Finally, the Sensor Head board relays data from the OM to the RAC electronics, which is not part of the MECA electronics (see section 1.3.2). Thus, MECA software does not address the Sensor Head board: OM images are acquired by sending a sequence request to the RAC software. The Sensor Head board is powered by a non-MECA power feed.

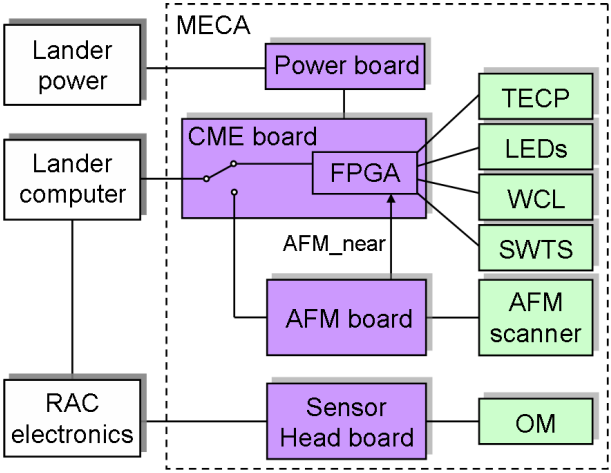

Figure 2.58: Schematics of the electronics boards of MECA. Note: the "TECP" and the "WCL" boxes include also the electronic boards of these instruments.

The switch of the CME prevents the MECA flight software (FSW) from communicating simultaneously with both the CME FPGA and the AFM electronics. This is particularly important when the SWTS brings a sample in front of the AFM. As soon as the sensor tip is in contact with the sample, the translation of the SWTS has to be stopped. When the tip and the sample are in contact, the AFM_near signal, generated by the AFM board, changes form high to low. In order to stop the SWTS, this information has to be sent to the CME,

as the switch selection prevents any communication between the AFM and the Lander computer. This is done via a special communication line, which is illustrated by an arrow between the AFM and the CME boards in figure 2.58.

2.4.2 Stand-alone configuration

As the numbers of CME and power boards were limited, Famars was often run in a stand-alone configuration during laboratory experiments, as shown in figure 2.59. This required a new board, called the M-Test board, which was designed and fabricated by the University of Basel. This board enabled the communication between the computer and the AFM board and brought the +5V and ±15V power lines. A special software delivered by Nanosurf AG, called easyScanMars, was installed on the computer and allowed to control the AFM (see 3.2).

Without the CME board, it was not possible to run the SWTS. Thus, a stepper motor also controlled by easyScanMars was used to bring the sample in contact with the sensor tip of Famars. The AFM_near line was brought to the computer through the M-Test board, and when the state of AFM_near changed from high to low, easyScanMars automatically stopped the motion of the stepper motor.

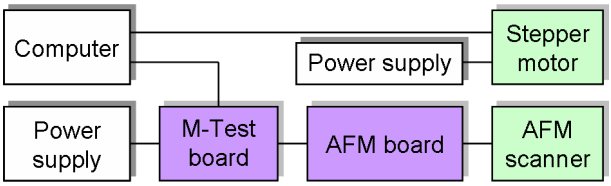

Figure 2.59: Schematics of Famars set up in stand-alone configuration.

2.4.3 Description of the Famars electronics

The AFM electronics board, shown in figure 2.60, is composed of different modules. The heart of this board is a microprocessor system, consisting of a microcontroller, a programmable read-only memory (PROM) chip (permanent memory containing the boot loader), a random access memory (RAM) chip (non-permanent memory to hold the downloaded AFM Control Software (AFMCSW) software, see chapter 3) and an Actel FPGA for the realization of the logic circuits.

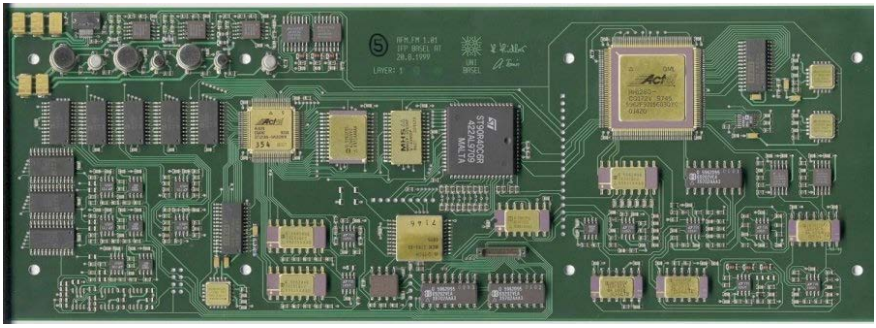

Figure 2.60: The AFM electronics board (300 x 110mm).

Other electronics modules allow performing the basic tasks needed for AFM measurements. A multiplexer is used to select the active cantilever, whose deflection is measured using a Wheatstone bridge combined with an amplifier, as shown in figure 2.61. The output of this circuit is the deflection signal V_{SIG}, also called lever signal. The rest of the circuit contains mainly 16-bit digital to analog converters (DACs) to drive the current coils of the scanner and to generate different voltages, a 12-bit analog to digital converter (ADC), a programmable gain amplifier (PGA) (gain=1-256), voltage buffers, voltage to current converters, a 24MHz quartz oscillator and a latch-up protection circuit.

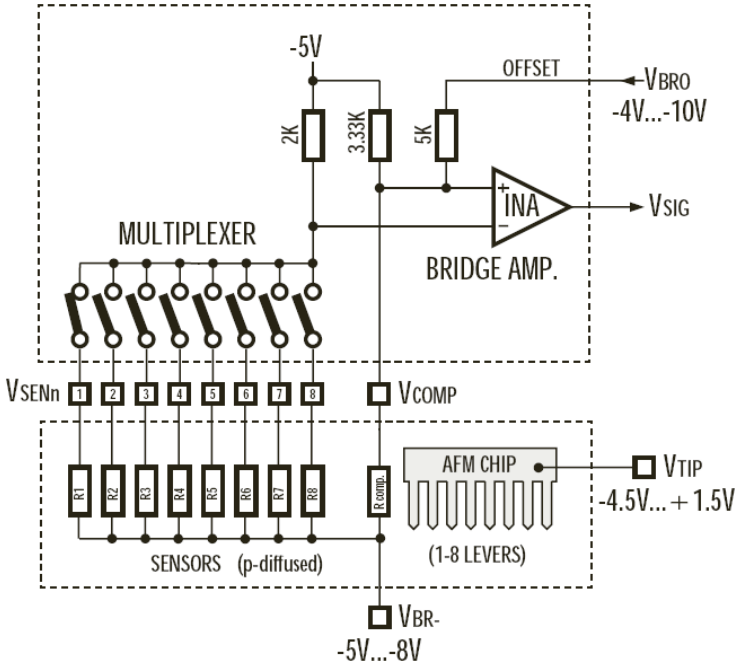

Figure 2.61: Schematics of the Wheatstone bridge of the detection circuit. The upper part is integrated in the AFM board, the lower part in the AFM chip. A multiplexer allows selecting the active piezoresistor. R_{SENn} and R_{COMP} are the piezoresistances on the n$^{\text{th}}$ cantilever and on the reference, respectively. The values of V_{BR-} and V_{TIP} are set by the microcontroller according to the choice of the user, whereas the value of V_{BRO} is generated by the microcontroller to have $V_{SENn} = V_{COMP}$ when the n$^{\text{th}}$ cantilever is free. When the cantilever is deflected, the value of the piezoresistance R_{SENn} changes and V_{SENn} is different from V_{COMP}. This difference is the input of an amplifier, the output V_{SIG} being the input of the feedback loop in static mode and the input of the phase circuit in dynamic mode. Courtesy University of Basel.

In static mode, the difference between the lever signal V_{SIG} and the setpoint is amplified by the PGA, and converted to numeric information by means of the 12-bit ADC. The controller tries to hold V_{SIG} to the same amplitude as the setpoint, to force the ADC input to zero. This means it strives to keep constant the deflection of the cantilever, i.e. the force between the tip and the surface. This height adjustment is done by changing the voltage on the current coils of the scanner. This compensation, called z-output, is recorded to get a picture of the sample topography at constant force.

In dynamic mode, the active cantilever is vibrated at its resonance frequency by means of a numerically controlled oscillator (NCO). The deflection signal V_{SIG} is the input of a PLL circuit, which is used first to find the resonance frequency of the cantilever, and then to keep constant the phase shift between the excitation signal V_{SHAKE} and the deflection signal V_{SIG}. The main output of the PLL circuit is the signal V_{FM}, which reflects the deviation of the signal from the initial resonance frequency. Then, the difference between V_{FM} and the frequency shift setpoint is amplified by the same PGA that is used in static mode, and converted to numeric information by means of the 12-bit ADC. As for static mode, the controller tries to hold the output of the ADC at zero, which means that the AFM is run at a constant frequency shift, i.e. at constant force gradient. As in static mode, this adjustment is done by changing the scanning height, and the compensating z-output is recorded to obtain the sample topography.

In addition to the z-output signal, the easyScanMars software and the FSW allow recording a second signal, called the error signal. In static mode, it is V_{SIG}, while it is V_{FM} in dynamic mode. Thus, for both modes, it gives the difference between the setpoint and the signal adjusted by the feedback loop. This signal gives precious information about the efficiency of the feedback loop.

Due to ionizing radiation, certain electronics parts can go into a latch-up state, where the supply current increases until the part is destroyed. Thus, a latch-up detection circuit monitors the current on each voltage line (+5V, ±15V) and interrupts all lines for 6 milliseconds if the current exceeds a defined threshold. This will let the parts recover from the latch-up condition and reboot the circuit. Additionally, all logical registers in the Actel chip use "triple voting" architecture to minimize software errors due to heavy radiation (by a factor of about 10,000). These two protective actions are described by S. Gautsch in his thesis dissertation [1].

2.4.4 Summary

About ten AFM electronics boards and a few M-Test boards were fabricated and delivered by the University of Basel. There were an EQM version and an FM version of the AFM boards. The difference was that many components of the EQM were not radiation hard, which allowed reducing significantly the production costs. In addition to the electronics, a detailed testing procedure was part of the delivery. The boards were always handled with care, as electronic discharge (ESD) was of concern. During the long time of use, the electronics showed a perfect efficiency, even though some boards had been built ten years ago. The PLL circuit did not find the resonance frequency of the Famars cantilevers, but their first harmonic frequency, as reported in section 2.2.5. However, the problem was probably the design of the Famars chip and not the electronics board itself.

2.5 Environmental testing

Environmental tests helped determine whether the instrument was robust enough to stand the extreme conditions in cruise and on Mars. Vibration and shock tests were performed at Oerlikon Space AG in Zürich. The resistance of Famars to thermal cycling was checked during preliminary tests at IMT and complete testing at JPL.

Table 2.7: Random vibration levels and root-mean-square acceleration (G_{rms}) for qualification and acceptance tests. The root-mean-square acceleration is often described as the square root of the area under the power spectral density curve. A more intuitive way to define G_{rms} is to consider it in the time domain. Indeed, it can be seen as the square root of the mean-square acceleration, the latter being the average of the square of the acceleration over time.

Frequency (Hz)	Qualification (g^2/Hz)	Acceptance (g^2/Hz)
20	0.025	0.01
80	0.1	0.04
500	0.1	0.04
2000	0.025	0.01
G_{rms}	10.7 g	6.8 g

2.5.1 Vibration test

The vibration test consisted of two distinct phases. The design integrity of Famars was first verified by a qualification test on a the EQM, which had already gone through the sterilization process (see 2.3.8). The purpose of this qualification test was to demonstrate with margin that the design withstood the requirements of the mission. Then, an acceptance test was applied to the FM and the FS of Famars. The goal of this second test, less demanding than the qualification test, was to detect workmanship errors or material defects in the manufacture and assembly of the flight hardware, and to demonstrate that it was representative of the EQM. The requirements for qualification and acceptance tests are given in table 2.7.

Qualification test

In order to observe any change caused to the EQM scanner by the environmental testing, AFM images of a calibration grid were taken

before the test, which could be compared with images taken afterwards. hen, a holder was conceived to install the scanner on the vibration table. It consisted of an aluminum cube with threaded holes meant to maintain the scanner and the flexprint circuit in a flight-like position (see figure 2.62). An accelerometer was fixed to the cube to record the acceleration spectrum of the vibration. Three tests were performed, one along each axis of the scanner. Their duration was two minutes, and the acceleration spectral density was based on the values given in table 2.7, as shown in figure 2.63.

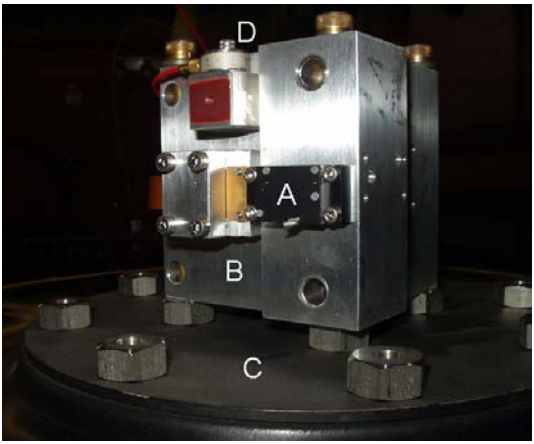

Figure 2.62: The Famars EQM prior to the vibration test along y-axis. The scanner (A) is mounted in a flight-like configuration on an aluminum cube (B), itself screwed on the vibration table (C). An accelerometer (D) allowed to record the amplitude of the vibrations.

After the vibration tests, the chip was still intact. In order to verify that it was also the case for the scanner, AFM images were taken on a calibration grid. As these images were similar to those taken prior to the vibration test, as shown in figure 2.64, the qualification test was considered to be passed.

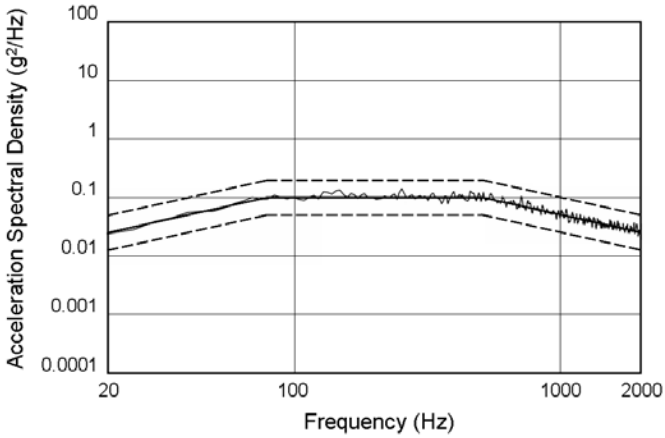

Figure 2.63: Acceleration spectral density measured during the qualification test along x-axis. The dashed lines represent the required spectrum +/- 3 dB. $G_{rms} = 10.95\ g$.

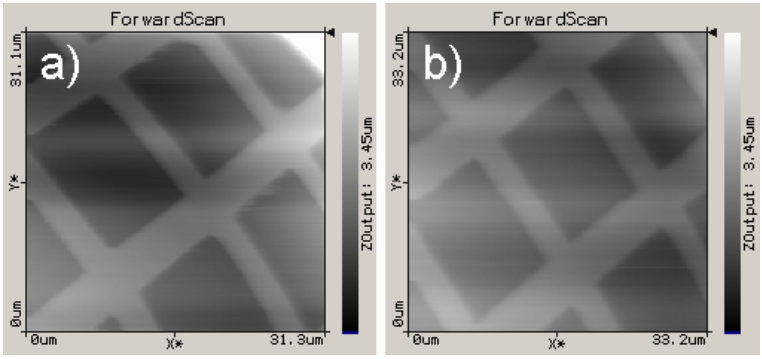

Figure 2.64: AFM images of a calibration grid (period=10μm) taken with the EQM a) before and b) after the vibration test.

Acceptance test

The acceptance test was performed on the FM and the FS scanners. The procedure was identical to the qualification test, the only differences being the duration (only one minute) and the realized spectrum (see figure 2.65). The holder allowed testing the two scanners at the same time, as shown in figure 2.66.

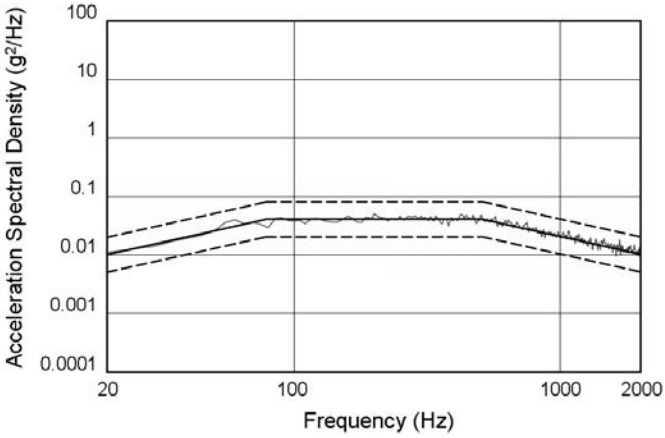

Figure 2.65: Acceleration spectral density measured during the acceptance test along x-axis. The dashed lines represent the required spectrum ± 3 dB. $G_{rms} = 6.88\ g$.

As expected, neither of the two scanners were damaged by the acceptance test. Figure 2.67 shows AFM images taken with the FM before and after this test.

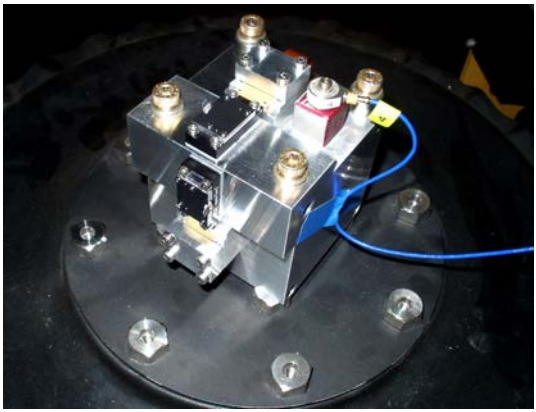

Figure 2.66: The Famars FM and FS prior to the vibration test along x-axis and z-axis, respectively.

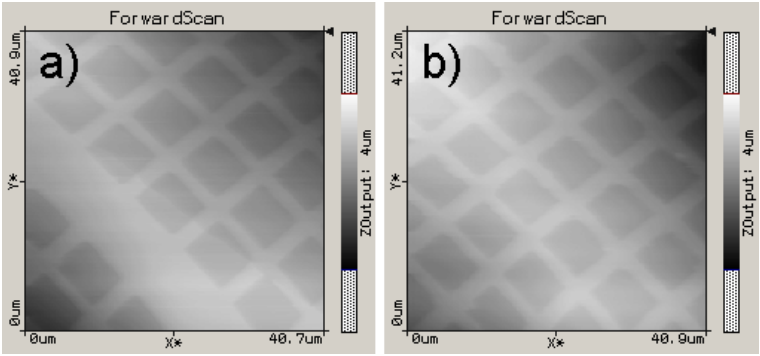

Figure 2.67: AFM images of a calibration grid (period=10μm) taken with the FM a) before and b) after the vibration test.

2.5.2 Shock test

A shock is a transient physical excitation, and is generally represented as a plot of acceleration versus time. During the Phoenix mission, the spacecraft hardware will be subjected to several shocks, the main one happening during the separation from the backshell, due to the firing of pyrotechnic bolts. In order to formulate laboratory tests simulating this shock, the shock response spectrum (SRS) was used.

The SRS shows the maximum acceleration response (to a shock pulse) of an infinite number of single degree of freedom (SDOF) systems, each of which has different natural frequencies [30]. The natural frequency of any given SDOF is shown in the abscissa and acceleration response is represented in the ordinate. The damping ratio of the SDOF systems is typically fixed at a constant value, such as 5%, which corresponds to an amplification factor of Q equal to 10. Note that the SRS does not contain all the information about the transient waveform from which it was created. Thus, different transient waveforms can produce the same SRS.

Since SRS is particularly suited for analyzing pyrotechnic shocks, NASA had specified the SRS of the backshell separation shock, calculated based on the acceleration time history, with Q equal to 10. Table 2.8 indicates the maximum acceleration response to this shock for three frequencies. In a logarithmic plot, the SRS function is obtained by connecting these data points by two straight lines. Note that these levels were those for the qualification test, no acceptance test being required.

Several techniques exist to generate the given shock response spectrum. The basic principle is a test fixture (a simple plate or a more complex structure) excited by a detonating charge or a mechanical impact. The test item attached to the fixture is subject to the direct shock wave and to the resonant response of the test fixture, which simulates the desired pyroshock. Preliminary tests are performed to adjust the set up versus the shock specifications.

Table 2.8: Shock response spectrum for the qualification test (Q=10).

Frequency (Hz)	Qualification (g)
100	47
3000	2370
10000	2370

First test

This test was performed on the EQM scanner which had already gone through the vibration test. The set up used was a conventional drop test machine, composed of a steel cylinder supporting the EQM scanner and accelerated against an arresting device, as shown in figure 2.68. This is not a standard equipment to simulate a pyrotechnic shock, as we will see later. However, the facility was easily accessible at Oerlikon Space AG and required less preparation than the methods described hereabove.

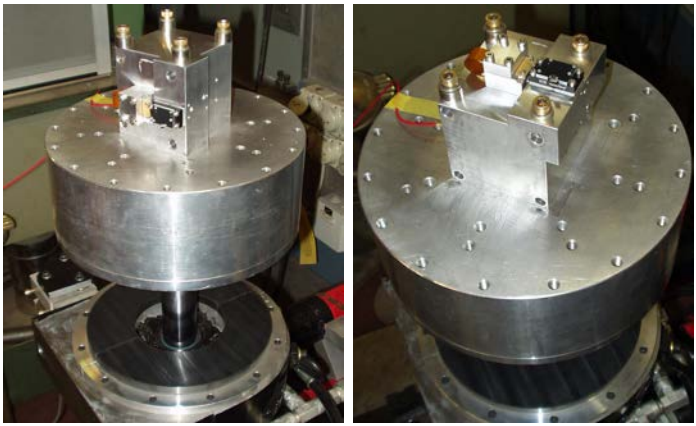

Figure 2.68: Drop test machine used for the first shock test. Left: test along y-axis. Right: test along z-axis

The EQM scanner and chip were tested along three directions. The acceleration versus time was recorded during each test, and the shock response spectrum was subsequently determined. Figure 2.69 shows the acceleration recorded during the test along the z-axis, and figure 2.70 the corresponding spectrum, in comparison with the test specifications. This spectrum was within the common tolerance of $\pm$ 6 dB, except for frequencies near 300 Hz, where it was above the tolerance, and frequencies above 7 kHz, where it was below the tolerance.

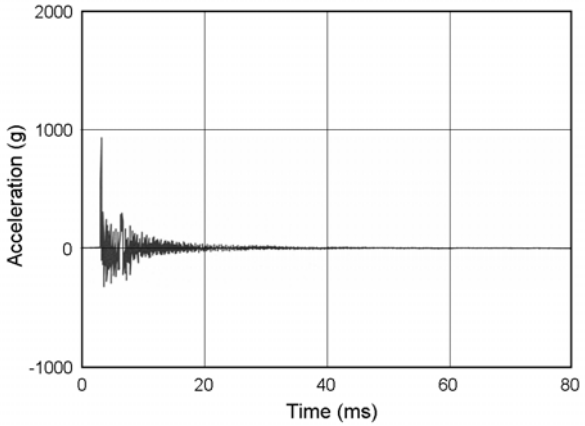

Figure 2.69: Acceleration versus time recorded for the test along the z-axis.

While the shocks realized along the lateral dimensions of the scanner (x-axis and y-axis) did not provoke any problem visible during the first optical inspection, five of the eight cantilevers were broken during the test along the z-axis. After the repetition of this test, another cantilever was broken. Only the third and the eighth cantilevers were still present at the end. Optical and SEM images of the broken chip are shown in figure 2.71.

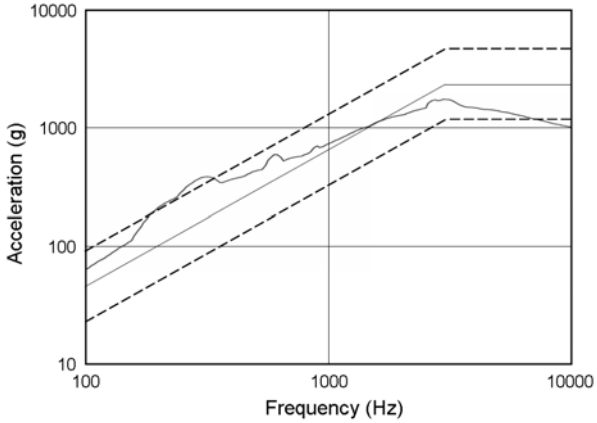

Figure 2.70: Shock response spectrum for the test along the z-axis. The SRS curve is calculated based on figure 2.69, the straight line represents the specifications given in table 2.8 and the dashed lines the tolerance of ± 6 dB (Q=10).

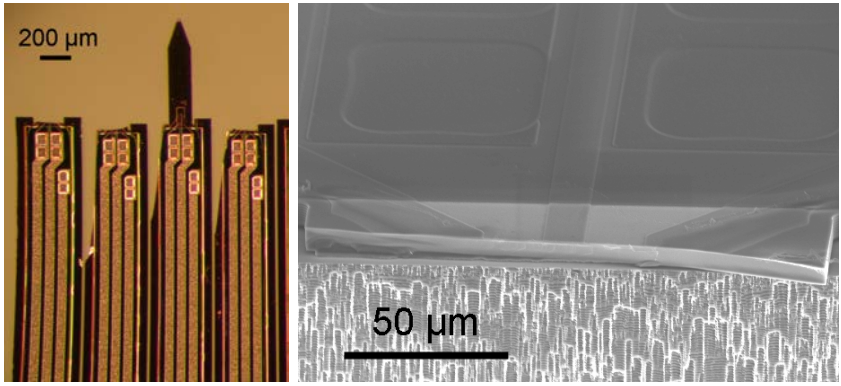

Figure 2.71: Optical image of the broken chip and SEM image of the fracture at the base of a cantilever.

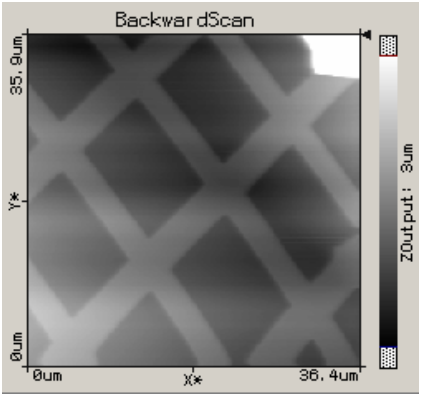

Figure 2.72: AFM image of a calibration grid taken after the first shock test.

Even if the Famars chip has not passed the shock test, AFM images were taken to check the behavior of the scanner. Since the first and the second sensors had been broken, the third one was used for imaging. Figure 2.64 shows an AFM image taken after the shock test. The scanning behavior has not changed, since the artifact at the upper right corner was already present before the shock test (see image 2.64.a).

After the failure of the shock test, a change in the design of Famars was first envisaged. The main idea was to add dampers in the scanner to dissipate the energy of the shock, therefore reducing the shock level on the sensor chip. However, in collaboration with JPL experts, it was decided that this was not necessary, since we had overtested our instrument. The drop test machine subjected the EQM of Famars to a large net velocity change, which is not representative of the pyrotechnic shock, as mentioned in [30]. In particular, it was suspected that this net velocity change caused a smash of the suspended platform against the fixed part of the scanner, propagating large shock waves to the AFM chip. Thus, the Famars scanner and chip were retested using a standard method for simulating pyrotechnic shock.

Second test

A more suitable test based on a metal-metal impact was realized on another EQM. The set up consisted of a simple steel plate which was shock excited into resonance by a mechanical impact from a dropping steel ball. The aluminum cube bearing the EQM scanner was fixed to the plate. With this method, the tested scanner was not subjected to a large net velocity change, as it had been the case for the drop test. The main difficulty was to produce the required spectrum, which implied a fair amount of tests. In the experiment, the tunable parameters were the height from where the steel ball was dropped and the location of the impact on the plate. After a few trials without the EQM scanner, a reproducible shock allowed obtaining the required shock response spectrum. As the shock waves propagated in all directions, it was enough to record the shock spectrum along x, y and z directions during a single shock.

The EQM was in fact submitted to three shocks, as the shock spectrum was obtained empirically. The first two shocks were slightly weaker than the requirements, and a higher drop for the third shock - whose acceleration versus time is shown in figure 2.73 - has allowed obtaining the desired spectrum, shown in figure 2.74. This spectrum was not very different from the one obtained during the first test (see figure 2.70). However, it is important to remember that the acceleration was measured close to the instrument, and not for the AFM chip. The fact that this second test has not induced a smash of the suspended platform against the fixed part of the scanner has probably greatly reduced the shock felt by the AFM chip, the shock waves being damped by the leaf-spring system.

An optical inspection showed that all cantilevers survived this shock test. As expected, the properties of the scanner were not changed, and several hundreds of AFM images were taken with it afterwards. As mentioned, the shock acceptance test was not performed on the flight hardware, since the vibration acceptance test was judged sufficient to detect any problem with the flight hardware.

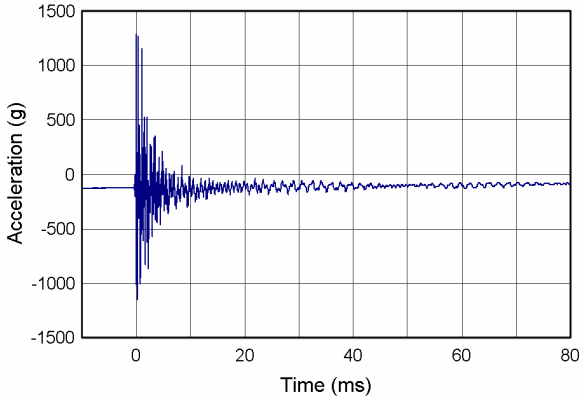

Figure 2.73: Acceleration versus time recorded for the second test along the z-axis.

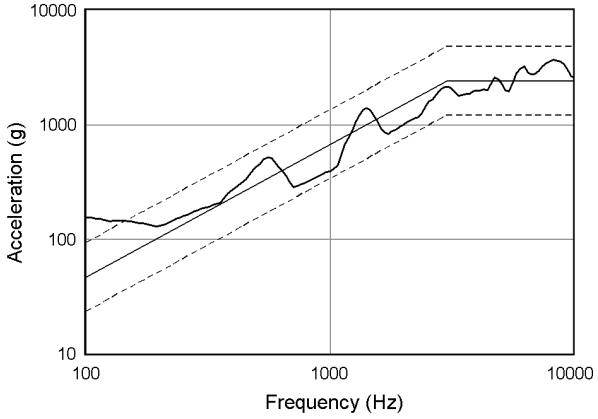

Figure 2.74: Shock response spectrum for the test along the z-axis during the second test. The SRS curve is calculated based on figure 2.73, the straight line represents the specifications given in table 2.8 and the dashed lines the tolerance of ± 6 dB (Q=10).

2.5.3 Thermal cycles

The thermal cycles allowed checking if Famars could withstand the temperatures of the mission given in 2.1. The thermal cycles test was performed at JPL after the integration of Famars FM into MECA. However, preliminary tests were conducted at IMT before sending the FM and the FS at JPL.

Preliminary tests at IMT

The first test was realized on an EQM model of Famars. Therefore, an EQM scanner with a chip was put in an environmental chamber. The chamber was first heated at 100 deg C for one hour, in order to dry it. After having purged the chamber with nitrogen and set the pressure to 10 mbar, a liquid nitrogen circuit allowed to cool down the scanner, and a thermocouple placed on it recorded its temperature.

The scanner and the chip reached -85 deg C in about thirty minutes. Then, the flow of liquid nitrogen was stopped and the temperature increased slowly until it reaches 20 deg C again. After this procedure, the chip was still alive and the scanner was working. The success of this first test allowed us to proceed with calibration and characterization of the flight hardware at low temperature.

During the calibration and the characterization of the FM and the FS, the flight scanners and chips were submitted to the following temperatures:

- + 100 deg C during 1 hour: drying of the vacuum chamber,
- - 50 deg C: 2 cycles from -50 deg C to + 20 deg C (see 2.2.5),
- - 30 deg C: 4 AFM images (see 4.3).

Even if these expositions to low temperature did not show any problem of the AFM, the latter had to go through the required thermal cycles in order to be fully qualified for the mission. As facilities already existed at JPL, this last tests were performed there.

Thermal cycles test at JPL

First, the MECA team performed the Package Qualification and Verification (PQV) testing on the AFM sensor head, which involved about three hundreds of cycles from low non-operational to high non-operational temperature limits, i.e. from -80 deg C to +40 deg C. The exact description of this test is not given here, as different temperature profiles were used and as the cycles were regularly interrupted after predetermined cycles in order to test the AFM.

Then, the Famars FM was integrated to the MECA flight hardware. A few thermal cycles were then performed, from -80 deg to +40 deg C when the instrument was not operating, and from -60 deg C to +40 deg C when it was. Note that "operating" does not mean scanning the surface, but having the scanner initialized in dynamic mode. Checkouts of the AFM performed during and after the cycles showed that the sensors were still working.

2.6 Conclusion

The hardware of Famars 2 was built based on the requirements of the Phoenix mission. A couple of months were spent on the fabrication and testing of AFM chips, whose design was a heritage of the MSP'01 mission. However, the main contribution of this thesis project was a new scanner head, since it included its design, fabrication, characterization and space qualification.

Famars chips were fabricated using a complex process. A new method for fabricating the doped piezoresistors was used, with help from T. Akiyama. During their characterization, biasing of p-n junctions within the chip was studied, and found to be the main cause of noise during AFM measurements. Characterization of the cantilever oscillations by means of a vibrometer also indicated that the active cantilever was not excited at its resonance frequency when working in dynamic mode, but at its first harmonic frequency. As this frequency is also modulated when the AFM tip enters into contact with

a sample, we concluded that the Famars instrument could operate in this mode.

The functionality of the new built scanner was demonstrated. In particular, the decay time of the spring system was at least two times shorter than the one of the previous version, which allowed increasing the scanning speed. The lifetime of the scanner was successfully tested against fatigue, and accelerated tests performed on the wire bonds between the chip and the flexprint circuit showed good results. An EQM scanner was submitted to a sterilization process, which induced some modifications of the scan properties. However, the EQM was still working and went through environmental testing. The vibration test was passed without problem, while failure of the chip was observed during the first shock test. Based on discussions with JPL experts, we realized that the instrument had been overtested, and a second test was performed in accordance with the procedure used for simulating a pyrotechnic shock. This second test being successful, the FM and the FS scanners went through acceptance test for vibration. Then, their chips were characterized at low temperatures. After a calibration of the FM and FS scanners, described in 4.3, they were delivered to the JPL, where thermal cycles were performed, completing the space qualification of the instrument.

References

[1] S. Gautsch. *Development of An Atomic Force Microscope and Measurement Concepts for Characterizing Martian Dust and Soil Particles.* PhD thesis, University of Neuchâtel, Switzerland, 2002.

[2] O. Wolter, Th. Bayer, and J. Greschner. Micromachined silicon sensors for scanning force microscopy. *J. of Vacuum Science & Technology B*, 9:1353–1357, 1991.

[3] K.E. Petersen. Silicon as a mechanical material. *Proceedings of the IEEE*, 70:420–455, 1982.

[4] M. Tortonese, R.C. Barrett, and C.F. Quate. Atomic resolution with an atomic force microscope using piezoresistive detection. *Applied Physics Letters*, 62:834, 1993.

[5] C. Beuret. *Development of a Double Molding Technique for the Microfabrication of Diamond Scanning Probe Tips.* PhD thesis, University of Neuchâtel, Switzerland, 1999.

[6] C. V. Nguyen, K.-J.Chao, R.M.D. Stevens, L. Delzeit, A. Cassell, J. Han, and M. Meyyappan. Carbon nanotube tip probes: stability and lateral resolution in scanning probe microscopy and application to surface science in semiconductors. *Nanotechnology*, 12(3):363–367, 2001.

[7] A.L. Window. *Strain Gauge Technology.* Springer, 2nd edition, 1992.

[8] C.S. Smith. Piezoresistance Effect in Germanium and Silicon. *Physical Review*, 94(1):42–49, 1954.

[9] S.M. Sze. *Semiconductor Devices, Physics and Technology.* John Wiley & Sons, New York, USA, 2nd edition, 2002.

[10] Lisa Tatge. *MECA Atomic Force Microscope User's Guide*. JPL, March 2006.

[11] 0.N. Tufte and E.L. Stelzer. Piezoresistance properties of silicon diffused layers. *J. of Applied Physics*, 34:313, 1963.

[12] J.A. Harley and T.W. Kenny. 1/f noise considerations for the design and process optimization of piezoresistive cantilevers. *J. of MEMS*, 9(2):226, 2000.

[13] W. Shockley. The Theory of p-n Junction in Semiconductors and p-n Junction Transistors. *Bell System Technical J.*, 28:435, 1949.

[14] Jet Propulsion Laboratory, Public Lessons Learned. http://www.nasa.gov/offices/oce/llis/0598.html. July 1998.

[15] S. Gautsch, T. Akiyama, R. Imer, N.F. de Rooij, U. Staufer, Ph. Niedermann, L. Howald, D. Brändlin-Müller, A. Tonin, H.-R. Hidber, and W.T. Pike. Measurements of Quartz Particles by Means of an Atomic Force Microscope for Planetary Applications. *Surface and Interface Analysis*, 33:163, 2002.

[16] S. Gautsch, T. Akiyama, N.F. de Rooij, U. Staufer, Ph. Niedermann, L. Howald, D. Brändlin-Müller, A. Tonin, H.-R. Hidber, W.T. Pike, and M.H. Hecht. Atomic Force Microscope for Planetary Applications. *Sensor and Actuators*, A 91:321, 2001.

[17] S. Gautsch, T. Akiyama, N.F. de Rooij, U. Staufer, Ph. Niedermann, L. Howald, D. Müller, A. Tonin, and H.-R. Hidber. Miniaturized Atomic Force Microscope for Planetary Applications. In *Proceedings of the 9th European Space Mechanisms & Tribology Symposium*, page 11, Liège, Be, 2001.

[18] S. Gautsch, T. Akiyama, N.F. de Rooij, U. Staufer, Ph. Niedermann, L. Howald, D. Müller, A. Tonin, H.-R. Hidber, and W.T. Pike. Development of an AFM Microsystem for Nanoscience in

Interplanetary Research. In *Proceedings of the 3rd Round table on Micro/Nanotechnologies for Space - Scientific Payloads*, page 173, Noordwijk, NL, 2000.

[19] S. Gautsch, T. Akiyama, N.F. de Rooij, U. Staufer, Ph. Niedermann, L. Howald, D. Müller, A. Tonin, H.-R. Hidber, W.T. Pike, and M.H. Hecht. Atomic force microscope for planetary applications. In *Solid-State Sensor and Actuator Workshop*, pages 267–270, Hilton Head Island, USA, June 4-8 2000.

[20] L. Howald, T. Akiyama, S. Gautsch, H.-R. Hidber, D. Müller, Ph. Niedermann, W.T. Pike, A. Tonin, and U. Staufer. Development of the Space SFM for Interplanetary Missions. In *Proceedings of the 4th Seminar on Quantitative Microscopy*, page 209, Semmering, A, 2000.

[21] W.T. Pike, M.H. Hecht, M.S. Anderson, S. Gautsch, T. Akiyama, N.F. de Rooij, U. Staufer, Ph. Niedermann, L. Howald, D. Müller, A. Tonin, and H.-R. Hidber. Atomic Force Microscope for Imaging and Spectroscopy. In *Proceedings of Concepts and approaches for Mars exploration*, Lunar and Planetary Institute, TX, USA, 2000.

[22] M. Del Pedro and P. Pahud. *Mécanique Vibratoire*. Presses polytechniques romandes, Lausanne, Switzerland, 1989.

[23] D. Parrat, S. Gautsch, L. Howald, D. Brändlin-Müller, N.F. de Rooij, and U. Staufer. Design and Evaluation of a Polyimide Spring System for the Scanning Force Microscope of the Phoenix Mars Mission 2007. In *Proceedings of the 11th European Space Mechanisms and Tribology Symposium*, pages 281–287, Lucerne, Switzerland, 21-23 September 2005.

[24] NASA Procedural Requirements. *Planetary Protection Provisions For Robotic Extraterrestrial Missions*. Number 8020.12C. NODIS, April 2005.

[25] A.D. Smigelskas and E.O. Kirkendall. Zinc Diffusion in Alpha Brass. *Transactions of AIME*, 171:130, 1947.

[26] H. Nakajima. The discovery and acceptance of the Kirkendall effect: The result of a short research career. *JOM*, 49:15–19, 1997.

[27] C. W. Horsting. Purple Plague and Gold Purity. In *10th Reliability Physics Symposium*, pages 155–158, Las Vegas, Nevada, 1972.

[28] R.S. Sorbello. Theory of Electromigration. *Solid State Physics*, 51:159–231, 1997.

[29] N. Bertolino, J. Garay, U. Anselmi-Tamburini, and Z.A. Munir. High-flux current effects in interfacial reactions in Au-Al multilayers. *Philosophical Magazine B*, 82(8):969–985, May 2002.

[30] E. Filippi, H. Attouoman, and C. Conti. Pyroshock Simulation Using The Alcatel Etca Test Facility. In *Launch Vehicle Vibrations. First European Conference*, CNES Toulouse, France, 1999.

Chapter 3

Software

3.1 Introduction

As we saw in 2.1.9, the instruments of the Phoenix mission can not be operated in real time on Mars. Thus, they are controlled autonomously through sequences sent once a day from Earth. These sequences are programmed in Virtual Machine Language (VML) [1, 2], and mainly call FSW commands, defined in 3.3.3 for the AFM. For most of the instruments, these commands control the hardware directly. However, Famars has its own control software, called the AFMCSW, which is located in the RAM of the AFM electronics. Thus, the FSW commands dedicated to Famars do not control the hardware directly, but call the AFMCSW basic commands which drive the Famars hardware.

3.1.1 History

At the beginning of this thesis project, the AFMCSW commands already existed as an heritage from the Famars 1 project [3]. The FSW commands had been described and partially written in pseudo-language by S. Gautsch [4], and they had therefore to be enhanced, coded and tested. The FSW commands were created with help from

D. Brändlin-Müller (Nanosurf AG). They were written in pseudo-language, and then coded by a programmer at the JPL. Testing of the FSW was performed in collaboration with the MECA team at JPL.

3.1.2 The AFM Control Software

The AFMCSW, conceived by Nanosurf AG, is the firmware of Famars, i.e. the part of the software which is embedded in its electronics during operations. As we have seen in 2.4.3, Famars is equipped with its own microcontroller. After powering, the microprocessor asks for the download of the AFMCSW code from the host computer to the RAM of the Famars electronic board. Once that is done, the microcontroller is able to perform on demand the basic tasks needed to run the instrument, by executing the commands of the AFMCSW.

The AFMCSW commands are divided in two groups. The "ATTR" commands, which simply allow reading or writing the AFMCSW attributes (listed in table A-IV), and the "CMD" commands, which perform more complex tasks, such as initializing the Wheatstone bridge or scanning a single line. The complete list of AFMCSW commands is presented in [3] and in [5], which are confidential documents.

3.2 Software for laboratory experiments

The creation of the FSW commands was based on the experience acquired when operating Famars in its stand-alone configuration, illustrated in figure 2.59. In that case, instructions to the microcontroller were sent by the user via a graphical user interface (GUI) installed on a personal computer (PC). This interface was generated by a program called the easyScanMars software, a commercial AFM software from Nanosurf which was modified by them for operating Famars. In addition to the user interface, this program included also the AFMCSW code to be downloaded into the RAM of the electronics.

The easyScanMars GUI was composed of several menus and windows, also called panels (see figure A-V in appendix A-2). The panels contained buttons, text boxes and other graphical elements which allowed communicating easily with the AFMCSW. The operations needed for AFM measurements, performed using the panels, are described hereafter.

3.2.1 Powering Famars

After having opened the easyScanMars software on the PC, the Famars electronics board was powered. This was done through the M-Test board, which also provided the communication between the AFM electronics and the PC (see 2.4.2). Soon after power was applied to the AFM board, the AFM Boot Loader (ABL) began requesting the load of the AFMCSW. The easyScanMars software then sent the AFMCSW code line by line to the microcontroller. After about 50 seconds, the AFMCSW code was loaded in the RAM of the electronics. Then, the "CMD_Start" command was automatically sent to the ABL to transfer control to the AFMCSW. From then on, the program flow was entirely controlled by the AFMCSW.

3.2.2 Preparing Famars

After downloading the AFMCSW, Famars was set in its default configuration, thus preparing it for the next operations. This required setting many parameters in the panels. The exact procedure is described in detail in [5]. In short, the AFM was set to static mode, with the default cantilever (stored in the State table, see 3.3.6) set as the active cantilever. The feedback loop was running, and the sensor tip was centered in the middle of the x, y and z scan axes.

3.2.3 Testing the piezoresistors

In order to measure the deflection of the cantilever, the Wheatstone bridge was initialized (see figure 2.61) in order to determine the bridge

offset voltage V_{BRO} for the active cantilever. This was also a health check of the cantilever's piezoresistor, as a dead piezoresistor would have caused an erroneous value of V_{BRO}. Note that this operation was automatically performed by the AFMCSW for all cantilevers.

If the value of V_{BRO} for the current cantilever was close to -5V (the expected value based on the resistance of the piezoresistor), the cantilever was considered to be "alive". In general, the lever signal V_{SIG} was monitored on an oscilloscope, which also allowed checking if the output of the bridge was close to 0V and if the noise was under a certain threshold. If this was the case, Famars was operational in static mode. This meant that any motion, desired or not, of the sample stage toward the AFM would be stopped automatically by AFM_near (see 3.2.5).

If the lever signal V_{SIG} was not close to 0V or was too noisy, the cantilever was not operational. In general, this meant trying the initialization again, possibly with another voltage applied to the tips. If the result was still bad, the next alive cantilever was selected for the measurements. In order to access the alive cantilever, the dead sensor had first to be removed, following the procedure described in 3.2.9.

3.2.4 Testing the dynamic behavior of the current lever

When Famars was operated in dynamic mode, a check-up was also performed to see whether the mechanical oscillation of the current cantilever at the resonance frequency was sufficiently large to allow measurements. First, the electronics were switched to dynamic mode. Then, the resonance frequency of the current cantilever was determined. In order to do this, a few parameters of the PLL were set in the Mars Panel, such as the frequency span in which the resonance frequency was expected. Another important parameter was the phase shift between the excitation frequency and the mechanical oscillation, kept constant by the PLL. The theory says that this phase shift is -90 degrees at resonance. However, as cross-talk was observed be-

tween the cantilevers, 18 different values could be assigned to this phase shift, from 0 to 340 deg, with a step of 20 deg.

For each possible value of the phase shift, an attempt was made to determine the resonance frequency of the current cantilever. This was done by performing a sweep of the excitation frequency in the given span of frequency, until the PLL was locked. Then, the amplitude of oscillation corresponding to the frequency found for the 18 different values of the phase shift had to be compared. The phase shift corresponding to the largest amplitude of oscillation was selected.

If the amplitude of oscillation was sufficient to allow measurements in dynamic mode, i.e. superior to a certain threshold fixed by the user, Famars was initialized in dynamic mode, using the PLL parameters found during this test. The setpoint and the gains of the feedback loop were also set. The instrument was then ready to detect any contact with the sample stage, as after the initialization in static mode.

If the amplitude of oscillation of the current cantilever was too weak, AFM images could no be taken in dynamic mode. Thus, one could either operate this cantilever in static mode, or initialize another cantilever in dynamic mode. In the latter case, the current cantilever was first removed following the procedure described in 3.2.9.

3.2.5 Approaching the sample

Before approaching the sample, the stepper motor was powered, and the alignment between the sample and the current sensor was checked optically. In addition, Famars had to be initialized in either static or dynamic mode. Once these conditions were met, the sample was moved toward the AFM, the cantilever being positioned in the middle of its physical z-range. The sensor tip was set in the center of the scan area, whose size was set by default to 0 micron. The speed of the stepper motor could also be chosen.

When the sample entered into contact with the sensor tip, i.e. when the setpoint was reached, the AFM electronics switched the AFM_near

signal from high (+5V) to low (0V). This change of the AFM_near signal was reported through the MTest board to the easyScanMars software, which automatically interrupted the stepper motor.

3.2.6 Imaging

Several parameters were set for taking an AFM image, as e.g. the scan size, the number of pixels, the scan direction, etc. Based on the parameters, the AFMCSW calculated the scan vectors used to move the sensor tip on the sample.

The easyScanMars software displayed the recorded image line by line. Different views (top view, line view, 3D-view) for the error and the topography signals could be selected. It was also possible to compare the differences between the forward and the backward scanlines. As the image was displayed in real time, its quality could be improved during the scan by modifying the feedback or the scan parameters. In case of problems, such as the topography signal being out of range, the scan could be immediately aborted.

3.2.7 Ending

At the end of a measurement, the AFM was always left in a safe position. Then, the AFM, the stage and the PC could be powered down.

3.2.8 Cleaning the current tip

If the current tip was contaminated with particles, there was a possibility to removed them. This was performed by bringing a "sticky" substrate in contact with the current tip. In some cases, the particles located at the very apex of the tip could adhere to the substrate, and stay on it after withdrawal of the tip (see 4.8). This task was in fact a standard approach in static mode toward a specific sample, except that no image was taken once in contact.

3.2.9 Removing the current tip

If the current tip was for some reason no longer usable (contaminated or blunt tip, broken cantilever), it was removed to allow accessing the next one. This was performed by breaking the beam supporting this sensor using a dedicated cleaving tool (see 4.7). First, the lateral alignment between this tool and the beam was checked. If the alignment was good, the cleaving tool was translated toward the Famars chip. The AFM_near signal was ignored, and even if the piezoresistor was still working, the translation continued until the beam broke.

3.2.10 Making decisions based on the results

Last but not least, decisions had to be made whenever operating the AFM. These decisions were based on the data sent back in the easyScanMars GUI. As an example, consider that the test of the piezoresistors has failed. In this case, one had to decide either to perform the test again or to remove the current sensor. Another choice occurred if the amplitude of oscillation of the current cantilever did not allow dynamic mode imaging. It could either be tested again, used in static mode, or the measurement session could be aborted.

3.2.11 Summary

Under laboratory conditions, running the Famars instrument was greatly simplified by the use of the easyScanMars GUI. Interacting with the AFMCSW was easy and the data were sent back immediately, which allowed event-driven decisions and optimizations. On Mars, however, there is no possibility to analyze neither the results of an initialization nor AFM images during a measurement session. Thus, maximal functionality should be included in the FSW commands. The experience acquired in our laboratory using Famars in stand-alone configuration, as well as the expertise of D. Brändlin in the AFMCSW was very helpful for the conception of the pseudo-language algorithms corresponding to the FSW commands described

in the following section.

3.3 Flight software description

3.3.1 Introduction

The FSW, located on the Phoenix Lander computer, is composed of several components. One of them is the MECA Flight Software (MFSW), which controls most of the MECA instrumentation [6]. The only exception is the OM, controlled by the RAC FSW (see 2.4.1). Thus, the commands used to take AFM images are all part of the MFSW. In this thesis, they are classified in three groups: the MFSW general commands, the MFSW AFM commands and the MFSW stage commands. Assembled in VML sequences, these commands should perform the same tasks as those described for Famars operated in its stand-alone configuration.

Thus, the MFSW AFM commands and two MFSW stage commands were conceived based on the experience acquired in running Famars with the easyScanMars software. In principle, these commands had to reproduce exactly the tasks performed by a user working with this software. However, the creation of such commands was quite complex due to the autonomy of the measurements on Mars. For example, the quality of a signal can not be checked on an oscilloscope and a recorded image can not be read in real time. In addition, the flight hardware configuration is different, especially the SWTS, which is much more complex than the sample stage used in our laboratory. Thus, the sample approach process had to be modified.

The realized MFSW commands and their corresponding arguments are described in this section, as well as other components of the MFSW, such as look-up tables and telemetry products. Note that arguments are variables which can be specified with the commands, while parameters are considered to stay sufficiently constant to be stored in look-up tables.

3.3.2 MECA Flight Software architecture

The MFSW runs on the Lander computer and communicates with the MECA hardware through the Payload Attitude Control Interface (PACI) card, as shown in figure 3.1. Commands come through a queue from a sequence engine (see 3.5). The MFSW receives the commands, validates them, and then transmit them to the hardware. When the MFSW receives the science data products in return, it formats them in packets, and hands them off to the spacecraft for downlink. The MFSW is also composed of tables storing parameters that have to be transmitted from one command to another.

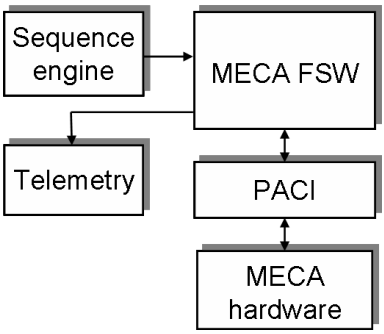

Figure 3.1: Software architecture of MECA.

In order to drive most of the MECA instruments, the MFSW communicates with the FPGA of the CME (see 2.4.1). However, when operating Famars, the MFSW has to talk to the AFM electronic board. Thus, a discrete line allows the MFSW swapping communications between the CME and the AFM electronics, depending on the task to execute.

3.3.3 MFSW AFM commands

The MFSW AFM commands, coded at JPL based on pseudo-language algorithms, are divided in three different levels. First, the raw MFSW

commands correspond to basic commands of the AFMCSW. Secondly, the MFSW low-level block commands correspond to several raw commands. Finally, the MFSW high-level block commands are composed of raw and low-level block commands arranged in routines. In principle, only high-level block commands, in combination with MFSW stage commands, are needed to operate Famars. However, the existence of lower level commands allows keeping a certain flexibility, and was also convenient during the testing of the FSW. In the following sections these commands are discussed in more details, from the low to the high end of the hierarchy.

Raw commands

Each MFSW raw command sent to the Famars electronics calls a single AFMCSW command. For example, the MFSW raw command "MECA_AFM_INITBRG" calls the AFMCSW command "CMD_BridgeInit". Table 3.1 gives the list of the MFSW raw commands with a brief description. The arguments of these commands are described in appendix A-2, table A-II.

As these commands perform very simple tasks, they are in general not used for building VML sequences. However, the commands MECA_AFM_ATTRSET and MECA_AFM_ATTRGET are sometimes used to write or read AFM attributes that are not settable in higher level MFSW commands. Note that the MECA_AFM_RAW command allows issuing any of the AFMCSW commands to the AFM. It is not expected to be issued during operations, but is provided for testing purposes.

Table 3.1: MFSW raw commands.

Command	Arguments	Function	Telemetry format
MECA_AFM_INIT-BRG	none	Initializes the Wheatstone bridge	afm_response
MECA_AFM_INIT-PLL	none	Initializes PLL for dynamic mode	none
MECA_AFM_INIT-PLN	none	Initializes the scan plane	afm_response
MECA_AFM_MV-START	none	Moves the tip to the starting point of the scan	afm_response
MECA_AFM_DO-LINE	none	Records a scan line	afm_scan
MECA_AFM_DO-FRAME	afm_scandir	Acquires an image	afm_scan
MECA_AFM_RD-ADCS	afm_adc_mask	Reads AFM ADC outputs	afm_response
MECA_AFM_ATTR-GET	afm_attrib_id	Returns the value of an AFM attribute	afm_response
MECA_AFM_ATTR-SET	afm_attrib_id, afm_value	Sets the value of an AFM attribute	none
MECA_AFM_RAW	afm_wd, afm_wd2, afm_wd3,..., afm_wd22	Allows issuing AFMCSW commands	afm_response

Low-level block commands

There are only two low-level block commands, MECA_AFM_STATIC and MECA_AFM_DYNAMIC, described hereafter. Even if they issue several AFMCSW commands, they are in principle not used during operations, as they are included in high-level block commands.

MECA_AFM_STATIC. This command has no argument. It sets the AFM in static mode, using parameters stored in the Parameter Value table (see 3.3.6). An initialization of the Wheatstone bridge is performed, but the state of the cantilever is not checked. As this command is included in the high-level block command MECA_AFM_TST-TIPS, it is in principle not used when building sequences. However, it could be use in the particular case when one wants to go from dynamic mode to static mode without further testing.

MECA_AFM_DYNAMIC. This command has no argument. It sets the AFM in dynamic mode, using parameters stored in the Parameter Value table (see 3.3.6). An initialization of the PLL is performed, but the result of the initialization is not analyzed. Thus, one does not know if the amplitude of oscillation is sufficient to image in dynamic mode. This command is included in the high-level block command MECA_AFM_FRQTEST, and is generally not used when building sequences.

High-level block commands

The high-level block commands execute high-level AFM tasks that require issuing several AFMCSW commands and may require on-board assessment of, and action taken on, the returned data. Only a small set of high-level block commands is needed to perform any AFM activity, and these commands are appropriate for concise scientific definition of the experiments. References to the corresponding tasks effectuated by means of the easyScanMars software are also given in the description of these commands.

MECA_AFM_BOOT. This command, which has no argument, is the first AFM command that has to be sent after enabling Famars. First, MECA_AFM_BOOT loads the AFMCSW code. The loading procedure is similar to the one performed by the easyScanMars software (see 3.2.1). The AFMCSW is stored on the Phoenix Lander computer in a separate ASCII file called "easymars.hex". Soon after the AFM is enabled, the ABL begins requesting a load. The MECA_AFM_BOOT command processes that request and sends the "easymars.hex" file to the ABL line by line. Once the download is complete, MECA_AFM_BOOT commands the ABL to swap to AFMCSW processing by issuing the AFMCSW command "CMD_Start".

Then, MECA_AFM_BOOT sets the AFM in static mode. This configuration of the AFM is comparable to the one obtained by means of easyScanMars after the "Preparing Famars" task (see 3.2.2). Note that the state of the current sensor is not known after the completion of this command.

MECA_AFM_TSTTIPS. This command has no argument. As a rule, the command MECA_AFM_BOOT has to be sent prior to issuing MECA_AFM_TSTTIPS. MECA_AFM_TSTTIPS checks the state of all piezoresistors and leaves the AFM in static mode if the current one is usable. It returns the state of each tip in the science data product afm_tips (see 3.3.7). Thus, the tasks performed by MECA_AFM_TSTTIPS are equivalent to the testing of the piezoresistors performed by means of the easyScanMars software (see 3.2.3).

However, the diagnostic on the state of the piezoresistors is done differently. As the returned value of V_{BRO} does not allow diagnosing the presence of noise in the lever signal V_{SIG}, another technique is employed. In static mode, the lever signal is equal to the error signal (see 2.4.3). Thus, a dummy scan line is performed "in the air" with a setpoint equal to 0V (no deflection) and a scan size of 0 μm. The recorded error signal, i.e. V_{SIG}, is a direct measure of the state of the cantilever. In the ideal case, the recorded scan line is flat and centered on the setpoint, at 0V. If there is noise, oscillations can be

seen in the error signal line. If the Wheatstone bridge is not well balanced, the line is shifted up or down. Finally, if the cantilever is dead, the line is completely at the bottom of the range.

The analysis of the scan line data is performed by MECA_AFM-_TSTTIPS, which diagnoses the state of the tips based on the criteria described above. The current lever is considered "alive" if the noise is not "too high" and if the scanline is not "too far" from the setpoint of 0V. In this case, the test is passed and Famars is set to static mode, with a setpoint different from zero and making possible detecting any contact with the sample. This means that any motion, desired or not, of the sample stage toward the AFM will be stopped automatically by means of AFM_near (see 3.2.5). If the lever signal is noisy, the whole test is performed a second time. If the result is still bad, the command fails and the AFM is disabled.

Note that this command is improperly dubbed, as the test is performed on the piezoresistors, and not on the tips. However, it was more easily understood by programmers, sometimes not familiar with AFM. In this case "tip" can be seen as an equivalent of "sensor".

MECA_AFM_FRQTEST. This command has no argument. As the piezoresistor of the sensor has to work for this test, the command MECA_AFM_TSTTIPS has to be sent before the MECA_AFM_FRQ-TEST command. The latter checks if the current cantilever can be set to dynamic mode by determining its resonance frequency based on 18 different PLL phase shifts. If the amplitude of oscillation of the cantilever at resonance is sufficient, it sets the AFM in dynamic mode. The found resonance frequency and the phase shift as well as the amplitude of oscillation are returned with the science data product afm_frqtest.

The tasks performed by MECA_AFM_FRQTEST are equivalent to the testing of the frequency performed by means of the easyScan-Mars software (see 3.2.4). The frequency which induced the largest oscillation is selected by comparing the 18 different values of V_{AP} obtained after the initialization of the PLL. If the oscillation is larger

than a certain value, fixed by a MFSW parameter, the AFM is set to dynamic mode, and is ready for an approach.

If the amplitude of oscillation of the current cantilever is too weak, no AFM images can be taken in dynamic mode. We will see in the following paragraph that MECA_AFM_IMAGE can be issued only if the mode is known. Thus, even if the cantilever is "alive" and therefore usable in static mode, the AFM is always disabled if it can not be set in dynamic mode. A better solution would have been to create a global variable indicating the mode of operation of the AFM to the VML sequence, but it was unfortunately not implemented before the deadline of the FSW delivery. Thus, conditional statements based on the mode of operation could not be created.

MECA_AFM_IMAGE. This command has many arguments: afm_scanrange, afm_xpts, afm_ypts, afm_msperln, afm_igain, afm_pgain, afm_setpt, afm_sampmsk, afm_fwdbk and afm_smartzoom. A short description of these arguments is given in appendix A-2, table A-II. Before executing this command, the AFM has to be initialized either in static mode or in dynamic mode, and a sample has to be brought into contact with the current sensor tip.

MECA_AFM_IMAGE sets the scan vectors based on the values of afm_scanrange, afm_xpts and afm_ypts. Then, it performs an AFM image in the mode set during the last initialization. Once the image is taken, the science data product afm_scan is transmitted to the Flight Lander computer for downlink.

As the arguments afm_igain, afm_pgain, afm_setpt depend on the mode of operation, it is critical to know, when writing the operation sequence, in which mode MECA_AFM_IMAGE will be used. Knowing this, one can set these three arguments to the right values. In order to avoid any conflicts, the AFM does not take an image in static mode if it is not possible to initialize the AFM in dynamic mode. So if an image in static mode has to be taken, the sequence has to be written accordingly.

As the amount of obtained data is limited by space requirements, the argument afm_fwdbk allows choosing if both scan directions are recorded, or only one of them. Another possibility is to record only one of the two channels (error channel or topography channel), using the argument afm_sampmsk. Finally, taking 256 x 256 pixels images instead of the possible 512 x 512 pixels images provides another way of limiting the data volume (arguments afm_xpts and afm_ypts). A trade-off between data volume and scientific information has to be made during operations for each situation. The size of the afm_scan packet varies greatly, depending on the values of theses arguments (see 3.3.7). Note that the level of compression performed by the flight computer could also be chosen, but not by the MFSW.

Once an image is taken, it would be useful to know which part of it is scientifically relevant, and to perform one or several nested zooms in this area. Thus, if the afm_smartzoom argument is set, a subroutine of MECA_AFM_IMAGE uses a jpeg-compression algorithm to detect the most interesting region. To do this, it divides the image in 16 parts and chooses the least compressible one. Then, it sets the scan plane ready to perform an image of that region, and takes another AFM image. This process can be iterated several times, the limit being mainly the size of the generated data.

The MECA_AFM_IMAGE also has a special feature. If it is sent with afm_scanrange equal to zero, it does not take a "0-μm image", but performs a routine dubbed "prescan", described in the next section.

Differences between MFSW and pseudo-language commands

The algorithms in pseudo-language were written to give Famars maximal functionality. However, a trade-off had to be made between their complexity and the possibility to implement them as FSW blocks. For this reason, some of the pseudo-language commands were simplified, integrated in higher-level FSW blocks or simply not implemented. The main changes are presented hereafter.

MECA_AFM_AUTOIMAGE. This very autonomous command was not implemented in MFSW. It should have been composed of several MFSW block commands, and able to take AFM images after having initialized the sensor either in static or dynamic mode. It was an heritage from the Famars 1 project [4], and back then VML sequencing was not planned for the canceled MSP'01 mission. For the Phoenix mission, a VML sequence replaces this high-level command by issuing several MFSW block commands.

MECA_AFM_VECTOR_SET. This routine, which calculates the two vectors of the scan plane, was integrated in MECA_AFM_IMAGE, and not coded as a separate command. This was done because this subroutine is only needed before scanning.

MECA_AFM_SMARTZOOM. While this subroutine of MECA-_AFM_IMAGE should have been able to zoom with a tunable nested ratio, the zoomed image has always a scanrange four times smaller than the initial one.

MECA_AFM_PRESCAN. This complex subroutine was written for finding the maximal scanrange at a given location, and also for adjusting the x-slope and y-slope of the scan plane. It was not implemented as a distinct block, but was called using MECA_AFM_IMAGE with the argument afm_scanrange equal to 0. The principle of the subroutine is to start with "safe" scanlines having a small length a, and then to increase a until the maximal scan size is reached. At the beginning of the test, a is equal to two micrometers. Three scanlines of a microns are taken along the x-axis at positions $-a/2$, 0 and $+a/2$ on the y-axis. If the data of the scanlines are all within the z-range, the x-slope (slope along the x-axis) is estimated by averaging the slopes of the scanlines. Then, the subroutine does three scanlines along the y-axis to estimate the y-slope. After having correcting the orientation of the scan plane with the new values of x-slope and y-slope, it multiplies a by two and performs the same procedure again,

obtaining new values for the slopes. The iteration is repeated until the data of one scanline is out of the z-range, the corresponding value of a being then interpreted as the maximal scanrange. This value is stored in the Parameter Value table, and is used to limit the size of future images taken at this location. Contrarily to what was first intended with the pseudo-language algorithm, the FSW subroutine automatically takes an image with the maximal scanrange after having determined it.

MECA_AFM_OPTIMIZATION. This subroutine of the command MECA_AFM_IMAGE should have analyzed the noise in test scanlines for different feedback parameters settings in order to find the best parameters for imaging the substrate. The complexity of this subroutine and the coming delivery deadline prevented it from being implemented in the FSW. If the default settings determined in laboratory conditions do not produce good images on Mars, new settings will be determined based on the returned data.

MECA_AFM_APPROACH. This command is in fact a stage command, as it involves only a motion of the stage. Thus, it was implemented with the name "MECA_STG_APPR". As we will see in 3.3.5 however, this FSW command shows a drawback: for each approach, the stage goes first in "Safe-To-Rotate" position. Thus, it is impossible to start an approach from another position.

Summary

The MFSW AFM commands, and particularly the high-level block commands, were written based on the experience acquired when using the easyScanMars software. Therefore, the FSW shows about the same capabilities as the latter. However, it was difficult to incorporate into it all the diagnostics and decisions made by the user in laboratory conditions. Some of them were implemented, such as for example the diagnostic of the state of the current tip, but others were not. For

example, one does not have the possibility to take AFM image in static mode if the dynamic mode is selected but the vibration of the cantilever is not sufficient to operate in dynamic mode.

Despite a few simplifications, the FSW still shows a good flexibility. Even if the commands have few arguments, tens of parameters can be changed using the MECA_CMD_SETPARM command, described in 3.3.4. For example, the noise threshold used in MECA-_AFM_TSTTIPS is one of this parameters. Thus, the use of high-level block commands, in combination with a few issues of MECA-_CMD_SETPARM, gives the needed flexibility for initialization and imaging.

Finally, note that the AFM commands do not allow the performance of all the tasks realized with the easyScanMars software. In addition to the powering, the approach (see 3.2.5) and the withdrawal of a sample (see 3.2.7), as well as the removal of a sensor tip (see 3.2.9) are missing. While the powering is effectuated through MFSW general commands, the other functions are realized through MFSW stage commands, as they involve the motion of the SWTS. These "non-AFM" commands are described hereafter.

3.3.4 MFSW general commands

The MFSW general commands are not specific to Famars, and are used for the whole MECA instrumentation. The list of command presented in table 3.2 is not exhaustive, and contains only the commands that are needed or important for running Famars.

To operate the AFM, the MECA electronics first have to be powered. This is done using MECA_EPS_POWER. Then, the AFM as well as the SWTS have to be enabled using MECA_CMD_ENABLE with the corresponding arguments. At the end of the experiments, the AFM and the SWTS have to be disabled using the same command, and MECA is shut down using MECA_EPS_POWER. The command MECA_CMD_RESET can be used to reset MECA, and hence to have the AFM enabled but not booted.

Table 3.2: General MFSW commands used for AFM measurements.

Command	Arguments	Function	Telemetry format
MECA_EPS_POWER	eps_off_on	Switches main EPS power to MECA	none
MECA_CMD_RESET	none	Resets MECA	none
MECA_CMD_ENABLE	cmd_component, cmd_enabled	Enables or disables a MECA component	none
MECA_CMD_SETPARM	cmd_par_id, cmd_par_value	Sets the value of a table parameter	none
MECA_TBL_DWNLD	table_type	Downlinks the data from a specific table	tbl
MECA_TBL_SAVE	none	Writes updated tables to the filesystem	none

During the experiments, the State table, the Tips table and the Parameter Value table are read or modified by the commands (see 3.3.6). Thus, the commands MECA_TBL_DWNLD and MECA_TBL_SAVE are very useful, as they allow downloading the tables or writing them to the filesystem, respectively. In addition, the command MECA_CMD_SETPARM allows modifying the value of the parameters stored in the Parameter Value table. For example, it allows modifying the default feedback setpoint used when approaching the sample toward the AFM (MECA_CMD_SETPARM, 5, *new value*).

3.3.5 MFSW stage commands

When Famars is used in its stand-alone configuration, the motion of the sample stage is achieved by means of a stepper motor controlled by the easyScanMars software. In particular, the approach is performed by calling the AFMCSW command "CMD_DoApproach" from the Approach Panel. This command translates the sample toward the AFM, and stops the motion as soon as the contact is detected.

However, "CMD_DoApproach" is not operational in the flight configuration, as the SWTS is not controlled by AFMCSW. The operation of the SWTS is quite complex, and has its own set of MFSW commands. The ones that are used during Famars operation are listed in table 3.3. Among these commands, MECA_STG_APPR and MECA_STG_BRKTIP were especially designed for AFM measurements and are described more in detail hereafter. The command MECA_STG_INIT, which initializes the stage at the beginning of a new experiments session, is also described.

MECA_STG_INIT Once the stage is enabled, MECA_STG_INIT is issued to determine if the limit switches (see 1.3.2) are working as expected and are at the step positions expected by the FSW. First, the SWTS is translated in order to determine the position of the translation limit switches, and is left in the "Safe-To-Rotate"

Table 3.3: Stage MFSW commands used for AFM measurements.

Command	Arguments	Function	Telemetry format
MECA_STG-_INIT	stg_motors, stg_ovrrd	Initializes the stage	none
MECA_STG-_APPR	none	Translates the SWTS for AFM imaging	none
MECA_STG-_BRKTIP	afm_tip	Translates the sample wheel for breaking the current tip	none
MECA_STG-_ABSXLT	stg_xlt_ref, stg_steps	Translates the SWTS relative to a reference position	cme_status
MECA_STG-_ABSROT	stg_rot_ref, stg_steps, stg_ovrrd	Rotates the SWTS relative to a reference position	cme_status
MECA_STG-_RELXLT	stg_dir, stg_steps	Translates the SWTS relative to the current position	cme_status
MECA_STG-_RELROT	stg_dir, stg_steps, stg_ovrrd	Rotates the SWTS relative to the current position	cme_status
MECA_STG-_HLTHCK	stg_motors, stg_ovrrd	Checks stage motors operation	none

position, where the wheel can be rotated without damaging the AFM. The wheel is then rotated both clockwise and counter-clockwise to check the rotation limit switches. If all of these tests are successfully passed, the SWTS is ready for use. If this is not the first time that the SWTS has been used, initialization may be skipped in favor of a standard health check (MECA_STG_HLTHCK), which determines if the motors are working properly. In general, a sample acquisition precedes AFM measurements.

MECA_STG_APPR Before approaching the sample, Famars must be initialized in either static or dynamic mode, and the SWTS must be initialized too. A sample must also be positioned properly in front of the current tip for the approach. Once these conditions are met, the approach is performed by sending the MECA_STG_APPR command. This moves the SWTS to the "Safe-To-Rotate" position, from where a coarse approach is performed until the "OM focus" position is reached. Then, it moves toward the AFM head by iterations of several steps. The numbers of iterations and motor steps are both defined by parameters (see 3.3.6). When the sample enters into contact with the sensor tip, the setpoint is reached, and the AFM electronics switches the AFM_near signal from high (+5V) to low (0V). In the flight configuration, this information is directly sent to the CME in order to stop the translation of the SWTS. After contact, the tip is therefore in position to start imaging.

The speed of the approach is not an argument of MECA_STG-_APPR. However, it is a parameter, and hence its default value can be modified before starting the approach using the command MECA_CMD_SETPARM (MECA_CMD_SETPARM, 98, *new value*).

At the end of a measurement, the SWTS is sent back to the "Safe-To-Rotate" position by a stage translation command.

MECA_STG_BRKTIP When the current sensor is no more usable, it is removed by the cleaving tool installed on the SWTS (see 4.7). This tool breaks the beam supporting the cantilever, which al-

lows accessing the next sensor tip. This action is often improperly referred to as "tip breaking", as it is easier to understand from a software point of view.

Before performing this operation, the cleaving tool has to be aligned with the current sensor. Then, an optical image is taken by means of the OM, and downlinked to Earth where the alignment can be checked. This means that the preparation for the cleaving procedure has to be performed at least a day before the command is used. In addition, no rotation of the wheel is allowed from the instant when the OM image is taken to the time when the MECA_STG_BRKTIP command is issued.

The MECA_STG_BRKTIP performs a translation of the SWTS toward the stage, ignoring the AFM_near signal. This signal has to be ignored, as the piezoresistor of the sensor to be removed is still alive in some cases. Otherwise, the contact with the cleaving tool would interrupt the motion of the SWTS. However, the translation of the SWTS has to be stopped after having broken the current sensor, otherwise it would damage the other sensors. Thus, the translation is automatically stopped after a certain number of steps, determined experimentally as being sufficiently large to remove the current sensor without damaging the remaining ones.

3.3.6 MFSW tables

The existence of tables is critical to supporting the other MFSW components by enabling post-launch customization of operations. As some MFSW commands can read or modify values which are stored in tables, the commands are more flexible than if they were only using constants.

The following MFSW tables are used:

- The State table
- The Parameter Value table
- The Parameter Range table
- The AFM Attribute table
- The Coupons table
- The Tips table
- The Reagent Release table

Except the Reagent Release table, used for the WCL, all these tables play a role in the control of Famars. Thus, they are described hereafter, with emphasis on the parts of them used for the AFM. A complete description of the tables can be found in [6].

State table

The State table holds configuration settings which may change in flight without explicit commands, and is maintained across reboots. The State table is uploaded by MFSW internals only, and is not changed explicitly by commands. For the AFM, it holds two important pieces of information. First, it indicates which sensor tip is in use. Secondly, it keeps track of the level of initialization of the AFM ("not booted", "booted", "tip tested" or "frequency tested"). Note that the level of initialization of the AFM is not saved across reboots.

Parameter Value table

The Parameter Value table gives the current value of many configuration parameters. These values can be changed using the MECA-_CMD_SETPARM command and are saved across reboots using the MECA_TBL_SAVE command. The list of AFM parameters is given in appendix A-2, table A-I. Stage parameters are also used for the approach. The parameters mtr_xlate_afm_appr_iterations and mtr_xlate_afm_appr_iter_steps allow setting the number of iterations

and the number of steps per iteration. The parameter mtr_xlate_pulse_width determines the speed of the translation.

Parameter Range table

The Parameter Range table indicates for each parameter the range within which a new value must fall. This table can only be changed by uploading a new file and forcing FSW reinitialization. For more information, see [6].

Tips table

The AFM Tips table lists current information about each of the AFM tips. This table can be changed by uploading a new file and forcing FSW reinitialization, but is also updated by running the AFM frequency test through the MECA_AFM_FRQTEST command. It persists across reboots. For each tip, this table contains:

- The default amplitude of excitation in mV
- The default phase shift of the PLL
- The lateral position relative to the first tip (in steps)
- The center frequency
- The frequency at which to start the frequency test
- The state of the tip (not_tested, dead, not_centered, out_of_range, noisy, ok)

AFM Attributes table

The AFM attributes table lists all of the AFM settings, which correspond to the AFMCSW attributes (3.1.2). The table does not give the default value of these attributes, but their hexadecimal AFMCSW code and the range of permissible values. This table can only be changed by uploading a new file and forcing FSW reinitialization through a system INIT command. The list of the AFM attributes is given in appendix A-2, table A-IV.

The values of the AFM attributes, which are not in a table, can be modified one by one using the command MECA_AFM_ATTRSET and read by the command MECA_AFM_ATTRGET. Note that the AFM attributes are modified by the MFSW AFM commands.

3.3.7 Telemetry

Two different types of data are generated by the MFSW and downlinked to Earth: the science data (non-channelized telemetry) and the engineering data (channelized telemetry).

Channelized telemetry

Channelized telemetry are engineering data sent down with the science data products, but only if their value has changed. They give information on the state of the MECA hardware as well as on the state of the issued commands. For example, the command counters (MC_CmdReject, MC_CmdStart and MC_CmdComp) allow checking if the execution of a sequence has been performed without errors. The rejected command counter MC_CmdReject should not increase during the sequence, although errors from previous runs may cause it to be non-zero. Commands started and commands completed (MC_CmdStart and MC_CmdComp) should increase during the run and terminate at the same value. In case there is a problem, the channelized telemetry would be very useful to determine which tasks of the sequence were successfully performed by the MFSW and which failed or were not executed.

As there are tens of MECA channelized telemetry items, table 3.4 only describes those giving information on the state of Famars. Note that these items can not be used for event-driven sequencing, as they are not accessible to the VML sequence.

Table 3.4: Channelized telemetry giving information on the state of Famars.

Item	Description
MC_AfmCurTip	The AFM tip currently being used (0 to 7).
MC_AfmFqTePa	The current pass of the frequency test (first pass = 0, second pass = 1).
MC_AfmFqTePh	The current phase of the frequency test.
MC_AfmFqTeVa	The last-computed V_{AP} of the frequency test.
MC_AfmHxLiLd	Lines of code uploaded into the AFM RAM (0 to 412).
MC_AfmPrScRn	During AFM imaging prescan, the range currently being evaluated.
MC_AfmScanLn	The number of the line currently being scanned (only shows every 10th line).
MC_AfmState	The current AFM initialization level (not booted, booted, tip tested, frequency tested)
MC_AfmTipInT	The tip currently under test (0 to 7).

Science Data Product Formats

The MFSW groups the science data products in telemetry packets which are sent to the ground through the Phoenix Lander software. These packets are processed by the Multimission Image Processing Lab (MIPL) at JPL, which stripped and/or combined them into experimental data records (EDRs). These packets come in various formats. The different types of packets produced by MFSW AFM commands are briefly discussed hereafter. In addition, since many AFM parameters are stored in tables, the packet type "tbl", which downlinked the contents of the tables, is also described.

Each packet contains a header, followed by the data itself. As a science data product can be divided in several packets, each packet header gives the total number of packets of the data product and the number of the packet within the data product. The header gives also other information on the time the command was issued, the telemetry type and the associated data.

The afm_scan packet format. afm_scan is used for all imaging data returned by the AFM, and it is therefore generated by the high-level block command MECA_AFM_IMAGE, and the raw commands MECA_AFM_DOFRAME and MECA_AFM_DOLINE. The volume of imaging data varies, depending on the arguments that are specified with the MECA_AFM_IMAGE command. The following alternatives are available:

- 1 or 2 scan directions (forward and/or backward)
- 1 or 2 channels (topography and/or error channel)
- different number of points per image (from 4 x 4 to 512 x 512, typically 256 x 256)

Thus, if two directions and two channels are recorded, four different images are obtained from a single MECA_AFM_IMAGE command.

The afm_scan packet consists of the packet header followed by the recorded scanlines. A line header at the beginning of each scan line gives the recorded direction and channel, as well as the vertical position of the line in the image. This line header also gives information on three important values: the height offset (z offset), the topography channel gain (which gives the actual z-range) and V_{AP}, related to the amplitude of oscillation of the cantilever during measurements.

The size of each line header is 64 bits. If the scan line is composed of n points, the total size of each scan line is therefore $64 + 8n$ bits, as the height information for each point is encoded with 8 bits. If the image is composed of m lines, the total size of the image is $(64+8n)m$ bits, which gives 540672 bits (about 0.54Mb) for a standard 256 x 256 image. If two channels are recorded, this value is multiplied by two, idem for two directions.

As the amount of data per packet is limited to 15752 bits, AFM images are downlinked in several packets. A 1-direction, 1-channel 256 x 256 image therefore requires 35 afm_scan packets. Thus, the total size of the afm_scan packets for this image is given by $540672 + 35 * 288$ bits (about 0.55Mb), where 288 is the size of the afm_scan packet header in bits. Table 3.5 gives the total size of science data products generated by different settings of MECA_AFM_IMAGE. As the telemetry corresponding to a 512 x 512 image is almost four times larger than those of a standard 256 x 256 image, 512 x 512 images will only be issued in rare cases, when high pixel resolution is required.

Table 3.5: Size of the generated data for different MECA_AFM_IMAGE settings.

afm_scan packet size	1 channel		2 channels	
	1 dir.	2 dir.	1 dir.	2 dir.
256 x 256 points	0.55 Mb	1.10 Mb	1.10 Mb	2.20 Mb
512 x 512 points	2.17 Mb	4.34 Mb	4.34 Mb	8.68 Mb

The size of the afm_scan packets generated by the commands MECA_AFM_DOLINE or MECA_AFM_DOFRAME is also influenced by the mentioned parameters. For these raw commands, however, these parameters are not arguments, but depend on the prior configuration of the AFM.

The afm_tips packet format. The afm_tips packet contains the results of the MECA_AFM_TSTTIPS command. For each tip, it contains the state of the sensor, the found bridge offset value, and the recorded "air" scan line which gives noise information. Note that if a second pass is performed by MECA_AFM_TSTTIPS, the values of both passes are present in the afm_tips packets. The total size of this packet is 66880 bits.

The afm_frqtest packet format. The afm_frqtest packet contains the results of the MECA_AFM_FRQTEST command. Thus, it contains the number of the tested tip (0-7) and the determined frequency, as well as the corresponding parameters. The value of V_{AP} is also returned, which gives the amplitude of oscillation of the tested cantilever. In addition, the initial (pre-test) values of these parameters are also returned. The size of this packet is 1184 bits.

The afm_response packet format. afm_response packets are used for miscellaneous AFM raw commands being neither imaging nor testing commands: MECA_AFM_ATTRGET, MECA_AFM_INITBRG, MECA_AFM_INITPLN, MECA_AFM_MVSTART, MECA_AFM_RAW and MECA_AFM_RDADCS. The science data product is constituted of a single afm_response packet of 544 bits.

The tbl packet format. The tbl packets are not generated by an AFM command, but by the MECA_TBL_DWNLD command. They contain all the values stored in the table requested by the argument of MECA_TBL_DWNLD. The total size of the data product depends therefore on the requested table: 1376 bits for the State table, 12384

bits for the Parameter Value table, 24480 bits for the Parameter Range table, 7168 bits for the AFM Attributes table, 2496 bits for the Coupons table, and 1824 bits for the Tips table. In this case, only one packet is generated for each science data product.

Example. The VML sequence given as an example in 3.5.3 generates a certain amount of science data products, an overview of which is given in table 3.6. Three cme_status packets, used for non-AFM commands with little associated telemetry, are generated here by the stage commands MECA_STG_ABSROT, MECA_STG_RELXLT and MECA_STG_ABSXLT. Note that the recorded AFM image represents 96% of the total unchannelized telemetry.

Table 3.6: Volume of science data products generated by the basic VML sequence described in 3.5.3.

Science data products	Size (bits)	Comments
afm_tips	66880	
afm_frqtest	1184	
afm_scan	2202432	2 channels, 2 directions
tbl	1376	State table
tbl	12384	Parameter Value table
tbl	1824	Tips table
cme_status	1392	3 packets
Total	2287472	= 2.29 Mb

Error messages

We saw that the channelized telemetry allows checking that the commands were correctly performed. In addition, the first assessment of health is also made by looking at the event reporting (EVR) messages, divided in two types. Informational EVRs are issued for significant

but nominal events, while warning EVRs (error messages) are issued when something has not gone as expected. If warning EVR has resulted from an operation, it has to be determined whether this comes from a problem with the instrument itself, or from some deficiency of the operational sequence. The complete list of warning EVRs is given in [6]. As more than one hundred of them concern the AFM, table A-III given in Appendix A-2 only listed the EVRs that cause the AFM to be disabled and powered off.

3.4 Flight software testing

Testing of the MFSW part dedicated to Famars was performed at JPL on the MECA testbed. Before doing this, the AFM and the stage of the testbed were checked using a special configuration (see 3.4.1). Then, the MFSW commands were tested by running them one after another on the testbed (see 3.4.2).

3.4.1 Checking of the testbed

A check-out of the testbed hardware was initially performed using easyScanMars, as when operating the instrument in its stand-alone configuration. However, modifications were needed, first because easyScanMars usually communicates with the AFM board using the dedicated M-Test board, and also because this program is unable to control the SWTS. As illustrated in figure 3.2, a manual switch allowed connecting the CME board to two different communication ports of the PC, alternatively. One port was used for the communication between the AFM board and the easyScanMars software, and the other was used for controlling the SWTS by means of a dedicated LabVIEW program. In addition, the electronic switch of the CME had to be set in the same state as the manual switch using the same LabVIEW program.

As in the flight configuration, the AFM_near line between the AFM board and the CME board was present. Thus, during the

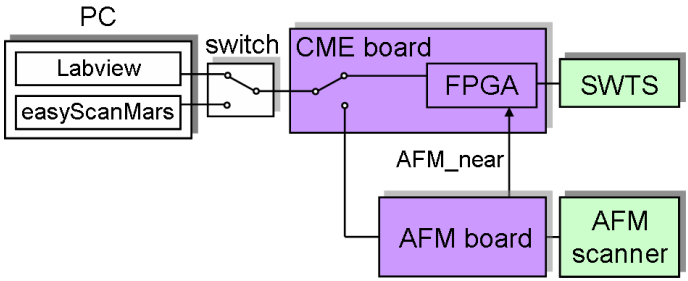

Figure 3.2: Schematics of Famars run with easyScanMars in the MECA configuration.

sample approach, the stage could be stopped without any input from the PC. The effect of the AFM_near signal on the motion of the wheel was therefore also checked by this preliminary testing. An oscilloscope was used to monitor the AFM_near signal, as well as V_{SIG} and V_{SHAKE}.

An EQM version of the AFM scanner was used, with the first cantilever of the chip already missing. The corresponding beam was therefore removed in order to access the next sensor. Checking of the testbed as well as FSW testing were both performed at room pressure and temperature.

Starting the measurements

After all the connections were checked, the CME was powered up by means of LabVIEW. Then, communication was established with the AFM by means of the LabVIEW GUI and the manual switch. The computer was therefore communicating with the AFM board, and after a few seconds the AFMCSW code was downloaded into the RAM. Using easyScanMars, the AFM was then set in its default configuration, as described in 3.2.2.

Initialization

The state of the piezoresistors was checked by initializing the AFM in static mode. As expected, the value of V_{BRO} determined for the first sensor showed that it was no longer present. For all the other sensors, the value was about -5V, as expected. Notably, the value was V_{BRO}=-5.149V for the second sensor, therefore set as the current cantilever. The noise was also checked on an oscilloscope, and found to be sufficiently low to allow AFM operations.

Then, the excitation frequency of the current cantilever was determined. A verification was made, that the corresponding oscillation was sufficiently large to allow measurements in dynamic mode, following the procedure described in 3.2.4. The excitation frequency was repeatedly found between 31817 and 31827 Hz. The corresponding phase shift was 40 deg, with a negative sign for V_{SHAKE}, which means an effective phase shift of 220 deg. The amplitude of oscillation was good, as V_{AP} was only about 1V (range is 0 to 10V). Thus, the AFM was initialized manually in dynamic mode, and was ready for the next step.

Approaching the sample

First, the "Approach" button in the easyScanMars GUI had to be clicked on, as it set the position of the cantilever in the middle of the z-range for the approach. This had however no effect on the sample stage, as the motion of the latter was controlled by LabVIEW. The easyScanMars software being ready for detecting the contact, the communication was switched to the CME (LabVIEW switch and manual switch) to drive the stage motor. Then, the translation of the stage toward the sensor tip was started by means of LabVIEW. After a certain number of steps, the motion of the stage was automatically stopped. The AFM_near "LED" on the LabVIEW GUI was asserted, indicating that the tip was in contact with the sample. However, when looking at the oscilloscope, we realized that AFM_near was flickering between the "low" and "high" states. Due

to the vibrations of the motor stage, the cantilever felt the sample too early, and was too far from it when the stage stopped. Two or three additional steps were needed to have AFM_near staying "low", indicating that the feedback loop was closed. The contact being established, communication was switched back to the AFM (LabVIEW switch and manual switch).

Imaging

As no samples were available at that time on the SWTS, AFM images were taken on the rim of the wheel. After having optimized the scan parameters, good images were taken in dynamic mode. Then, the approach and imaging process were repeated in static mode, in order to check that the detection worked in both modes.

Summary

This first test showed that Famars hardware functioned when integrated into the MECA testbed. In particular, the AFM_near signal generated by the AFM board was correctly interpreted by the stage. A problem due to the vibrations of the stage during its translation was however identified, and led to a modification of the FSW. Each time the translation of the stage is stopped during the approach, the state of AFM_near is checked after a few seconds. If its state is "high", a new translation toward the sensor tip is started.

In addition, the AFM parameters used for approaching the sample and taking images in both modes were kept as references for the FSW testing. If a problem happened, we would know if it came from the hardware or from the FSW itself.

3.4.2 Testing of the MFSW commands

In order to test the MFSW, the testbed had to be set in a flight-like configuration. Thus, the manual switch was removed, and the CME was connected directly to the PC, which emulated the flight

computer. A special interface installed on the PC allowed issuing MFSW commands. The generated telemetry could be read either directly (channelized telemetry, afm_tips, afm_frqtest, afm_response) or by using a special program written in Matlab (afm_scan, afm_tbl).

Testing of the MFSW was performed command by command, and following the order of appearance in a typical sequence. Priority was given to the absolutely needed commands, while additional commands with more complexity were tested at the end of the session. The MFSW AFM raw commands were not tested, as they were part of the AFM block commands.

Since the commands were coded based on our algorithms, we knew their expected effects. However, we had no access to the code itself due to International Traffic in Arms Regulations (ITAR) restrictions. Thus, the first debugging was performed by the JPL programmer who coded the FSW, and our contribution consisted in verifying that the commands performed the right tasks when issued to the hardware. When a doubt subsisted, discussions between the FSW programmer and the author allowed ensuring that the commands were written as expected. A few changes were brought during this testing by issuing engineering change requests (ECRs).

Adaptation of the FSW to the testbed

As the parameters stored in the Parameter Value table were those of the FM, a few adaptations had to be made to use the FSW on the testbed without problems. There were mainly three differences between the testbed and the FM. First, the powering of the CME board was not realized the same way, and when the FSW checked the voltages, it generated errors. Thus, a few "voltage" parameters had to be modified in the Parameter Value table.

The positions of the limit switches of the SWTS were also slightly different. After having determined them for the testbed, the values of the corresponding parameters also had to be modified. Additionally, the Famars scanner was not the FM, and the values of the calibration

parameters had to be set to those determined for this scanner during the preliminary testing, described in 3.4.1. Finally, the active tip was set to the second one in the State table, since we knew the first one was removed.

As the intention was not to modify permanently the FSW tables, a scenario constituted of several afm_cmd_setparm was created and executed each time that the FSW was used on the testbed.

Testing of MECA_AFM_BOOT

After having enabled the AFM (MECA_CMD_ENABLE, "AFM", "enable"), the MECA_AFM_BOOT was issued. The AFMCSW was downloaded successfully into the AFM electronics. To verify that the AFM was correctly configured after the completion of the command, all AFM attributes were read by issuing MECA_AFM_ATTRGET commands. As expected, the second sensor was set in static mode, with the Wheatstone bridge initialized. The value of the bridge offset voltage V_{BRO} was -5.150 V, in accordance with the value determined by means of easyScanMars (-5.149 V).

Testing of MECA_AFM_TSTTIPS

Testing of all the piezoresistors was performed by issuing MECA_AFM-_TSTTIPS. The results were sent back in the afm_tips packet, and were as expected. The first piezoresistor was diagnosed as "dead" and the others as "OK", except one that was "noisy". If the threshold value for the noise amplitude was decreased, the repetition of the test gave four "noisy" tips.

Then, the command should set the AFM in static mode by calling the low-level block command MECA_AFM_STATIC. The AFM attributes were checked, and found to be as expected. We also verified that sending MECA_AFM_STATIC after issuing MECA_AFM_TSTTIPS had no effect on the AFM attributes. Since it was the case, MECA_AFM_STATIC will never be used after MECA_AFM_TSTTIPS in the future. It could however be used to switch between

dynamic mode and static mode without testing all the piezoresistors again.

Testing of MECA_AFM_FRQTEST

The command MECA_AFM_FRQTEST was tested first on the active cantilever, i.e. the second one. In the returned afm_frqtest packet, we read a frequency of 31823 Hz, in accordance with our previous experiments. Even if the experiment was carried out at room pressure, the amplitude of oscillation was large, based on the signal V_{SIG} displayed on the oscilloscope. Then, the remaining cantilevers were tested. While the command also determined the right frequency for the fourth and the seventh cantilevers (30919 Hz and 32989 Hz respectively), the command failed for the third, the fifth, the sixth and the eighth cantilevers. We discovered that the frequency search always started at 30 kHz, instead of starting at 1 kHz lower than the expected resonance frequency of the tested cantilever. It explained why the test succeeded for the cantilevers having a resonance frequency close to 30 kHz, while it failed for the others (the command probably found local maxima of the resonance curve before reaching the real maximum). Therefore, the starting frequency for each sensor was modified to the right value in the Tips table. Note that the resonance frequency and the corresponding phase of the excitation signal are also stored in the Tips table, and modified if MECA_AFM_FRQTEST is successfully completed.

Once this command finds the resonance frequency, it should compare V_{AP} with a threshold value. If V_{AP} is lower than this value, it sets the AFM attributes for dynamic mode by calling the low-level block command MECA_AFM_DYNAMIC. If V_{AP} is higher, it should restart the test, and abort if it fails again.

After the test of the second cantilever, the AFM attributes were checked, and found to be those used for an approach in dynamic mode. In particular, the parameters of the excitation signal were equal to those read in the afm_frqtest packet. Finally, we verified that

sending MECA_AFM_DYNAMIC after issuing MECA_AFM_FRQTEST had no effect on the AFM attributes. As it was effectively the case, we will not use this low-level block command in the future before starting the sample approach.

Finally, we observed once on the oscilloscope that the amplitude of the excitation signal V_{SHAKE} was not set properly for the frequency test. In fact, this problem did not come from the frequency test routine itself, but from the transition between static and dynamic mode. Thus, this phenomenon was further studied in Neuchâtel using easyScanMars.

When trying to set the AFM in dynamic mode, five out of seventy attempts did not set the amplitude of V_{SHAKE} to the right value of 1V, but to a few tens of millivolts, as seen when testing MECA_AFM_FRQTEST at JPL. For these five cases, it was however possible to recover from this situation by setting V_{SHAKE} to another value, and then to the desired value. Thus, we decided to set V_{SHAKE} to +1V and then to -1V before each MECA_AFM_FRQTEST by sending two MECA_AFM_ATTRSET commands. This allowed avoiding any trouble with the excitation signal, and was later implemented in the VML sequences.

Testing of MECA_STG_APPR

The approach of the sample toward the AFM was tested in static mode and in dynamic mode. Before we started the testing, the command was modified to avoid stopping the translation too early, as explained in 3.4.1. In addition to this change, we noticed that it was necessary to perform a translation of one step (for example) to initialize AFM_near before sending MECA_STG_APPR.

When the command was performed with the AFM in static mode, the SWTS was always stopped when the sample entered into contact with the sensor tip. In dynamic mode, however, one out of five attempts failed. This was not surprising, as similar behavior had already been observed when working with easyScanMars. We iden-

tified two possible reasons for this failure: a too large speed of the stage or a too small amplitude of vibration of the cantilever. A study was therefore performed at the IMT, in order to see how much these parameters influence the approach. Hundreds of approaches were realized in static and dynamic mode. Approaches in static mode showed 100% reliability, contrarily to approaches in dynamic mode. However, under certain conditions, the contact was always detected. First, the oscillation had to be sufficient, with a V_{AP} value smaller than about 2.5 V. Secondly, the translational speed of the stage should be less than 3 μm/s, which corresponds to about 12 motor steps per second for the FM stage.

As the speed of the stage during the testing of MECA_STG_APPR was about 4 μm/s, the observed failure was predictable. Thus, it was decided to reduce the speed of the stage by sending a MECA_CMD-_SETPARM command before executing MECA_STG_APPR. A few approaches were realized successfully on the payload interoperability testbed (PIT) after this modification, and further testing will be performed prior to the operations.

Testing of MECA_AFM_IMAGE

Once the tip was in contact with the sample, in this case the rim of the sample wheel, the MECA_AFM_IMAGE command was sent. We were able to take images of the surface, but in some cases we quickly lost contact with the sample.

After reexaminating the code, we noticed that the cantilever could not access the half of the z-range closest to the sample. This limitation was intended for the approach, as the cantilever has to be in the center of the z-range when reaching the sample. However, once in contact, the full z-range was needed, otherwise the tip could not access locations deeper than the contact point. Thus, the AFM attribute limiting the z-range was set to the right value after the completion of MECA_STG_APPR. This problem being solved, several images were taken in both modes using the same parameters as those used in 3.4.1.

Figure 3.3 shows images of the sample wheel surface taken in dynamic mode with the full z-range. Views a) and b) correspond to an image taken with a 10-μm scanrange, c) and d) corresponding to a 16-μm image taken at the same location. The format of the images was naturally not the same as the .ezd generated by easyScanMars. The AFM images were sent in afm_scan packets containing the data and an header, and were imported into a Matlab display tool. However, information was missing in the afm_scan header. In particular, the scanrange of the images was not given. In order to get all the missing information on the images, we had to get the AFM attributes immediately after the completion of each MECA_AFM_IMAGE command. This will also be true during the operations on Mars. However, as telemetry could be lost during transmission, the scanrange will certainly also be written in the afm_scan header, using 8 out of the 16 bits attributed to the command token.

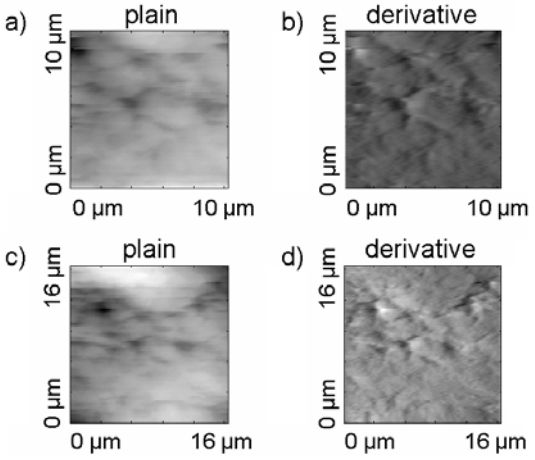

Figure 3.3: AFM images of the sample wheel aluminum surface taken at the same location, with full z-range (13.8 μm). Top) 10-μm image displayed in a) plain and b) derivative view. Bottom) 16-μm image displayed in c) plain and d) derivative view. One can clearly identify the same surface features on both images.

The MECA_AFM_IMAGE commands were always sent with the "smartzoom" argument being "off", meaning that no automatic zooming was performed. Thus, this subroutine was not tested with the hardware. However, the efficiency of the jpeg-compression algorithm for the selection of interesting area was tested. As we were not allowed to use the FSW code, a Matlab routine measuring the entropy was applied to regions of AFM images. The part of the image showing the highest entropy was the least compressible, and would therefore have been selected by "smartzoom".

Several images were tested, and figure 3.4 shows the results for four of them. Images a) and b) show polystyrene particles, image c) silica particles and images d) the tip characterizer sample. As one can see, the algorithm produced good results for images a), b) and c), even if it would have been better to select the square with two particles in image a). For image d), however, the artifacts generated by the AFM created an area of high entropy, and "smartzoom" would have selected the least interesting area of the image. Note that image c) also included bad scanlines on the top, but in this case the cluster of particles showed a higher entropy than the areas containing the bad scanlines.

When imaging particles, the AFM tip frequently traps or moves particles, which produces bad scanlines. Based on the preliminary results above-mentioned, there is a certain risk that the "smartzoom" routine would zoom on the bad scanlines. Even worse, if one part of the image is out of the z-range, it could probably pick that part to zoom. Another drawback of this routine is the fact that the image is always subdivided in sixteen regions, which reduces our flexibility for the operations. Therefore, even if the possibility of using "smartzoom" was kept for the operations, centered zooms having a tunable nest ratio are more likely to be used. This could be coded easily in VML, as we will see in section 3.5.

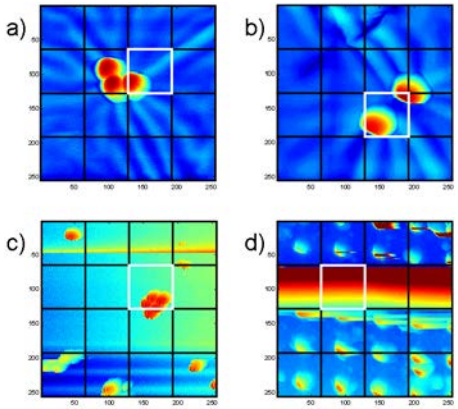

Figure 3.4: AFM images divided in 16 squares, the white square indicating the highest entropy area. For images a), b) and c), the "smartzoom" subroutine would zoom on a location of interest, while it would zoom on an AFM artifact for image d).

In order to test the "prescan" routine, MECA_AFM_IMAGE was sent with a scanrange equal to zero immediately after the MECA-_STG_APPR command. The motion of the cantilever was observed by means of an optical microscope, and this confirmed that the scanning followed the desired strategy, i.e. started scanning small lines and progressively increased their size. At the end, we noticed that a complete image was taken, with a scanrange corresponding to the largest possible scanrange. When looking at the slopes determined by means of this process, the routine appeared not to be working properly, as some erroneous values were obtained. We discovered that the FSW considered the height information of the scan data as unsigned, while it was signed. This error was corrected, but "prescan" still did not work properly. We suspected that scan lines out of the z range could have lead to miscalculations in the algorithms. As this command seemed to generate more risk of failure, and that the goal was to minimize it, we decided not to use it for the operations.

Testing of MECA_STG_BRKTIP

This command was not tested at JPL, as no cleaving tool was available there at the time. However, a cleaving of a beam was performed successfully on the PIT a few months later using MECA_STG_BRKTIP. The command itself is quite simple: it translates the stage with a certain number of steps, ignoring the AFM_near signal. However, experimental work has still to be performed on the MECA testbed and on the PIT to determine the number of steps needed to remove each beam. Experimental data obtained at the IMT are described in 4.7.

Other modification

In addition to the above-mentioned changes, another modification concerning several commands was made. During the testing, we observed that the sensor used for each FSW command was initially defined as being the current sensor stored in the State table. Thus, it was not possible to for example perform a frequency test on the next cantilever if the current one failed. To solve this problem, the code was modified, allowing selecting another sensor by sending MECA_AFM_ATTRSET, 16, *tip* before executing the FSW command. Note that the value of the current sensor had to be reset to the right value at the end.

Summary

While most of the tested FSW commands worked as expected, a few of them needed modifications, either because they did not correspond to the algorithms in pseudo-language, or because the pseudo-language algorithms themselves contained errors or omissions. As each change of the FSW had to be negotiated and undergo a full validation process, workarounds were often used, issuing for example MECA_CMD_SETPARM to modify some parameters outside of the block commands. A modified version of the FSW was released

a few weeks after the testing, and was ready to be used inside VML sequences.

3.5 The Virtual Machine Language (VML)

3.5.1 Introduction

VML is a procedural sequencing language which simplifies spacecraft operations, minimizes uplink product size, and allows, with the associated flight code, autonomous operations aboard a mission. The language is a mission-independent, high-level, human readable script. It has been used for several JPL missions, such as for example Mars Odyssey.

The VML system consists of several components on Earth and on the spacecraft. First, a text editor allows creating the sequences in a human-readable version. Then, they are translated in a binary format by the VML compiler, located in the ground system. The obtained binary is uplinked to the spacecraft, where it is handled by the VML flight component. The latter runs within the flight code, providing a configurable number of parallel threads of execution of the flight software commands. This parallelism is achieved by instantiating a fixed number of virtual machines, also called sequence engines. Similarly to a processor, a sequence engine is able to interpret instructions, with memory, dynamic data storage and an instruction pointer. Each engine can be used either for storage or for execution of the VML sequences.

3.5.2 Description

The sequences coded in VML are defined as functions. They may admit input parameters and may also return a value to a calling function. If they are intended to be reused as subroutines, they are called blocks. Sets of one or more functions are defined as modules, and only one module is allowed per source file and per engine.

While a module loaded into an execution engine always includes a single function (the master sequence), a library module loaded into a storage engine can include several blocks. Once a library module is loaded, it becomes available to all the engines for execution.

A block may be executed inside another function using the "CALL" statement. The calling function is suspended, the block is executed, and then the calling function resumes. The block may also be run in parallel to the main function using the "SPAWN" statement. The spawning function may pass parameters to the spawned function, but no return value is possible. In this case, two instructions pointers work in parallel: one on the execution engine for the spawning function and one on the storage engine for the spawned block.

The sequences developed in VML are procedural in nature. At any particular time, only one instruction is considered to be "next" on a sequence engine. This means sequencing can be approached as a structured programming problem, allowing the use of high-level language constructs, such as conditionals or "WHILE" and "FOR" loops. Event-driven sequencing is also possible using "WAIT" and "WAIT_CHANGE" statements. Time tags are used before each instruction of the functions, and can be absolute or relative. Absolute time tags have the form A2007-330T14:00:00.0 (26th of November 2007, at 2 p.m.) and relative time tags have the form R0000-001T00:00:10.0 (10 seconds) or simply R00:00:10.0.

In addition to the functions, the VML language contains a variety of variable types and a rich set of operators. It can issue flight software commands, such as for example the MFSW commands, using the special external call "ISSUE" or "ISSUE_DYNAMIC". The variables of the VML language can be either local or global. While a local variable is defined within a function (or sometimes a module) and is not readable outside of it, a global variable is visible to all functions. Global variables are the means by which the FSW communicates with the sequence. Thus, only global variables can be used for event-driven sequencing.

3.5.3 Application to Famars

Fifteen sequence engines are used for the Phoenix mission, two of them being assigned to MECA: engine 7 for the execution of the master sequence, and engine 1 for the storage of the library. Depending on the operating instrument of MECA, two different libraries can be loaded in engine 1: an OM/AFM/TECP library or a WCL/TECP library. If MECA is safed for any reason, engines 1 and 7 are automatically unloaded. If a problem appears during the execution of an OM subroutine, the electronics of the RAC is also safed, and the RAC engine (number 8) is automatically unloaded. Finally, the subroutines applicable to all the instruments of MECA are part of the surface science library, loaded in engine 15. They include command sequences to turn MECA on or off, and a sequence to assign tokens.

The use of the VML language associated with the MFSW commands allow developing autonomous sequences for the operation of Famars. Master sequences call subroutines in the OM/AFM library and the surface science libraries, and these subroutines mainly issue MFSW commands described in 3.3. Some parameters of the master sequences are inputs of the subroutines, giving some flexibility in the execution.

However, interactions between the MFSW and the VML sequences are limited, mainly because the telemetry data produced by the MFSW commands are not accessible for event-driven sequencing. The only AFM global variable that VML can read is gv_meca_afm_done, incremented each time an MFSW AFM command is successfully completed. For example, after the completion of the MECA_AFM_IMAGE command, the VML sequence only knows if an image was taken, without getting information about the recorded scanlines. Even if this reduces our possibility to create sophisticated sequences, it has the advantage of simplifying the algorithms. It would be more complicated to predict the behavior of the instrument if the FSW was able to act strongly on the sequence.

Despite this limitation, coding in VML offers many possibilities. For example, if one wants to take several AFM images of the same sample with nested zooms, a "FOR" loop can be created. The lines hereafter produce three AFM images of the sample, zooming two times the region of interest. Note that the time tags are relative. Absolute time tags are only given when all the sequences of an operation day are brought together.

```
R00:00:00.1   i:=1
              ; Start with a 40-microns image:
R00:00:00.1   scanrange:=40
R00:00:00.0   FOR i := 1 TO 3 DO
                ; Take an image (auto-zoom subroutine
                disabled):
R00:00:00.1     ISSUE_DYNAMIC "MECA_AFM_IMAGE",
                scanrange, 256, 256, 3500, 8, 9, 2000, 3, 1, "off"
                ; Divide the scan range by 2:
R00:00:00.1     scanrange:=scanrange/2
R00:00:00.0   END_FOR
```

A basic VML sequence

The following example shows the basic sequence "meca_afm_test" written for taking an AFM image. It was built based on the scenario used to test the FSW commands, and does not correspond to the actual VML sequence used for operations on Mars. The latter is more complicated, using VML constructs and calling subroutines of the OM/AFM library.

```
MODULE
BLOCK meca_afm_test
BODY
              ; Turn MECA on:
R00:00:00.1   ISSUE_DYNAMIC "MECA_EPS_POWER", "on"
```

```
                ; Enable the AFM:
R00:00:00.1     ISSUE_DYNAMIC "MECA_CMD_ENABLE",
                "afm", "enable"
                ; Boot the AFM:
R00:00:00.1     ISSUE_DYNAMIC "MECA_AFM_BOOT"
                ; Test all the piezoresistors:
R00:00:00.1     ISSUE_DYNAMIC "MECA_AFM_TSTTIPS"
                ; Find the resonance frequency of the current can-
                tilever:
R00:00:00.1     ISSUE_DYNAMIC "MECA_AFM_FRQTEST"
                ; Enable the SWTS:
R00:00:00.1     ISSUE_DYNAMIC "MECA_CMD_ENABLE",
                "stage", "enable"
                ; Initialize the SWTS (without ignoring the "Safe-
                To-Rotate limit switch"):
R00:00:00.1     ISSUE_DYNAMIC "MECA_STG_INIT", "transla-
                tion and rotation", "do not ignore"
                ; Place the substrate to be measured in front of the
                AFM:
R00:00:00.1     ISSUE_DYNAMIC "MECA_STG_ABSROT",
                "OM64", 0, "do not ignore"
                ; Force stage update to get status of AFM Near:
R00:00:00.1     ISSUE_DYNAMIC "MECA_STG_RELXLT", "cw-
                in", 1, "do not ignore"
                ; Reduce the stage speed:
R00:00:00.1     ISSUE_DYNAMIC "MECA_CMD_SETPARM",
                98, 2000
                ; Approach the sample until it reaches the sensor
                tip:
R00:00:00.1     ISSUE_DYNAMIC "MECA_STG_APPR"
                ; Before an image, choose the full z-range:
R00:00:00.1     ISSUE MECA_AFM_ATTRSET, 33, 32767
```

```
                ; Take an AFM image:
R00:00:00.1     ISSUE_DYNAMIC "MECA_AFM_IMAGE", 10,
                256, 256, 3500, 8, 9, 2000, 3, "both_dirs", "off"
                ; Read the tables:
R00:00:00.1     ISSUE_DYNAMIC "MECA_TBL_DWNLD",
                "state"
R00:00:00.1     ISSUE_DYNAMIC "MECA_TBL_DWNLD",
                "paramvalues"
R00:00:00.1     ISSUE_DYNAMIC "MECA_TBL_DWNLD",
                "tips"
                ; Translate the SWTS to "safe-to-rotate" position:
R00:00:00.1     ISSUE_DYNAMIC "MECA_STG_ABSXLT", "safe
                LS on", 0
                ; Disable the AFM:
R00:00:00.1     ISSUE_DYNAMIC "MECA_CMD_ENABLE",
                "afm", "disable"
                ; Disable the stage:
R00:00:00.1     ISSUE_DYNAMIC "MECA_CMD_ENABLE",
                "stage", "disable"
                ; Reset MECA:
R00:00:00.1     ISSUE_DYNAMIC "MECA_CMD_RESET"
                ; Switch MECA off:
R00:00:00.1     ISSUE_DYNAMIC "MECA_EPS_POWER", "off"
                ; End of sequence:
END_BODY
END_MODULE
```

An image was taken successfully on the PIT by members of the MECA team using sequences similar to "meca_afm_test". As Famars was not well aligned with the SWTS at that time, the image was taken on the aluminum rim of the sample wheel. Figure 3.5 shows two different top views of the acquired image, on which features of the aluminum surface can be distinguished.

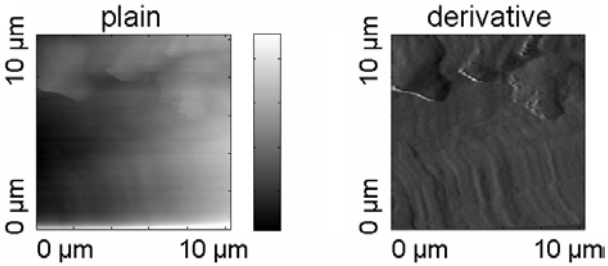

Figure 3.5: AFM image of the sample wheel aluminum surface taken using a basic VML sequence on the PIT. The scanrange was 10 μm, and the vertical range 3.45 μm. Left) plain view of the forward scan. Right) derivative view of the forward scan.

3.5.4 Sequences for operations

The sequences which will drive the AFM on Mars were created in advance, since they had to be validated before being uplinked to the spacecraft. This implied also an off-the-shelf use during operations, with little or no changes to the code. Therefore, a full set of master sequences and a complete OM/AFM library for all the possible activities of Famars were needed.

The main limitation was the storage capacity of the engines. The master sequence, stored in engine 7, should not exceed 2000 instructions, and the AFM/OM/TECP library, stored in engine 1, should not exceed 4000 instructions. Note that various operations in VML contribute to increase the number of instructions in a sequence. For example, calling a subroutine costs two instructions, plus one instruction for each argument of the subroutine. VML constructs also use instructions, a "FOR" loop being equivalent to 34 instructions. As the AFM activities require many lines of VML code, it was important to use the storage capacities of the engines optimally. The strategy was to store the frequently used functions in a library, which reduced the size of the master sequence loaded in engine 7.

All the created sequences, including those of the library, had to go through the validation process. After a visual inspection of the code, the source file was compiled, and an output binary file was produced which could be loaded into engine 7 for the main sequence or into engine 1 for the library. The compilation also returned diagnostic files that had to be read to ensure that the compilation had succeeded, and that the sequences were successfully loaded in the engines. If that was the case, the master sequence was run by a simulation software which emulated the behavior of the flight hardware. If the simulation did not produce errors, the sequence was run on the PIT. Later, the produced telemetry as well as the execution time of the sequence were analyzed. If they were as expected, the sequence could be validated, and ready to be sent in the future to the real spacecraft. Since the PIT hardware has a few differences with the flight hardware, a few adaptations were made to the sequences. For example, the positions of the limit-switches of the SWTS are different, as well as the resonance frequencies of the AFM cantilevers. Thus, a few parameters have to be modified before sending a validated sequence to the spacecraft.

As the number of validated master sequences is limited, they will be modified to handle the daily activities. For example, consider that a validated sequence takes one AFM image of 40 μm. If during operations an image of 20 μm has to be taken, we could certainly use this sequence, as the change of the scanrange does not cause large variations in terms of duration, needed resources and generated data. However, if two images of 20 μm have to be taken, this could probably not be done using the validated sequence, as it would take more time and produce more data. Thus, the master sequences created prior to the operations should have maximal functionality. In the case discussed here, the validated sequence should include the possibility of taking several images, and should have been validated using this option. At the time of writing, two master sequences have been created, one performing a check-out of the instrument (meca_afm_checkout), and the other performing a whole AFM measurement session, with

the possibility of taking several images.

The master sequence meca_afm_checkout has been validated, as well as a first version of the library. In October 2007, it was run successfully on the PIT during an Operational Readiness Test (ORT), producing afm_tips and afm_frqtest data for all cantilevers. The imaging sequences have not been validated yet, but they will be in the near future. The OM/AFM library will need new validation too, as some blocks had been added to it. Finally, the "tip breaking" sequence needs to be created and validated.

3.6 Conclusion

Based on the experience acquired using the easyScanMars software and on existing descriptions, the FSW commands for Famars were created. Testing of these commands was performed on a testbed at JPL, where a few problems were detected. Some of them led to modifications of the FSW, while others were solved by issuing low-level commands in the operations sequence. At the end, the FSW commands functioned perfectly, except the "prescan" routine, which will not be used during the operations. Some doubts were also expressed regarding the "smartzoom" subroutine, since its efficiency could be very low for images presenting artifacts. These two subroutines were not critical for the operations, and the modified FSW commands allowed taking several images on the testbed.

Based on the procedure used to take these images, a simple VML sequence calling the FSW commands was created. Using this sequence, images were successfully acquired on the PIT. Then, more complex VML sequences were built, as the creation of sequences for the operations on Mars was subject to constraints. First, the storage capacity for the master sequences and the library subroutines is limited. Secondly, as they have to be validated weeks before the operations, they should contain all the functionality required to perform the desired experiments. Creation and validation of the AFM sequences is in progress, and a few of them were already used suc-

cessfully during an ORT.

References

[1] C.A. Grasso. The Fully Programmable Spacecraft: Procedural Sequencing for JPL Deep Space Missions Using VML. *IEEE*, 1:75–81, 2002.

[2] C.A. Grasso. Techniques for simplifying operations using VML sequencing on Mars Odyssey and SIRTF. *IEEE*, 8:3603–3613, 2003.

[3] D. Brändlin-Müller. *easyScan Serial Protocol Manual v1.12*. Nanosurf AG, Liestal, Switzerland, May 2006.

[4] S. Gautsch. *Development of An Atomic Force Microscope and Measurement Concepts for Characterizing Martian Dust and Soil Particles*. PhD thesis, University of Neuchâtel, Switzerland, 2002.

[5] Lisa Tatge. *MECA Atomic Force Microscope User's Guide*. JPL, March 2006.

[6] Alan Mazer. *MECA Flight Software Design Document*. JPL, July 2006.

Chapter 4

AFM measurements

4.1 Introduction

This chapter describes the AFM measurements performed by means of the Famars instrument. The first images were taken to calibrate the scanner in the range of temperatures expected during operations (4.3). Then, its ability to measure particles was scrutinized. A characterization of the instrument was performed by measuring particles artificially fixed to a silicon substrate (see 4.4.1). In particular, the ability of the instrument to determine the size, the shape and the size distribution of particles was presented. Samples closer to what is expected during operations on Mars were also prepared and measured (see 4.4.2). They consisted of geological samples showing compositions similar to those expected on Mars, but with different size distributions.

In order to increase the adhesion of the particles, special substrates had been designed by our partners. AFM measurements were performed on these substrates by means of the Famars instrument (see 4.5). Except for one of them, particles were not deposited, as the main objective was to determine if the instrument could image them properly, despite e.g. magnetic fields or aspect ratios close to one.

Since important artifacts were observed during measurements, methods for correcting them were implemented (see 4.6). In particular, the non-linear distortions of the scanner and the tip artifacts were corrected using image processing algorithms implemented in Matlab.

Finally, the procedure used to exchanging a sensor tip was tested (see 4.7), as well as the one for cleaning a contaminated tip (see 4.8).

4.2 Experimental setup

The measurements described in this thesis were taken at the IMT, using Famars in its stand-alone configuration (see 2.4.2). As illustrated in figure 4.1, the AFM scanner head was mounted in front of a sample stage. The whole setup, including the electronics, was placed in a vacuum chamber located on an optical table. Low temperatures could be reached inside the chamber using a liquid nitrogen circuit, and were read using a resistance thermometer (Pt-100 sensor) installed on the AFM scanner. An electrical feedthrough allowed connecting the AFM electronic board to the M-Test board, and also monitoring signals of the AFM board on an oscilloscope (V_{SIG}, V_{SHAKE} and AFM_near).

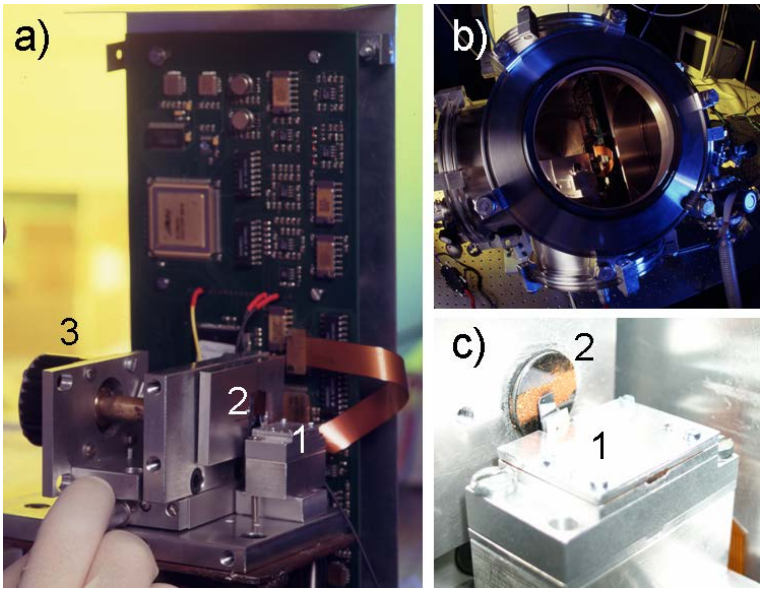

Figure 4.1: a) Setup for measurements. An AFM scanner head (1) is mounted on an aluminum support, and connected to the electronics through the flexprint PCB. The sample (2) is installed on a plate supported in three points, two being fixed and the third one allowing approaching the plate toward the AFM using a stepper motor (3). The lateral alignment between the sample and the AFM sensor chip is performed manually using a micrometer screw. b) Vacuum chamber used to run the AFM under Mars conditions. The AFM and the sample can be seen through a window during the measurements. c) Larger view of an EQM AFM scanner head (1) installed in front of a geological sample (2).

4.3 Calibration

The Famars instrument needs to be calibrated to ensure a correct interpretation of the AFM images of particles. A first calibration of the instrument was therefore performed at the IMT before its delivery by measuring a reference sample (see 4.3.1). Since the calibration parameters can change slightly before starting the measurements on Mars, an in-situ calibration will also be performed, using dedicated samples located on the SWTS (see 4.3.2).

4.3.1 Pre-launch calibration

After having passed the environmental testing described in 2.5, the FM and the FS scanners were calibrated at room temperature. In order to do this, a calibration grid sample, shown in 4.2, was imaged using different settings for the scan parameters. After a few adjustments, an AFM image showing the same dimensions and angles than the original grid was obtained. The corresponding scan parameters values were stored in the datasheets of the FM and the FS scanners. Figure 4.3 shows two AFM images of the grid taken by means of the calibrated FM scanner.

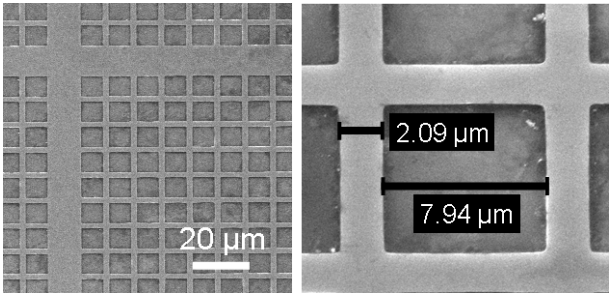

Figure 4.2: SEM images of the 10-μm grid used for the calibration of the Famars scanner at the IMT. The height of the structures is 200nm.

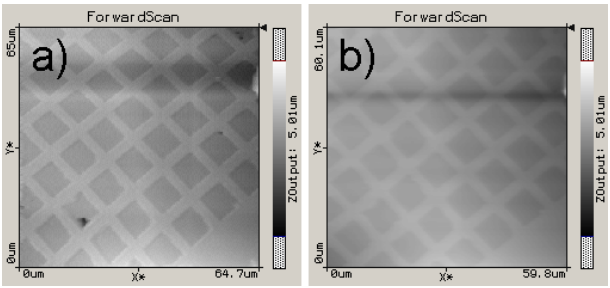

Figure 4.3: AFM image of the calibration grid taken by means of the FM scanner a) in dynamic mode, b) in static mode. The displayed vertical range is 5 μm for both images.

Then, AFM images of the calibration grid were taken under martian conditions inside the vacuum chamber described in 4.2. Figure 4.4 shows images taken at different temperatures by means of the FM, with the scan parameters set to the values determined at room temperature. In image 4.4.a), a Y-shaped valley was visible. The latter did not correspond to a real topographic feature, but was an artifact repeatedly observed in images taken at temperature close to 0 deg C. This phenomena is probably due to the internal properties of the scanner, in particular of the flexprint springs, as the flexprint springs showed their largest change of damping properties near 0 deg C (see 2.47). The shapes and the sizes of the squares showed also nonlinear distortions, as well as shrinking of the scan area. For image b), recorded at -12 deg C, the only remain of the Y-shape artifact was a small line on the lower half of the image. However, nonlinear distortions and shrinking of the scan area were still there. In image c), which was taken from -19 deg C to -13 deg C (starting at the bottom of the image), the top of the image was not recorded, as the scanner reached the limit of its vertical range. Since gradients of temperatures existed between the scanner and the sample stage, the distance between them was modified during the scan due to different thermal expansions. An adjustment of the liquid nitrogen flow

was performed manually to compensate the drift, but was not always sufficient to avoid loosing contact, explaining the missing top of image c). Distortion in image c) was comparable to those of image b). Note that the horizontal white line was an artifact due to the particle present on the left of the image and played no role for the calibration.

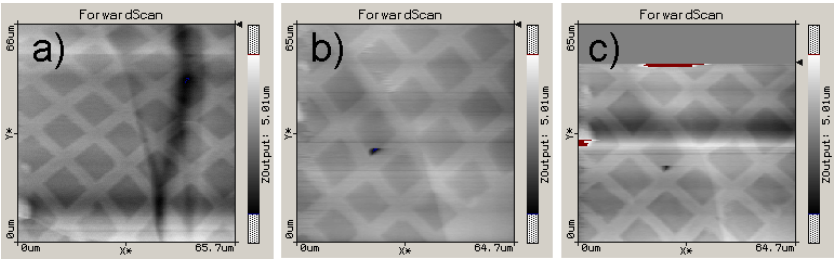

Figure 4.4: AFM image of the calibration grid taken in dynamic mode at a) +4 to +6 deg C, b) -12±1 deg C, c) -19 to -13 deg C.

In summary, it was observed that nonlinear distortions were larger at low temperature than at room temperature. The scan area was shrunk by about 30% of its initial value at -20 deg C. However, the requirement of a 40-μm XY scan range was fulfilled, even at low temperature. Undesirable effects were caused by a temperature drift between the sample and the stage. Even if this phenomenon will probably be smaller on Mars, further tests should be performed on a testbed in order to characterize the relative thermal drift between the AFM scanner and the SWTS. The most critical drift is in the z-direction (the direction normal to the sample's surface), as a large drift could move the surface out of the z range of the scanner, as observed in image 4.4.c). Knowing the drifts in x and y direction is important too, as they allow distinguishing distortions due to the scanner itself from distortions due to thermal effects. This is critical information for the post-processing calibration of the AFM images, which allow correcting the nonlinear distortions of the AFM images (see 4.6).

4.3.2 In-situ calibration

During the first days of operations of Famars, an in-situ calibration of the instrument will be performed. This will include a scanner calibration similar to the one performed on Earth, and a determination of the sensor tip position relative to the sample wheel.

Scanner calibration

For calibrating the scanner, a linear calibration substrate (see figure 4.5.a), as well as a tip characterizer substrate (see figure 4.5.b) were installed on the sample wheel. These substrates show orthogonal features with a known period, and the scanner can be calibrated by imaging them, similarly to the process followed on Earth. The pre-launch calibration parameters will then be replaced in the FSW Parameter Table (see 3.3.6) by the values determined on Mars.

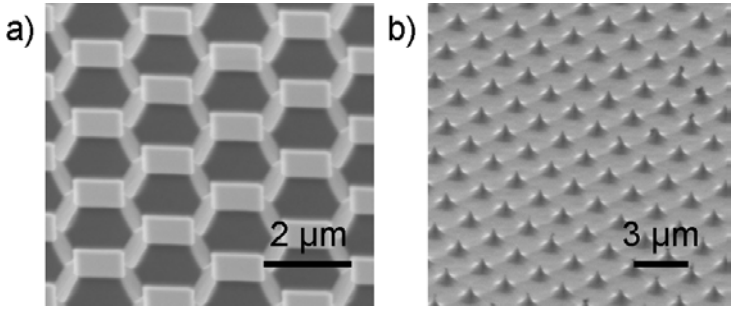

Figure 4.5: a) SEM image of the linear calibration substrate. This substrate is the standard grating TGX01 from NT-MDT, used for the lateral calibration of SPM scanners. The period is 3 μm and the height of the structures about 0.6 μm. b) SEM image of the tip characterizer substrate. This substrate is the standard grating TGT01 from NT-MDT, used mainly for the determination of the tip shape and sometimes for the scanner calibration. The period is 2.1 μm and the height 0.4$\pm$0.1μm, the variation being indicated from one substrate to another.

In addition to this coarse calibration, imaging of the calibration samples will be performed before and after each AFM image. As the scan size as well as the nonlinear distortions depend on the temperature, these images will allow calibrating more precisely the AFM images of unknown samples (see 4.6.1). In addition, imaging the tip characterizer substrate will give an estimation of the shape of the AFM tip, which will be used to remove tip artifacts in other AFM images (see 4.6.2).

Alignment relative to the sample wheel.

The lateral and vertical positions of the AFM sensor relative to the sample wheel will also be determined on Mars. The vertical position allows defining an horizontal band in the OM image which indicates the region of the substrate accessible to the current sensor tip. As the x and y scan axes are tilted with 45 deg (see figure 2.17), the width of this band is equal to the maximal scanrange of the scanner multiplied by $\sqrt{2}$, i.e. about 60 micrometers. Using the information on the position of the tip, a location in the OM image within this band can be targeted for AFM measurements.

In order to determine this position, a sample dubbed the tip finder substrate and located on the sample wheel will be measured by Famars. This silicon substrate, shown in figure 4.6.a), presents microfabricated patterns encoding the vertical and horizontal position on the sample wheel. An AFM image of this sample larger than thirty micrometers is sufficient for defining unequivocally the exact position. Figure 4.6.b) showed an AFM image taken by our partners at Imperial College. The code was clearly readable and the position on the sample could be determined. Once the position of the first sensor tip is determined, the positions of the other tips can be calculated. Note that these positions were not determined before the mission, as the alignment between the instruments could perhaps change during launch, cruise and landing phases.

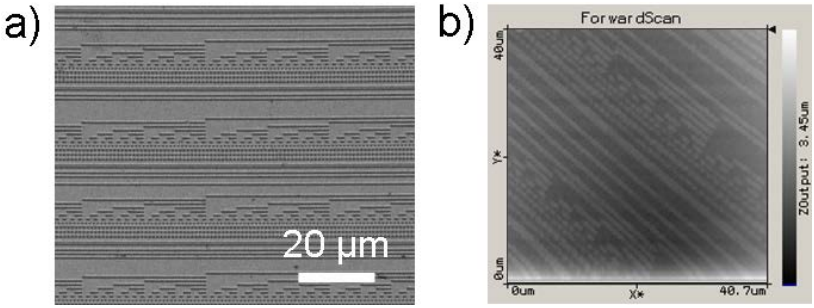

Figure 4.6: a) SEM image of the tip finder substrate. The lines represent a binary code which identifies the horizontal and vertical position of the sensor tip on the sample. b) AFM image of the tip finder substrate. Courtesy Imperial College.

4.4 Particles measurements

The ability of the AFM to distinguish the size and the shape of particles ranging from 0.1 to 5 micrometers was scrutinized by taking images of various samples. While AFM is well adapted to characterize surfaces with little topography, imaging particles is more challenging, the two main problems being the high aspect ratio of the measured features and the possible detachment of particles by the AFM tip. These two questions are discussed more in detail hereafter.

The z-range of the Famars scanner is more than 10 micrometers and the height of the AFM sensor tip is about 7 micrometers. Thus, measuring particles having a maximal diameter of 5 micrometers should not cause problems, except a few artifacts due to the geometry of the AFM tip (see 4.6.2). However, according to end-to-end experiments performed under laboratory conditions on testbeds of MECA, particles can form piles on the collecting substrate, reaching sometimes several hundreds of micrometers in height. In that case, limitations of the hardware could prevent any measurements. First, if the measured features are higher than the height of the sen-

sor tip ($\cong$ 7 μm), they can interact with the cantilever. Second, if they are larger than the vertical range of the scanner ($\cong$ 10 μm), they could create an excessive bending of the cantilever, as the tip could no longer follow the topography. Third, if the measured features are higher than about 60 micrometers, the next sensor tip could make contact with the sample, as the tips are separated laterally by a distance of 350 micrometers, with an angle of ten degrees relative to the substrate (see figure 2.2).

In addition to issues relative to the height of the measured features, the adhesion of the particles plays a crucial role for AFM imaging. As the AFM tip applies lateral forces to the particles, they can be detached from the surface and moved by the tip. This can lead to contamination of the tip and create artifacts in the recorded image, and even totally prevent the AFM from imaging.

For those reasons, two different kinds of measurements were performed at the IMT. In order to characterize the scanner, particles with known dimensions were first measured. The problem of the adhesion of these particles was avoided by fixing them to the substrate (see 4.4.1). Then, the ability of Famars to image loose particles was determined. In order to do this, different geological samples were dispersed on flat silicon substrates, without using any artificial means to increase their adhesion (see 4.4.2).

As reported by S. Gautsch [1], static mode detection is not adapted for particles measurements, as the lateral forces applied by the tip to the particles generally moves them out of the scan area. Thus, all particles measurements described in this thesis were performed in dynamic mode. Note however that in rare cases, the adhesion of the particles was sufficient to allow imaging them in static mode, as illustrated in figure 4.7.

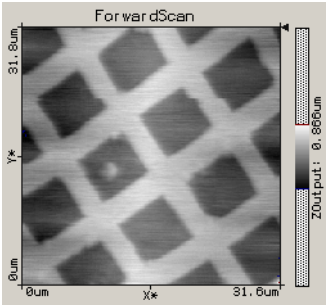

Figure 4.7: AFM image of the 10-μm calibration grid taken in static mode. A particle having a diameter of about two micrometers is visible in one of the squares.

4.4.1 Fixed particles

The goal of these measurements was to characterize the ability of Famars to distinguish the size, the size distribution and the shape of particles, independently of the fact that they could be moved by the AFM tip. Thus, different samples were prepared, consisting in particles with known characteristics and firmly attached to a flat surface. This section described these samples and their measurements by means of Famars.

Polystyrene microbeads

The first kind of measured particles were monodispersed polystyrene microbeads[1]. These particles, delivered in an aqueous suspension, had a perfect spherical shape. Two different size of particles were used, with respective diameters of 1 and 3 micrometers (coefficient of variance 3%).

[1]Polybead® Microspheres, Polysciences, Inc. Warrington, PA, USA

Sample preparation. The particles were fixed on a flat silicon substrate using UV curing adhesive[2]. The adhesive was deposited on the surface by spinning (1000 rpm during 1 minute), and then heated to 125 deg C during one hour. This treatment partially cured the adhesive, leaving a firm and sticky surface. A small drop of a suspension containing the microbeads was then deposited on the surface. Since it was observed that the concentration of particles in the delivered suspension was high, water was often added to it before application to the substrate. After evaporation of the water, which left the particles sticked to the adhesive layer, the sample was postbaked at 75 deg C during 30 minutes. SEM images of the samples were finally taken as a reference for the AFM measurements. Therefore, a few tens of nanometers of gold were sometimes deposited by flash-sputtering on the samples in order to avoid charging effects when imaging them.

Results. Figure 4.8.a) shows an SEM image of a sample covered by a gold layer. Small clusters of microbeads were dispersed on the surface. Most of the beads had a diameter of one micrometer, but smaller particles were also visible. Surface pleats were also observed in the vicinity of the microbeads, and were probably due to deformation of the adhesive layer during the gold sputtering. Figure 4.8.b) represents an AFM image of three microbeads grouped in a cluster. First, the pleats observed under SEM were also present in the AFM image. Second, the observed size of the particles was too large. Hence, according to the reference circle given in image b), the diameter of the beads was about 1.5 micrometers on the AFM image, which was 50% more than the true diameter. However, this overestimation of the size was expected, as we will see in 4.6.2. Due to the orientation and the shape of the Famars tip, the diameter of spherical particles is overestimated with at least 40% in the better case.

Another sample was prepared, without any deposition of gold at the end. Some charging effects were therefore observed when measur-

[2]Norland Products, Inc. Cranbury, NJ, USA

ing it by SEM, but pleats were no longer present at the substrate's surface. Figure 4.9.a) shows an SEM image of one of these samples, showing a single-layer structure of 1-μm polystyrene beads. On a large part of the sample, the microbeads were grouped in such structures, and measurements performed by means of Famars reproduced these features, as illustrated in 4.9.b). While the particles located on the borders were enlarged by tip artifacts, it was possible to estimate the diameter of the particle to a value of 0.90$\pm$0.15μm, using the structure periodicity.

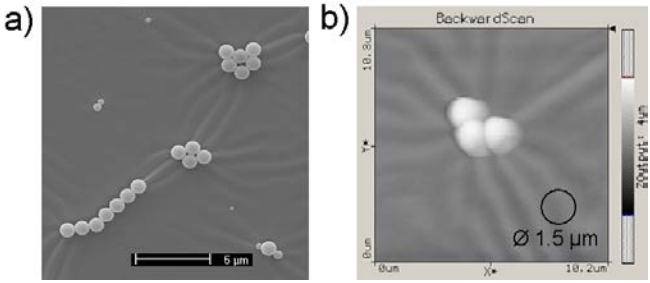

Figure 4.8: a) SEM image of 1-μm polystyrene clusters (gold coated). b) AFM image of a cluster of three microbeads. In both images, pleats are visible at the substrate's surface.

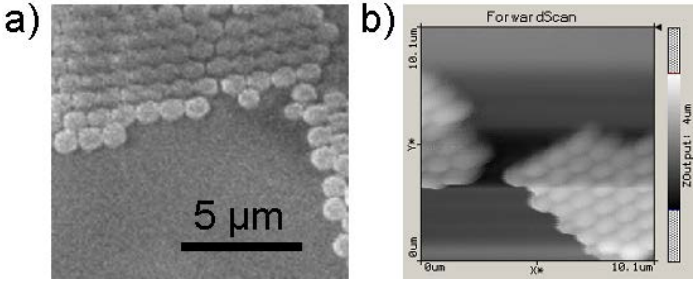

Figure 4.9: a) SEM image of 1-μm polystyrene beads grouped in single-layer structures. b) AFM image of the same substrate.

In addition, AFM images of 1-μm polystyrene beads were taken at locations were they were more dispersed. Figure 4.10 shows an AFM image of isolated and clustered microbeads, recorded for the forward and backward scans. The scan speed was 5.7 μm/s, using usual values for the feedback loop parameters. As it can be seen, the particles' shapes were different for each scan direction. This indicates that the feedback loop was not sufficiently fast to adapt the height of the AFM tip during scanning. The problem can be solved either by increasing the gains of the feedback loop, or by reducing the scan speed. As increasing the gains could lead to ringing, a reduction of the scan speed is preferred for measurements on Mars, as the feedback loop can not be adjusted in real time. In addition, this illustrates the importance of recording the image for both scan directions. If only one of them is recorded, distortions can be misinterpreted as the real shape of the particles or as tip artifacts.

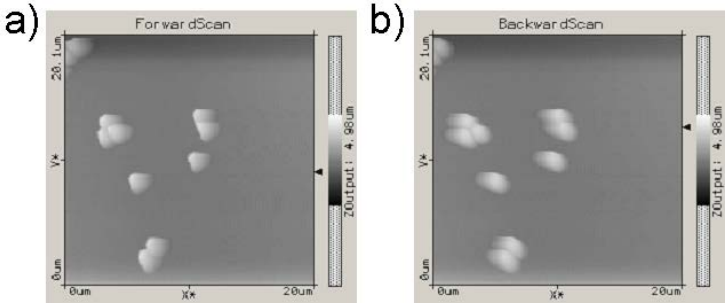

Figure 4.10: AFM image of 1-μm polystyrene microbeads recorded in a) forward and b) backward directions.

Silica microbeads

Monodispersed silica beads[3] having a specified diameter of 0.45±0.03μm were also measured. They were also delivered in an aqueous suspen-

[3]Silica Microspheres, Polysciences, Inc. Warrington, PA, USA

sion, and the sample preparation was identical to the one used for the polystyrene particles. In order to avoid the formation of pleats in the substrate, the sample were imaged by SEM without gold sputtering.

Results. Figure 4.11.a) shows an SEM image of a prepared sample. While most of the particles had the specified diameter, a few of them were smaller. This was confirmed by AFM images of the sample, as shown in figure 4.11.b).

A study of the size distribution was performed by measuring and counting the particles in a 42 x 32 μm SEM image of the substrate. The particles could be ordered in two classes: the large particles, having a diameter of 450±50nm, and the small ones, having a diameter of 150±50nm. In the SEM image, 185 large particles were counted, for only 48 small particles. This corresponded to 0.137±0.001 and 0.036±0.003 particles per micrometer square, respectively.

A similar study was conducted for the AFM image 4.11.b). As the particles were not spherical due to tip artifacts, a "mean" diameter was calculated for each particle by averaging the smallest and the largest lateral dimensions. As for the SEM image, two size classes were observed. For a value of 750±100nm, 52 particles were counted, and for a value of 350±100nm, only 10 particles were counted. By dividing these results by the area of the AFM image, one obtained 0.131±0.010 and 0.025±0.013 particles per micrometer square, respectively. Figure 4.12 compares the size distributions per unit area determined based on the SEM image and the AFM image.

The first important result was the ability of Famars to identify the two kinds of particles dispersed on the substrate. In addition, the numbers of particles per unit area for the two sizes of particles were close to those found by SEM. However, the size for the large and the small particles were about 1.7 times and 2.3 times larger than those determined by SEM, respectively. These differences were mostly generated by tip artifacts, as it has already been noticed for image 4.8.b). In addition, the fact that the relative increase in size was larger for the smaller particles is typically the signature of a tip

blunt at its very end. Algorithms correcting the tip artifacts can be used to find more realistic values for the diameters of the particles, but they could unfortunately not be applied in this case since no image of the tip characterizer sample was taken before imaging the substrate.

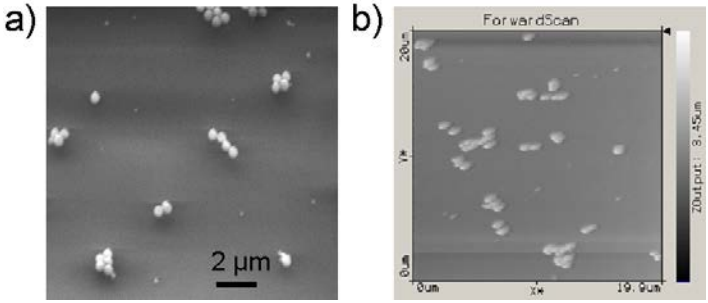

Figure 4.11: a) SEM image of the 0.45-μm silica beads. b) AFM image taken at a location close to the one imaged by SEM. On both images, one distinguished particles with a diameter smaller than the specified 0.45 micrometers.

When imaging particles, having the possibility of zooming in the regions of interest is critical. This was possible with Famars, as illustrated in figure 4.13. After having taken a 15-μm image of a group of silica microbeads, shown in a), a zoom was needed in order to characterize more precisely the microbeads located at the bottom of the image. The center of the next image was specified using an x-offset of +1.5 μm and a y-offset of -5 μm, which corresponded to the reference position indicated in a). Image b) shows the AFM image resulting from the zooming. The cluster of four silica microbeads is more visible. This functionality was used very often when measuring particles. In the FSW, a routine called autozoom was implemented to zoom automatically in the areas of interest, but its efficiency was not demonstrated (see 3.3).

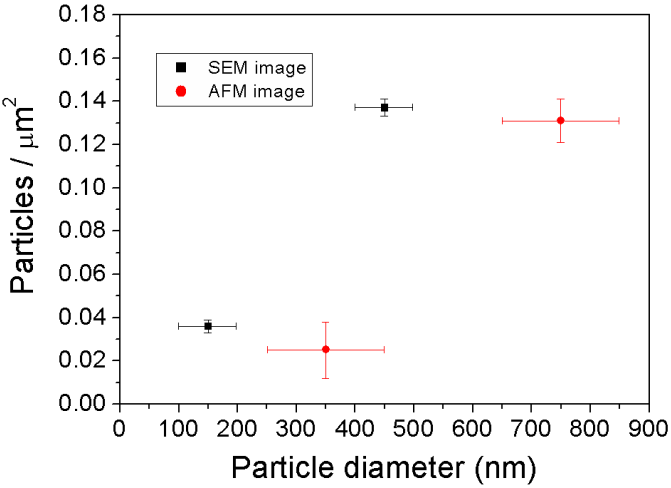

Figure 4.12: Size distributions determined using AFM and SEM images.

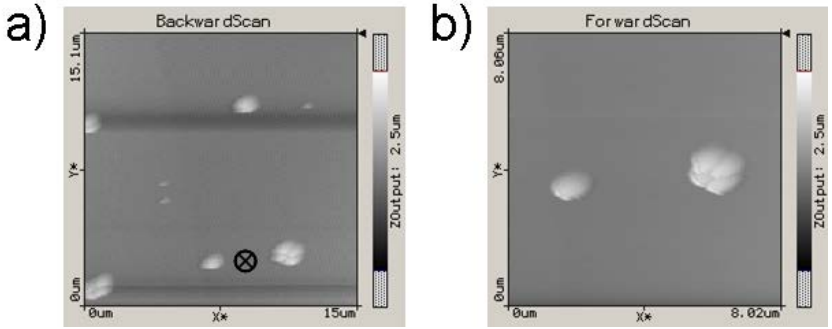

Figure 4.13: a) AFM image showing several silica microbeads. b) Zoom centered on the position specified by ⊗ in image a).

Silica nanobeads

This sample had already been prepared for characterizing a standard AFM at the IMT, and consisted in silica nanobeads fixed on a glass substrate. These nanobeads were really monodispersed, and had a diameter of 100nm.

Results. The silica nanobeads were measured as they had a size corresponding to the resolution requirement for Famars. In addition, the experiment would show whether the instrument was able to determine their shape. Figure 4.14.a) shows an AFM image of these nanobeads taken with a standard AFM[4], while figure 4.14.b) shows the same substrate imaged by the Famars instrument. Even though the standard AFM provided a more precise image of the substrate, the nanobeads could be distinguished on the Famars image as well. The size and the spherical shape of the particles was also visible, especially on the three-dimensional view obtained by importing the data in Matlab (see figure 4.15). Note that this view showed the data before any processing.

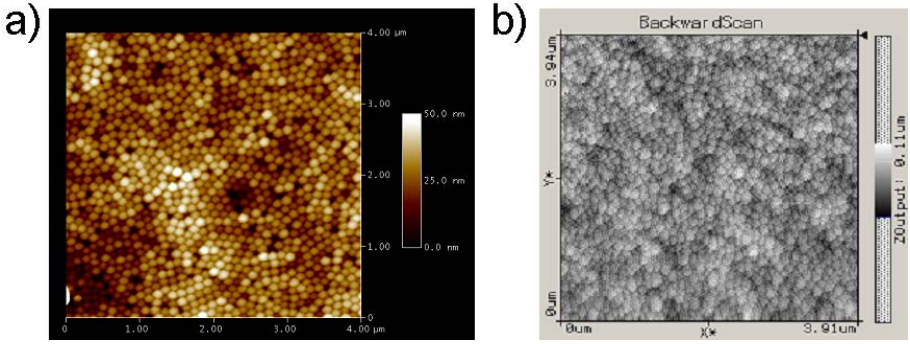

Figure 4.14: Four-micrometer AFM images of silica nanobeads taken in dynamic mode a) by a standard AFM, b) by Famars.

[4]Veeco NanoScope IV MultiMode AFM

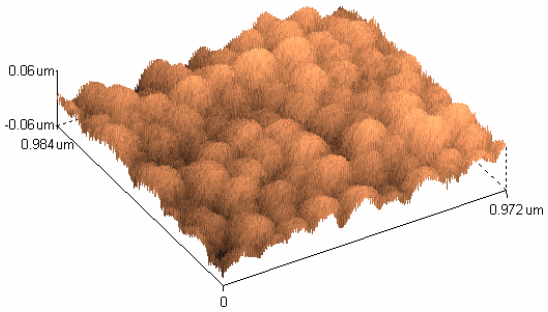

Figure 4.15: Three-dimensional view of the silica nanobeads imaged by Famars.

Nanocubes

As Famars should detect eventual edges in the shape of the measured particles, a sample presenting small cubic particles was prepared.

Sample preparation. The preparation of this sample was based on the precipitation of iron oxide particles when etching silicon wafers in a KOH solution [2]. The amount of deposited material is independent of the etching time, but varies with the dopant type and concentration. The size of these cubic particles ranges from one to several hundreds of nanometers.

Experiments were performed at the IMT by etching n-doped silicon wafers in a 40 % KOH solution. Cubic particles precipitated, showing a very good adhesion to the silicon surface. This property of the contaminants was well-known, as a bath of HCL is needed in standard processes to detach them from the wafers. It was, however, an advantage for our application, as no adhesion layer had to be deposited to fix the particles. Thus, a simple rinsing in deionized water was performed. Note also that the wafers were only immersed in the KOH solution during a couple of minutes. That way, the increase of roughness of the Si surface was limited.

Figue 4.16 shows three SEM images of the silicon surface after

immersion in the KOH solution and rinsing, and showing cubic iron oxide particles. The size of most of them was close to 190nm, as shown in b), while a few were larger, up to a size of 1 μm. The cube in image c) had a side of 500nm, and presented an irregular excrescence.

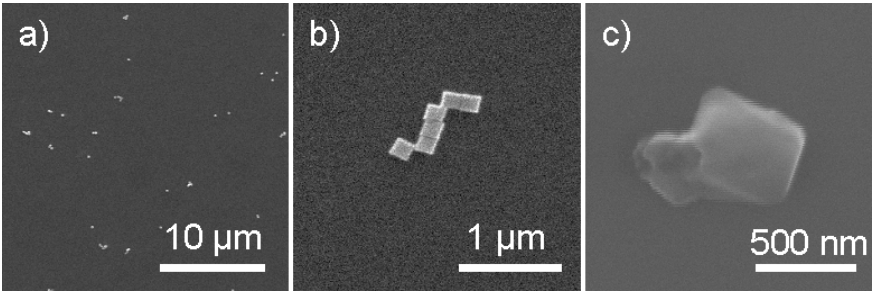

Figure 4.16: SEM images of iron oxide particles with cubic shape deposited on a silicon surface in a KOH solution. a) General distribution. b) Cluster of six 190-nm particles. c) Large view of a 500-nm cube showing an irregular feature in one corner.

Results. Figure 4.17.a) shows an AFM image of the sample imaged by SEM. As expected, many contamination particles were observed at its surface. Figure 4.17.b) is a zoomed image of one of them, and revealed a particle with two orthogonal angles on the lower part and a less defined outline on the upper part. Using the two orthogonal edges, the outline of a square was superimposed to the shape of the particle in image c). The size of this square was 270nm. If the measured particle was a 190nm square, which was certainly the case, the increase of size corresponded 42% of the real value (a square of 190nm is given as a reference in image c) for comparison). This size amplification was in accordance with a first estimation of the tip artifacts for Famars. Concerning the feature which was not included in the 270-nm square, it was certainly a feature comparable to the one observed in figure 4.16.c. However, it seemed that the structure imaged

by AFM was more angular, being perhaps a smaller nanocube. An inspection of the AFM tip after these measurements proved at least that this shape had not been generated by a contaminant attached to the tip.

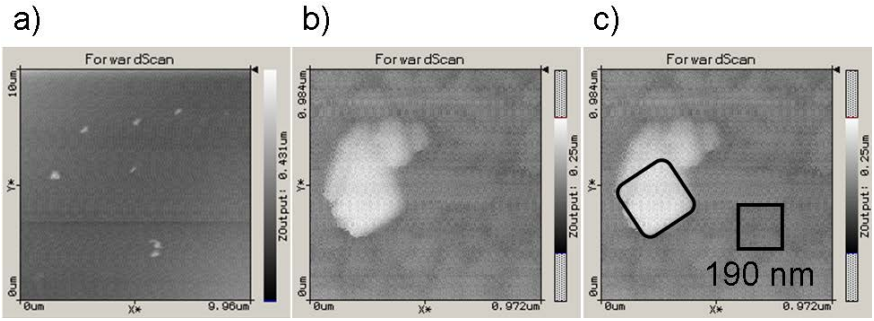

Figure 4.17: AFM images of the oxide iron nanocubes. a) 10-μm image, showing a few particles. b) 1-μm image of an iron oxide particle, with a smaller feature visible next to it. c) Comparison between the size of the measured particle and a reference square of 190 nm.

Lake sediments

The last experiment on fixed particles was performed on a testbed at JPL. The goal was to measure a sample showing a high dynamic range in the z-direction. A sample was prepared by C. Mogensen, member of the MECA team, and placed on the sample wheel in front of the AFM. The sample consisted of lake sedimental particles having a diameter smaller than 100 μm. The particles were poured on a thin sheet of stainless steel onto which a thin layer of Cyanolit (glue based on cyanoacrylate) was applied first. The particles which were not fixed to the sheet by the glue were then removed.

Results. As the substrate could potentially be harmful for the AFM chip, an optical control was performed when approaching the

substrate toward the sensor tip. This allowed accessing a safe region and imaging it. Figure 4.18 shows the obtained AFM image of a large particle in the center and a few smaller ones. The maximal and minimal lateral dimensions of the particle were about 10 and 6 μm, and the height was about 5 μm. Even if the sensor tip was not very sharp, the coarse shape of this particle was determined, facets and edges being visible. Note that the derivative view can give more information about the shape than the standard raw view.

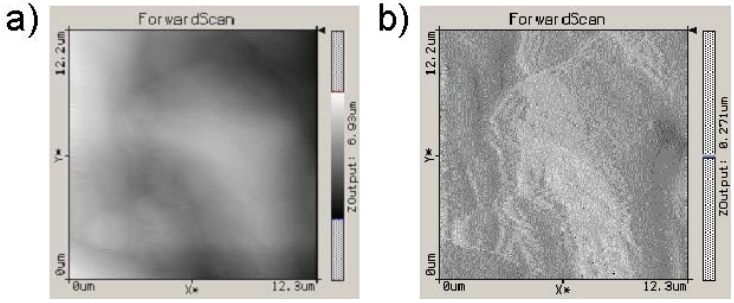

Figure 4.18: AFM image of a sedimental particle represented in a) raw and b) derivative views. Other smaller particles are visible on the lower left and on the top of the image.

Summary

Measurements performed on fixed particles demonstrated that the Famars instrument could measure particles in a size range comprised between 0.1 and 5 microns. However, the lateral dimensions of the particles were systematically overestimated, mainly due to tip artifacts. In addition to these artifacts, the size of the recorded features could be influenced by the feedback loop settings, as shown in figure 4.10. Thus, it was very important to check that images recorded in forward and backward directions produced the same features.

Tip artifacts also played a role in the ability of Famars to recognize the shape of the measured particles. While the spherical shape of

the polystyrene beads was in general detected, deformations caused by the shape of the AFM tip were observed for the smaller silica beads. The difficulty of imaging the coarse shape of these small particles probably indicated that the very end of the sensor tip was blunt. However, when the tip was intact, very fine details could be observed. When imaging the tiny iron oxide particles, their edges and orthogonal angles were distinguished successfully. The shape of a large sedimental particle was also determined.

Finally, the size distribution of silica beads was determined according to an AFM image, and produced results close to a similar study performed on a large SEM image, the main difference coming from the size overestimation. This showed that the AFM could differentiate between two kinds of particles showing very small sizes. Further studies should be performed on samples showing a broader range of particle sizes.

4.4.2 Loose particles

Imaging loose particles is difficult, as they can be moved by the AFM sensor tip. As the sample is in a vertical position, a particle stays in place if its adhesion momentum is larger than the total momentum created by the gravitational force and the lateral force applied by the AFM tip, the latter being certainly dominant. In these experiments, lateral forces were minimized by using dynamic mode, but the adhesion of the particles was not enhanced by any method. The measured samples consisted of a flat silicon substrate, on which different geological samples were deposited. Before the deposition, the substrates and the particles were dried during two days in a vacuum oven at 200 deg C, as humidity could increase the adhesion between the particles and the silicon substrate. After that, they were placed in a glove box under vacuum and low humidity conditions, where the particles were poured on the substrates. By doing that, it was noticed that many electrostatic forces were acting on the particles.

In order to simulate the effect of the scraper installed above the

sample wheel of MECA, a blade was slid on two 200-μm glass plates located on both sides of the substrate. Finally, the samples were transferred from the glove box to an environmental vacuum chamber, where AFM measurements were performed under a low pressure nitrogen atmosphere.

The prepared samples and the results of the AFM measurements are described hereafter. An optical image showing the general aspect of the sample is given, as images of the OM will be consulted during operations on Mars before starting (or not) AFM measurements.

Satlen Skov particles

The first sample was covered with particles from Salten Skov, a Danish forest whose soil is rich in iron oxides, being therefore often used as a martian dust analogue [3]. Note that the sizes of the particles of our sample were larger than the expected size of martian dust particles. Figure 4.19 is an optical image of the prepared sample, showing large particles of about two hundreds micrometers. Thus, imaging this sample by AFM was really challenging.

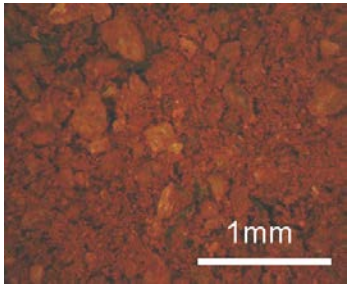

Figure 4.19: Optical image of the sample with particles from Salten Skov.

The first problem was to establish the contact between the sample and the sensor tip. When the sample was approached toward the AFM sensor tip, the cantilever could enter in contact with the

sample before the tip, as the dimensions of the particles were larger than the height of the sensor tip. The next cantilevers or tips could even touched the surface before the active sensor, for similar reasons. Thus, this resulted in a large contamination, illustrated in figure 4.20. In addition, contact with the sample was sometimes lost immediately, as the loose particle hit by the tip was displaced. In other cases, the contact was similarly lost during the scan.

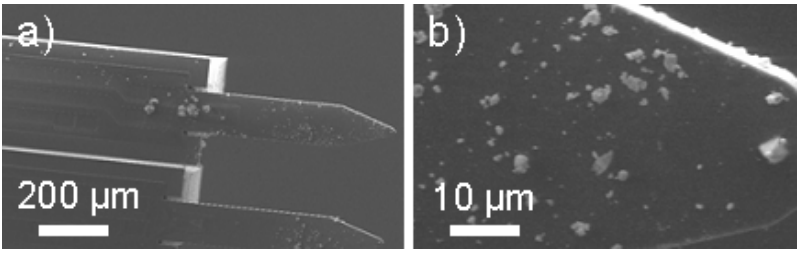

Figure 4.20: a) SEM image of the contamination on the first and the second cantilevers after measurements of the Salten Skov particles. b) Larger view of the first cantilever. The sensor tip is visible on the right.

Despite these problems, a few images of this substrate were taken, as illustrated in figure 4.21. First, one distinguished some smooth surfaces on both images. As the substrate was hidden under the particles, these surfaces were interpreted as portions of large particles. This hypothesis was confirmed by the fact that the scan plane had to be tilted with more than 20 degrees in some cases, as the surface of the particle was not perpendicular to the AFM tip. Second, many horizontal lines were seen on the images. These lines corresponded to large "jumps" in the vertical range, probably caused by the motion of the particles pushed by the tip. In addition, the scanrange had to be small, or the contact with the measured particle was lost. Some small particles could be observed, but only a few of them were imaged entirely. In addition, as the scan slopes were very large, their size was certainly overestimated by a large factor.

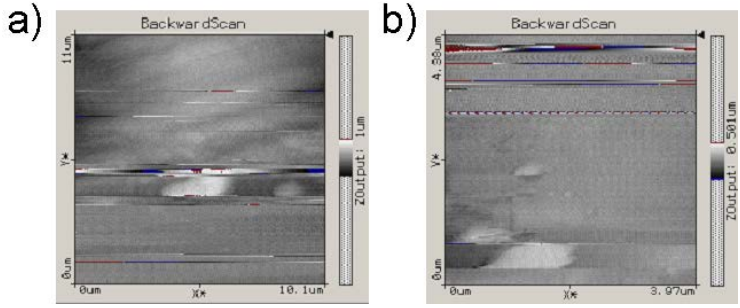

Figure 4.21: AFM images of the Salten Skov particles taken with a scanrange of about 4 μm (a) and 10 μm (b). The slopes used to take these images were a) x-slope=0 deg, y-slope=-25 deg and b) x-slope=-6 deg, y-slope=-18 deg. Image a) was recorded from top to bottom and image b) from bottom to top.

In summary, imaging this sample required a lot of attempts and adjustments, which could not be implemented for a Mars mission. In addition, using the safest scan parameters has not always produced a satisfying image, due to the motion of the loose particles. Finally, contamination of several cantilevers was observed during these measurements.

Riverside nontronite

As Riverside nontronite is an iron-rich clay which should be an important component of the martian surface soil [4], a sample was prepared using this material, as illustrated in figure 4.22. The sizes of the particles was smaller than a few tens of micrometers, and the silicon surface could be seen at certain locations. The sizes of the particles were still enormous for atomic force microscopy, but the fact that the substrate was reachable at some locations was an advantage compared to the Salten Skov sample. A few images were taken, as illustrated in figure 4.23. As the background of the image was the silicon substrate, the slope corrections were less than ten degrees for both axes.

The scanranges of the images were still small, but some interesting features were imaged. Some particles were completely imaged, and some edges were visible. However, a scientific interpretation of the data was difficult, mainly because some information on the context was missing. Note that the top of image 4.23.a) shows two times the same features, which indicated that the relative position of the tip and the sample has been changed during the scan.

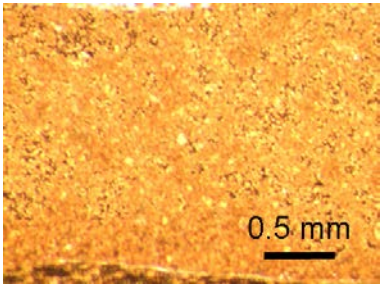

Figure 4.22: Optical image of the Riverside nontronite sample.

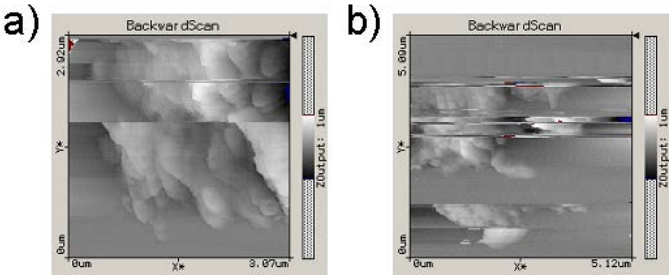

Figure 4.23: AFM images of the Riverside nontronite particles taken with a scanrange of about 3 μm (a) and 5 μm (b). The slopes used to take these two images were x-slope=-3 deg and y-slope=-7 deg. The two images were scanned from bottom to top.

Crushed basalt particles

This sample was composed of crushed basalt particles, which is another material expected on Mars [5, 6]. Figure 4.24 shows an optical image of this sample. The particles coverage was much smaller than for the previous samples. Therefore, this sample was more adapted to AFM measurements, and relevant images were taken. Figure 4.25 show two AFM images displayed in raw and derivative views. In the upper right corner of image a), a particle with sharp edges is discernible. In the raw view (b), particles imaged and/or pushed by the probe are visible. In image c), many small particles are visible. Since the same feature is repeated several times, it is defined by tip artifacts, and the real size of the particles is smaller. In the center of this image, a particle was pushed by the sensor tip. This is more clear when looking at the raw view (d). At the bottom of this image, a portion of a particle (or a cluster) of several micrometers is observable.

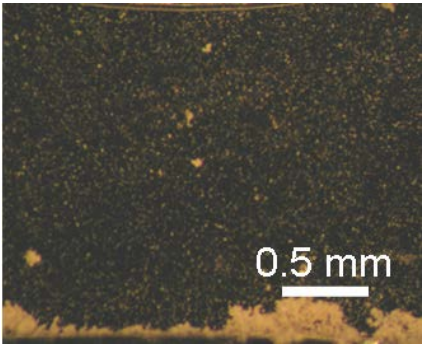

Figure 4.24: Optical image of the basalt particles sample. The large amount of particles at the bottom were accumulated when the sample was placed in a vertical position for AFM measurements.

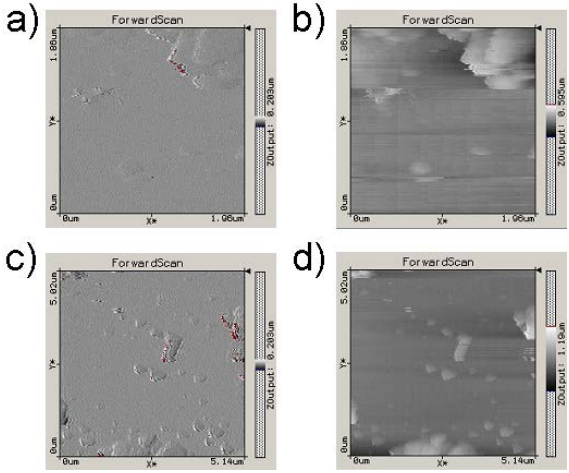

Figure 4.25: AFM image of the crushed basalt particles taken with a scan range of 2 μm (a: derivative, b: raw) and a scan range of 5 μm (c: derivative, d: raw). Both images were taken from bottom to top.

In summary, AFM measurements of this sample has produced valuable information on the particles. Their size could theoretically be determined, on the condition to correct tip artifacts. The shape of the particles showed sharp edges, probably caused by the crushing process. The main advantage of this sample was that the particles were not in pile, but were in contact with the silicon substrate. Based on macroscopic observations, electrostatic forces played certainly a major role in the adhesion of the particles to the substrate.

Summary

According to these first measurements, measuring loose particles was possible. However, certain conditions had to be fulfilled. First, the size of the particles should not have be larger than a few micrometers, as it increased the risk of touching the sample with another part than the sensor tip. Second, piles of particles had to be avoided, as the

particles at the top were too easily moved by the AFM tip. When the particles were directly in contact with the substrate, AFM images could be repeatedly taken. Note that one could have guess by looking at the optical images which substrates were the more appropriate for AFM measurements.

For the operations on Mars, the first consequence is that one should probably not try to image a sample whose substrate is completely covered by particles, as it could probably happen with the magnetic substrates, described in (4.5.1). The information on the particle coverage should be given by an optical image of the sample taken by the OM two martian sols before the AFM measurements. The next condition is of course to have a good adhesion between the particles and the substrate. In order to satisfy this condition, different kind of substrates will be imaged on Mars. Preliminary measurements of these substrates are described in 4.5.

4.5 Measurements of the SWTS substrates

As it is described in 1.3.2, a set of six substrates is exposed for each sample acquisition. Except for the two microbuckets substrates, not intended for atomic force microscopy, preliminary measurements were performed at the IMT on these substrates to determine if they could be imaged by the Famars instrument.

4.5.1 Magnets

Two kinds of magnetic substrates were designed and fabricated at the University of Copenhagen to attract magnetic particles from dust samples [7]. They show two different magnetic field strengths, and are therefore referred to as "weak" and "strong" magnet substrates. In addition to catching magnetic particles, scientific information could be obtained by observing the differences between the distributions of particles on magnetic and non-magnetic substrates. The magnets are not in direct contact with the particles, but are inserted in housing

structures which can be mounted on the sample wheel. The housing structures are in aluminum, and the surface exposed to samples was polished. Figure 4.26 shows the surface of the weak and strong magnet substrates. The magnets themselves were behind the surface, at a distance of 0.20 mm for the strong magnet and 0.75 mm for the weak magnet. Since the Famars scanner is based on electromagnetic actuation, a possible influence of the magnetic substrates on the behavior of Famars was studied. In order to do that, AFM measurements of the surfaces of these substrates were performed.

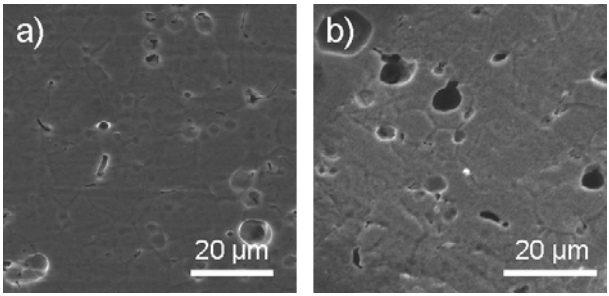

Figure 4.26: SEM image of the aluminum surface of the weak (a) and the strong (b) magnet substrates. On both images, holes in the aluminum and lines left by polishing are visible.

AFM images of both substrates were successfully taken. Figure 4.27 shows two AFM images of the strong magnet substrate taken at the same location with two different scan ranges. The scanner behavior was not disturbed by the magnetic field of the strong magnet. This result was expected, as the magnetic field of the magnet was not in the direction of the AFM scanner. In addition, the features observed in the SEM images were reproduced in the AFM images. In image b), one can also see that three dust particles were detected by Famars. One of them was completely imaged, while the others were detached by the sensor tip after a few lines of scan. However, as the origin and the composition of these particles were not known, it was satisfying to see that images of particles could be taken.

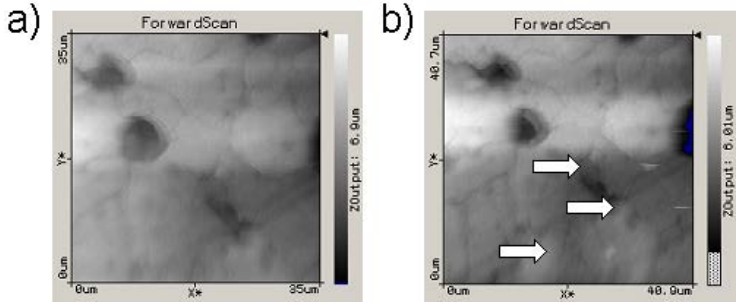

Figure 4.27: AFM images of the strong magnet substrate, taken with scanranges of 35 μm (a) and 40 μm (b). Diagonal trenches due to polishing are visible on both images, as well as the grain structure of the material. In image b), the arrows indicate the emplacements of particles imaged and/or pushed by the AFM tip.

After having demonstrated that Famars could take images of the magnetic substrates, end-to-end tests were realized by our partners at Imperial College, which simulated the delivery of samples to the sample wheel, either by means of the RA or by air fall experiments. These tests showed that samples delivered by the RA could result in piles of several hundreds of micrometers on the magnet substrates. In that case, trying to measure these substrates could damage the Famars chip, as it is explained in 4.4. However, for samples produced by air fall experiments, a few small particles were deposited on the magnetic substrates. Thus, the substrates were suitable for AFM measurements and images of particles were successfully taken.

4.5.2 Micromachined silicon substrate

The micromachined silicon substrate was designed and fabricated by our partners [8]. Using DRIE, small patterns were created in a silicon bulk to trap and sort dust particles. These patterns consist of arrays of pits or pillars with different lateral dimensions. Their height or

depth was given by the DRIE process and was close to 5 micrometers.

One substrate was delivered to the IMT, and AFM imaging of the pits showing the highest aspect ratio were performed. Figure 4.28 shows an SEM image of these 5-μm pits. The crescent-shaped pits indicate the lateral position on the substrate, depending on their orientation. AFM images of the pits were taken successfully, as shown in figure 4.29. The marks for the alignment were visible, and allow finding the lateral position of the tip on the substrate. However, the depth of the pits was smaller than expected, being close to 4 micrometers. According to a first estimation of the artifacts caused by the AFM tip (see 4.6.2), Famars should be able to reach the bottom of circular holes having an aspect ratio smaller than 1.5. As the aspect ratio was close to one for the 5-μm, it should have measured the real depth of the pits. Thus, an inspection of the tip was performed by SEM, and it revealed that half of it had previously been broken, which explained the observed artifacts.

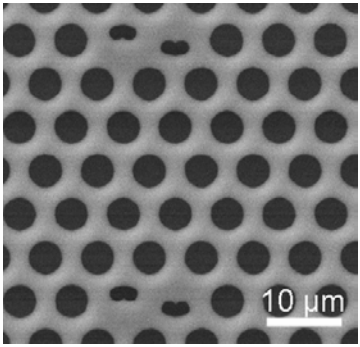

Figure 4.28: SEM image of the microfabricated "5-μm pits" substrate. The crescent-shaped pits correspond to a code for the location on the substrate. Courtesy Imperial College.

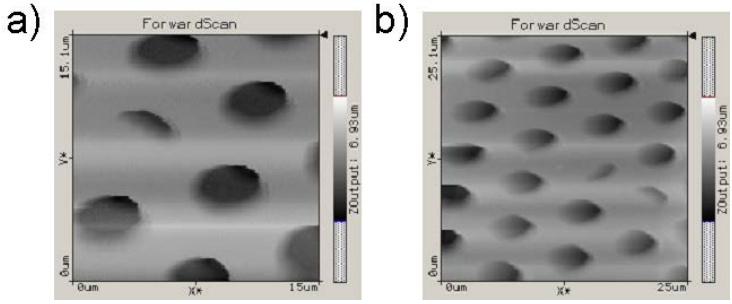

Figure 4.29: AFM images of the microfabricated "5-μm pits" substrate taken with scanranges of 15 μm (a) and 25 μm (b). The orientation of the crescent-shaped pits was clearly visible.

This experiment indicated that the 5-μm pits can be used to estimate the shape of the tip. While the tip characterizer substrate (see figure 4.5.b) can be used to estimated the very apex of the tip, it does not allow determining the general shape of the tip, since the sharp silicon tips of that substrate are smaller than one micrometer. This missing information can therefore be obtained by measuring this sample, which is sufficiently deep to allow characterizing a large part of the tip.

Finally, as the particle caught in those pits during operations should have an aspect ratio close to one, the bottom of the pits is certainly not the most interesting part of the image, as it was confirmed by images taken at Imperial College.

4.5.3 Silicone substrate

This substrate is simply composed of a piece of silicone, which should be sufficiently sticky to keep the particles in place during AFM measurements. In order to check that, 0.5-μm silica beads were deposited on it following the same procedure as when depositing the particles on the UV-cure adhesive layer (see 4.4.1). A very dense repartition of the beads was observed, similar to the one observed for the polystyrene

on the adhesive layer (see figure 4.9). Figure 4.30 shows an AFM image of the silicone substrate covered by the silica nanobeads. While the distortions due to a blunt tip were large, it seemed that no particles were detached from the silicone, which proved the efficiency of this substrate in catching particles. However, the substrate was not tested at low temperature, at which the properties of the silicone can change.

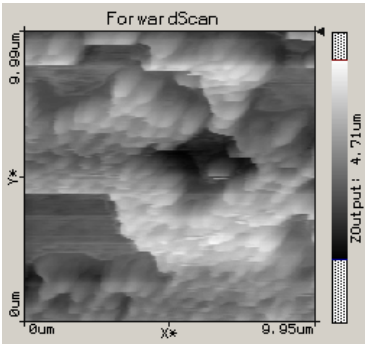

Figure 4.30: AFM image of 0.5-μm silica beads dispersed on the silicone substrate.

4.6 Image processing

Image processing tools were created for correcting two different kinds of artifacts present in AFM images. First, AFM images could be stretched, shrunk, or distorted due to the properties of the scanner, as described in 4.3. Secondly, the shape and the orientation of the tip influences the size and the shape of the measured features. Using AFM images of known samples, we were able to estimate these artifacts, and then correct AFM images of unknown samples, assuming that they had been taken in the same conditions. As the data coming from Mars will be stored and handled in Matlab by the MECA team, the correction algorithms were implemented in this program.

4.6.1 Correction of the distortion

For small displacements, the motion of the scanner is considered to be linear. However, due to the scanning principle described in 2.3.2, the AFM tip follows curved trajectories, resulting in a paraboloid-like scan plane. In addition, the internal properties of the scanner lead to nonlinear distortions of the image. This chapter describes the methods used to correct these distortions, and gives some examples of their application.

Theory

An AFM image is a three-dimensional map of a surface. Thus, if an image consists of n points, distortion can be seen as the deviation from the ideal positions (x_i, y_i, z_i), to the positions $(x_i + \Delta x_i, y_i + \Delta y_i, z_i + \Delta z_i)$, for i = 1 to n.

Thus, the correction matrices $\Delta X = [\Delta x_i]$, $\Delta Y = [\Delta y_i]$ and $\Delta Z = [\Delta z_i]$ have to be determined, based on an AFM image of a reference sample, in general a grid. In order to do that, matching between n points of the AFM image (typically the intersections of the grid) and the corresponding points on the reference sample is performed.

Knowing the correction matrices, a 3D transformation which sends the n points of the AFM image to those of the reference sample is determined. An unwrapped AFM image is then obtained by interpolation, applying the transformation to all points of the AFM image. Finally, this transformation can be used to correct any AFM image taken with the same scan parameters. Thus, AFM imaging of a reference sample should always precede imaging of unknown samples, such as martian soil samples.

However, the matching of the points as well as the determination of the transformation was difficult to implement for a three-dimensional problem. Thus, the problem was split in two. First, we determined a transformation correcting the distortion in height, and then a 2D transformation correcting the distortions in the xy-plane.

A mathematical justification is possible if both operations are linear, but as it was in general not the case, we justified this simplification by the quality of the obtained results. Figure 4.31 illustrates an example showing that the order of applications of the algorithms has a small influence on the resulting image.

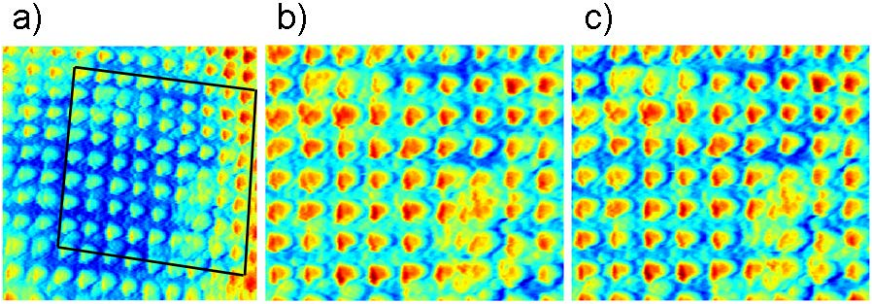

Figure 4.31: a) AFM image of the tip characterizer substrate imported in Matlab. The quadrilateral corresponds to the corrected images shown in b) and c). b) Obtained image after having corrected the height distortion, and then the xy distortion. c) Obtained image after having corrected the xy distortion, and then the height distortion.

Distortion in height. After having performed an AFM image of a reference sample, the distortion in height was corrected. Two different methods were studied.

For the first one, all points of the AFM image were interpolated by a 2D polynomial, whose degree M was generally equal to 2, 3 or 4. By considering the variations in height of the samples relatively small compared to the distortion, this polynomial could be seen as the distortion of the AFM image. Thus, by subtracting the polynomial from the AFM image, we could obtained a flatten image of the reference sample. The polynomial could also be used to flatten any other AFM image taken with the same scanning parameters. This

2D polynomial, given by

$$P(x,y) = \sum_{i=1}^{M} \sum_{j=1}^{M} a_{ij}\ x^{i-1} y^{j-1}, \tag{4.1}$$

can be determined using the least squares method [9]. For an image having K lines and L columns, its coefficients a_{ij} are given by

$$A = [a_{ij}] = (V_x^T V_x)^{-1} V_x^T\ \Delta Z\ V_y (V_y^T V_y)^{-1}, \tag{4.2}$$

where ΔZ is the KxL correction matrix, and V_x and V_y are KxK and LxL Vandermonde matrices, respectively. As the reference sample is considered to be at $z = 0$, the components of ΔZ are the heights of the KxL points.

The Vandermonde matrix V_x is given by

$$V_x = \begin{pmatrix} 1 & x_1 & x_1^2 & ... & x_1^M \\ 1 & x_2 & x_2^2 & ... & x_2^M \\ ... & ... & ... & ... & ... \\ 1 & x_K & x_K^2 & ... & x_K^M \end{pmatrix}. \tag{4.3}$$

V_y has the same form, except than x is replaced by y, and K by L. Note that as we used the least squares method, K an L are much larger than M.

For the second method, only the points of the AFM image known to be at the same height (on the reference sample) were selected to be interpolated by a 2D polynomial. For example, if the tip characterizer was used (see figure 4.5.b), these points were all located between the sharp tips. As they were not equidistant, the interpolation by means of the least squares method was more complicated to implement. A "pseudo-Vandermonde" matrix was created by the author and allowed to solve the problem. If n points were selected, the coefficients a_{ij} were given in this case by

$$A = [a_{ij}] = (V_{xy}^T V_{xy})^{-1} V_{xy}^T\ \Delta Z, \tag{4.4}$$

where ΔZ is this time a vector with the heights of the n points, and V_{xy} a "pseudo-Vandermonde" matrix given by

$$V_{xy} = \begin{pmatrix} 1 & x_1 & y_1 & x_1^2 & x_1y_1 & y_1^2 & ... & x_1y_1^{M-1} & y_1^M \\ 1 & x_2 & y_2 & x_2^2 & x_2y_2 & y_2^2 & ... & x_2y_2^{M-1} & y_2^M \\ ... & ... & ... & ... & ... & ... & ... & ... & ... \\ 1 & x_n & y_n & x_n^2 & x_ny_n & y_n^2 & ... & x_ny_n^{M-1} & y_n^M \end{pmatrix}. \quad (4.5)$$

These two methods were used to correct the height distortion in AFM images. However, the first one showed better efficiency, probably because a larger number of points was used for the interpolation. For the second method, the selection of the points was critical for obtaining a good interpolation. A large number of points had of course to be selected, but these points had also to be well distributed in the AFM image. In the example given later, the first method was used.

Distortion in the xy-plane. The distortion in the scan plane was corrected by matching n points of the reference AFM image with the corresponding points on a reference sample. This points were typically the intersections of a grid, but could also be the centers of the sharp silicon tips if the tip characterizer sample was the reference. This task could be performed easily using a Matlab GUI called the "Control Points Selection" tool.

Once the n pairs of points were obtained, the spatial transformation which sends the n points of the AFM image to those of the reference sample was determined, using the Matlab function "cp2tform". This function allowed choosing the type of the obtained transformation, for example linear, projective or polynomial. Since the distortions to be corrected were nonlinear, a polynomial transformation was selected, with a degree equal to 2, 3 or 4. Using this transformation, the AFM image of the reference substrate could be corrected, as well as any AFM image taken with the same scanning parameters. As the period of the reference grid was known, this allowed also calibrating precisely the images.

Note that the theory underlying under the "cp2tform" function is the same as the one used for the correction of the height distortion. The only difference is that the polynomial interpolation is realized for ΔX and ΔY instead of ΔZ. The correction process is however slightly more complicated, as the pixels of the AFM image are moved along x and y directions, while a simple subtraction of the polynomial was performed for the height correction.

Application to an AFM image of a reference sample

On Mars, the reference sample could be either the linear calibration substrate (see figure 4.5) or the tip characterizer substrate (see figure 4.5.b). The advantage of the tip characterizer substrate is that a single AFM image could be used both to correct the scanner artifacts and to estimate the shape of the AFM sensor tip. The calibration grid showed in figure 4.2 was also sometimes used for correcting distortions in images taken at the IMT.

In the example showed hereafter, the reference sample was the tip characterizer. An AFM image of this sample was taken in dynamic mode, shown in figure 4.32.a). The given scanrange was 35 μm, but it is not represented in the image, as calibration has not yet been performed. The columns and the rows of the tip array were curved, and the height of the surface was distorted, the center of the image being lower than the borders.

First, the distortion in height was estimated by interpolating all points of this image with a 2D polynomial. Figure 4.32.b) shows the degree-three polynomial which was obtained. Then, the image was corrected by subtracting this polynomial from the initial AFM image, which resulted in the image 4.32.c). On this corrected image, one can clearly see that a leveling of the whole image was obtained.

Then, the polynomial transformation which corrects the distortion in the xy-plane were determined. First, the positions of the tips on the AFM image were matched with the intersections of an ideal grid having the periodicity of the tip characterizer substrate.

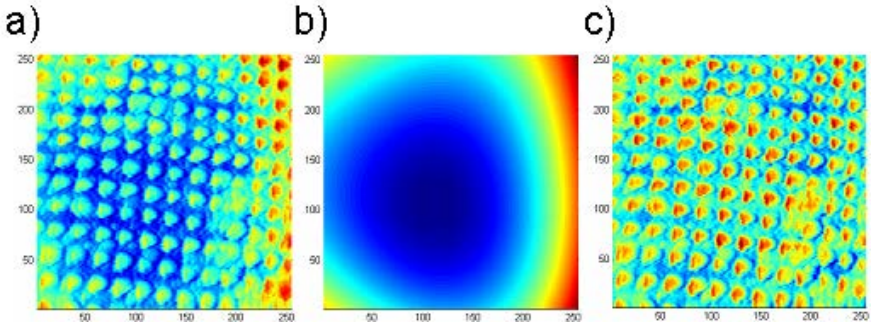

Figure 4.32: a) AFM image of the tip characterizer substrate imported in Matlab. Distortions are visible. b) Bidimensional polynomial determined by interpolation of image a). c) Flatten AFM image obtained by subtracting the polynomial b) from image a).

Then, using the "cp2tform" function, a polynomial transformation was obtained, and used to correct image 4.32.c). Figure 4.33 shows the AFM image after correction of the lateral distortions. Note that the lateral calibration was automatically performed at the same time, the real range of the image being displayed in micrometers. The new orientation of the image depends on the orientation of the ideal grid used for matching.

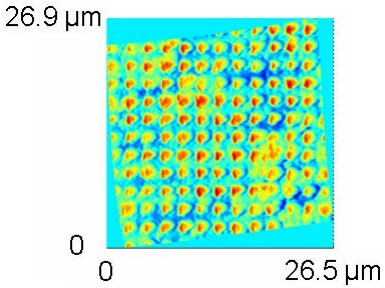

Figure 4.33: AFM image of the tip characterizer after correction of the distortions in height and in the xy-plane.

Application to an AFM image of an unknown sample

Shortly after the AFM image of the tip characterizer sample, an image of the strong magnet substrate (see 4.26) was taken, as shown in 4.34.a). The scanning parameters, were the same, including the scanrange of 35 μm. Thus, the distortion observed in the reference image should be about the same in this image. According to this hypothesis, the height distortion was corrected by subtracting the polynomial shown in 4.32.b) from the initial image of the magnet. The result is illustrated in figure 4.34.b). Finally, lateral distortions were corrected by applying the polynomial transformation found by means of the reference image, which has led to the final image shown in 4.34.c). A qualitative judgment of the result is difficult, as these particular holes at the surface of the magnet substrate were not imaged by means of SEM.

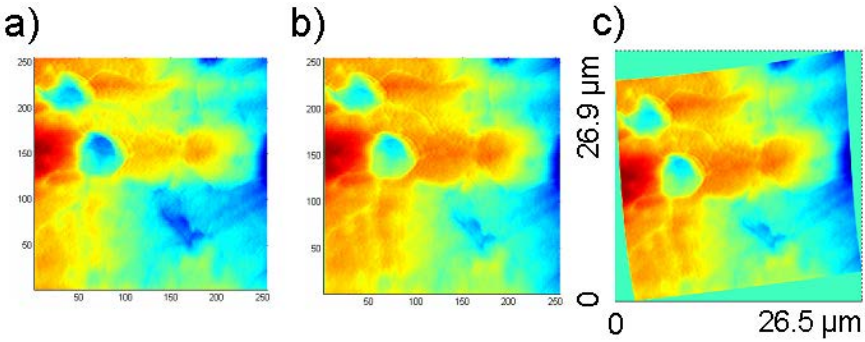

Figure 4.34: a) AFM image of the strong magnet substrate. b) Flatten image obtained by subtracting from a) the polynomial determined by means of the reference substrate. c) Image of the strong magnet substrate after correction of the distortions in height and in the xy-plane.

Summary

The algorithms implemented in Matlab allowed correcting the nonlinear distortions in the AFM images, at least for the observed amount of distortions. Reference images were used for finding the spatial transformations, and these transformations were then applied to AFM images of unknown samples. In parallel to the correction of the distortion, calibration of the images was performed. However, these methods show a few limitations.

Among the technical limitations, the size of the unknown sample image has to be equal to or smaller than the size of the calibration sample image. Otherwise, the spatial transformation determined by means of the reference substrate can only correct the center of the AFM image of the unknown sample. Then, if a lateral offset is used to take one of the two images, one has to incorporate this information in the algorithms. Then, the calibration of the height is only possible if a known step is present in the reference image. In the given example, the height was not calibrated since the tip characterizer substrate is not well adapted for the vertical calibration. According to that, the linear calibration substrate should be more efficient for fully calibrating the images.

Finally, if temperature drift is observed during the measurements, the AFM image could not be corrected using the transformations determined by means of the reference substrate, except if the drift is the same for both images. Thus, temperature will be measured before and after each AFM image. In the future, effect of temperature drift could possibly be implemented in the algorithms.

4.6.2 Correction of the tip artifacts

In addition to the nonlinearities of the scanner, the shape and the orientation of the sensor tip are well-known sources of artifacts [10, 11]. Whereas AFM provides atomic resolution when scanning flat samples, artifacts are introduced when the measured features are sharper than the sensor tip, as illustrated in figure 4.35. On the first hand, if

the sensor tip is much sharper than the sample patterns, the recorded image is a good replica of the specimen surface (a). On the other hand, if the tip is less sharp than the sample patterns, the recorded image presents tip artifacts, i.e. modifications of the shape and the size of the measured objects (b). The typical signature of tip artifacts is a repeated feature in the AFM image. A first approximation of the implication of these artifacts for particles measurement is presented in 4.6.2. Then, a theory describing the AFM image formation from a mathematical point of view is given. Based on this theory, algorithms for correcting tip artifacts were implemented in Matlab, and a few examples of applications to images taken by Famars are presented.

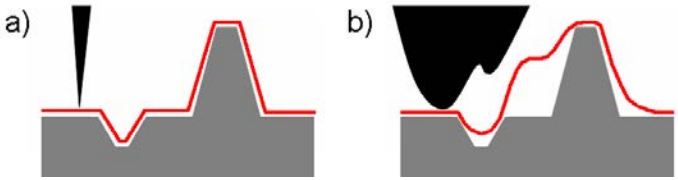

Figure 4.35: Illustration of the effect of the tip geometry on the recorded image. a) If the tip is sharper than the measured features, the AFM image (thick line) gives the exact topography of the sample. b) If is not the case, the size and the shape of the features in the AFM image are modified by the geometry of the tip.

A first approximation

The overestimation of the particle sizes due to tip artifacts can be estimated by considering a simple case, illustrated in figure 4.36. If the tip has an aperture α, and is tilted with an angle β relative to the substrate's normal, measuring a spherical particle having a diameter D leads to a recorded diameter D_{eff} given by

$$D_{eff} = \frac{D/2}{tan(\pi/4 - \alpha/4 + \beta/2)} + \frac{D/2}{tan(\pi/4 - \alpha/4 - \beta/2)} , \qquad (4.6)$$

or

$$D_{eff} = \mu(\alpha, \beta)\ D\ , \tag{4.7}$$

where $\mu(\alpha, \beta)$ is the size amplification factor. Figure 4.37 gives the values of μ for tip apertures equal to 30, 35 and 40 deg, and for a tip orientation varying from 0 to 20 deg. The aperture of the Famars tip is at least 35 deg, and the chip is tilted with two 10-deg angles relative to the substrate. Thus, in the two directions of the 10-degree tilts, the size of a spherical particle is overestimated with at least 40 % by using the Famars instrument.

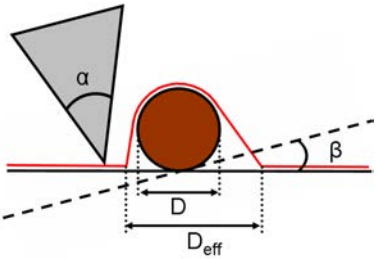

Figure 4.36: Schematic 2D illustration of a sphere being imaged by a tip having an aperture α and being tilted with an angle β.

Another frequent problem is that the AFM tip can not scan the bottom of a hole. Using an approach similar to the one used for a spherical particle, on can show that a tip having an aperture α and a tilt angle β reaches the bottom of a circular hole only if the aspect ratio AR of the hole is smaller than

$$AR_{max} = \frac{1}{tan(\alpha/2 + \beta) + tan(\alpha/2 - \beta)}\ . \tag{4.8}$$

Figure 4.38 gives the values of AR for tip apertures equal to 30, 35 and 40 deg, and for a tip orientation varying from 0 to 20 deg. For Famars, it means that the bottom of any circular hole having an aspect ratio larger than about 1.5 is not reached by the tip. Note that if the aspect ratio is smaller, it means only that *a portion* of the bottom can be imaged, not the whole area.

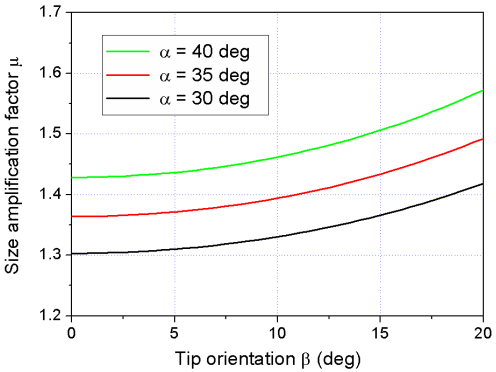

Figure 4.37: Size amplification factor for the diameter of a spherical particle imaged by a tip having an opening α, and tilted with an angle β relative to the substrate's normal.

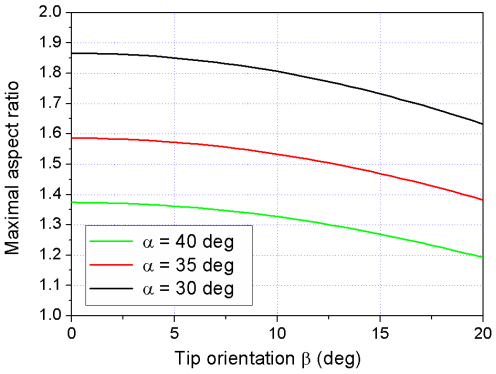

Figure 4.38: Maximal aspect ratio AR_{max} of a circular hole imaged by a tip having an opening α, and tilted with an angle β relative to the substrate's normal. If the aspect ratio is larger, the depth of the hole can not be determined.

Theory

The image obtained by scanning a tip on a sample formally corresponds to a dilation [12]. Considering the tip-surface interaction as this morphological operation, many important pieces of information can be obtained. First, the shape of the AFM tip can be estimated from the AFM image of a "known substrate", applying a morphological operation called erosion. Then, a specimen surface can be reconstructed given its AFM image and the estimation of the AFM tip, applying another erosion process. The reconstructed image is proven to be the best estimation of the specimen surface, but some difference can exist between it and the real surface. The locations were the real image can be different are determined by the algorithms, and displayed in a certainty map.

AFM imaging can be seen as a geometrical problem, the image height being defined as the position of the tip apex when the tip makes contact with the sample surface, at one or more points. Using this definition, it can be shown [12] that the bidimensional function $i(x, y)$ describing the AFM image is given by

$$i(x,y) = \max_{(u,v)} [\ s(x-u, y-v) - t(-u,-v)\ ]\ , \tag{4.9}$$

where $s(x, y)$ is the function defining the sample surface, and $t(x, y)$ the shape of the sensor tip, the apex being at the origin. By defining $p(x, y) = -t(-x, -y)$, which is the reflection of the tip through the origin, one obtains

$$i(x,y) = \max_{(u,v)} [\ s(x-u, y-v) + p(u,v)\ ]\ . \tag{4.10}$$

According to the set theory, $i(x, y)$ is therefore a dilation, which can be written as

$$I = S \oplus P, \tag{4.11}$$

where I, S and P are the sets of which the functions i, s and p are the respective tops, the symbol $\oplus$ designating dilation. This equation

describes the formation of the image knowing the geometries of the tip and the sample. However, we are generally more interested either in estimating the shape of the tip from an AFM image of a known sample surface, or in reconstructing the sample, knowing the shape of the tip. The answers to these two questions are given by another morphological operation, called erosion.

On the first hand, if the shape S of the sample is known, one can obtain an estimation P_r of the tip shape by eroding the AFM image I with S:

$$P_r = I \ominus S, \tag{4.12}$$

which can also be written as

$$p_r(x, y) = \min_{(u,v)} [\ i(x + u, y + v) + s(u, v)\ ]\ , \tag{4.13}$$

where p_r is the top of the set P_r. P_r is an upper bound of the real shape P of the sensor tip, and is the best estimation for the geometrical model describing AFM imaging. We will see later that we can also estimate which parts of P_r can be different to P, and plot this information in a "certainty map".

On the other hand, if the shape of the tip is known, one can obtain an estimation of the sample surface S_r, using the formula

$$S_r = I \ominus P. \tag{4.14}$$

Similarly to P_r and P, S_r is an upper bound of the real topography S, and the parts of S_r which can differ from S can also be represented in a "certainty map".

The certainty map $c(x, y)$ is an array of the same size as the reconstructed image $s_r(x, y)$, and contains only 0's and 1's. Where $c(x, y)$=1, the reconstructed image is equal to the real one. Where $c(x, y)$=0, the reconstructed image can be equal or greater than the real surface. Following the geometrical reasoning, the pixels where $c(x, y)$=1 correspond to locations where the tip and the surface have a single point of contact, while pixels where $c(x, y)$=0 correspond

to locations where the tip and the surface have multiple points of contact.

There are however a few limitations to these algorithms. First, applying erosion algorithms to noisy AFM images would produce bad reconstructed surfaces, as noise spikes would be interpreted as real topographic features. Thus, filtering has to be performed before eroding the AFM images. Then, distortions due to the scanner properties also lead to wrong results. Thus, the correction of the distortion has to be performed first, using the algorithms described in 4.6.1.

Examples

The algorithms for erosion and for determining the certainty mapping were coded in Matlab. Before applying the erosion algorithms to the images, the distortions due to the AFM scanner were corrected and a median filter was used to reduce the noise.

Estimation of the tip shape. Many different substrates can be used for the estimation of the tip shape, such as microspheres, circular depressions or sharp features. For Famars, the tip characterizer is an array of sharp silicon tips (see 4.5). As there are many identical sharp tips on this substrate, we can get a statistical estimation of the AFM tip shape.

As an example, consider the AFM image of the tip characterizer shown in 4.33, whose distortions have been previously corrected. This image I was composed of about one hundred dilations between the unknown shape P of the AFM tip and the known shape T of the tips of the characterizer substrate. Thus, eroding I by T gave about one hundred estimations of P. In order to perform the erosion algorithm, T was modeled by a cone having the height and the opening angle of the tips of the substrate. Note that the pixels of T were set to the same width in μm than the pixels of I.

Image 4.39.a) shows the results of $I \ominus T$ for an area located near the upper right corner of I. Each bump therefore represented an

estimation of the AFM tip. In order to obtain the best estimation, statistical average of the results or similar operation could be interesting. However, for preliminary testing of the algorithms, a single estimation P_r was chosen among all the results, and is shown in figure 4.39.b).

Before using this estimation in further algorithms, one should note that the "floor" of the image is not an estimation of the AFM tip. Due to the limited height of the sharp tips on the substrate, only the parts of the AFM tip which entered into contact with the substrate could be estimated. Thus, one had to remove the "floor" in image 4.39.b) before using it to correct other AFM images.

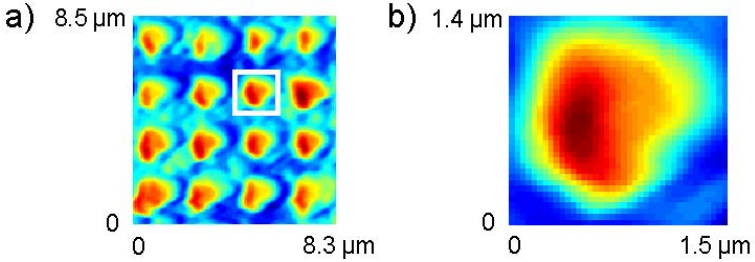

Figure 4.39: a) Some of the estimations of the AFM tip shape found by erosion of image 4.33. The estimation in the white square was selected. b) Larger view of the selected estimation.

Reconstruction of an unknown image. Using the obtained estimation P_r of the AFM tip shape, the topography of any sample imaged by the same tip could be reconstructed, assuming that the shape of the tip has not changed between the two images. Thus, the AFM image J of the strong magnet discussed previously (see figure 4.34.c) could be eroded by P_r to obtain a better representation S_r of the surface. Figure 4.40 shows the AFM image J on the left and the reconstructed image S_r on the right. The diameters of the two holes are larger on the reconstructed image, with about 10%. This

is why this operation is called erosion, by analogy to the geological phenomenon. A drawback of the erosion is the treatment of the borders of the AFM image. For the upper hole, the borders of the image were "too eroded". This is a typical artifact of the erosion algorithm, as information about the surroundings of the AFM image was not available, but could have played a role in the image formation.

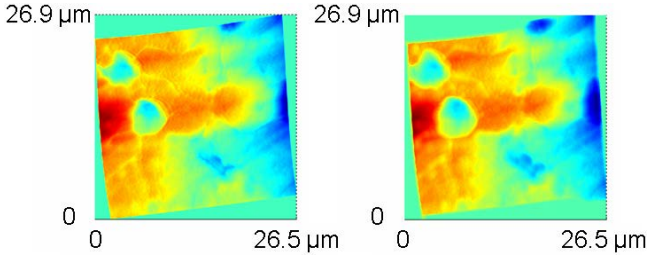

Figure 4.40: a) AFM image of the strong magnet substrate (after correction of the distortions). b) Reconstructed image obtained by eroding image a) by the estimated shape of the sensor tip.

Even if the result of the erosion was closer to the real topography than the initial image, this representation was only an approximation. First, locations on the sample which could not be accessed by the tip during measurements were naturally still unknown, such as holes with high aspect ratios. Secondly, the AFM image J was eroded with an approximation of the tip P_r, and not by the real shape P of the tip. Since P_r only approximated a certain portion of the AFM tip (starting from the apex), the features deeper or higher than the sharp tips of the characterizer substrate were not corrected. In other words, if the contact point between the tip and the sample was in the unknown portion of the AFM tip estimation (near the base), the erosion algorithm has not eroded sufficiently the AFM image. Therefore, we known that the erosion is a "minimal" process, i.e. that the real size of the holes are equal to or larger than the obtained sizes, and those of the bumps are equal to or smaller than the obtained ones.

Certainty map. Certainty map allows knowing which points of the reconstructed image are equal to the real surface and which points can be different. However, this map can be obtained using the standard algorithms only if the height or the depth of the measured features is smaller than the height of the estimated tip P_r. Thus, as the holes of the strong magnet substrate were deeper than the height of P_r, another example is taken here to illustrate the certainty map algorithm. Image 4.41.a) is an AFM image of silica particles having a diameter of 0.5 μm (see also figure 4.13.b). This image was eroded by an estimation of the AFM tip shape, obtained by means of the tip characterizer substrate. Image b) shows the result of the erosion, and image c) the certainty map superimposed on the result of the erosion. The black pixels represent locations where the reconstructed image can be different from the reality, while the others should be equal to the real sample topography. Thus, the black area around the particles gives us the error margin for the size measurement. The border are also black, for the reasons mentioned above. The widths of the four borders are not the same, as they depend on the position of the maximum in the image P_r.

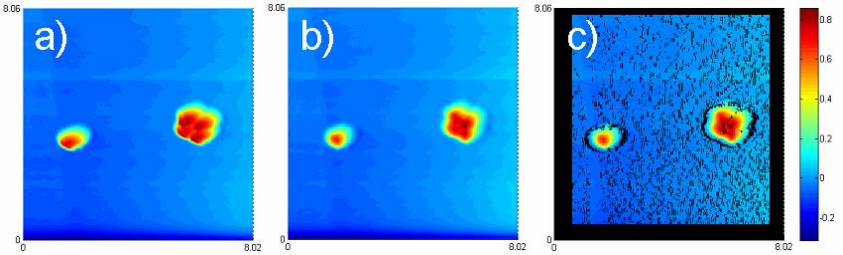

Figure 4.41: a) AFM image of 0.5-μm silica particles. b) Reconstruction obtained by erosion of image a) by an estimation of the tip shape. c) Certainty map superimposed in image b).

Summary

As the shape of the tip influences the size and the shape of the measured features, it is critical for our application to correct these artifacts. Applications of the erosion algorithms on several AFM images showed good results, but some points could still be improved. First, the modelization of the tips of the characterizer substrate by a cone was not optimal, as their opening angle varies versus height. Then, the statistics produced by the large number of imaged tips should be used. Finally, the major problem observed when applying these algorithms was that the only the apex of the AFM tip was estimated, due to the geometry of the tip characterizer substrate. According to an observation made when imaging the micromachined silicon substrate by means of a blunt tip (see 4.5.2), a larger portion of the AFM tip could be estimated by imaging the 5-μm pits. The next step should therefore to adapt the algorithms to obtain an estimation of the tip by eroding an AFM image of the pits.

4.7 Tip exchange

The Famars chip is composed of eight cantilevers ended by a sensor tip. As we saw in chapter 2, the chip is mounted with two tilt angles relative to the sample wheel surface, such as only one tip is touching the surface (see figure 2.2). If this tip is no longer usable, it is removed in order to access the surface with the next one. The whole beam sustaining the cantilever to be removed is therefore broken at its base using a special tool mounted on the SWTS, dubbed the cleaving tool. The cleaving procedure is given in this section, as well as the results of tests performed by the author at the IMT and by partners at Imperial College.

4.7.1 Description

The cleaving tool is a small bump protruding from a cylindrical base, which could be inserted in one of the holes of the sample wheel. Figure 4.42 shows drawings of the tool and of its mounting on the SWTS.

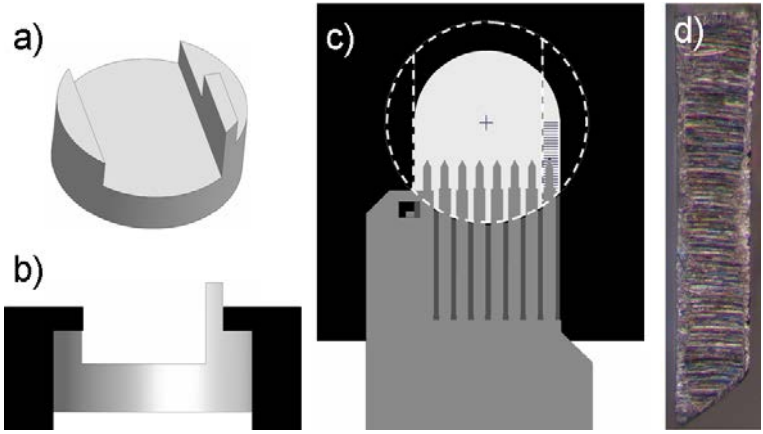

Figure 4.42: a) Drawing of the cleaving tool substrate, having a diameter of 4.15 mm. b) Schematics of the cleaving tool substrate inserted in the sample wheel (side view). The thickness of the SWTS rim is 0.5 mm. c) Schematics of the cleaving tool substrate inserted in the SWTS (front view), with the first AFM sensor in position for breaking. The dashed lines shows the borders of the cleaving tool hidden by the wheel. Note also that the rim of the wheel below this substrate was removed. d) Large view of the cleaving tool surface. The width of the tool is 0.35 mm. Note that the finishing lines are horizontal.

Some cleaving tools already existed from the 2001 mission, in a very limited number. A few experiments performed with them at JPL showed that they probably were too short for breaking the beams. Therefore, new cleaving tools with three different heights were built

at the IMT in a aluminum alloy[5] with a very good shape stability. Once mounted on the SWTS, the different tools were 300, 500 or 700 μm higher than the surface.

In addition, it was observed both at the JPL and at the IMT that the beam to be broken slid on the surface of the tool, resulting in a vertical motion of the whole chip. We limited this phenomenon by machining the tool such as the finishing lines at its surface were horizontal. Thus, the edge of the beam was somehow trapped between the lines, which reduced the sliding.

4.7.2 Testing of the cleaving procedure

The goal of this testing was to demonstrate the repeatability of the cleaving procedure. The distance needed to break the beam was measured, from the position of contact between the tool and the tip to the position of rupture of the beam. We also checked that the remaining sensors were not damaged during the process, both optically and using the signal generated by the piezoresistor of the next sensor.

4.7.3 Experiment

As no testbed was installed at the IMT, testing of the cleaving tool was performed using a setup especially built for that purpose. A Famars scanner was installed in front of a stage which could be translated manually using a micrometer screw. The cleaving tool was mounted on the stage, and lateral alignment with the beam to be broken was obtained using a second micrometer screw. The scanner was connected to the AFM electronics, and could therefore be controlled by means of the easyScanMars software. The AFM_near and V_{SIG} signals were monitored on an oscilloscope.

This setup was as similar as possible to the flight configuration. The vertical alignment between the AFM and the cleaving tool was

[5] Planoxal® (EN AW-6082), Alusuisse Nederland B.V., Breda, NL

checked, and the stage translation was normal to the front of the AFM scanner. The main difference was that the cleaving tool was not inserted in the SWTS, but glued to a flat aluminum surface. Not that most of the chip sensors were still alive, which allowed determining precisely the position of contact between the tool and the current tip.

The lateral and vertical alignments of the cleaving tool was checked using a microscope. Figure 4.43 shows the cleaving tool aligned on the first beam. Then, the sensor to be removed was initialized in static mode using easyScanMars, and the tool was translated toward it. By looking at the AFM_near signal displayed on the oscilloscope, we were able to stop the translation as soon as the tool reached the sensor tip. The corresponding position was read on the micrometer screw. Then, the next cantilever was set in static mode. The idea was to perform a sweep of the lever signal for this cantilever, triggered by the change of deflection produced by the breaking of the previous beam. Hence, the shape of this signal indicated if the cantilever touched any part of the cleaving tool substrate. Once the oscilloscope trigger was set, the tool was pushed slowly against the beam to be broken. As the chip is located on the suspended platform of the scanner (see 2.3), the force applied on the beam by the cleaving tool first resulted in a displacement of the platform, up and backwards. Then, if the translation was pursued, the beam broke, and the platform suddenly moved back toward the cleaving tool substrate. This motion could possibly damage the other cantilevers if they were too close from the substrate, so we looked at the position of the cantilevers after the process, as well as the recorded signal of the next alive sensor on the oscilloscope.

4.7.4 Results and discussion

The distance needed to break the beam was comprised between 0.51 mm and 0.66 mm for the tested chip, the references being the contact positions between the tool and each tip. The shock wave caused by the breaking of the beam has never created any problem neither for

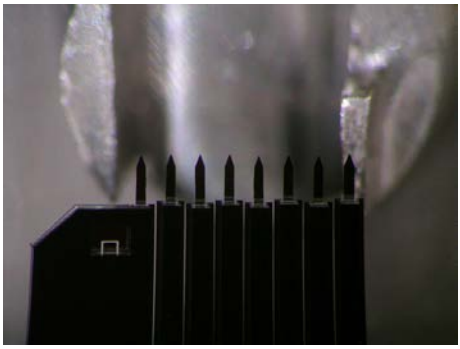

Figure 4.43: Optical image of the chip with the first cantilever in front of the cleaving tool.

the remaining sensors, nor for the other parts of the hardware.

The signal of the following cantilever's piezoresistor proved that the corresponding tip has never made contact with any part of the substrate, as expected based on the first optical check. Figure 4.44 shows the signal on the second piezoresistor recorded when the first beam was removed. The cantilever was bent a lot during this process, but went back in its initial position following regular damped oscillations. If it had touched the surface, the decay oscillations would have shown one or several positive peaks being cut, as the extension toward the substrate would have been interrupted by the surface.

In fact, we remarked that the part of the chip which could potentially be damaged was not the next cantilever, but the left part of the chip, where the reference piezoresistor is located. As one can see in image 4.43, this part was above the left protrusion of the cleaving tool substrate, especially when the first three beams were cleaved off. If a 500-μm high cleaving tool is used, there is a calculated gap of about 0.85 mm between the surface of the SWTS and the chip when the first tip touches the cleaving tool. As the distance needed to break the beam from that point should be less than 0.70 mm, the chip should not touch the wheel when it comes back in its initial position, with

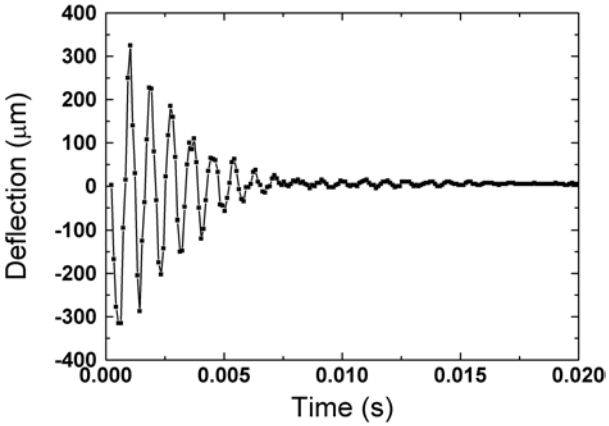

Figure 4.44: Deflection on the second piezoresistor recorded after the break of the first one. A positive value means a deflection toward the sample.

a margin of at least 150 μm.

Finally, the position of the break was not always at the base of the beam. In few cases, the break was several hundreds of micrometers above the base, as illustrated in figure 4.45. This could be a problem for accessing the surface with the last tips, as it was observed on a testbed at the Imperial College.

Figure 4.45: Image of the base of the beams after their removal by the cleaving tool. The position of breaking varies from one beam to another.

4.7.5 Test at Imperial College

After these preliminary results, further experiments were performed by our partners on the testbed at Imperial College, as it better reflected the characteristics of the flight system. In particular, the fact that the cleaving tool was mounted on the sample wheel was not included in the previous test. Figure 4.46.a) shows an image of the cleaving tool taken by the OM, with the two first AFM cantilevers visible at the bottom.

The results of these tests showed that the distance between the wheel and the cantilevers was sufficient to prevent any damage during the cleaving procedure. However, a problem was noticed. When performing the experiments, the first two beams were broken slightly above the base of the beam. This was not a problem in the beginning of the test, but when the seventh cantilever had to be removed, it was not accessible to the cleaving tool, as the rest of the first two beams already touched the surface of the wheel. This situation is depicted in figure 4.46.b).

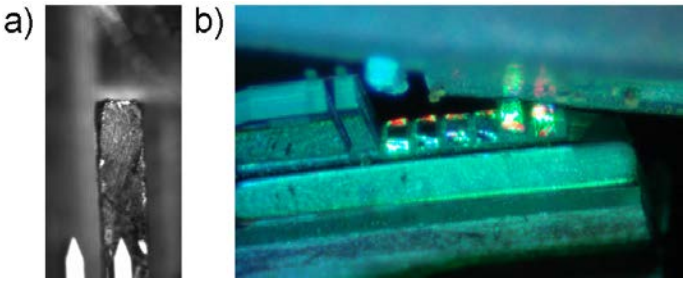

Figure 4.46: a) OM image of the cleaving tool in front of the first cantilever taken on a MECA testbed. b) Top view of the AFM chip pushed against the sample wheel. As the two first beams were not completely removed, they prevented the seventh cantilever from accessing the surface of the wheel. Note that in this image, the seventh cantilever was not positioned to be cleaved off. Courtesy Imperial College.

As the remnants of the beams were too low to be accessible with the cleaving tool, an attempt was made to crash them on the surface of the wheel. Using this audacious technique, our partners were finally able to access the surface with the last tips. This method includes of course some risks, as for example damaging the body of the chip, but it is the only applicable solution in this situation. However, as it appeared only for the two last tips, this is not a major issue for an instrument.

Finally, further testing was performed on the PIT by the MECA team, and a cantilever was broken successfully by means of one of the new cleaving tools. However, the VML sequence for the operations on Mars has still to be written and tested.

4.8 Tip cleaning

4.8.1 The cleaning substrate

During measurements, the AFM could catch particles. In that case, these particles either prevented taking images or at least created many artifacts in the images, such as black lines. This is due to the fact that these particles can move during scanning.

As we saw previously, the tip could be exchange in case of contamination. However, before doing that, it could possibly be cleaned using the so-called cleaning substrate. The latter, located on the SWTS, is a piece of silicone showing good adhesion properties. Thus, if it is brought into contact with the polluted tip, particles could adhere on the silicone, leaving the top of the tip free of particles.

In order to do so, the AFM is initialized in static mode. Then, a standard approach is performed, the stage being stopped when the silicone surface meets the sensor tip. Finally, the sample is withdrawn after this contact.

During the operations on Mars, the only way to see if the procedure was successful is to take an image of the tip characterizer substrate. Thus, an image of this substrate has to be taken after

each attempt. During measurements on Earth, an SEM of the tip could also be taken to check the state of the tip. Figure 4.47 shows two SEM images of a tip, taken before and after a cleaning procedure. The particle present on the top of the tip was removed.

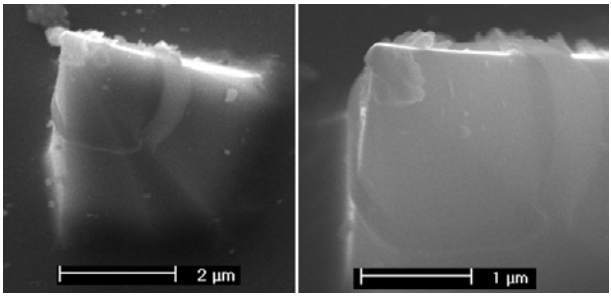

Figure 4.47: SEM image of a tip before (left) and after (right) the cleaning procedure. The particle at the very end was removed successfully.

4.8.2 Cleaning of the next sensors

In addition to the cleaning procedure described above, we accidentally discovered that breaking a beam by means of the cleaving tool means also cleaning the remaining sensors. Hence, the shock produced by the break tended to eject the particles present on the next cantilevers. In the left image of figure 4.48, one can see a broken cantilever and many particles on the other cantilevers, in particular on the next one. After having removed the cantilever-free beam, most of these particles were removed, as illustrated in the center image. The SEM image on the right shows the end of the current cantilever, which is almost free of contamination.

Note that this technique can not be used to clean the active sensor for trivial reasons. However, it is very useful to know that any contamination of the next sensors is greatly reduced when the current one is removed. In addition to reducing the risk of recording

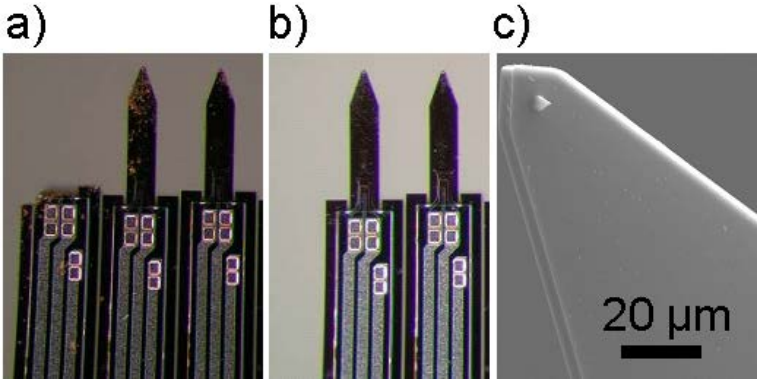

Figure 4.48: a) Picture of a broken cantilever with contamination on the others. The cantilever-free beam has to be removed. b) Picture taken after the removal of the beam. The contamination on the other cantilevers has almost disappeared. c) SEM image of the current cantilever after the removal of the first beam.

bad AFM images, it also prevents any cross-contamination of the substrates by particles attached to the cantilevers. As the particles are ejected toward the cleaving tool, the risk of a particle hitting the OM objective is also very small.

4.9 Conclusion

The Famars 2 scanner was calibrated under martian conditions. The requirement for the scan range was fulfilled, even if a reduction of about one third of its value at room temperature was observed at -20 deg C. Non-linear deformations of the scan area were observed, particularly for temperatures close to 0 deg C. However, imaging a calibration grid before each measurement should allow correcting these distortions in all AFM images, using the algorithms described in this chapter.

Measurements performed on fixed particles demonstrated that the instrument could measure particles in the size range of the martian dust. The shape and the size of the particles were modified by the geometry of the sensor tip, but these modifications could be estimated and corrected by means of erosion algorithms. An estimation of the size distribution of a known sample was performed according to AFM images, and showed satisfying results.

Mars analogues measurements indicated that the instrument could not be operated successfully in any situation. The size of the particles, their arrangement on the substrate and their adhesion with it were key parameters, and it was shown that optical observation of the sample provided a good way to estimate them. One of the prepared samples was acceptable for AFM measurements, and produced valuable data on the size and the shape of the particles.

AFM images of the SWTS substrates were realized. First, it was verified that magnetic fields of the magnet substrates did not affect the scanning behavior of Famars. Second, measurements on the silicon micromachined substrate showed that the instrument could have difficulties accessing the bottom of pits with an aspect ratio of one. This indicated also that this substrate could be use to estimate the shape of the AFM tip, as a complement of the estimation produced with the tip characterizer substrate. Finally, it was proven that particles deposited on the silicone substrate stayed in place during AFM measurements.

Based on the mentioned observations, the following procedure should be applied when interpreting AFM images of particles. First, the distortions due to the scanner have to be corrected, using an image of a calibration grid. Then, the recorded error signal should be checked, in order to verify that the feedback loop was efficient. If this is the case, the topographic images recorded in forward and backward directions show the same features. Note that if noise is present in the images, median filtering can be applied to reduce it. Then, the deformations and the enlargements caused by the shape of the AFM tip should be corrected by applying the erosion algorithms. At that

point, the features on the AFM image should be close to the sample geometry. In order to facilitate the interpretation of these images for a human eye, the images can be displayed in three-dimensional or derivative view. This should allow having a first idea of the size and the shape of the particles. Then, software tools can be applied to the AFM images in order to determine precisely the size, the shape and the distribution of the particles.

In parallel to imaging, the tip exchange procedure was tested. The cleaving tool was able to remove the desired sensor without damaging the next one. However, the break position was not always exactly at the base of the silicon beams, and this could have prevented the last sensors from accessing the surface of the SWTS. Finally, the decontamination of the apex of a tip by means of a silicone substrate was demonstrated.

References

[1] S. Gautsch. *Development of An Atomic Force Microscope and Measurement Concepts for Characterizing Martian Dust and Soil Particles.* PhD thesis, University of Neuchâtel, Switzerland, 2002.

[2] C. Bergenstof Nielsen, C. Christensen, C. Pedersen, and E.V. Thomsen. Particle Precipitation in Connection with KOH Etching of Silicon. *J. of The Electrochemical Society*, 151:G338–G342, 2004.

[3] P. Nornberg, H.P. Gunnlaugsson, K. Kinch, and J. Merrison. Salten Skov I: A Martian dust analogue. *Geophysical Research Abstracts*, 6:03168, 2004.

[4] P. Toulmin, A.K. Baird, B.C. Clark, K. Keil, H.J. Rose, P.R. Christensen, P.H. Evans, and W.C. Kelliher. Geo-chemical and Mineralogical Interpretation of the Viking Inorganic Chemical Results. *J. of Geophysical Research*, 82:4625, 1977.

[5] P. Chylek and G.W. Grams. Scattering by Nonspherical Particles and Optical Properties of Martian Dust. *Icarus*, 36:198–203, 1978.

[6] O.I. Korablev, V.A. Krasnopolsky, and A.V. Rodin. Vertical Structure of Martian Dust Measured by Solar Infrared Occultation from the Phobos Spacecraft. *Icarus*, 102:76, 1993.

[7] K. Leer et al. Magnetic Properties Experiments and the SSI calibration target onboard the Mars Phoenix 2007 Lander. Design, calibration and science goals. *Submitted to J. of Geophysical Research*, 2007.

[8] S. Vijendran, H.M. Sykulska, and W.T. Pike. AFM investigation of Martian soil simulants on micromachined Si substrates. *J. of Microscopy*, 227:236–245, 2007.

[9] M. Unser, M. Eden, and L. Trus. Unwarping of slightly distorted periodic structures using bidimensional polynomial representations. *Signal Processing*, 12:83–91, 1987.

[10] K.L. Westra, A.W. Mitchell, and D.J. Thomson. Tip Artifacts in Atomic Force Microscope imaging of Thin Film Surfaces. *J. Appl. Phys.*, 74:3608, 1993.

[11] D. Nyyssonen, L. Landstein, and E. Coombs. Two-dimensional atomic force microprobe trench metrology system. *J. Vac. Sci. Technol. B*, 9:3612, 1991.

[12] J.S. Villarrubia. Algorithms for Scanned Probe Microscope Image Simulation, Surface Reconstruction, and Tip Estimation. *J. Res. Natl. Inst. Stand. Technol*, 102:425, 1997.

Chapter 5

Summary, Conclusions and Outlook

5.1 Technical achievements

5.1.1 Hardware

An atomic force microscope was built for the Phoenix Mars mission. The scanner head of the instrument was designed by further development of a previous version, and ten scanners were constructed. The scanner produced a maximal x-y scan range of more than forty micrometers, and a vertical range of about ten micrometers. As it relied on an original polyimide spring-system, its properties at low temperature were improved compared to the former version. However, non-linear deformations of the scan plane were observed, and image processing tools were created to correct them.

Using the former design, new silicon chips were fabricated, characterized and mounted on the scanners. A study of the p-n junctions within the chip showed that there was a threshold value for the voltage applied to the sensor tips, generally close to -3V.

The instrument went successfully through fatigue tests, accelerated tests for the wire bonds and environmental testing. After having

been calibrated, the flight and the flight spare scanners were delivered to the Jet Propulsion Laboratory.

5.1.2 Software

Flight software commands were written in pseudo-language, based on the experience acquired using the instrument under laboratory conditions. After their encoding by a programmer from JPL, testing of the commands was performed on the hardware. Even if a few simplifications were brought compared to the algorithms described in pseudo-language, the final set of commands allowed taking good images on a testbed. Finally, these commands were implemented in a simple VML sequence, and images were taken by sending it to the Phoenix Lander testbed.

5.2 AFM measurements

Measurements performed on fixed particles demonstrated that the instrument could measure objects with diameters between 0.1 and 5 micrometers. The shape and the size of the particles were modified due to tip artifacts, which could be estimated and corrected by means of erosion algorithms. These algorithms were tested on AFM images, and initial results were encouraging. The size distribution of the particles in an image was also determined successfully, tip artifacts causing however a shift in the measured sizes.

Measurements of Mars analogues indicated that the instrument could not operate on any kind of samples delivered to it. The size of the particles, their arrangement on the substrate and their adhesion with it were key parameters. In particular, it was observed that imaging particles arranged in piles was very difficult, and possibly harmful for the sensor chip. During the operations on Mars, imaging the samples by means of the optical microscope should allow determining the feasibility of AFM measurements. If it appears that the particle coverage for the samples delivered by the robotic

arm does not permit atomic force microscopy, samples acquired by air fall experiments should at least allow characterizing the martian dust particles.

In order to increase the adhesion of the particles, various substrates had been fabricated by our partners and installed on the sample wheel. Two of these substrates relied on magnetic properties. As the scanner was based on electromagnetic actuation, a possible influence of these magnetic substrates on its behavior was studied. It was shown that such was not the case, and some particles were imaged on the magnets. A microstructured silicon substrate had also been built to catch and fix the particles. Imaging this substrate without particles showed that the sensor tip could have difficulties accessing the bottom of the pits presenting an aspect ratio equal or larger than about one. That artifact can theoretically be used to estimate the shape of the AFM tip, similarly to what was already achieved by measuring an array of sharp pins. Finally, it was proven that particles deposited on the silicone substrate stayed in place during AFM measurements.

The possibility of using all the sensor tips of the chip was scrutinized by testing the exchange procedure. While the cleaving tool removed the desired sensor without damaging the next ones, the use of the last two sensors was not always possible, as the rest of the first sensors prevented them from accessing the sample. The decontamination of the apex of a tip by means of a silicone substrate was demonstrated, which allows using the same tip for several experiments.

5.3 Further work

At the time of writing, the Phoenix Lander is in cruise, and the different teams of the mission are preparing the operations. Concerning the Famars instrument, a few important tasks still have to be done.

First, all the VML sequences for the instrument have to be delivered in the near future. In particular, a sequence allowing taking

nested scans has to be developed, as well as a sequence for exchanging the sensor tip. The latter needs further testing, as only a couple of sensors have been removed using flight software commands. The sequence for imaging needs also to be tested on the Lander testbed, during an interoperability experiment including the robotic arm, the sample wheel and the optical microscope.

Further measurements on various kinds of particles should be performed on the testbeds, in order to create a wider database for interpreting the measurements on Mars. As time and resources risk being limited until the operations, this task could also be pursued after the mission.

Finally, the image processing toolbox has to be improved. The erosion algorithms should be improved by performing a statistical approximation of the tip. In addition, they should be able to approximate the shape of the sensor tip based on an AFM image of the micromachined 5-μm pits. The distortion algorithms need also to be improved, as images taking with x or y offsets can not be corrected at the moment. Finally, a tool for automatically determining the size distribution in an AFM image should be created.

5.4 Outlook

5.4.1 Applications for space

The silicon sensor chip of Famars could open new horizons for MEMS in space. If the working behavior of the chip is demonstrated after the launch, the cruise and the landing on Mars, it will confirm that microfabricated devices are a real option for planetary exploration.

The research on the properties of Kapton at room and low temperature have shown that polyimides could be used as mechanical parts in future space applications. The integration of metal lines as electrical connections could be very interesting for special applications.

5.4.2 AFM for Mars Exploration

As long as sample return missions are not sent to Mars, atomic force microscopy will probably remain the best method to characterize the size and the shape of sub-microscopic particles of the martian dust and soil. It could therefore be involved in other Scout missions, or in other projects, as for example the Astrobiology Field Lab proposed by NASA, which would conduct a robotic search for life. As it would analyze in detail the geologic environments favorable to life, an AFM could give precious information. AFM could also be used in human missions to Mars. As in this case an operator could run the instrument in real time, it would greatly facilitate the measurements (sample selection, scan settings adjustment, sensor exchange).

Even if humans are not involved in the measurements, further improvements could be achieved. The delivery process could sort the particles to keep only the smallest ones, which are not harmful to the sensors. A fine grid placed over the collecting substrate could work as a sieve. Use of mechanical vibrations could probably prevent the material from staying perched on the grid.

Moreover, extended functionality could be brought to the instrument itself. An automatic adjustment of the scan settings would be very useful. For the Phoenix mission, this adjustment can only be made a posteriori by looking at the quality of the returned data. The development of the "smartzoom" routine could also be pursued, as it would increase the scientific contents of the AFM images.

List of Acronyms

ABL AFM Boot Loader

AFM atomic force microscope

AFMCSW AFM Control Software

ADC analog to digital converter

BSG borosilicate glass

CME Control and Measurement Electronics

CVD chemical vapor deposition

DAC digital to analog converter

DRIE deep reactive-ion etching

EDR experimental data record

EQM engineering qualification model

ESD electronic discharge

EVR event reporting

Famars First AFM on Mars

Famars 1 first generation of Famars

Famars 2 second generation of Famars

FM flight model

FPGA field programmable gate array

FSW flight software

FS flight spare model

GUI graphical user interface

IC integrated circuit

ITAR International Traffic in Arms Regulations

IMT Institute of Microtechnology

JPL Jet Propulsion Laboratory

LS limit switch

MCO Mars Climate Orbiter

MGS Mars Global Surveyor

MARDI Mars Descent Imager

MECA Microscopy, Electrochemistry, and Conductivity Analyzer

MET Meteorological Station

MER Mars Exploration Rovers

MFSW MECA Flight Software

MEMS Micro Electro Mechanical Systems

MPL Mars Polar Lander

MSP'01 Mars Surveyor Program 2001

NCO numerically controlled oscillator

OM Optical Microscope

ORT Operational Readiness Test

PACI Payload Attitude Control Interface

PC personal computer

PCB printed circuit board

PECVD plasma-enhanced chemical vapor deposition

PGA programmable gain amplifier

PIT payload interoperability testbed

PLL phase locked loop

PROM programmable read-only memory

PSG phosphosilicate glass

RA Robotic Arm

RAM random access memory

RAC Robotic Arm Camera

SEM scanning electron microscope

SOI silicon-on-insulator

SPM scanning probe microscope

SSI Surface Stereoscopic Imager

STM scanning tunneling microscope

SWTS Sample Wheel and Translation Stage

TECP Thermal and Electrical Conductivity Probe

TEGA Thermal and Evolved Gas Analyzer

VML Virtual Machine Language

WCL Wet Chemistry Laboratory

Acknowledgments

I would like to express my gratitude to all the people who have contributed to my thesis. First of all, I sincerely thank Prof. Urs Staufer, my thesis director. I appreciated his never-ending flow of ideas, and the time that he devoted to discussions with me (even though there was always a PhD student knocking on his door). My heartfelt thanks go to Prof. Nico de Rooij, who gave me the opportunity to work in his enthusiastic team in a stimulating research environment. I am also grateful to Prof. W.T. Pike and Prof. H. Shea for accepting the co-examination of this doctoral thesis, as well as for their support during my thesis (see below).

The realization of the Famars instrument is the result of an intensive collaboration with many research partners. I would like to thank the people at Nanosurf in Liestal, who conceived the Famars control software and contributed to the design of the new scanner. Especially, my thanks go to Dominik Brändlin-Müller and Lukas Howald for their advice and help in solving many problems.

The space-qualified electronics have been designed, assembled and characterized by the electronics department of the Institute of Physics of the University of Basel. Many thanks to Hans-Rudolf Hidber and Andreas Tonin, who put their skills in electronics to work once more when Famars was reselected for a Mars mission.

Without the MECA team, flying the Famars instrument would not have been possible. I would like to thank the JPL team, led by Michael Hecht, for all the support and the discussions. Thanks to Michael Hecht also for his great hospitality, his advice and the trust he had in our team. Among other people at JPL, I would especially like to thank John Michael Morookian, Alan Mazer and Claus Mogensen for their fruitful collaboration. Thanks also to Prof W. Thomas Pike and his group at the Imperial College in London, who did an impressive work in the characterization of Famars. Thanks to Hanna Sykulska and Sanjay Vijendran for their constant efforts and their friendship. I look forward to working with the whole MECA team again during the operations!

Of course it would not have been possible to accomplish all the work without the help of the samlab team. Thus, I sincerely thank:

- Sebastian Gautsch, for the heritage he left the Famars project, and for introducing me to it. His encouragements at the beginning of my thesis were very appreciated, as well as his answers to my questions.
- Terunobu Akiyama, the father of the Famars chip, for sharing his microfabrication secrets. Thanks also for the enormous box of baby clothes...
- The other members of the nanotools team: Friedjof Heuck (the extreme climber), Raphaël Imer (the nano-butcher, who also contributed to the Famars project), Laure Bridget Aeschimann (my teacher in teaching microfabrication), Maurizio Gullo (recruited by Nanosurf), Thomas Hug (who taught me how to fill a nanochannel), Gregor Schürmann (who made a too short appearance), Anpan Han (a Sablons veteran), Kaspar Suter (my companion during those hectic nights of thesis writing), Dara Bayat (my right hand, see below).
- The cleanroom staff, for their contributions to the Famars project and to the students courses: Sylvain Jeanneret, Pierre-André

Clerc, Rémy Fournier, Stéphane Ischer, Sabina Jenny, Edith Millotte, Sylviane Pochon (still a small wire bonding to do...), Eduardo Santoli, Jose Vaquera, Gianni Mondin, and Nicole Hegelbach Guye. Thanks also to Giovanni Bergonzi for introducing a Jurassian to Labview programming.

- Peter van der Wal for his expertise in the chemistry lab and his sarcastic jokes.
- Massoud Dadras and Mireille Leboeuf for their excellent microscopy service and Christmas desserts.
- Florence Rohrbach and Karine Frossard for their helpful skills in administration. I hope that everything is fine with the customs now...
- The computer guru Claudio Novelli for his great support and his famous morning jokes.
- Antonia Neels and Laure-Emmanuelle Perret-Aebi for the good working atmosphere in the office we shared.
- All my colleagues for their help and/or for making the lunch time a good break in the day.

Staying in the surroundings, I would like to thank Prof. H. Shea and the LMTS group for their friendship, for sharing their lab equipment, and for the access to their vast library.

Several students have contributed to this work during their six-month projects, namely Anupama Gangadharaiah, Dara Bayat and Arif Zeeshan. I was also helped by Daniel Schwyn, who did an internship at the samlab during a sabbatical break. It was a pleasure to work with them all, even when some AFM tips were accidentally broken.

I also think with gratitude of my high-school mathematics teacher, Jean-Louis Sauser, who awoke a scientific interest in a Latinist student.

I am very grateful to my parents Monique and Jean-Paul for their loving support during all my years of study, and to my wife Charlotta for the time she spent correcting my English.

Last but not least, this work would not have been possible without the valuable financial support of the Wolfermann-Nägeli Foundation and the Space Center at EPFL.

Posters and publications

D. Parrat, S. Gautsch, T. Akiyama, N.F. de Rooij and U. Staufer, Design and evaluation of a polyimide spring system for the Scanning Force Microscope of the Phoenix Mars Mission 2007, *6th CMI-ComLab revue*, Ecole Polytechnique Fédérale de Lausanne, Lausanne, Switzerland, 2005.

D. Parrat, S. Gautsch, L. Howald, D. Brändlin-Müller, N.F. de Rooij and U. Staufer, Design and Evaluation of a Polyimide Spring System for the Scanning Force Microscope of the Phoenix Mars Mission 2007, *Proceedings of the 11th European Space Mechanisms and Tribology Symposium*, pages 281-287, Lucerne, Switzerland, 21-23 September 2005.

D. Parrat, S. Gautsch, T. Akiyama, L. Howald, D. Brändlin-Müller, A. Tonin, H.-R. Hidber, M. Hecht, W.T. Pike, N.F. de Rooij and U. Staufer, The FAMARS Instrument: An Atomic Force Micrscope for the Phoenix Mission, *Proceedings of the Fourth International Conference on Mars Polar Science and Exploration*, Davos, Switzerland, 2-6 October 2006.

D. Parrat, S. Gautsch, L. Howald, D. Brändlin-Müller, C. Mogensen, M. Hecht, N.F. de Rooij and U. Staufer, Polyimide Spring System for the Scanning Force Microscope of the Phoenix Mars Mission 2007, *7th CMI-ComLab revue*, Ecole Polytechnique Fédérale de Lausanne, Lausanne, Switzerland, 2006.

M.H. Hecht, J. Marshall, W.T. Pike, U. Staufer, D. Blaney, D. Brändlin, S. Gautsch, W. Goetz, H.-R. Hidber, H.U. Keller, W.J. Markiewicz, A. Mazer, T.P. Meloy, J.M. Morookian, C. Mogensen, D. Parrat, P. Smith, H. Sykulska, R.J. Tanner, A. Tonin, S. Vijendran, M. Weilert and P.M. Woida, Microscopy capabilities of the Microscopy, Electrochemistry, and Conductivity Analyzer (MECA), *Submitted to J. of Geophysical Research*, 2008.

A-1 Hardware

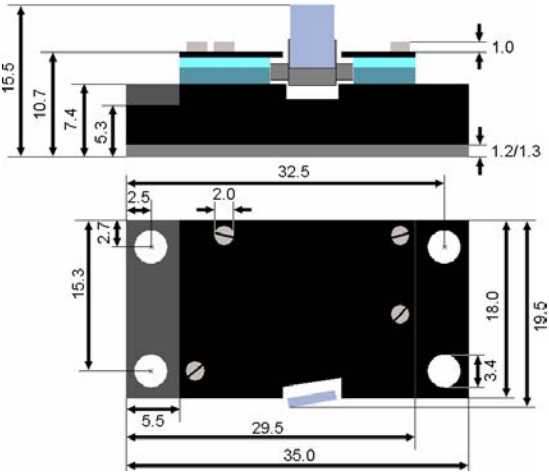

Figure A-I: External dimensions of the AFM scanner (without the flexprint PCB).

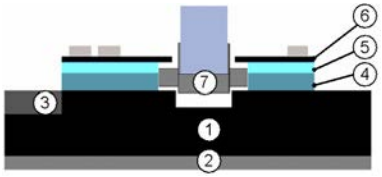

Figure A-II: Names of the aluminum parts composing the AFM scanner: 1) Main part; 2) Bottom part; 3) Lateral part; 4) Lower plate; 5) Upper plate; 6) Cover; 7) Suspended platform.

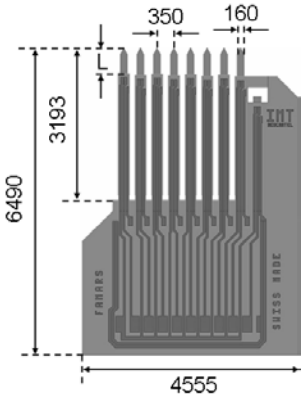

Figure A-III: Dimensions of the Famars sensor chip (in micrometers). The length L is different for each cantilever (value between 568 and 633 micrometers) to reduce the cross talk between the cantilevers.

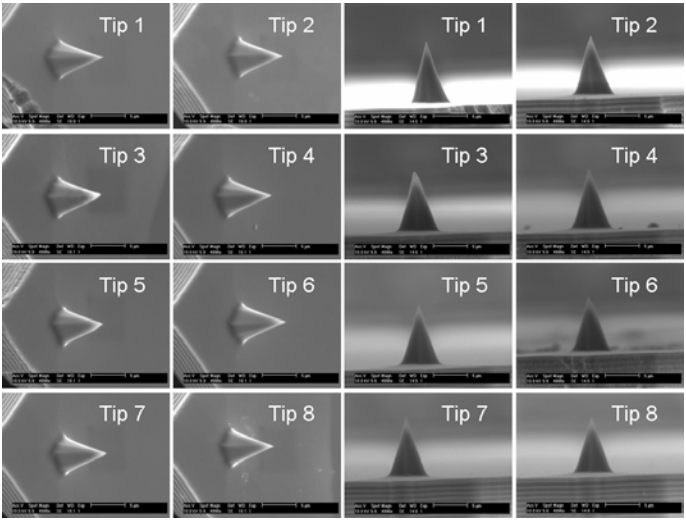

Figure A-IV: SEM images of the Flight Model tips taken with two different angles of view.

A-2 Software

Table A-I: MECA Flight Software AFM parameters.

ID	Parameter	Definition
0	afmbrk_coupon	The coupon index of the coupon to use for breaking tips, where the first coupon is numbered 0.
1	afmbrk_steps	The number of steps past AFM-near assertion required to break the tip.
2	afm_dynamic_i_gain	I-gain to use for dynamic mode.
3	afm_dynamic_p_gain	P-gain to use for dynamic mode.
4	afm_dynamic_set-point_hivap_in_mv	Setpoint used when Vap is high but not unusable.
5	afm_dynamic_set-point_lovap_in_mv	Setpoint used for nominal Vaps.
6	afm_gap_voltage_in_mv	Voltage applied to the tip.
7	afm_hexfile_length	Length of the file in bytes.
8	afm_max_imaging_re-starts	The max. number of times MFSW will restart imaging in dynamic mode after stopping for a bad Vap.
9	afm_max_range	The max range in microns for both axes.
10	afm_max_tip_noise	The maximum acceptable range of values during a tip test. The variation represents noise about zero.
11	afm_max_x	Unused.
12	afm_max_y	Unused.
13	afm_max_z	Unused.
14	afm_middle_vap_thres-hold_in_mv	If the Vap value is higher than this threshold, MFSW uses the higher setpoint specified by parameter 4.

ID	Parameter (*contd.*)	Definition (*contd.*)
15	afm_noise_middle_threshold	The threshold against which the sum of min and max scan values from the tip test are compared. As the sum should be close to zero, a sum above this threshold indicates a bad tip.
16	afm_physical_max_x_in_um	The physical maximum for the x dimension in micrometers.
17	afm_physical_max_y_in_um	The physical maximum for the y dimension in micrometers.
18	afm_physical_max_z_in_dum	The physical maximum for the z dimension in tenths of a micrometer.
19	afm_pll_i_gain_appr	The PLL I-gain to use for approach.
20	afm_pll_i_gain_frqtest	The PLL I-gain to use for the frequency test.
21	afm_pll_loop_gain	The PLL loop gain, as described in the AFM protocol manual.
22	afm_pll_steps_in_sweep	The number of steps the PLL should make in looking for a resonance frequency. This parameter multiplied by parameter 27 gives the total sweep range in Hz.
23	afm_prescan_z_threshold	The maximum sample height expected by the prescan algorithm.
24	afm_static_i_gain	I-gain to use for static mode.
25	afm_static_p_gain	P-gain to use for static mode.
26	afm_static_setpoint_in_mv	Default setpoint to use for static mode.
27	afm_step_frq_in_hz	The frequency step the PLL should use in looking for a resonance frequency.
28	afm_tip_break_enabled	If 0, tip breaking is disabled.

ID	Parameter (*contd.*)	Definition (*contd.*)
29	afm_upload_length	The number of bytes of AFM code actually uploaded to the AFM. Doesnt include file whitespace.
30	afm_upper_vap_threshold_in_mv	The highest Vap allowable in dynamic mode.
31	afm_x2y	A value between -10 and 10, scaled to the -1 to 1 range, indicating how y varies with changes in x.
32	afm_x_slope_in_deg_current	The current estimated slope in x.
33	afm_x_slope_in_deg_nominal	The baseline slope in x.
34	afm_y2x	A value between -10 and 10, scaled to the -1 to 1 range, indicating how x varies with changes in y.
35	afm_y_slope_in_deg_current	The current estimated slope in y.
36	afm_y_slope_in_deg_nominal	The baseline slope in y.
37	apid_afm	The APID used for AFM science data, including low-level responses.

Table A-II: MFSW command arguments used for AFM measurements.

Argument	Description
afm_adc_mask	Specifies which ADCs to read.
afm_attrib_id	Specifies which AFM attribute to set.
afm_fwdbk	Specifies if the forward and/or the backward scans are recorded.
afm_igain	Specifies the integration gain of the feedback loop.

Arg. (*contd.*)	Description (*contd.*)
afm_msperln	Specifies the scan speed in milliseconds per line.
afm_pgain	Specifies the proportional gain of the feedback loop.
afm_sampmsk	Specifies if the output and/or the lever signals are recorded.
afm_scandir	Specifies the scan direction along the slow axis (up or down).
afm_scanrange	Specifies the size of the image.
afm_setpt	Specifies the setpoint of the feedback loop.
afm_smartzoom	Specifies if smartzoom is enabled.
afm_tip	Specifies the current AFM tip number.
afm_value	Specifies the value to give to an attribute.
afm_wd	Gives the address of the raw AFMCSW to execute.
afm_wd2	Gives the address of the raw AFMCSW to execute.
afm_wd(...)	Gives the address of the raw AFMCSW to execute.
afm_wd22	Gives the address of the raw AFMCSW to execute.
afm_xpts	Specifies the maximal scan width in pixels.
afm_ypts	Specifies the maximal scan height in pixels.
eps_off_on	Specifies whether or not power should be on.
stg_dir	Specifies the motor movement direction.
stg_motors	Specifies which motor(s) to initialize.
stg_ovrrd	Specifies whether to ignore safe-to-rotate limit switch.
stg_rot_ref	Specifies the reference position for rotation.
stg_steps	Specifies the motor steps (position or movement).
stg_xlt_ref	Specifies the reference position for translation.
cmd_component	Identifies the component to be enabled or disabled.

Arg. (*contd.*)	Description (*contd.*)
cmd_enabled	Determines if a component is to be enabled or disabled.
cmd_par_id	Specifies the parameter table item id.
cmd_par_value	Specifies the new value for the selected item.
tbl_type	Specifies which table to reference.

Table A-III: EVRs critical for the AFM.

Item	Description
mc_afm_bad_setup_fast_evr_id	FSW encountered error configuring fast scan axis
mc_afm_bad_setup_slow_evr_id	FSW encountered error configuring slow scan axis
mc_afm_boot_failed_evr_id	Bootup failed
mc_afm_cmd_error_backward_evr_id	Attempt to read backward scan data from AFM failed
mc_afm_cmd_error_forward_evr_id	Attempt to read forward scan data from AFM failed
mc_afm_getline_aborted_evr_id	Line scan was aborted because the instrument is saf-ing
mc_afm_getline_error_evr_id	Internal error bad AFM command passed to FSW afmGetLine routine
mc_afm_hexfile_length_evr_id	AFM code upload had unexpected length
mc_afm_init_failed_evr_id	General init failed
mc_afm_lever_dead_evr_id	AFM tip appears to be dead
mc_afm_lever_noisy_evr_id	AFM tip is noisy but otherwise acceptable
mc_afm_lever_not_centered_evr_id	AFM noise is not centered around zero

Item (*contd.*)	Description (*contd.*)
mc_afm_lever_out_of_range_evr_id	AFM tip appears to be dead (FSW will retry one time before giving up)
mc_afm_piezo_dead_evr_id	Frequency test shows piezo excitation to be dead
mc_afm_scanning_failed_evr_id	Scanning paused and then failed
mc_afm_scanning_failed_2_evr_id	Scanning restarted and then failed
mc_afm_upload_failed_evr_id	Indicates that uploading code to AFM processor failed in one or more steps
mc_afm_upload_length_evr_id	The number of bytes successfully uploaded was unexpected
mc_afm_vector_bad_npts_evr_id	Internal error FSW routine afmVector request has zeroed number of points
mc_afm_vector_bad_range_evr_id	Internal error range is zero in X, Y or Z, in afmVector request
mc_afm_vector_bad_slope_evr_id	Internal error FSW is trying to scan sample with vertical slope
mc_cme_afm_read_timeout_evr_id	A FSW attempt to read data from the AFM instrument timed out
mc_cme_meca_afm_write_evr_id	An attempt to command the AFM through the PACI failed immediately, without sending any data

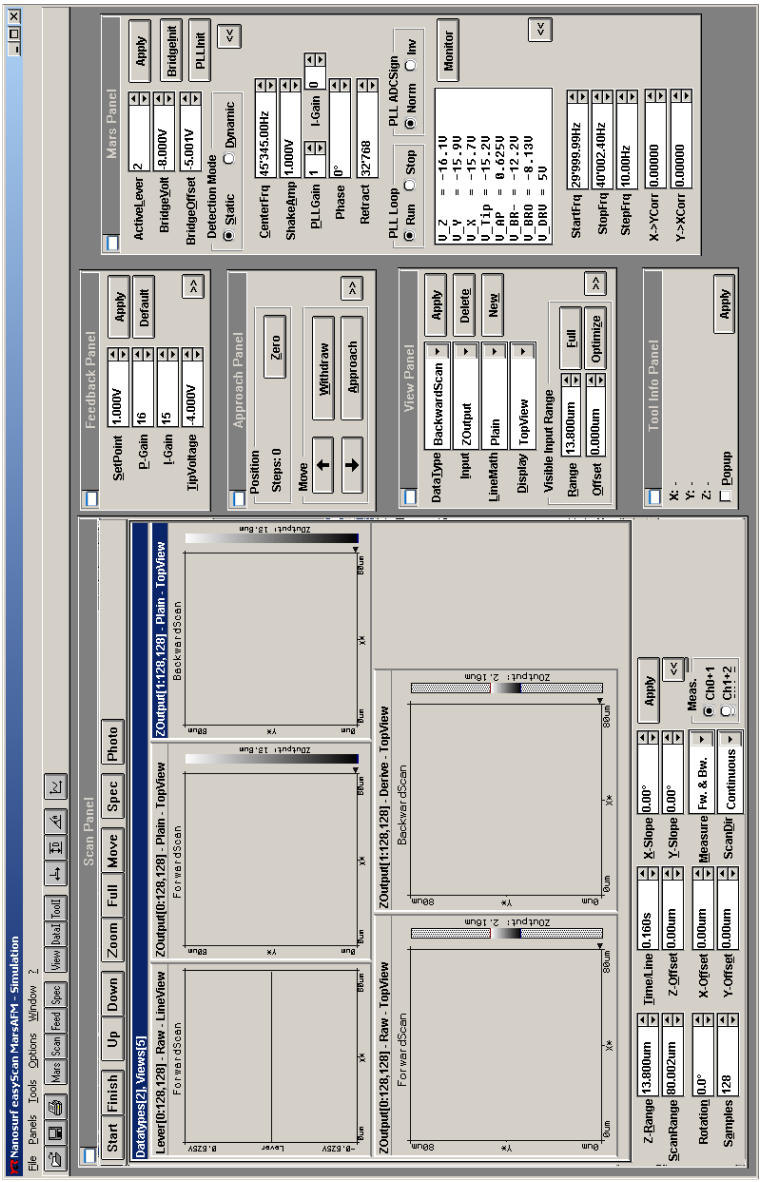

Figure A-V: The easyScanMars GUI.

Table A-IV: MECA Flight Software AFM attributes. These attributes correspond to the AFMCSW attributes.

ID	Attribute	ID	Attribute
0	auto_z_mode	22	pll_repeat
1	auto_ch1_gain	23	pll_start_frq
2	axis_select	24	pll_step_frq
3	axis_range	25	reg_hold
4	axis_position	26	reg_i_gain
5	bridge_neg	27	reg_input_corr
6	bridge_off	28	reg_locked
7	chan_gain	29	reg_p_gain
8	chan_offset	30	reg_pol_mask
9	chan_select	31	reg_set_point
10	chan_value	32	reg_zero
11	dyn_mode	33	retract
12	dyn_status	34	sample_mask
13	gap_voltage	35	serial_nr
14	lever_alive_mask	36	time_per_unit
15	lever_amp	37	offset_x
16	lever_select	38	axis_units_x
17	pll_ctr_frq	39	offset_y
18	pll_i_gain	40	axis_units_y
19	pll_loop_gain	41	offset_z
20	pll_mode	42	axis_units_z
21	pll_phase		